VHE Emission from TeV J2032+4130 and Iterative Deconvolution in Ground Based Gamma-ray Astronomy

Gary E. Kenny B.Sc.

Thesis submitted to the National University of Ireland, Galway
for the award of Ph.D in the
Department of Physics

Supervisor: Dr. M. Lang
Co-Supervisor: Dr. G. Gillanders

September 2007

For Helena & Hannah Beth

Abstract

This thesis describes an investigation of Very High Energy (VHE) γ-ray emission from the unidentified γ-ray source TeV J2032+4130. The analysis was based on archival data from the 1989-1990 observing seasons obtained using the Whipple 10-metre imaging atmospheric Cherenkov telescope in southern Arizona. Fifty hours of data were analysed using the standard *Supercuts* criteria, a set of optimised energy dependent parameter cuts, and the application of the multivariate *Kernel* analysis method. On the basis of detailed simulations of the detector, the VHE flux of TeV J2032+4130, above 1 TeV, was determined to be $(1.3 \pm 0.4 \pm 0.5) \times 10^{-8}$ $\mathrm{m}^{-2}\mathrm{s}^{-1}$. This corresponds to $\sim 6.2\%$ of the flux of the Crab Nebula and suggests the source is steady over a decade long interval.

An investigation into the effect of iteratively deconvolving the telescope point spread function from atmospheric Cherenkov images was also carried out. The Richardson - Lucy algorithm was used along with the measured point spread function of the instrument to sharpen images in an attempt to enhance our ability to discriminate against background Cosmic ray events. The improvement in signal using this method was not statistically significant. Also reported is the development of a semi-automated alignment system for aligning the mirror facets of the telescopes of the new VERITAS array.

Contents

List of Figures

List of Tables

Key to Abbreviations

VHE	Very High Energy
EAS	Extensive Air Showers
BL Lacs	BL Lacertae type AGN
AGN	Active Galactic Nuclei
Mrk	Markarian
UV	Ultra Violet
IACT	Imaging Atmospheric Cherenkov Telescope
PMT	Photomultiplier Tube
AC	Alternating Current
DC	Direct Current
ADCs	Analogue to Digital Converters
PST	Pattern Selection Trigger
DAQC	Data Aquisition Computer
RMS	Root Mean Squared
pe	Photoelectrons
FWHM	Full Width Half Maximum
PSF	Point Spread Function
SAAS	Semi-Automated Alignmnet System

Acknowledgements

During the past five years a large number of people have contributed in some way to the realisation of this thesis. Everyone at the Physics Department in NUI Galway deserve many thanks, especially my supervisors Dr Mark Lang and Dr Gary Gillanders, whose support and advice was always greatly helpful as was the advice I received from Dr Pat Moriarty in GMIT, and Tess Mahony who was always there to help in matters of adminstration. I am also grateful to Dr Trevor Weekes and the other members of the VERITAS collaboration for making all my visits to Tucson rewarding. I also would like to thank the Irish Council for Research in Science Engineering and Technology for granting me a scholarship to undertake this research.

I must also mention the friendship and help of many others; particularly Christian Kelly, Stephan Lautram, Carol Maron and Mark Galligan from my days as an undergraduate physics student in GMIT; Kieran Forde, Helena Hession, Drs Phelan and Foley, Andrew Cronin, John Toner, Brendan Sheehan, Caoilfhionn Lane from the Galway Physics Society; Andrew and Victor in GMIT; Lorcan, Conor, Davy and Al, my best men; Sam, Jessie, Jo, Jim, John, Mick, Tommy, Pat and Gareth, my colleagues in GMIT who were a great support in the latter days of the writing of this thesis; Tim and Nancy Roe who were instrumental in me developing an interest in physics; My parents, Brian and Jean and the rest of my family and Mark Rahman;

My wifes parents, Benny and Eithne and all her family.

Most importantly, I would like to thank my wife, Helena. Without her love, support and words of encouragement, I would not have made it this far. To her and our baby girl Hannah Beth, I dedicate this thesis.

Chapter 1

A Brief History of γ-ray Astrophysics and Thesis Overview

1.1 Introduction

It is only in recent years that the γ-ray window on the Universe has begun to be opened to astrophysical exploration and study. The most energetic range of the electromagnetic spectrum is comprised of γ-radiation and hence it is this region that can provide us with information regarding the most energetic and violent regions of the Universe. In 1912, using an instrument carried high into the Earth's atmosphere by a balloon, Victor Hess made the discovery that the Earth is continuously being bombarded by high-energy particles that have since come to be known as cosmic rays (Hess, 1912). Some of these particles can have energies as high as 3.2×10^{20} eV (Bird et al., 1995). Cosmic rays are comprised mostly ($\sim$ 90%) of protons. However, a proportion of cosmic rays is composed of helium nuclei (alpha particles) and other heavier nuclei (~9%) and the remainder are electrons (~1%). The origin of very high energy cosmic rays is a question that has dogged astronomers since their discovery and still continues to pose as one of the major mysteries of modern astrophysics. The cause of this mystery lies with the nature of the cosmic ray itself. Since a cosmic ray is a charged particle, its path through space can be modified if it traverses magnetic fields that pervade space. When the cosmic ray finally impinges on our atmosphere there is no way of telling where the particle accelerator that created it is located. However the Pierre Auger Observatory have recently reported a correlation between the arrival directions of twenty seven cosmic rays of energy greater than 6×10^{19} eV and the positions of several active galactic nuclei (Abraham et al., 2007).

A possible solution to the problem of the unknown accelerator is the determination of the location of cosmic accelerators by indirect methods. A by-product of cosmic ray production is a γ-ray photon by means of π^0 decay or inverse Compton scattering. As they are neutral particles, the trajectory of γ-rays will be unaffected by magnetic fields. Hence, γ-rays arrive at the Earth's atmosphere with an indication of their origin and provide a possible means for the identification of cosmic ray sources. This realisation led to the creation of the field of γ-ray astronomy. As well as the continued quest to determine the origin of cosmic rays, γ-ray astronomy has itself created many new areas of research, including searches for dark matter and primordial black holes.

1.2 Early Balloon and Space-based Experiments

Initial attempts at γ-ray astronomy were performed with balloon experiments high in the atmosphere from the 1940s onwards and with satellite space-based experiments from the 1960s onward. These early balloon experiments were limited due to the difficulty in separating High Energy (HE) photons, coming from relatively weak γ-ray sources, from the huge background of secondary charged particles in the atmosphere. As a result, these balloon experiments were unable to identify isolated sources. The first detections of γ-rays from space were made by Explorer XI in 1961 (Kraushaar et al., 1965) and by OSO-III in 1968 (Kraushaar et al., 1972).

When NASA launched the HE γ-ray satellite, Small Astronomy Satellite (SAS-II), in 1972, it represented a major step forward for γ-ray astronomy (Fichtel, 1973). It comprised of a set of spark chambers providing energy and direction estimates for photons of energy > 30 MeV. SAS-II detected several isolated γ-ray sources including the Crab and Vela pulsars, and Cygnus X-3 (Fichtel et al., 1975; Hartman et al., 1979). However the instrument only had an angular resolution of $\sim 2^\circ$, which resulted in difficulty in identification of the detections with known sources. Generally the association of the excesses with sources was done using a timing analysis.

The successor to SAS-II was the European Space Agency satellite, COS-B. Launched in 1975, data from COS-B provided the first HE source catalogue and accurate maps of the Milky Way in HE γ-rays (Swanenburg et al., 1981). The catalogue contained 25 sources, mostly on the Galactic plane. A review of the achievements of the COS-B experiment can be found in Bennett (1990).

1.3 Advances in Ground-Based Techniques

As the flux of γ-rays falls at higher energies, an increased collection area is required for reasonable detection rates. So the limited size of space-based detectors prevents them from observing beyond about 100 GeV. In fact the newest space-based γ-ray detector (GLAST), due to be launched early next year, will have an energy range of 20 MeV - 300 GeV (Morselli, 2003). To extend past these energy limits, and to observe effectively within the Very High Energy (VHE) domain, requires other observing techniques. With collection areas approaching 5×10^4 m^2, ground-based detectors offer a solution to this problem. However, ground-based techniques don't directly detect the primary particle.

In his 1948 note in the Royal Society's report on the night-sky light and aurora, Blackett (1948) made the suggestion that 0.01% of the night-sky light should come from the Cherenkov light emitted when a cosmic ray or γ-ray impinges on the atmosphere. To test this hypothesis, two research physicists, Bill Galbraith and John Jelley, assembled the world's first, albeit crude, atmospheric Cherenkov telescope using a 25 cm parabolic mirror and a 5 cm diameter photomultiplier tube coupled to an amplifier and oscilloscope display. Their crude system detected light pulses exceeding the average noise level of the night-sky background every two minutes or so, and thus a new branch of astronomy was born.

Since the pioneering efforts of Galbraith and Jelley the field of VHE astronomy has grown rapidly. Ground-based instruments were developed to exploit the fact that VHE photons interact with nuclei high in the atmosphere to create extensive air-showers (EAS) of electrons, positrons and γ-rays. When the primary energy is high enough ($\gtrsim$ 40 TeV), some of the particles in the resulting air-shower may survive long enough to be detected at mountain level. In this case, arrays of particle detectors spread out over a large area at high-altitude sites, can detect the secondary particles of the EAS. With detectors located at very high altitudes it is possible to detect secondary particles from primaries with energies $\gtrsim$ 4 - 5 TeV. At lower energies (100 GeV - 10 TeV) Cherenkov light emitted from the EAS in the atmosphere can be detected at ground level by an optical reflector, resembling the dish of a radio telescope, and a light detector consisting of an array of photomultiplier tubes that optically image the Cherenkov photons. This is known as the Imaging Atmospheric Cherenkov Technique and was proposed by Weekes & Turver (1977) and pioneered at the Fred Lawrence Whipple Observatory in southern Arizona. A full description of this technique and the various ground-based experiments is given later in this thesis. In 1989 the first statistically significant detection of a VHE source was reported. The Crab Nebula was detected at a 9σ confidence level using the Whipple 10 m imaging atmospheric Cherenkov telescope (Weekes et al., 1989).

1.4 Modern Satellite γ-ray Astronomy

1.4.1 The Compton Gamma Ray Observatory

The field of space-based detection of HE photons progressed further with the operation of NASA's Compton Gamma Ray Observatory (CGRO) between 1991-2000. CGRO consisted of four separate instruments and covered the energy range 30 keV to 30 GeV: OSSE (60 keV - 10 MeV), COMPTEL (800 keV - 30 MeV), BATSE (30 keV - 1.9 MeV) and EGRET (20 MeV to 30 GeV). The Energetic Gamma Ray Experiment Telescope (EGRET) on board was the largest γ-ray space-based detector operated to date. During its lifetime EGRET had a huge impact on the field of high-energy astronomy, providing numerous new sources for target observation lists for VHE astronomy.

EGRET

EGRET was of most interest to the VHE γ-ray community and during its lifetime EGRET detected more than 70 Active Galactic Nuclei (AGN) and seven pulsars (Mukherjee et al., 1997; Hartman et al., 1999). EGRET also detected six Gamma Ray Bursts (GRBs) in the HE band. In addition to these, the EGRET experiment also detected approximately 170 HE sources not associated with any object known at other energies. Figure 1.1 illustrates the catalogue of sources detected by the EGRET instrument. Many of these unidentified objects populate the galactic equator and hence may be galactic in nature. A detailed description of the EGRET instrument can be found in Kanbach et al. (1988).

1.4.2 Next Generation Satellite Experiments

INTEGRAL

The INTEGRAL detector was launched in 2002 (Winkler et al., 2003) and consists of four instruments: a γ-ray spectrometer (20 keV - 8 MeV), an imager (15 keV - 10 MeV), an X-ray monitor (3 - 35 keV) and an optical monitor. The combination of these four instruments means that INTEGRAL can observe sources simultaneously in optical, X-ray and γ-ray bands, with high spectral and spatial resolution, making it perfectly suited to observe Gamma Ray Bursts (GRBs) over multiple wavelengths.

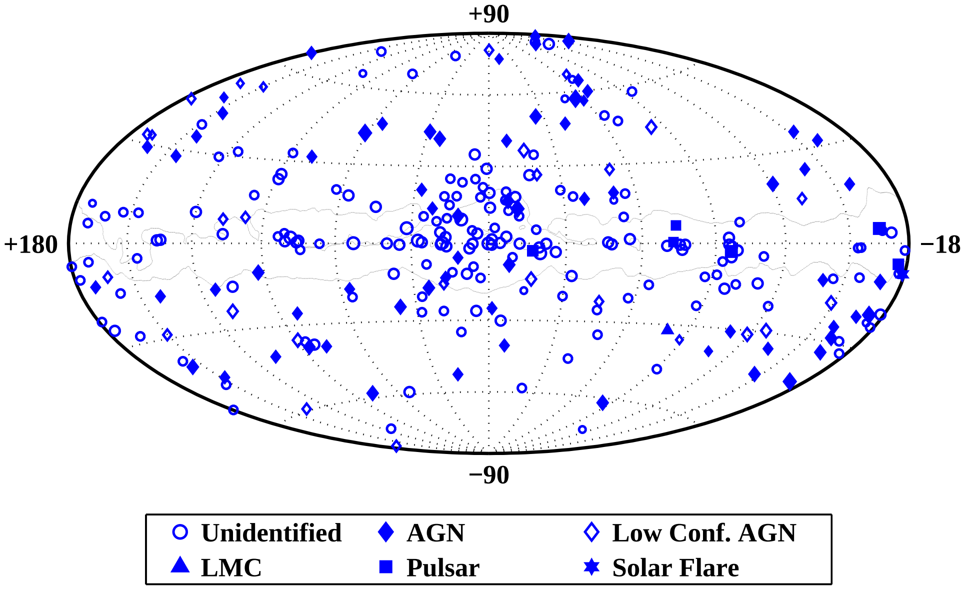

Figure 1.1: Catalogue of sources detected by EGRET during its lifetime including unidentified sources, pulsars, AGN and low confidence identifications with AGN. Figure from Fegan (2003).

Swift

Swift was launched into a low-Earth orbit on November 20, 2004. The main objective of its mission is the rapid response to GRB detections, recording and reporting their locations and determining if there is also an afterglow signal in the X-ray, ultraviolet (UV) and optical bands (Barthelmy et al., 2001). Swift has three main co-aligned instruments onboard, the Burst Alert Telescope (BAT), an X-ray telescope (XRT), and an UV/Optical telescope (UVOT). BAT is a coded-aperture γ-ray imager with a wide field-of-view that can produce arcminute GRB positions onboard within 10 seconds. The spacecraft can execute rapid autonomous slews that point the X-ray and UV telescopes at the BAT position in typically ~ 50 s to provide critical afterglow data.

GLAST

The Gamma-ray Large Area Space Telescope (GLAST), shown in Figure 1.2 (Mattox et al., 1996; Morselli, 2003) is scheduled to be launched in 2008. GLAST is the natural successor to EGRET as its instruments are based on the same basic principles of operation. However, GLAST employs new technologies in the hope of improving the performance of the detector. GLAST will operate two instruments, the Large Area Telescope (LAT) and the GLAST Burst Monitor (GBM). The LAT is an imaging γ-ray detector sensitive to photons in the energy range 20 MeV to 300 GeV while the GBM is designed to detect bursts of photons with energy from 5 keV to 25 MeV.

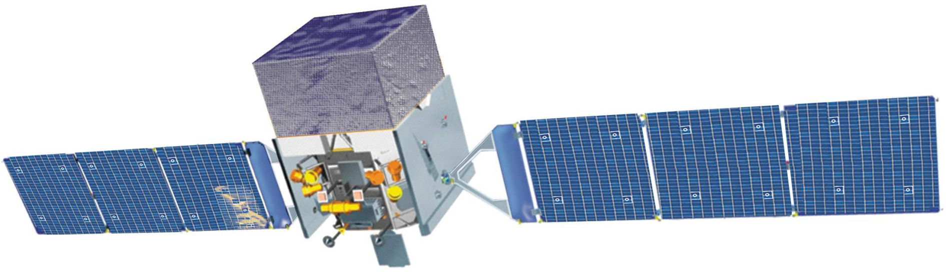

Figure 1.2: The Gamma-ray Large Area Space Telescope (GLAST). The top section of the spacecraft contains the LAT instrument and the lower section contains the GBM. See text for more details. Figure from NASA (education and public outreach).

The LAT instrument is composed of alternate sheets of high-Z absorber interlaced with silicon strip detectors for tracking motion of electron-positron pairs. This aids in determining arrival direction of the incoming photon. The silicon strip detectors are inexpensive, lightweight, and can offer a long lifetime, since no consumable materials are used in their operation (such as gas, which would be consumed in a spark chamber). An upper strip detector acts as a charged-particle anti-coincidence shield, and energy measurements are provided by a segmented CsI calorimeter located beneath the layered strip detector. Table 1.1 summarises the various space-based detectors used to collect data from High Energy astrophysical sources.

AGILE

AGILE is a 350 kg satellite dedicated to high-energy astrophysics funded and managed by the Italian Space Agency (ASI) (Mereghetti et al., 2000). Its main goal is the simultaneous detection of X-ray and γ-ray radiation in the energy bands 15-60 keV and 30 MeV - 50 GeV with optimal imaging and timing. AGILE was successfully launched on April 23, 2007 and is currently in its science performance verification phase.

Detector	**Epoch**	**Energy Range**
SAS-2	1972-1973	30 MeV - 200 MeV
COS-B	1975-1982	30 MeV - 5 GeV
EGRET	1991-2000	20 MeV - 30 GeV
INTEGRAL	2002 →	15 keV - 10 MeV
Swift	2004 →	< 150 keV
AGILE	2007 →	30 MeV - 50 GeV
GLAST	2008 →	20 MeV - 300 GeV

Table 1.1: A summary of space-based gamma-ray detectors stating the region of the spectrum each was/is sensitive to.

1.5 Thesis Overview

The work carried out in this thesis involved the detection and analysis of very high energy γ-rays using the imaging atmospheric Cherenkov technique. More specifically the scientific research presented here can be considered as two separate sections. The first part describes work carried out on improving the optical performance of the 10 - 12 m class of imaging atmospheric Cherenkov telescope using an innovative mirror alignment system and the iterative deconvolution of Cherenkov images. The second part is the description of an in-depth reanalysis of archival data from the unidentified source TeV J2032+4130. The reanalysis of this data led to a clearer flux determination for the 1989/1990 period of activity than was previously known.

In the sequence of this report, Chapter 2 explains the main production mechanisms of very high energy γ-rays. Chapter 2 also describes the imaging atmospheric Cherenkov technique. Chapter 3 details the specifics of detecting γ-rays using the Whipple 10 m telescope. Chapter 4 details the astrophysics of γ-ray emission from several relevant types of astrophysical object and describes the main ground-based experiments that are used to detect the electromagnetic air shower induced by very high energy photons. Chapter 5 discusses the operational and design details of the mirror alignment system developed for use on the telescopes of the VERITAS array and presents results of recent point spread function measurements carried out by the collaboration.

The remaining work, described in Chapters 6, 7 and 8, was carried out solely by the author. The attempted iterative deconvolution of Cherenkov images is presented in Chapter 6 and details the work involved in developing the Richardson-Lucy algorithm to iteratively deconvolve Cherenkov images and presents the results of applying such image processing to Cherenkov images. Chapter 7 discusses the reanalysis of archival data from the unidentified source TeV J2032+4130 in which several analysis methods were applied in an attempt to improve the detected signal in the data set. Following from this, the differential and integral γ-ray fluxes were determined and presented. The final chapter discusses the results of the flux determination of TeV J2032+4130. Chapter 8 also includes a discussion on possible γ-ray production methods in light of the γ-ray flux results and recent results from X-ray and radio observations. Due to the rapidly expanding catalogue of VHE γ-ray sources in the field of ground-based γ-ray astronomy, information regarding various sources and experiments can be considered current up to the 25th of September 2007.

1.6 Contributory Summary

The work described in this thesis was carried out as part of a large international collaborative project. The main contributions made by the author to the collaboration are detailed here. The construction of the VERITAS alignment instrument (as described in Chapter 4) was carried out during the first half of 2003 at NUI, Galway. Subsequent to its construction, the alignment system was then shipped to southern Arizona in June of 2003 to the location of the VERITAS array and tested on site.

Throughout the course of the project, several trips to the Fred Lawrence Whipple Observatory in southern Arizona were made for the purposes of astrophysical observations with the Whipple 10 m imaging Cherenkov telescope. During these trips, valuable hands-on experience was obtained with regard to the observational techniques being used. In addition to learning about the observational techniques employed in ground based γ-ray astronomy, there were other areas where experience was gained. These included point spread function measurements, mirror alignment surveys, mirror alignment as well as having to attend to unforseen electronic, mechanical and tracking problems that arose during the course of observation runs. During a visit to the VERITAS site, a contribution was made to the construction of the first telescope (T1) of the VERITAS array. This contribution involved the assembly and mounting of the individual mirror mounts of T1.

On the basis of the above contributions to the VERITAS and Whipple programmes during the course of this Ph.D project, the author is listed as lead author on a 29^{th} International Cosmic Ray Conference presentation paper, a co-author on 13 VERITAS Collaboration scientific publications and co-author on the VERITAS Collaboration presentation papers of 28^{th} and 29^{th} International Cosmic Ray Conferences. The topics of these papers varied from technical descriptions of the Whipple 10 m telescope and the VERITAS array, mirror alignments of the VERITAS array, progress reports on the VERITAS array to results from observational studies of various galactic and extragalactic objects of interest. These observations included multi-wavelength studies of Mrk 421, spectral studies of 1ES 1959+650, a survey of EGRET unidentified sources using the Whipple 10 m telescope, a search for emission from radio quasars, and observations of M87, Starburst Galaxies, H1426+428, TeV J2032+4130, 1ES 2344+514 and a search for primordial black holes amongst others. A detailed list of all associated publications is given in Appendix A.

Chapter 2

Ground-Based γ-ray Astronomy & the Imaging Atmospheric Cherenkov Technique

2.1 Introduction

Following the first tentative detections of high energy photons in the 1960s (Clark et al., 1968; Kraushaar et al., 1965), γ-ray astronomy was slow to gain acceptance in the wider astronomical community. However, in the last fifteen years, ground-based techniques of detecting Very High Energy (VHE) photons have evolved to the point where ground-based γ-ray astronomy is now developing rapidly as bigger and better Cherenkov telescopes come online. Because of these new array systems the VHE universe is rapidly becoming a more charted region.

Modern experiments like VERITAS and HESS take new strides into this area of astronomy. In particular, results from the HESS Collaboration are breaking new ground in making detections of astrophysical objects that appear to shine only in γ-rays as well as new detections of more traditional VHE γ-ray sources like supernova remnants and active galactic nuclei. As such, the catalogue of very high energy sources is rapidly expanding. This chapter will cover the different astrophysical processes that lead to γ-ray emission and will describe the different types of sources and possible production models that were studied during the course of this project. Descriptions of the main ground-based γ-ray experiments that are of relevance to this work are also given.

2.2 The High Energy Universe

Our universe is an area of contrasting activity. There are vast regions of absolute inactivity and then there are isolated regions of unimaginable violence that lead to the emission of immense amounts of energy. Evidence of this violence comes in the form of cosmic rays whose energy per particle can range from 10^7 eV to beyond 10^{20} eV. It is clear that these particles must originate in the most energetic environments in the universe such as supernovae, active galactic nuclei (AGN) and gamma-ray bursts (GRBs). These cosmic particle accelerators provide us with great natural laboratories that cannot be duplicated on Earth.

Since their discovery by Hess (1912), the nature and origin of cosmic rays has been a central focus of high energy astrophysics. As mentioned in Chapter 1, there is an inherent inability to determine the point of origin of charged VHE cosmic rays as they arrive at the Earth. They appear from random directions carrying little information regarding their source and origin. Since photons are uncharged, they retain directional information and hence provide us with information regarding the point of origin.

Of the electromagnetic radiation that can be detected on Earth, it is the photons of the highest energy that are of interest to γ-ray astronomy. It is these photons that provide us with direct evidence of the locations of the very high energy galactic and extra-galactic processes in the Universe. Since VHE γ-rays are neutral, they can only be produced by secondary interactions involving other charged particles, for example the collision of a hadronic beam with matter that produces secondary pions which then decay into γ-rays (Mannheim, 1993; Romero et al., 2003). VHE γ-rays may also be produced via a leptonic process, for example emission due to the Synchrotron Self-Compton (SSC) model in which lower energy photons produced via synchrotron emission from relativistic electrons that are then up-scattered to very high energies by their parent electrons (Blumenthal & Gould, 1970; Maraschi et al., 1992; Atoyan & Aharonian, 1999; Bosch-Ramon et al., 2006). The presence of VHE γ-rays in regions of our galaxy and beyond, suggests areas of particle acceleration to energies of an order of magnitude greater than that of the γ-rays themselves.

Before experiments could provide direct detections of these VHE photons, work by Feenberg & Primakoff (1948), Hayakawa (1952), and Morrison (1958) advocated the potential importance of γ-ray astronomy as a method of studying high-energy astrophysical processes directly. Since these early theoretical studies, there have been technological advances that have provided a means of detecting these VHE photons. Recent developments have seen many advances in both ground-based and satellite-borne γ-ray detection, leading to a revolution in the field and moving it from a little understood curiosity to a mainstream branch of astronomy.

Classification	**Energy Range**	**Detection Technique**
Low Energy (LE)	0.1 - 10 MeV	Scintillator (Satellite)
Medium Energy (ME)	10 - 30 MeV	Compton Telescope (Satellite)
High Energy (HE)	30 MeV - 0.1 TeV	Spark Chamber (Satellite)
Very High Energy (VHE)	0.1 TeV - 100 TeV	Ground-based: Cherenkov Telescope (Mountain/Sea Level)
Ultra High Energy (UHE)	0.1 PeV - 100 PeV	Ground-based: Air Shower Array (Mountain)
Extremely High Energy (EHE)	$>$ 100 PeV	Ground-based: Fluorescence detector (Sea Level)

Table 2.1: Subdivisions of the γ-ray spectrum, the labels used to differentiate between energy bands and the corresponding detection methods. Adapted from Weekes (1988)

The γ-ray energy domain is the most extensive of the electromagnetic spectrum, spanning at least fifteen decades in energy. Weekes (2003) defines the γ-ray as a generic term used to describe photons of energy from about 500 keV to $>$ 100 EeV. This range is as large as the rest of the observed spectrum combined and a variety of detector technologies is required to span it. Therefore, it is convenient to introduce several subdivisions, taking into account the specific scientific objectives and detection methods relevant to different energy bands. Generally, observational γ-ray astronomy can be divided into five bands, defined by Weekes (1988) as: Low Energy (LE), Medium Energy (ME), High Energy (HE), Very High Energy (VHE) and

Ultra High Energy (UHE). These conventional subdivisions are shown in Table 2.1 along with their corresponding energy ranges in eV.

While low to high energy γ-rays are observed by satellite or balloon-borne detectors, the highest energy γ-ray regimes (VHE and UHE) are best detected using ground-based instruments. It is the VHE range which is investigated in this thesis.

2.3 Astrophysical Production Mechanisms of TeV γ-rays.

Electromagnetic radiation can be considered to be thermal or non-thermal in origin. Thermal radiation, or blackbody radiation, is emitted from a hot body such as a star. The emission spectrum is a function of the temperature of the hot body. Total intensity of the emitted radiation is directly proportional to the temperature of the star raised to the fourth power, *i.e.*, $I \propto T^4$. For hot stars with surface temperatures of around 10^4 Kelvin, the peak thermal emission occurs at an energy less than 1 keV. Since the spectra of sources of VHE γ-rays can have peak energies greater than 10^7 eV, it is clear that γ-rays are a form of non-thermal radiation. The production of non-thermal radiation is due to the acceleration of charged particles and, in order to explain the origin of galactic γ-rays, an understanding of the acceleration mechanisms involved is required. The following section outlines the principal processes responsible for the production of γ-ray photons. These processes can generally be divided into several groups, each of which is briefly discussed.

2.3.1 Acceleration of Charged particles

There are several processes (Hillier, 1984; Aharonian, 2004) that can accelerate charged particles and, hence, result in the emission of electromagnetic radiation. With regard to the astrophysical objects studied in this work, the leading γ-ray production models specific to these sources are discussed in detail later in this chapter. The main production mechanisms resulting in non-thermal γ-ray emission via particle acceleration are briefly described here.

Synchrotron Radiation

The simplest form of accelerated motion of a charged particle in a magnetic field is due to non-relativistic gyration around the field line. Emission due to this acceleration is known as cyclotron radiation. When observed, circularly polarised or linearly polarised waves are detected radiating from the charged particle. The polarisation depends on the orientation of the observer relative to the magnetic field direction.

Cyclotron radiation will change to synchrotron radiation when the speed of the charged particle moving in the magnetic field approaches the speed of light. To achieve production of synchrotron radiation at γ-ray energies, ultra-relativistic electrons must be moving in extremely strong magnetic fields, see Figure 2.1. If the electron is traveling relativistically with a Lorentz factor γ, the emission is beamed tangentially in a narrow cone of half angle $\sim 1/\gamma$ directed along the instantaneous direction of motion.[1] A continuous spectrum of polarised radiation results since there is a large population of relativistic electrons each emitting at different frequencies. The overall spectrum of the

---

[1] The Lorentz factor $\gamma = \frac{1}{\sqrt{1-\beta^2}}$ where $\beta = u/c$ with the particle velocity u and speed of light c.

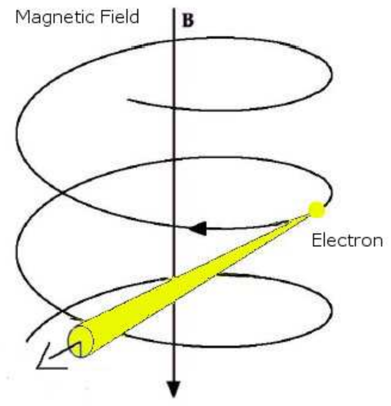

Figure 2.1: A representation of synchrotron radiation production. As the electron spirals along a magnetic field line, a cone of synchrotron radiation is emitted at a tangent to the electron's trajectory.

emission consists of the sum of a large number of harmonics of the basic cyclotron emission. The spectrum has a peak, with maximum emission at ν_c, where ν_c is the critical frequency:

$$\nu_c = \frac{\gamma^2 eB}{2\pi m_e} \frac{3}{2} sin\theta \tag{2.1}$$

where B is the magnetic field strength perpendicular to the direction of motion and θ is the pitch angle between the particle trajectory and the direction of the magnetic field. While emitting synchrotron radiation an electron will cool as its energy is depleted. The rate of this cooling is given by:

$$\frac{dE_e}{dt} = 10^{-14} B^2 \gamma^2 \tag{2.2}$$

The electron will lose half its energy by synchrotron emission in a time t given by:

$$t = \frac{5}{\gamma B^2} \tag{2.3}$$

An electron population radiating in an astrophysical environment will typically have a power-law spectrum:

$$\frac{dN_e}{dE_e} \propto E_e^{-p} \tag{2.4}$$

and the resulting synchrotron radiation will have a spectral energy distribution $F_\nu \propto \nu^\alpha$ where

$$\alpha = \frac{1-p}{2} \tag{2.5}$$

The study of the synchrotron spectrum can provide much insight into the particle population within a cosmic accelerator. It can be noted that higher-energy electrons radiate more rapidly and thus lose energy faster. The depletion of the higher energy electrons would lead to a steeper power-law synchrotron spectrum above the critical frequency (ν_c) which is dependent on the magnetic field

A source emitting high-energy radiation with a power-law spectrum and with a high degree of polarisation would generally indicate that synchrotron acceleration is present. To produce γ-rays directly by synchrotron radiation, either the electrons must be very highly relativistic, or a very intense magnetic field is required. The observation of a synchrotron component can also indicate the presence of relativistic electrons which may provide a target field for photons and generate γ-rays by the inverse-Compton mechanism.

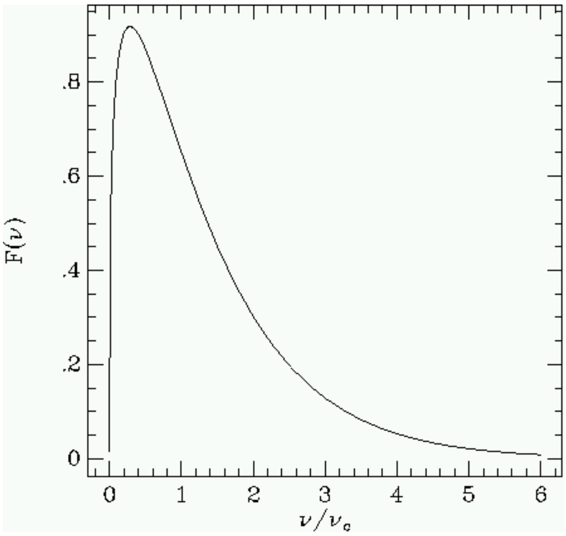

Figure 2.2: Frequency distribution of synchrotron electrons showing the characteristic peak emission near $0.29\nu_c$ where ν_c is the critical frequency as defined in Equation 2.1

Inverse-Compton Scattering

When a high energy electron collides with a lower energy photon there is a transfer of energy from the electron to the photon (Figure 2.3). This interaction is of considerable importance in astrophysical environments where the density of low-energy photons is high and where there is a supply of relativistic electrons. The process known as the synchrotron self-Compton process occurs when low energy synchrotron photons gain energy from the same population of electrons from which they originate. The synchrotron self-Compton production mechanism is assumed to be the main VHE γ-ray production mechanism that results in VHE emission from supernova remnants (Cowsik & Sarkar, 1980; Allen et al., 1997) and possibly active galactic nuclei (Krawczynski et al., 2002; Wilson, 2001). Calculated synchrotron self-Compton spectra provide a good fit to the observed spectrum from the Crab Nebula (de Jager et al., 1996).

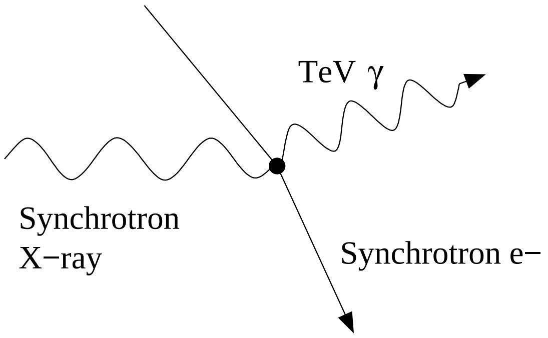

Figure 2.3: A representation of Inverse-Compton Scattering.

In the collision between a relativistic electron with energy $E_e = \gamma m_e c^2$ and a photon of energy $\varepsilon = h\nu$, the scattered photon energy in the laboratory system, averaged over all angles of incidence and scattering, is $\approx \frac{4}{3}\gamma^2\varepsilon$. This process can turn a radio photon into a γ-ray photon. The low-energy photons may belong to the cosmic background radiation ($T = 2.7$ K), which has an energy density of 0.4×10^{-13} J.m^{-3}. Alternatively, as mentioned above, the low-energy photons may be the synchrotron photons emitted by the energetic electron population itself.

The energy transferred to the photon depends on the cross-section and on the scattering angle at which the electron and photon meet. For a maximum energy transfer (E_{max}), the particles must meet head-on, reversing the photon direction in the collision, while a minimum energy (E_{min}) will be transferred when the scattering angle is 90°.

The probability of the electron-photon interaction, i.e. the cross-section, is given by the Klein-Nishina formula:

$$\sigma_{\mathrm{KN}} = \pi r_e^2 \frac{1}{\eta} \left[\left(1 - \frac{2(\eta+1)}{\eta^2} \right) \ln(2\eta+1) + \frac{1}{2} + \frac{4}{\eta} - \frac{1}{2(2\eta+1)^2} \right] \tag{2.6}$$

where $\eta = \gamma\varepsilon / m_e c$, and $r_e = 2.818 \times 10^{-15}$ m is the classical electron radius.

For low-energy collisions, the cross-section is simply the Thomson cross-section $\sigma_T = \frac{8}{3}\pi r_e^2$, independent of energy. However, for very high energy electron-photon interactions ($\varepsilon >> m_e c^2$) the Klein-Nishina formula reduces to:

$$\sigma \approx \frac{3}{8}\sigma_T \frac{m_e c^2}{\gamma\varepsilon} \left[\ln\left(\frac{2\gamma\varepsilon}{m_e c^2} \right) + \frac{1}{2} \right] \propto \frac{\ln E_e}{E_e} \tag{2.7}$$

so that the interaction probability decreases at higher energies. In this regime, the electron energy loss through scattering becomes independent of the incident photon energy. Such an ultra-relativistic encounter with ($\varepsilon >> m_e c^2$) would yield photon energies:

$$E_{\mathrm{min}} \approx \frac{m_e c^2}{4\gamma}$$

$$E_{\mathrm{max}} \approx E_e = \gamma m_e c^2$$

Using a power-law energy distribution for the electrons, $dN_e/dE_e \propto E_e^{-\alpha}$, the inverse-Compton spectrum takes the form of a two-component distribution peaking on the border between the Thomson and Klein-Nishina regimes where $\frac{4}{3}\gamma^2\varepsilon \sim \gamma m_e c^2$

2.3.2 Particle Decay

When a particle decays, a γ-ray may be produced. An example of such a process is the decay of a neutral pion.

$$\pi^0 \rightarrow 2\gamma$$

Pions are created during strong interaction events. These events could be the collisions of cosmic rays with the nuclei of interstellar gas clouds. For example a common interaction of a cosmic ray proton is a collision with stationary hydrogen gas, producing excited states that lead to the emission of π mesons. The most common interaction has the form:

$$\mathrm{p} + \mathrm{p} \rightarrow \mathrm{N} + \mathrm{N} + \pi^+ + \pi^- + \pi^0$$

where N is a proton or neutron. The neutral pion (π^0) is unstable and decays rapidly (with a half-life $\sim 10^{-16}$ s) into two photons. The energy distribution peaks at half the rest mass of the pion $\sim$ 70 MeV. This peak is the characteristic feature of p-p interactions and the signature of hadrons as the progenitors in γ-ray sources. Pions that decay while traveling at relativistic velocities may produce VHE or UHE γ-rays. The decay of subatomic particles is also an important factor in the development of electromagnetic cascades in the atmosphere. There is also the possibility that VHE γ-rays may be created by the annihilation of dark matter.

2.4 The Imaging Atmospheric Cherenkov Technique

The key element to the success of ground-based γ-ray astronomy in detecting very high energy (VHE) photons in the 50GeV to 50TeV range lies with the imaging atmospheric Cherenkov technique. This chapter will describe the imaging atmospheric Cherenkov technique, its associated instruments, and analysis methods, as pioneered by the Whipple collaboration.

An atmospheric Cherenkov telescope is very different to an optical telescope, and superficially it has the appearance of a radio telescope. Since the atmosphere is opaque to high-energy photons, the atmospheric Cherenkov telescope doesn't physically detect the γ-ray photon but instead detects its interactions with nuclei high up in the earth's atmosphere. These interactions lead to showers of secondary particles that can be detected at ground level by means of the imaging atmospheric Cherenkov technique and telescope.

The result of the shower of secondary particles in the atmosphere is a brief, faint flash of Cherenkov light emitted in the ultraviolet/visible range. The atmospheric Cherenkov telescope then detects this faint light and reconstructs the energy and direction of the original VHE photon that produced the air shower. Unlike space-based γ-ray detectors whose collection areas can be restrictive in size, the imaging atmospheric Cherenkov technique uses the Earth's atmosphere as its detector. An atmospheric Cherenkov telescope with a physical aperture of $\sim$ 10 m can have an effective collection area of $\sim$ 5 x 10^4 m^2.

The first statistically significant detection of VHE γ-ray emission was reported by the Whipple Collaboration in 1989 using the imaging atmospheric Cherenkov technique (Weekes et al., 1989). The source under study at the time was the much observed Crab Nebula supernova remnant (Figure 2.4).

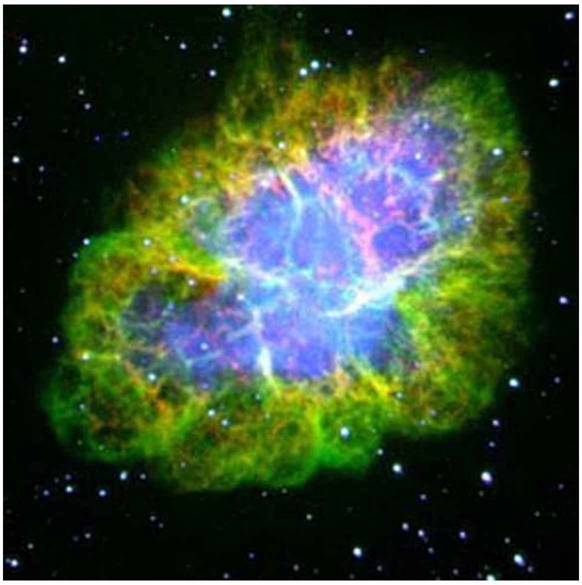

Figure 2.4: The Crab Nebula supernova remnant observed with the Hubble Space Telescope. Figure courtesy of the Hubble Heritage Team (heritage.stsci.edu).

2.5 Cherenkov Radiation

2.5.1 Introduction

Cherenkov radiation is electromagnetic radiation emitted when a charged particle passes through a transparent medium at a speed greater than the speed of light in that medium. It is named after the Russian scientist Pavel Alekseyevich Cherenkov who won the 1958 Nobel Prize after his intensive studies of this phenomenon (Cherenkov et al., 1958). The speed of light in a vacuum is a universal constant (c), however the speed of light in a material can be significantly less than c. When cosmic rays, traveling close to c enter the Earth's atmosphere (the medium) at a speed greater than the phase velocity of light in that medium, the result is a very brief flash of light.

A common analogy to use here is that of the sonic boom of a supersonic aircraft. The sound waves created by the aircraft do not move fast enough to get out of the way of the aircraft. This results in the waves stacking up and a shock front is formed. Similarly, superluminal charged particles generate photonic shock waves as they travel through the Earth's atmosphere that manifest themselves as a very brief flash of light towards the blue end of the spectrum. For a detailed description on the characteristics and production of Cherenkov radiation see Jelley & Porter (1963). The following gives a brief outline of the production of Cherenkov radiation.

2.5.2 Cherenkov radiation production

When a charged particle passes through a dielectric medium, it polarises the atoms close to where it passes. Once it has passed, the atoms can then relax back to their initial state and in doing so emit a brief pulse of electromagnetic radiation. When these pulses are emitted coherently, Cherenkov radiation results. For the pulses to be in phase, the particle must travel through the

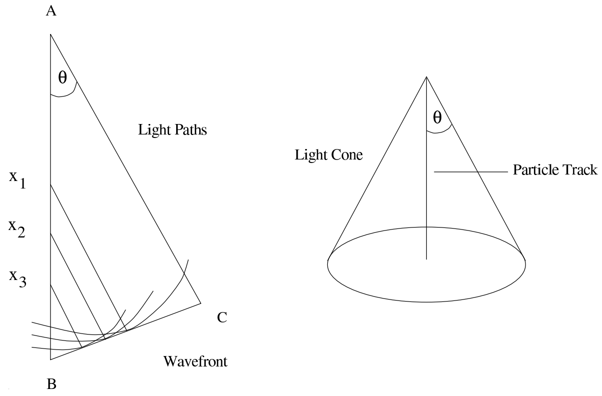

Figure 2.5: Left: Cherenkov radiation wavefront production. Right: The cone shape trajectory of the charged particle. Note the Cherenkov angle is the apex angle.

medium with a speed greater than the velocity of light in the medium. When this criterion is fulfilled, Cherenkov radiation is emitted at a specific angle θ_c, with respect to the direction of the particle. The velocity of light in the medium is given as:

$$v = \frac{c}{n} \tag{2.8}$$

where c is the velocity of light in a vacuum and n is the refractive index of the medium and v is the velocity of light in the medium. If the velocity of the particle is greater than this then Cherenkov emission will occur. By looking at Figure 2.5 it can be seen that the Cherenkov emission angle θ_c is given by:

$$cos\theta_c = \frac{1}{\beta n} \tag{2.9}$$

where product βc is the velocity of the particle. This is known as the Cherenkov relation. Equation 2.9 describes the emitted Cherenkov radiation from the charged particle as being symmetrical about the particle's trajectory and takes the form of a cone with an apex angle θ_c (Figure 2.5). If θ_c is set to zero then the threshold velocity below which no emission can occur is given by:

$$v_\tau = \frac{c}{n} \tag{2.10}$$

Equation 2.10 now suggests an energy threshold for Cherenkov radiation production given by:

$$E_\tau = \frac{m_o c^2}{\sqrt{1 - \left(\frac{v_\tau}{c}\right)^2}} \tag{2.11}$$

For an electron moving through the atmosphere (refractive index 1.00029 at sea level) the energy threshold is $\sim$ 21 MeV. When the particle moves with a velocity of $v_p/c \rightarrow 1$, (at very high relativistic velocities) the maximum angle of Cherenkov emission is given by:

$$\theta_{max} = \cos^{-1}\left(\frac{1}{n}\right) \tag{2.12}$$

The Cherenkov angle is 1.3° at sea level and decreases with altitude. The energy thresholds for Cherenkov radiation production for muons and protons are 4.4 GeV and 39 GeV respectively. Since there are higher populations of electrons in an extensive air showers, it is generally expected that they contribute to the majority of Cherenkov light in extensive air showers.

2.6 Extensive Air Showers

When a VHE photon or cosmic ray impinges on the top of the atmosphere, a cascade of secondary particles is initiated. Providing the energy of secondary particles in the shower is greater than E_τ from Equation 2.11, Cherenkov light will be generated. The resulting shower can contain $\sim 10^5$ secondary particles. At ground level these showers can cover an area of approximately 10^5 m^2 and are known as Extensive Air Showers (EAS).

2.6.1 Electromagnetic Air Showers

γ-ray initiated EAS are produced when a VHE photon interacts or passes close to the nucleus of an atom in the atmosphere and produces a relativistic electron/positron pair:

$$\gamma \rightarrow e^+e^-$$

For the ultra-relativistic case of an air shower, the radiation length[2] for pair-production is 37.7 g cm^{-2}. This means that a γ-ray induced shower is initiated near the top of the atmosphere (total depth of the atmosphere is $\sim$ 1000 g cm^{-2}). Figure 2.6 shows the processes involved in a γ-ray induced EAS.

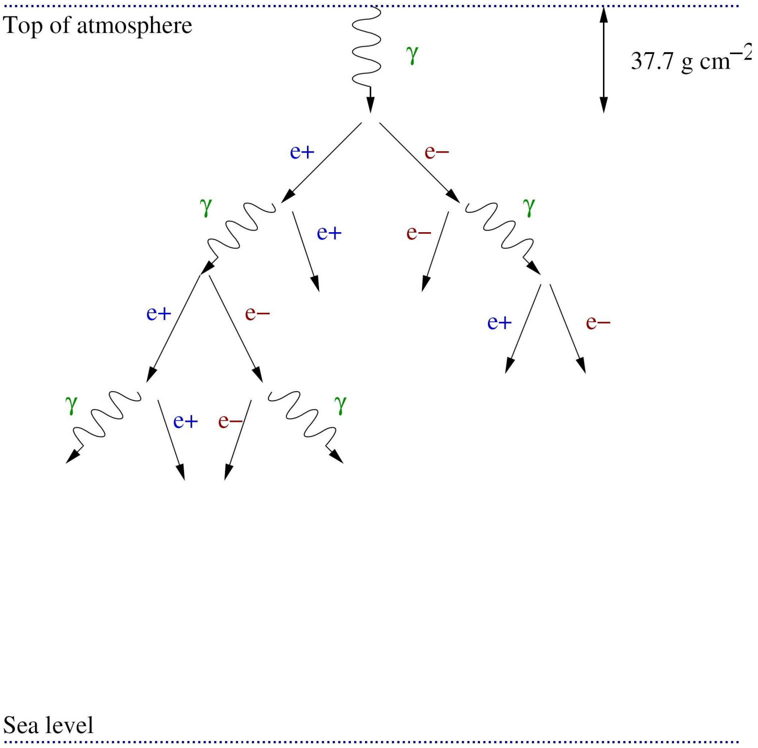

Figure 2.6: Gamma-ray shower development.

The first pair-produced secondary electrons (electron/positron) only travel a short distance before interacting with other nuclei to produce two new high-energy γ-rays. This process repeats, producing more secondary electrons and γ-rays. The shower will grow exponentially until ionisation losses are approximately equal to radiation losses. At this point, for a 100 GeV

---

[2] The mean distance a particle will travel before interacting with another particle.

γ-ray, the shower is at its maximum and contains $\sim 10^2$ particles and occurs at $\sim$ 10 km above sea level . The height of shower maximum is dependent on the primary energy, with the result that showers from higher energy γ-rays penetrate deeper into the atmosphere. After shower maximum, the shower will quickly attenuate through ionisation losses of the electrons and Compton scattering of the photons, and the shower is no longer self-propagating. The shower will shortly fade completely since the average energy of the photons will fall below what is required for efficient pair production.

Even though there is potential for muon production in γ-ray cascades through photo-nuclear interactions, the probability of this is 10^{-4} times that of electron/positron pair production and so γ-ray induced cascades can be considered mainly electromagnetic in nature. Additionally, since the secondary electrons have a low transverse momentum, the cascade is strongly beamed in the direction of the initial VHE photon and the result is a relatively narrow shower. However, the shower can still spread out over a large area (3 x 10^4 m^2). This is mainly due to Coulomb scattering experienced by the secondary electrons in the shower. This spreading of the shower over a relatively large area means that any ground based detector lying inside this area should detect the EAS. This results in the large effective collection area mentioned already in the introduction of this chapter.

2.6.2 Hadronic Air Showers

A hadronic air shower is initiated when a primary cosmic ray nucleus or proton collides with matter contained in the Earth's atmosphere. A major difference between hadronic showers and γ-ray induced showers is the depth in the atmosphere at which the shower starts. In air, the mean free path for a proton of around 1 TeV is $\sim$ 80 g cm^{-2}. This leads to the particle surviving to a greater atmospheric depth a than for a γ-ray which has a mean free path of 37 g cm^{-2}. The implication is that for a γ-ray induced shower and a hadron induced shower of the same energy, there is normally a greater number of particles reaching detector level from the hadronic shower. The collisions between the cosmic ray and atmospheric matter cause the primary hadron to lose much of its initial energy by producing nucleons and pions and other secondary particles, all of which are beamed in the direction of the primary particle. The neutral pions decay into photons and the charged pions decay into muons via the following decay mechanisms:

$$\pi^0 \rightarrow 2\gamma$$
$$\pi^+ \rightarrow \mu^+ + \nu_\mu$$
$$\pi^- \rightarrow \mu^- + \overline{\nu}_\mu$$

The muons are weakly interacting and do not contribute any further to the shower development, but can themselves initiate smaller electromagnetic cascades that do contribute. However, since relativistic muons have relatively long lifetimes, they can sometimes remain in the shower until they reach ground level. If the trajectory of a local muon is parallel to the optic axis then, depending on its distance from the optic axis, local muons can produce Cherenkov images similar to showers initiated by low energy (< 200 GeV) γ-rays. The image generated by the local muon in the camera may appear as a full ring or, a partial ring. This can have a detrimental effect when trying to distinguish between γ-ray induced showers and hadronic showers, especially with single ground-based detectors.

Other secondary nucleons and charged pions will continue to multiply in successive generations until each particle's energy drops below ~ 1 GeV (energy required for multiple pion production). The γ-rays produced by the decay of the π^0 pair produce to create smaller electromagnetic cascades, which are self regenerating and so are the dominating element in hadronic air showers. Once the shower maximum is reached, the electrons and positrons will lose most of their energy through ionisation losses. Figure 2.7 illustrates a simplistic graphical representation of a hadronic shower cascade.

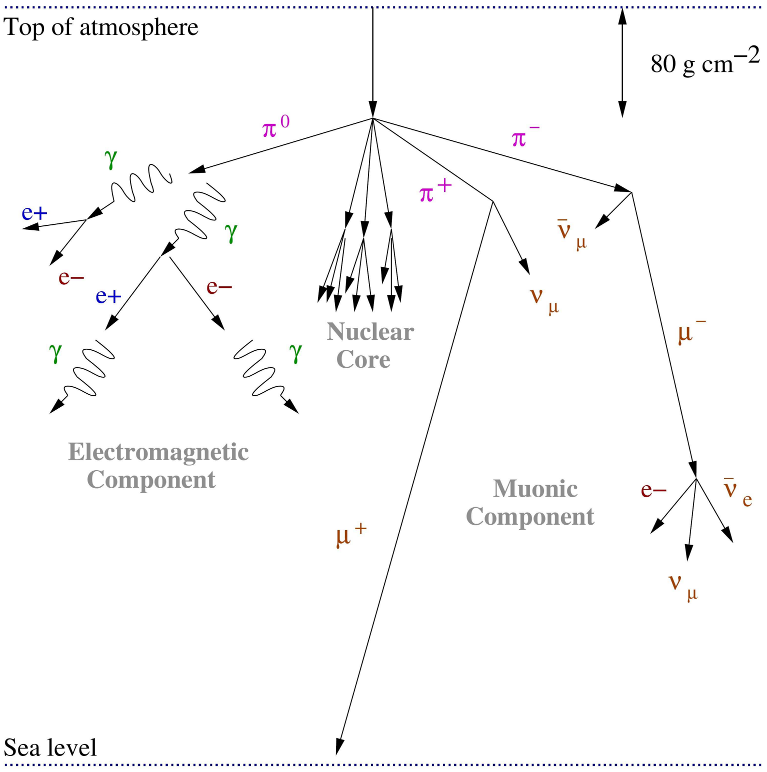

Figure 2.7: Hadronic shower development.

A major difference between hadronic showers and γ-ray showers is that the hadronic showers tend to be less compact and more random in shape and orientation than γ-ray showers. This is due to larger fluctuations and large opening angles of the pion interactions resulting in larger transverse momentum being given to particles during the shower development. This is an important consideration in that it gives ground-based detectors the potential for discrimination between hadronic showers and γ-ray showers.

2.7 Discrimination between hadronic and γ-ray initiated EAS

To discriminate between cosmic rays and γ-rays, an atmospheric Cherenkov telescope must have a dedicated data acquisition system to record and identify the EAS it detects. The main task of discrimination between the two types of showers is carried out off-line after the observations have been completed.

As discussed previously, the nature of the primary particle in an air shower governs the air shower's development through the atmosphere, resulting in several differences between hadronic showers and γ-ray showers. It is these subtle differences that are exploited when discriminating between showers initiated by hadrons and showers initiated by γ-rays. For instance, a γ-ray is undeflected by galactic and inter-stellar magnetic fields and travels in a straight line from its origin. In other words, the γ-ray initiated shower will be aligned in the direction of the source. This is an advantage when compared with cosmic rays, whose arrival directions have been altered by galactic and interstellar magnetic fields and appear isotropically across the sky.

Early computer simulations were performed by Hillas (1985) to investigate the differences between γ-ray and cosmic ray initiated EAS. The results of these simulations suggested that discrimination should be possible by analysing the Cherenkov images on the basis of their shape and orientation as they appear on the Cherenkov imaging detector. Further descriptions of simulations of the EAS induced by cosmic rays and γ-rays can be found in Kertzman & Sembroski (1994) and Mohanty (1995). This section will

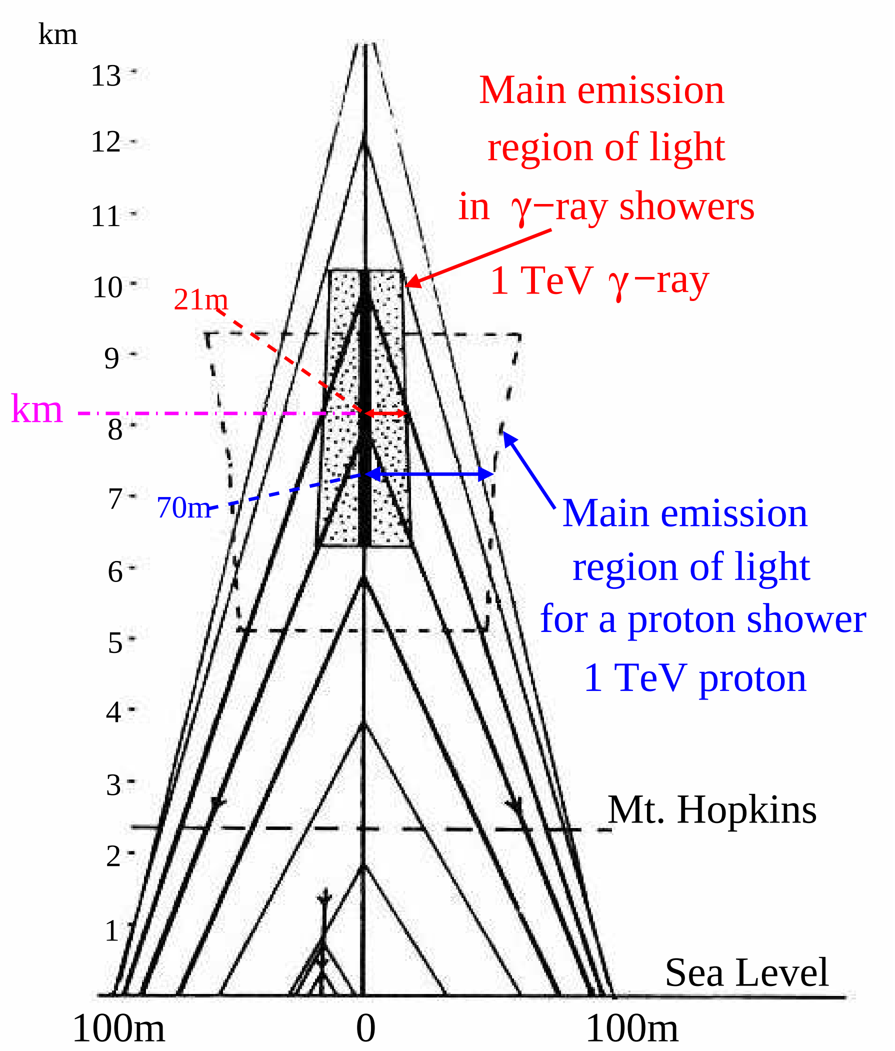

Figure 2.8: A simple model of Cherenkov radiation produced by γ-rays and hadrons. The diagram illustrates some of the differences between hadron-induced showers and γ-ray induced showers. The shaded region represents the maximum extent of a γ-ray induced shower while the dashed box the maximum extent of a hadron-induced shower. Also shown is the altitude where shower maximum occurs (Hillas, 1996).

summarise the findings of these studies.

A collimated γ-ray shower produces a pool of Cherenkov light with a radius of approximately 120 m. Beyond this range the light intensity falls off quickly. Hadronic showers tend to have a different distribution of light due to the fact some of the particles in hadronic showers have higher transverse momenta as mentioned in Section 2.6.2. A simple model of Cherenkov radiation development is shown in Figure 2.8 and shows some the differences in light production between hadron induced showers and γ-ray showers including shower maximum, penetration depths, and the core region of the shower.

Property	**Hadron Shower**	**γ-ray Shower**
Initial collision	Lower in atmosphere	Higher in atmosphere
Shower spread	Broad	Compact
Orientation of shower images	Random	Towards source
Uniformity of particle spread	Irregular	Uniform and regular
UV/visible ratio	High	Low
Atmospheric penetration	Muonic component can reach Earth's surface	Low

Table 2.2: Summary of the main differences between γ-ray showers and hadron showers

At maximum development for a shower induced by a 1 TeV γ-ray, most of the particles that contribute to the generation of Cherenkov radiation will lie within 21 m from the shower axis, while for a hadron initiated shower this value is around 70 m from the shower axis. Figure 2.9 shows the longitudinal and lateral development profiles of showers initiated by a 1 TeV γ-ray and a 1 TeV proton. Table 2.2 outlines the main differences between γ-ray showers and hadronic showers.

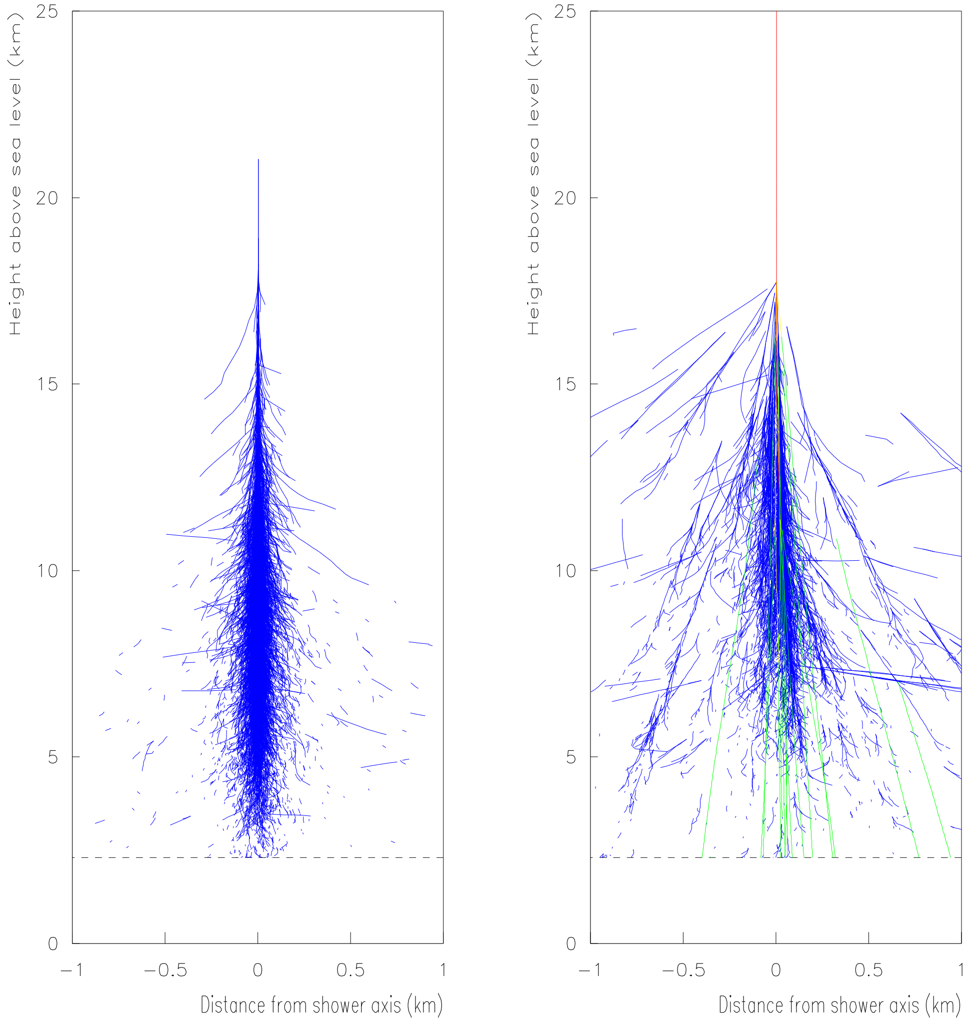

(a) γ-ray (b) Cosmic ray

2.9: An illustration of the longitudinal development of a simulated 1 TeV γ-ray initiated shower (left) and a 1 TeV proton-initiated shower (right) (Rodgers, 1997).

2.7.1 Detecting Cherenkov Radiation

There are several methods that can be employed to detect the EAS caused by high-energy particles impacting with nuclei in the Earth's atmosphere. Figure 2.10 illustrates the main detection methods used in γ-ray astronomy. For the imaging atmospheric Cherenkov technique the basic requirements are, a light collector, a fast detector (photo-multiplier tube (PMT) array), a data acquisition system to record the Cherenkov flashes, and software to analyse the images. The main task of the atmospheric Cherenkov telescope is the need to be able to differentiate a typical Cherenkov flash from a 1 TeV γ-ray induced shower, that lasts for $\sim$ 5 ns and yields about 100 photons m^{-2}, from the dominant night sky flux of $\sim 10^{12}$ photons $\mathrm{m}^{-2}\mathrm{s}^{-1}\mathrm{sr}^{-1}$ between 330 and 450 nm. If the field of view of the telescope is matched to the angular extent of the Cherenkov flash ($\sim 1°$), then only 1 or 2 optical photons m^{-2} are detected from the night-sky in 5 ns. Thus, using a suitable detector with fast integration times, the Cherenkov flash can be easily detected above the night-sky background.

This means that the night-sky background is one of the main factors in determining the energy threshold for an atmospheric Cherenkov telescope system (Cawley & Weekes, 1995). For a simple detector comprising of a single photomultiplier tube situated at the focus of a reflecting dish, and assuming the noise is Poissonion, the signal to noise ratio is given by:

$$\frac{S}{N} = \frac{\int_{\lambda_1}^{\lambda_2} C(\lambda)\epsilon(\lambda)A d\lambda}{\sqrt{\int_{\lambda_1}^{\lambda_2} B(\lambda)\epsilon(\lambda)\Omega t A d\lambda}} = \int_{\lambda_1}^{\lambda_2} C(\lambda)\sqrt{\frac{\epsilon(\lambda)A}{B(\lambda)t\Omega}} d\lambda \tag{2.13}$$

where

- C(λ) is the Cherenkov photon flux

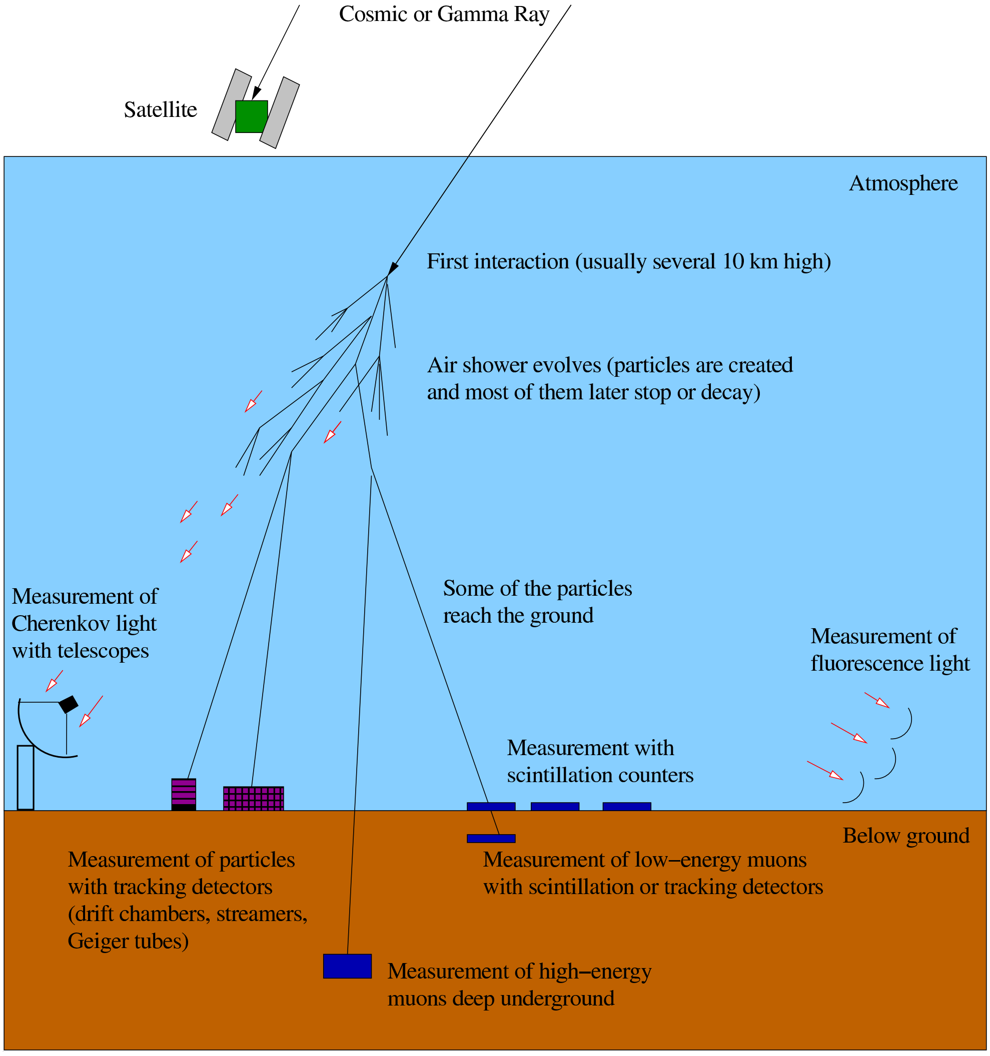

Figure 2.10: Various methods of cosmic and γ-ray detection used in γ-ray astronomy (Schroedter, 2004).

- $B(\lambda)$ is the background light flux
- $\epsilon(\lambda)$ is the quantum efficiency of the PMT
- Ω is the solid angle
- t is the integration time (must be $\geq$ the length of the Cherenkov flash)
- A is the mirror area
- λ_1 and λ_2 specify the wavelength range over which the PMTs are responsive.

So the smallest detectable Cherenkov flash is inversely proportional to the signal to noise ratio giving a expression for the energy threshold (E_t) of the detector as:

$$E_t \propto \frac{1}{C(\lambda)}\sqrt{\frac{B(\lambda)t\Omega}{\epsilon(\lambda)A}} \tag{2.14}$$

By making the detector as large as possible, and matching the integration time to the duration of the Cherenkov flash, the minimum-energy threshold can be obtained. The minimum energy air shower detectable can be optimised further by maximising the quantum efficiency of the PMTs used. By having these parameters optimised, the atmospheric Cherenkov telescope will detect Cherenkov flashes above night-sky background.

Chapter 3

The Whipple 10 m Telescope

3.1 Introduction

This chapter describes the operation of the Whipple 10 m telescope operated and maintained by the VERITAS Collaboration in Southern Arizona. The

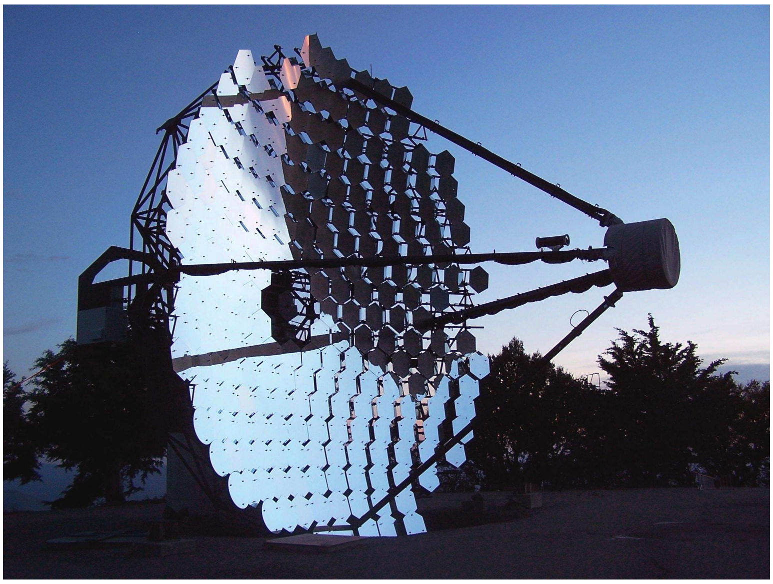

Figure 3.1: The Whipple 10 m γ-ray telescope.

Whipple 10 m telescope (Figure 3.1) is located at the Fred Lawrence Whipple Observatory on Mt. Hopkins in South East Arizona (longitude 110°53.1'W, latitude 31°41.3'N, and 2320 m above sea level). The dry desert climate and clear skies in Southern Arizona are ideal for ground-based γ-ray astronomy. The Whipple 10 m reflector was built in 1969 (Weekes et al., 1972) and its primary function is the search for sources of VHE γ-rays. Since its imaging systems were installed in 1982, it has been in continual use and was the most effective and active instrument in the field of ground-based γ-ray astronomy during the 90s. However a series of newer instruments have recently superseded it in terms of sensitivity and reliability (Hofmann et al., 2000; Weekes et al., 2002).

The telescope can be considered the sum of two components: the reflector and the detector or camera. Although the detector has undergone many changes and modifications in an attempt to enhance the sensitivity of the instrument (Fegan et al., 1983; Cawley et al., 1990; Finley et al., 2001), the reflector is much as it was when it was first constructed.

3.1.1 Davies-Cotton Reflector Design

The reflector design is based on the Quartermaster solar-collector design as proposed by Davies & Cotton (1957) and was first used for astronomical purposes by Hanbury-Brown (1966). In the Davies-Cotton design the optical support structure (OSS) or dish section of a light collecting instrument is spherical in shape and has a radius of curvature exactly half that of the individual mirror facets that make up its tessellated structure. Cherenkov light is collected by the reflecting dish and focused to a detector located at the focal point of the reflector. The main advantages of the Davies-Cotton design include the fact that all facet mirrors are identical, the structure is rigid, off-axis aberrations are reduced and the facet alignment procedure is relatively straight forward. With regard the off-axis properties, the Davies-Cotton design is considered superior to that of a parabolic reflector (Lewis, 1990).

The design does however have a disadvantage in that it is not isochronous. Due to its spherical shape, parallel rays of light from a source reach the outer mirror facets first and, as a result, reach the focal plane before rays reflected from the inner portion of the reflector. This causes a temporal broadening of the optical signal detected by the PMT camera on the order of ~ 6 ns, requiring a longer integration time. This has the effect of reducing the signal to noise ratio. Nevertheless, this reduction is negligible in comparison to the noise contributions of the electronics when the signal is processed later in the data acquisition systems. A further downside of this temporal aberration is that the temporal properties of the Cherenkov light pulse cannot be investigated. Even though the an-isochronous characteristics of the Davies-Cotton design are an undesired attribute, it does not constitute a serious constraint to the detection of VHE γ-rays with the Whipple 10 m telescope.

The Whipple 10 m optical reflector consists of 248 identical hexagonal mirror facets which are mounted on the optical support structure. Each mirror facet has a radius of curvature of 14.6 m. The facets are arranged in a hexagonal pattern of nine concentric rings, covering a spherical dish of radius of curvature 7.3 m and an opening diameter of 10 m. The focal plane is located at the centre of curvature of the dish, resulting in an f/0.7 system. The mirrors can be manually aligned by placing an alignment instrument on the optic axis at a position twice the dish radius of curvature from the telescope. This is known as the alignment point. A discussion of the alignment procedure will be given in Chapter 4. Figure 3.2 shows a ray-trace of a beam

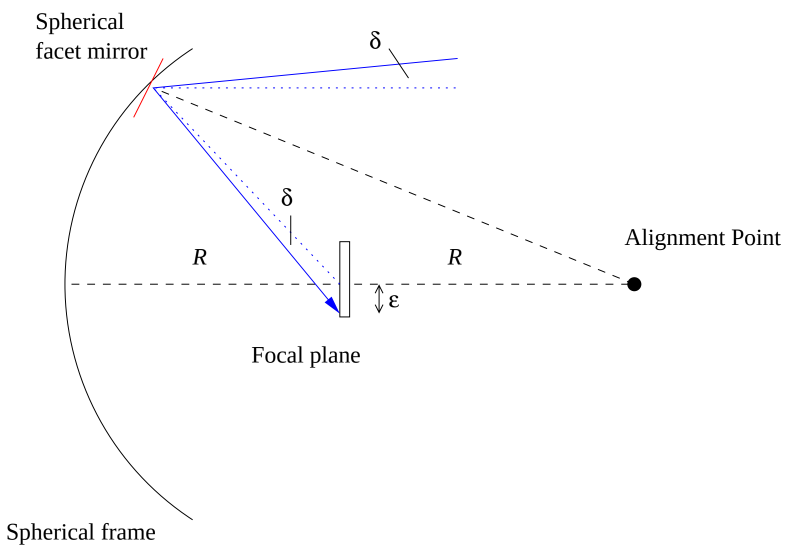

Figure 3.2: The Davies-Cotton reflector design: a spherical dish with radius of curvature half that of its individual mirror facets. Also shown schematically is the plate-scale factor (ε/δ) and the alignment point which is twice the focal length of the reflector.

of light from infinity being focused to the focal plane of the telescope. It also shows the plate scale, *i.e.* the linear displacement on the focal plane per angular displacement of a ray from the optic axis; ε/δ. The Whipple reflector has a plate scale of 12.74 cm/deg. Every mirror element has a width of 61cm and considering all facets results in a reflective surface of 75 m^2.

To increase the reflectivity of the blue/ultraviolet light (the main component of the Cherenkov signal) the facets are front-alluminized. However due to weathering, the mirror reflectivity degrades over time, requiring re-coating of mirrors every three years. Figure 3.3 illustrates the the average reflectivity of a sample batch of 66 mirrors over a range of wavelengths before and after re-coating, and highlights the benefit of this practice. Each facet is individually mounted on the optical support structure via a manually adjustable

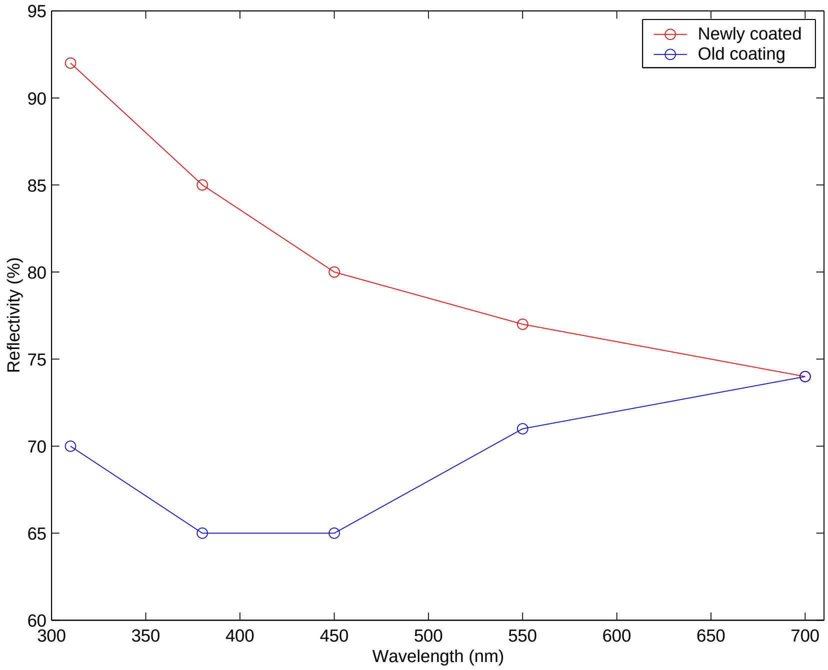

Figure 3.3: Average mirror reflectivities, before and after re-coating. Figure from the VERITAS collaboration. Note here that uncertainties for this data were unavailable.

tripod mount to allow for alignment. A focus box containing the camera elements is located in the focal plane of the structure and is supported by quadrapod arms and can be seen in Figure 3.4 which shows a schematic drawing of the telescope and its main components. Table 3.1 summarises the general dimensions and attributes of the Whipple 10 m telescope.

3.2 Camera

The function of the reflector is to reflect the Cherenkov light produced in the air shower to the focal plane where a closely packed array of photomultiplier tubes (PMTs) is located, herein known as the PMT camera. A picture of

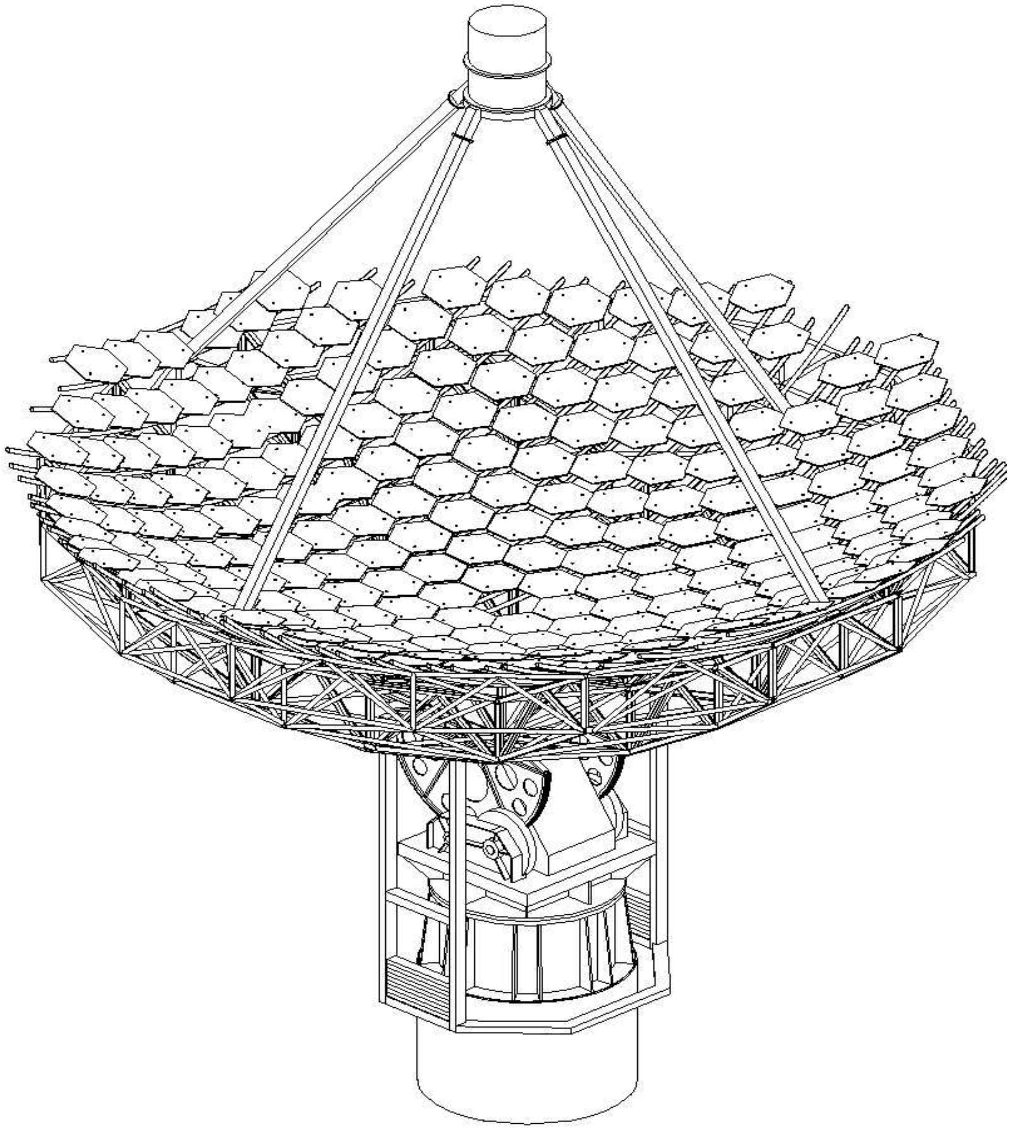

Figure 3.4: A schematic of the Whipple 10 m γ-ray telescope, showing the tessellated mirror facets, camera mounting, and optical support structure. Figure from the VERITAS collaboration.

Attribute	**Value**
Opening Diameter	10 m
Focal Length	7.3 m
Radius of curvature of Dish	7.3 m
Radius of curvature of Facet-Mirror	14.6 m
No. of Facet-Mirrors	248
Reflecting Surface Area	75 m^2
Plate-Scale	12.74 cm/deg
Mount	Alt/Azimuth
Alignment Point	14.6 m

Table 3.1: General dimensions and attributes of the Whipple reflector.

the PMT camera is shown in Figure 3.5. The camera currently consists of an array of 379 fast response, high quantum efficiency ($\sim$ 20%), PMT pixels. Each are 12.6 mm Hamamatsu H3165 PMTs and each individual tube has a field-of-view of 0.116°. This combination of PMTs results in a total field-of-view of 2.8°. As mentioned, the PMT response must be fast since the width of the Cherenkov pulse is $\sim$ 6ns. Also the spectral response should match the peak of the Cherenkov spectrum in the blue to ultraviolet region. This helps to reduce the amount of unwanted night-sky background light whose peak is closer to the red end of the spectrum.

To further aid in the light collecting efficiency of the PMTs, light-guides, or light cones, are placed over the inner tubes in an effort to regain photons that might be lost due to the dead space in between the hexagonal spacing of the PMTs. The light cones are designed to accept only the light reflected by the telescopes mirrors. This too reduces noise from extraneous light. A full outline of the fabrication of the light cones can be found in Hillas (1997) and Krennrich et al. (2001).

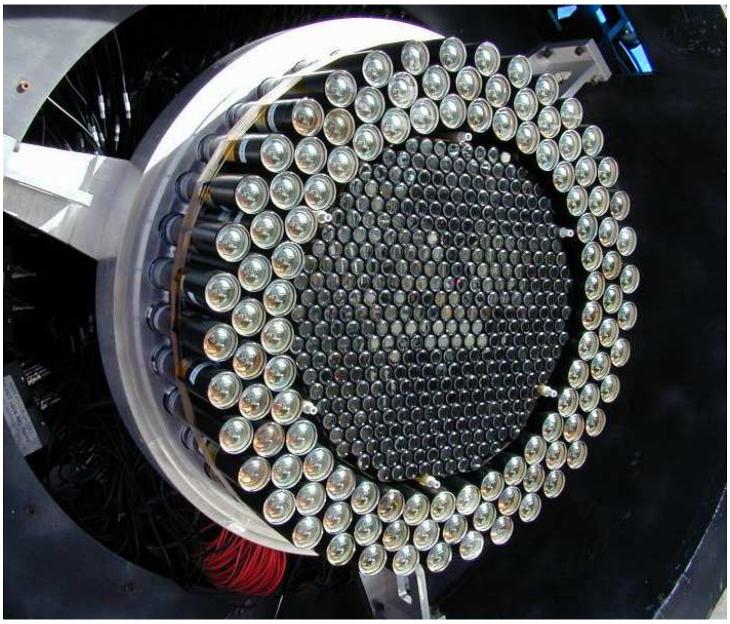

Figure 3.5: The Whipple High Resolution Camera showing the 379 inner PMTs. The outer rings of the larger PMTs that are no longer used are also shown here.

3.2.1 Camera development

Over the 35 years since its construction, the camera on the Whipple telescope has undergone many modifications and changes up to its current configuration. The evolution of the Whipple camera is shown in Figure 3.6. The earliest camera consisted of a single PMT with a 1° field-of-view in 1968. The camera used to collect the archival data of TeV J2032+4130, as dis-

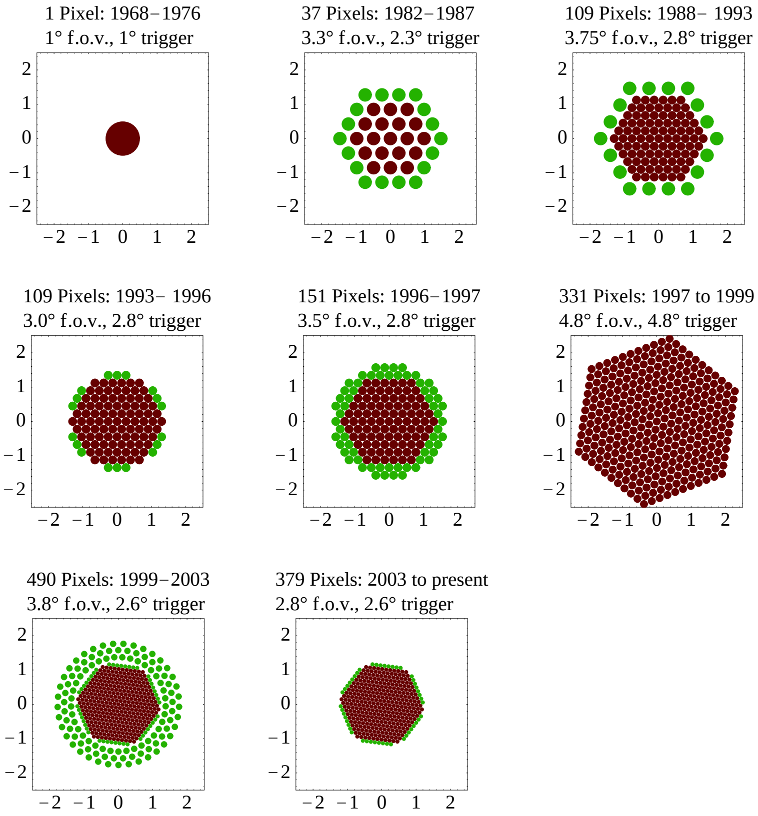

Figure 3.6: The evolution of Whipple 10 m camera with the angular extent shown in degrees. PMTs contributing to the trigger (see section 3.7.3) are shown in red. The 109 camera used to collect the archived TeV J2032+4130 data is seen at the top right. Figure courtesy of Schroedter (2004)

cussed in Chapter 6, was the 109 PMT camera used between 1988 and 1993. This older camera consisted of an array of PMTs similar in design to the 379 PMT camera with several subtle differences. The older array consisted of 91 inner PMTs of diameter 29 mm, arranged in five concentric rings centered on a central tube surrounded by a single ring of 18 tubes of diameter 50 mm, resulting in a total field-of-view of 3.75°. A detailed description of the 109 PMT camera can be found in Cawley et al. (1990). The current camera configuration with a total of 490 pixels was initially installed in the autumn of 1999 and was operated with 379 pixels from 2003 onwards.

3.3 Data Acquisition System

Signals from the PMT array are processed by the data acquisition system built using the fast electronic CAMAC bus system of crates and modules (Rose et al., 1995). A schematic of the system used is shown in Figure 3.7. Using this system, instructions and data are passed to a crate housing several programmable electronic devices. Crate controllers manage the flow of information by Ethernet to the work crates and the data acquisition system computer. This computer passes instructions to the data acquisition system devices through the crate controllers and receives data from the analogue to digital converters (ADCs) and other equipment by means of a CAMAC data buffer known as a list processor.

3.3.1 Amplification

The signals are transferred from the inner 379 PMTs to the pre-amplifiers of the data acquisition system via RG58 coaxial cable. The amplifiers used for the PMTs are LeCroy 612A amplifiers with a gain factor of ten. Of the

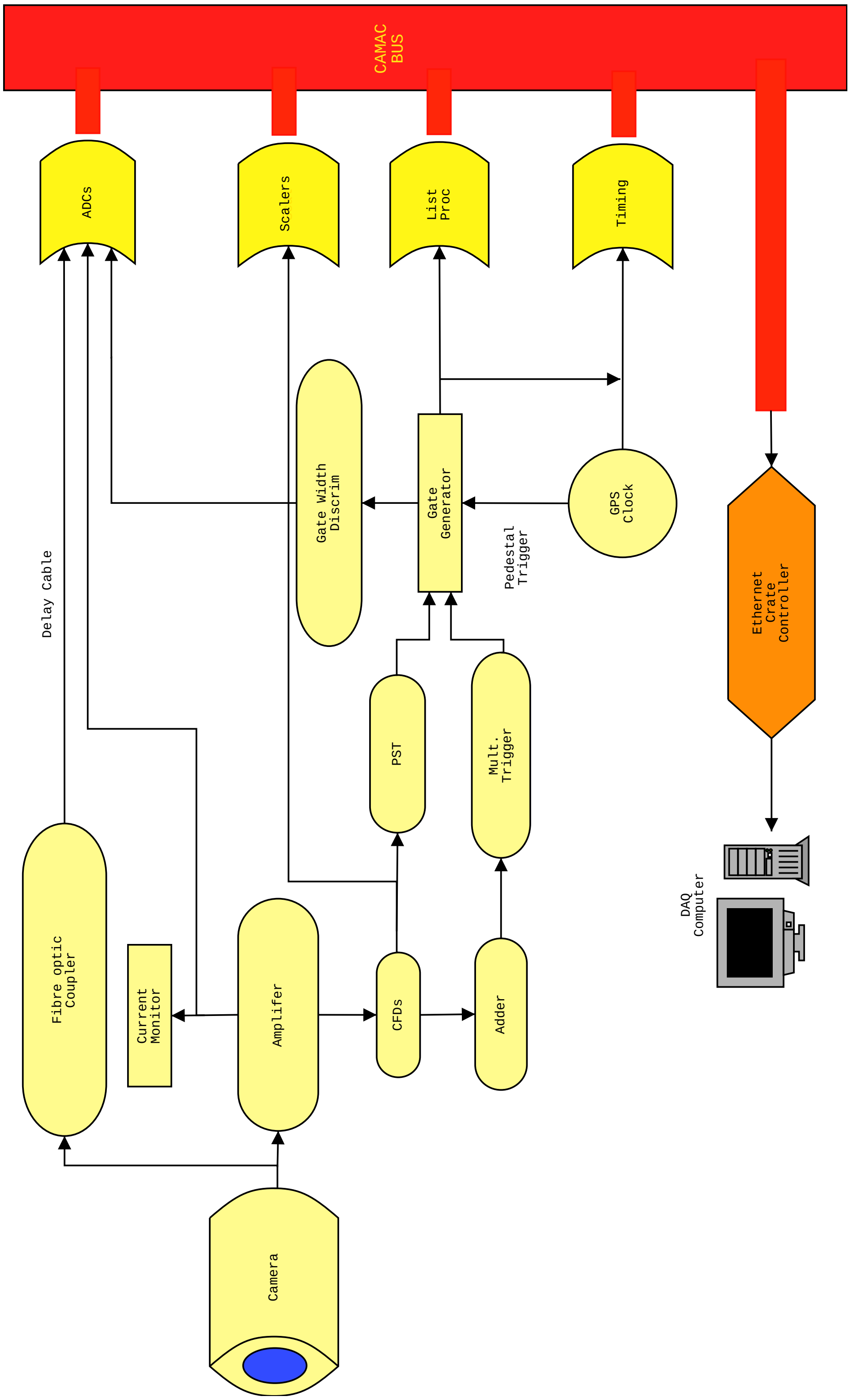

Figure 3.7: Schematic representation of the data acquisition system for the 490 PMT camera. PST refers to the pattern selection trigger as described in Section 3.3.3 and CFDs refer to the constant fraction discriminators.

379 channels, 311 are used in the trigger system. The outer most PMTs are not part of the trigger system as Cherenkov images on the outer edge of the camera can be truncated. There are three outputs from each amplifier.

- One output is AC coupled to the ADCs, but with a delay incorporated via a length of coaxial cable to allow time for the trigger decision to be made.
- The signal from each inner PMT is passed through a constant fraction discriminator.
- The final output is coupled to the current monitor. See Section 3.6.5.

LeCroy 3420 constant fraction discriminators (CFDs) are used to determine whether a PMT has fired. If the signal from a PMT rises above a preset threshold, the discriminator will output a pulse of preset amplitude and duration. The timing of the leading edge of the output signal is determined using a constant fraction of the input signal, resulting in a more accurate synchronisation of signal and trigger pulse than a standard fixed value discriminator. The constant fraction discriminators have three outputs. One set is fed into the single rate scalers. The single rate scalers count the number of times individual tubes have fired. This information is used to monitor any problems with specific tubes. The scalers are only read during a pedestal event, see Section 3.3.4. The remaining constant fraction discriminator outputs are to the pattern selection trigger (PST) and to an adder which sums the signals and outputs a pulse (proportional to the number of PMTs that fired) directly to the multiplicity trigger.

3.3.2 Multiplicity Trigger

The multiplicity trigger determines if the required number of tubes have fired in order for data to be recorded. The required number of tubes is called the multiplicity of the system. Generally the Whipple camera uses a three-fold trigger. This trigger helps keep the amount of accidental triggers due to background light down and provides a low time-jitter signal to initiate signal integration by the ADCs.

3.3.3 Pattern Selection Trigger

The pattern selection trigger was developed to further reduce the number of background events triggering the camera (Bradbury & Rose, 2002). The pattern selection trigger uses the location of signals output from the constant fraction discriminators to determine if the trigger is background related. As described in 3.3.2, the multiplicity trigger operates when any three tubes are above the preset threshold. The pattern selection trigger will only trigger if the three tubes (assuming three-fold multiplicity) that triggered the multiplicity trigger are adjacent. This trigger system further reduces the chance of background light triggering the camera. This in turn allows the system to operate at a lower constant fraction discriminator threshold while at the same time maintaining a reasonable trigger rate. Figure 3.8 shows an example of a bias curve during the 2000 observing season. A bias curve is a plot of trigger rate versus constant fraction discriminator threshold for the multiplicity trigger and the pattern selection trigger and is used to determine the constant fraction discriminators threshold for each season. In the example shown the threshold was found to be 36 mV. As seen, the trigger rate increases from a high constant fraction discriminator threshold to a low constant fraction

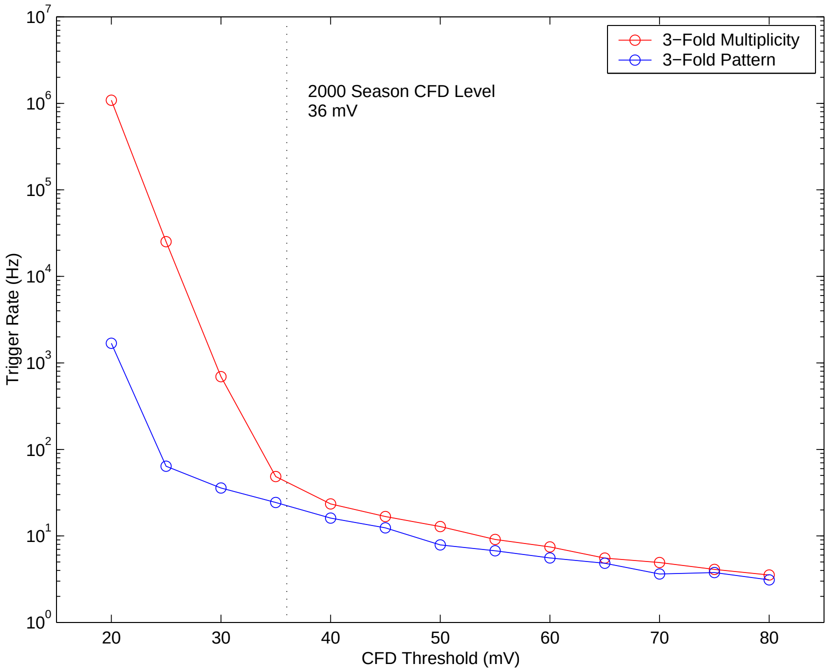

Figure 3.8: Bias curves of trigger rate vs. Constant fraction discriminator threshold for Multiplicity and Pattern Triggers.

discriminator threshold. At high values the trigger rate is dominated by cosmic rays. As the threshold gets lower, the trigger rate increases rapidly. At these lower values the trigger rate is dominated by random fluctuations in the night sky. The constant fraction discriminator trigger is chosen to be as low as possible without being in the regime dominated by the night sky background. It can also be seen from the diagram how a lower threshold level can be attained by using a pattern selection triggering system.

3.3.4 Pedestal Trigger

Since the PMT signals are AC coupled before they reach the ADCs, the effects of the average night sky background current as well as other dark currents are removed. However, positive and negative fluctuations from the average current can occur in the 25 ns ADC integration time. These fluctuations must be measured in order to characterise the background noise in the system. This is achieved by injecting a constant "pedestal" current into the ADCs along with the signal from the PMTs. The main requirement here is that the size of the current is set so that the majority of the negative night sky fluctuations will still result in a positive ADC signal when integrated over the gate. The pedestal current level is usually set to produce a level of ~ 20 digital counts which corresponds to the ADC output for zero input. When the data are analysed the level of these pedestals must be determined and then removed from the data leaving only the night sky fluctuations and any Cherenkov signals.

To do this a pedestal event is artificially triggered by means of a global positioning satellite (GPS) clock once every second and is tagged by the data acquisition system to distinguish it from real events. It is assumed that all the recorded ADC counts in these triggered images are due solely to night sky noise. By recording each pedestal event over the duration of a 28 minute run, the mean amplitude of the injected pedestal for each channel can be calculated. The RMS deviation from the mean is also calculated and is called the “pedestal variance” (“pedvar”). This value is representative of the size of the average sky fluctuation for each channel.

From the pedvar values the median is found. Each PMT’s pedvar is then compared with the median value and if found to be too large ($>$ 1.5 times median value), then it is assumed that the tube had a star or bright region of the sky in its field of view during the observation run. In this case the analysis software ignores this channel so it does not influence the outcome of the analysis result. Similarly, if the pedvar of a channel is found to be too low ($<$ 0.6 times median value), it is also disabled by in the analysis routines as the tube may actually have been switched off or not functioning properly.

3.3.5 Data Read out and Recording

If all the trigger requirements are met, the signal is sent into the gate generator, which in turn outputs a negative square pulse to the ADCs via a discriminator. The ADCs are LeCroy 10 bit 2249 modules. Even though Cherenkov pulses are about 5 ns in duration, the width of the square pulse is set to $\sim$ 25 ns. This allows for dispersion of the signal introduced by the electronics. The PMT signal is integrated over the duration of the gate signal.

After signal integration the data is transferred via the CAMAC bus to the list processor. The list processor is essentially a data buffer between the CAMAC crates and the data acquisition computer. This buffer also stores timing and scaler information until the data acquisition computer is ready to receive the data. The data acquisition computer operates under VMS and controls each observation run. The final task of the of the data acquisition computer is to record all data, including tracking, timing and monitoring information, to the hard drive. These data are then archived for off-line analysis at a later date.

3.4 Data Analysis Techniques

Previous sections have detailed the physics behind EAS, the instruments used to detect the Cherenkov flash caused by EAS, and the observational methods used as part of the imaging atmospheric Cherenkov technique. Once the events, that have triggered the camera, have been recorded and stored by the data acquisation system it is then the task of the analysis routines to identify and differentiate the γ-ray events from the large number of hadronic events. This section describes the remaining element used in the imaging atmospheric Cherenkov technique; analysis and identification of Cherenkov images.

3.4.1 Data Calibration

Before the data can be analysed they must be prepared for analysis via the following steps:

- Pedestal Subtraction: the removal of the positive offset added to the ADC outputs as described in Section 3.3.4.
- Flat Fielding: Since each PMT has a slightly different gain, it is necessary to scale the signals recorded in each tube accordingly so PMTs with larger gains do not distort the final analysed image. This is done using the nitrogen lamp as discussed in Section 3.6.3.

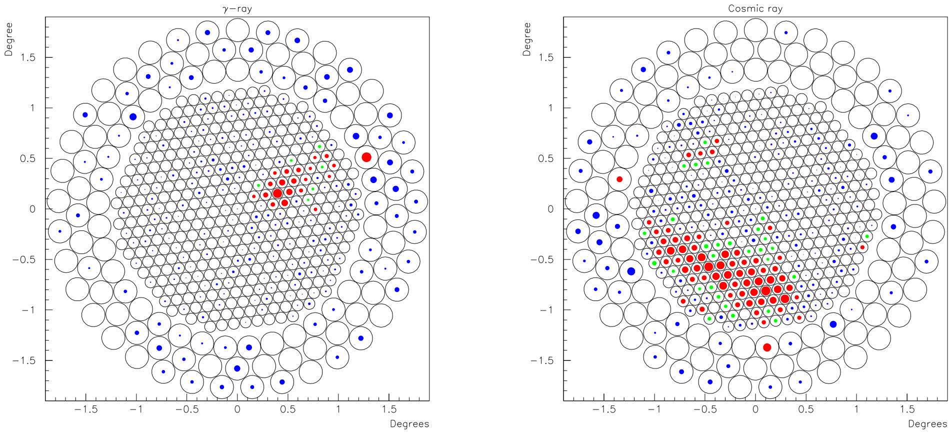

(a) γ-ray (b) Cosmic ray

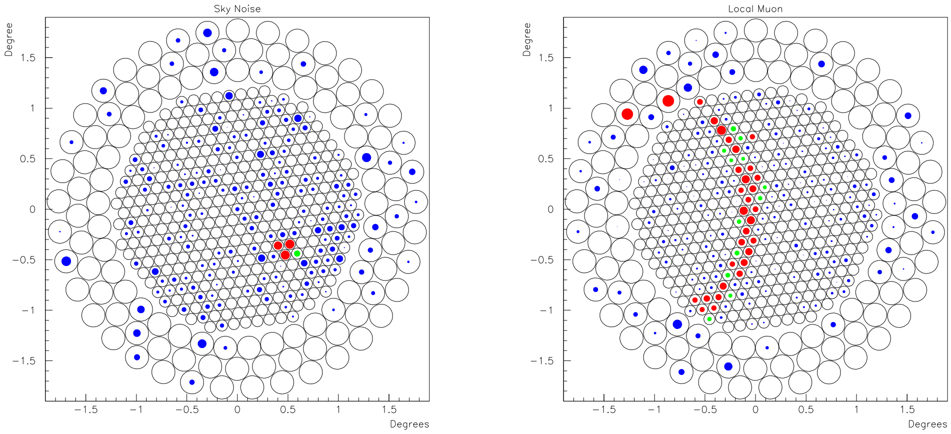

(c) Sky noise (d) Local Muon

Figure 3.9: Examples of the four main types of events that can trigger the camera during an observation run. Top left, a γ-ray image; top right, a cosmic ray image; bottom left, sky noise trigger; bottom right, part of a muon ring image. Taken from Dunlea (2001)

- Noise padding. During the course of an observation run the sky brightness of the *ON* (the source being observed) or *OFF* (the control observation) region (see Section 3.5) can vary significantly. This means pedestal deviations can differ accordingly and can introduce a bias, distorting the results of the analysis procedure. To rectify this problem the noise levels must be equalised in the *ON* and the *OFF* runs. To do this artificial noise is added to the data from the darker of the two sky regions.

- Finally, before parameterisation, the images must be cleaned. Once the above processes are complete, what is left is an image of the signal due to the Cherenkov flash and noise due to the night sky background. Hence, before analysis, the night sky background element of the signal must be removed as best as possible. This is achieved by the following method of applying picture and boundary thresholds. Picture and boundary thresholds are what define the boundaries of the image and are defined as :
  - The picture threshold is defined as the multiple of the RMS pedestal deviation which the tube must exceed to be part of the picture.
  - The boundary threshold is defined as the multiple which tubes adjacent to the picture must exceed to be part of the boundary. Picture and boundary thresholds are optimised and set at 4.25σ and 2.25σ respectively (Punch et al., 1991).

This project utilised two different analysis techniques in an attempt to correctly identify the Cherenkov flash induced by a high energy γ-ray photon; *Supercuts* and *Kernel* analysis. Both of these techniques are very successful in rejecting nearly 100% of noise events while retaining over 50% of genuine

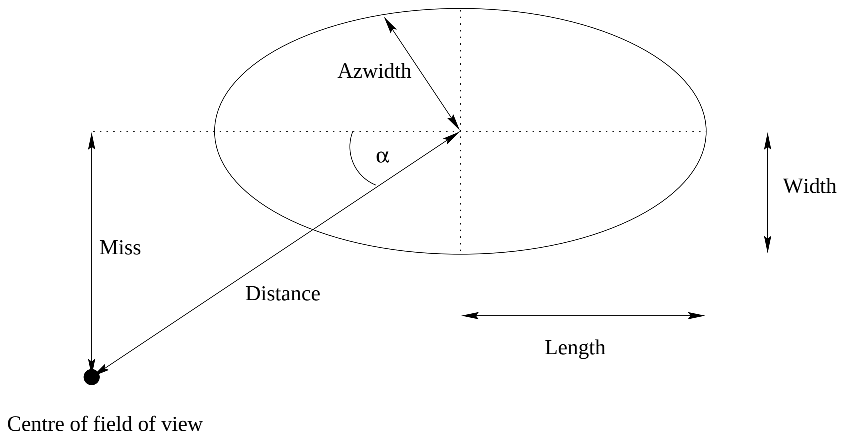

Figure 3.10: The Hillas parameters.

γ-rays (Fegan, 1997; Moriarty & Samuelson, 2000). The *Supercuts* technique was used in conjunction with the deconvolution of Cherenkov images while a *Kernel* analysis was performed on archival Whipple data for the first time.

3.4.2 Standard Image Analysis (*Supercuts*)

The standard analysis software used by the VERITAS Collaboration, known as *Supercuts*, uses moment fitting routines to fit an ellipse to the recorded Cherenkov images. Generally, a Cherenkov image from a γ-ray induced air shower will appear as an elliptical image pointing towards the centre of the field of view of the PMT array. Figure 3.9(a) shows a typical, uncleaned, Cherenkov image from a γ-ray induced air shower. Figure 3.9 (b), (c) and (d) illustrate typical hadronic events, noise events and a single muon event. It is these events shown in Figure 3.9 (b),(c) and (d), that contribute to over 99% of events recorded by imaging atmospheric Cherenkov telescopes. From the diagram the subtle differences between each of the events can clearly be seen. Hillas (1985) derived a moment fitting procedure to try and exploit these

*Length**	The RMS spread of light along the major axis of the ellipse (longitudinal development of the shower).
*Width**	The RMS spread of light along the minor axis of the ellipse (lateral development of the shower).
*Azwidth**	The RMS Spread of light perpendicular to the line connecting the image centroid with the centre of the field of view; a measure of the shape and orientation of the image.
*Miss**	The perpendicular distance between the major axis of the image and the centre of the field of view.
*Distance**	The distance between the centroid of the image and the centre of the field of view.
Alpha	The angle between the major axis of the ellipse and a line joining the centroid of the ellipse to the centre of the field of view.
*Frac3**	Fraction of the total light in the image contained in the three highest tubes; used to eliminate events caused by sky noise and particles physically passing through the camera.
Size	The total number of digital counts in all of the tubes; a number proportional to the energy of the primary particle.
Asymmetry	A measure of how symmetric the image is.
Max1, Max2 & Max3	The signals in the highest three tubes.
Length/Size	A measure of the compactness of the image in relation to its total light content; helps to eliminate background due to local muons.

Table 3.2: The Hillas Parameters. * Denotes the original six Hillas parameters.

differences and in turn provide a means to differentiate between unwanted noise events and true γ-ray induced events.

Knowing that images produced by γ-ray induced showers, from sources located at the centre of the field of view, resemble compact ellipsoids with their major axes pointing towards the centre of the field of view, Hillas defined a set of six parameters to describe the shape and orientation of a Cherenkov image (illustrated in Figure 3.10). Table 3.2 defines the original set of Hillas parameters and additional parameters introduced to increase the γ-ray selection efficiency. A full description of the moment fitting technique can be found in Reynolds et al. (1993).

By choosing an appropriate range of selection cuts to each of the parameters listed in Table 3.2, it is possible to reject over 98% of the cosmic ray background whilst keeping $\sim 60\%$ of the γ-ray events. Since they were first developed, the Hillas parameters have evolved to adapt to a changing instrument.

A variant of the original Hillas parameters, *Supercuts* has since become the most successful selection mechanism used by the VERITAS Collaboration. Having been optimised using observations of the Crab Nebula (Punch et al., 1991), the VERITAS Collaboration has since used *Supercuts* in the discovery of several new sources (Horan et al., 2002; Holder et al., 2003). The *Supercuts* selection criteria as used by the VERITAS Collaboration are listed in Table 3.3.

3.4.3 Kernel Analysis

In addition to the standard *Supercuts* analysis technique, the *Kernel* multivariate analysis technique was applied to a portion of the work in this project as will be discussed in Chapter 6. *Supercuts* essentially classifies events, each

***Supercuts* Parameter Values**
0.05°< *Width* < 0.12°
0.13°< *Length* < 0.25°
0.40°< *Distance* < 1.0°
0°< *Alpha* < 15°
Max1 > 30 d.c.
Max2 > 30 d.c.
0.0°< *Length/Size* < 0.0004°

Table 3.3: The most recent values used as the standard *Supercuts* selection criteria for the Whipple 10 m imaging atmospheric telescope that candidate γ-ray events are expected to pass.

described by a set of n Hillas parameters, by choosing a surface in parameter space. It is a box selection technique whose boundaries are defined by the *Supercuts* values with the Hillas parameters being the axes of this multidimensional phase space. Events are identified as being initiated by a γ-ray or a background event depending whether or not they lie within the box once all the selection cuts have been applied to the data set.

The *Kernel* analysis technique is different to *Supercuts* in that it looks at the γ-ray probability distribution as a function of the Hillas parameter space. The *Kernel* analysis technique allows for correlations between parameters to be taken into account. The usefulness of the *Kernel* technique in very high energy γ-ray astronomy has been shown previously by Moriarty & Samuelson (2000). Further detailed descriptions of the technique can be found in Kildea (2002) and Dunlea (2001).

In brief, the *Kernel* technique uses Monte Carlo simulations of γ-ray events as generated by the KASCADE[1] simulation software (Kertzman &

---

[1] KASCADE is a detailed computer program that simulates, in three dimensions, the generation, propagation, and detection of Cherenkov photons produced during extensive air showers.

Sembroski, 1994) along with real background events to define a probability surface where events on one side of the surface have a high probability of being γ-rays and events on the other side are predominantly background events. For a point p in parameter space this surface is calculated using the log-likelihood function:

$$\log\left(R(p)\right) = \log\left(\frac{f_\gamma(p)}{f_b(p)}\right) \tag{3.1}$$

where $f_\gamma(p)$ is the γ-ray probability distribution as a function of location, p, in Hillas parameter space and $f_b(p)$ is the corresponding background probability distribution function. That is, $f_\gamma(p)$ is the likelihood the real data event being analysed corresponds to a γ-ray and $f_b(p)$ is the likelihood it is a background event. The calculation of these distributions is the key to the *Kernel* analysis technique (Dunlea et al., 2001). log(*R(p)*) gives an indication as to the identity of each event in a data set. A suitable log(*R(p)*), or cut value, may be chosen such that any real events with a score lower than this are rejected and assumed to be background events.

Since γ-ray events and background events populate this parameter space in a complex way, it is not possible to describe their probability density distribution analytically in terms of a simple function, although attempts have been made Samuelson (1999). The simplest probability density estimator is a histogram. However a histogram in this instance is not ideal since each cell has a fixed width, and a limited range, as well as cell boundary discontinuities (Hand, 1982). In an attempt to remove these problems, the *Kernel* convolves each data point with a point-spread function and sums the results, producing a smooth, continuous approximation to the probability distribution. The basic *Kernel* estimator is found using a set of N_γ simulations and is given by:

$$f_\gamma = \frac{1}{N_\gamma h_\gamma^n} \sum_{i=1}^{N_\gamma} K\left(\frac{p - p_{\gamma_i}}{h_\gamma}\right) \tag{3.2}$$

where p is a sample point in Hillas parameter space at which the probability density is calculated, h_γ is a scaling factor that describes the width of the point spread function, and p_{γ_1},...,$p_{\gamma_{N_\gamma}}$ are vectors of parameters of N_γ. The point spread function is the *Kernel* function (K) and can be any scalar function in n-dimensional space (Hand, 1982; Scott, 1992). Samuelson (1999) and Moriarty & Samuelson (2000) have shown that for imaging atmospheric Cherenkov technique data, a multivariate Gaussian is an appropriate *Kernel* function:

$$K = \frac{1}{\sqrt{(2\pi)^n \left|\xi_\gamma\right|}}\ e^{-\frac{1}{2}\left(\left(\frac{p-p_{\gamma_i}}{h_\gamma}\right)^{\mathsf{T}} \xi_\gamma^{-1} \left(\frac{p-p_{\gamma_i}}{h_\gamma}\right)\right)} \tag{3.3}$$

Here n is the number of parameters and ξ_γ is the covariance matrix of the γ-ray dataset, which is the means by which each parameter is correlated with every other one. The background distribution is similarly defined using real background events:

$$K = \frac{1}{\sqrt{(2\pi)^n \left|\xi_b\right|}}\ e^{-\frac{1}{2}\left(\left(\frac{p-p_{b_i}}{h_b}\right)^{\mathsf{T}} \xi_b^{-1} \left(\frac{p-p_{b_i}}{h_b}\right)\right)} \tag{3.4}$$

If the *Kernel* is the product of Gaussians (one for each dimension), Scott (1992) has shown that the scaling factor that minimises the error between an actual distribution and its *Kernel* estimator is:

$$h_\gamma = \left(\frac{4}{N_\gamma\left(n+2\right)}\right)^{1/(n+4)} \tag{3.5}$$

In this work a multivariate Gaussian is used and the γ-ray probability density distribution is defined by substituting Equation 3.3 for K in Equation 3.2.

The probability density distribution for a set of background events, f_b can be similarly defined. In practice the *Kernel* technique is computationally intensive since each real event is compared to every simulated event and every background event, to calculate $f_\gamma(p)$ and $f_b(p)$, and hence a probability score, log(*R(p)*), for each event. A selection cut is then applied to the values in order to achieve an optimum signal-to-noise ratio.

To reduce computational time somewhat, as a form of pre-selection, a loose set of cuts can be applied to the data prior to the probability distribution calculation (Moriarty & Samuelson, 2000). Further details and analysis results using the *Kernel* technique are covered in Chapter 6.

3.5 Observations and Operation

The imaging atmospheric Cherenkov technique is a powerful method of detecting γ-rays that penetrate into the Earth's upper atmosphere causing EAS (Fegan, 1996). However EAS are also created by hadrons and are also imaged by the imaging atmospheric Cherenkov technique. Unfortunately there are many orders of magnitude more hadron-initiated events in the field of view of the telescope than there are γ-ray events, even in the field of view containing strong steady sources. In addition to hadrons, contributions from night-sky background noise fluctuations and Cherenkov radiation from local muons can also trigger the camera. In order to extract the γ-ray signal from the overwhelmingly large number of noise events, an estimation of the contribution of the background noise is required. There are two techniques used to estimate the background; *ON/OFF* mode or *TRACKING* mode.

ON/OFF

In *ON/OFF* mode a putative source of VHE γ-rays is first observed for 28 minutes. This is the *ON* run and is followed by another 28 minute run with the telescope position offset by 30 minutes in right ascension from the *ON*-source position. This is the *OFF* run or a region of sky with no VHE γ-ray signal. Together the *ON/OFF* runs are called pairs. The *OFF* run can then be used as an estimate of the background in the *ON* run. Assuming a Poissonian noise distribution, the significance[2], σ, of the excess *ON*-source γ-ray events above the background of *OFF*-source events can be calculated using the Li & Ma (1983) method

$$\sigma = \frac{ON - OFF}{\sqrt{ON + OFF}} \tag{3.6}$$

where *ON* is the number of events that pass the γ-ray selection criteria in the *ON*-source run and *OFF* is the number passing in the *OFF*-source run. A signal of 5σ of more, along with an equivalent result from an independent group, is considered as a source detection (Weekes, 1999). The corresponding γ-ray rate and its error, expressed in γ-ray events per minute, is calculated using

$$Rate = \frac{ON - OFF}{time} \pm \frac{\sqrt{ON + OFF}}{time} \tag{3.7}$$

where *time* is the total time spent *ON*-source. The *ON/OFF* mode of observations has been in use now for many years and is accepted as an effective method for use with the imaging atmospheric Cherenkov technique. It does

---

[2] The ratio of the signal to its standard deviation

however have an obvious disadvantage in that only 50% of observation time is spent *ON*-source due to the very nature of the *ON/OFF* observations. This disadvantage can become an issue when observing variable sources such as flaring AGN. In these cases it would be preferable to spend as much time *ON*-source as possible. The solution to this problem is the *TRACKING* mode of observations.

TRACKING

In *TRACKING* mode the target source is tracked continuously ON-source without taking an *OFF* run. The impact of this is that there are no independent control data associated with the run, so the background level of γ-rays must be estimated from the *TRACKING* run.

This estimation is essential in order to predict the number of non γ-ray events that pass the analysis cuts. This estimation is an indication of the number of cosmic ray events that would have been accepted by the cuts in the absence of the candidate γ-ray source. To perform this estimation some understanding of the image parameterisation procedure is required. After the pedestals have been subtracted, the imaged flat-fielded and cleaned, it must now be parameterised. The procedure calculates the first, second and third moments of the distribution of light in the camera plane and an ellipse is fitted to each event as shown in Figure 3.10.

The parameter of interest to help in the estimation of the background event excess for the *TRACKING* mode is the *Alpha* parameter. From Table 3.2, *Alpha* is defined as the angle between the major axis of the fitted ellipse and a line drawn from the centre of the field of view. For showers induced by γ-rays, coming from the centre of the field of view, an elliptical image will be recorded with its major axis pointing towards the centre of the camera, *i.e.* a small value of *Alpha*. For each run the number of *Alpha* values can be binned according to their value and a histogram can be plotted. The "*Alpha* plot" for a positive source will generally have a large excess with small values of the *Alpha* parameter.

With *TRACKING* runs, the background level of γ-ray like events in the field of view can be estimated by using a pool of *OFF* runs known as "darkfield data" and the shape of the resulting *Alpha* plot is characterised. To do this, a large database of darkfield data is analysed and an approximately flat *Alpha* plot is obtained, as expected when no γ-rays are present.

In reality this *Alpha* plot isn't completely flat and any fluctuations seen are due to the finite size of the pixels and truncation effects due to events being imaged at the edge of the field of view. In particular, events with an *Alpha* value $> 65°$ are sensitive to truncation effects and hence are not used in the determination of the level of background. Generally the *Alpha* plot is flat up 65°.

As mentioned, γ-ray events from a source located at the centre of the field of view will tend to have lower values of *Alpha*, *i.e.* $< 20°$, so the distribution above 20° is assumed not to be associated with any γ-ray source. With these *Alpha* limits in mind, the range of *Alpha* values between 20° and 65° is representative of the background level of γ-ray like events in the field of view. Using darkfield data, a ratio is calculated to scale the number of events between 20° and 65° to the number that pass the standard *Alpha* cut in the darkfield data. This ratio is the "*tracking ratio*" (ρ) and is then used to scale the 20°and 65°region for the *TRACKING* run, to estimate the background level of events passing all cuts. The *tracking ratio* is calculated as follows:

$$\rho \pm \Delta\rho = \frac{N_{source}}{N_{control}} \pm \sqrt{\frac{N_{control}}{N_{source}^2} + \frac{N_{control}^2}{N_{source}^3}} \tag{3.8}$$

where N_{source} is the number of events in the darkfield data that pass the *Alpha* cut and $N_{control}$ is the number of events that are in the 20°- 65° region in the darkfield *Alpha* plot.

The γ-ray rate and its statistical uncertainty ($\Delta Rate$) using this method are given by:

$$Rate \pm \Delta Rate = \frac{N_{on} - \rho N_{off}}{time} \pm \frac{\sqrt{N_{on} + \rho^2 N_{off} + \Delta\rho^2 N_{off}^2}}{time} \tag{3.9}$$

where N_{on} is the number of events passing the *Alpha* cut (of the *TRACKING* run), N_{off} the number of events in the 20°- 65° region of the *Alpha* plot (of the *TRACKING* run) and *time* is the duration of the *TRACKING* run. The significance is given by:

$$\sigma = \frac{Rate}{\Delta Rate} \tag{3.10}$$

3.6 Monitoring

3.6.1 Timing

As with any astrophysical observation, timing is an important consideration. The 10 m Whipple telescope uses two separate (GPS) clocks to provide a timing accuracy of 250 μs. This is improved to 0.1 μs by means of a 10 MHz oscillator. When the trigger electronics output an event, timing information is sent to the list processor and output from the oscillator is fed into two scalers. The first scaler gets activated at the start of each run and records the elapsed time. The second scaler is also activated at the start of the run. However it only operates when the trigger gate is open, and thus provides a measure of the live time of the system.

3.6.2 Tracking

The Whipple 10 m telescope has an Alt-Azimuth mount. Each axis is driven independently by a variable speed motor with a resolution of 0.01°. The mount has a slew rate of 1° per second and has an azimuth range of 270° in both east and west directions and an elevation range of 0° to 90°. The pointing of the telescope is controlled by a computer located in the control room. The equatorial coordinates of a given source are stored in a database and an integrated software algorithm constantly calculates the altitude and azimuth of the source by reference to local sidereal time. Sidereal time is obtained from a remote Network Time Server. This enables the telescope to continuously track the source in the sky.

As a safety measure, there are limit switches to prevent the telescope from moving beyond its range, both in elevation and azimuth. There is a software limit that, when reached, instructs the drive controllers to stop. In the case of a software failure, there are also hardware limit switches installed on the telescope mount that will stop the drive motors.

Tracking accuracy is normally checked several times during a nights observation by lining up the telescope with a guide star. This is known as a “pointing check”. Once the telescope has centered the guide star, the currents in the inner seven PMTs are monitored. If the pointing is accurate then the central PMT will have the largest current reading, while the remaining six PMTs will have some overflow of excess current.

3.6.3 Nitrogen Lamp

A blue nitrogen arc lamp, used to calibrate the PMT camera, is located at the centre of the telescope dish. At the beginning of every night the lamp is activated and pulses at high frequency, providing uniform illumination across the camera. The data acquisation system starts this “nitrogen run” which lasts for one minute. During this time the camera is triggered by a large number of artificial events, which in turn are used to calculate the gain of each tube relative to the average gain. These gains are then applied later in the analysis of the data in a process known as “flat fielding”, where each PMT output is scaled by the appropriate gain value.

3.6.4 High Voltage System

In order for the PMT camera to operate, a high voltage system is required to power each PMT. Three LeCroy high voltage (HV) modules supply the required HV to all PMTs. The HV modules are located on the telescope counterweights and are operated remotely, via Ethernet, from the control room. Here a computer monitors the voltage settings on each tube and can, if required, shut down individual PMTs. Individual PMT HV settings can also be adjusted by using the camera-related software in the control room.

3.6.5 Current Monitor

As well as monitoring the HV applied to the PMT, the anode current of each PMT is also measured and monitored in parallel with the main data acquisition. After the amplification stage, the PMT signals are sent to the current monitor. The ADCs in the current monitor have an integration time much greater than the ADCs in the data acquisition system allowing the presence of steady back ground light to be seen. This is particularly useful for detecting stars that may be in the field of view during a data run.

Information on PMT currents is sent to the HV control program via a serial link and a colour coded graphical display detailing tube current status, as well as HV information, is output to a screen. If there is a problem with any of these systems the telescope operator is alerted and can act accordingly. The tube current display is particularly useful for indicating when a star enters the field-of-view. The observer can then temporally disable any affected tubes thus avoiding damage from excess current.

3.6.6 Weather Monitoring

As with most other types of astronomy, good weather conditions are of the utmost importance to γ-ray astronomy. With this in mind, there are several weather monitoring tools available to measure observing conditions during the course of a night's observations. Each night the atmospheric conditions are recorded in the observer log sheet with conditions rated as A,B or C, corresponding to very good, fair, or poor weather conditions. During 2001/2002, a weather station and far-infrared (FIR) pyrometer were installed and tested on the 10 m site. The weather station measured temperature, wind speed and humidity. The pyrometer gave a further indication of sky clarity by measuring the night-sky temperature. Clouds passing within the FOV produce an increase in the reported pyrometer temperature. This temperature increase is proportional to the height, thickness and water content of the cloud. With no cloud present, the temperature decreases to the quiescent level, which is almost entirely dependent upon the water vapour content in the atmosphere above the detector (Dowdall, 2003). The weather station and FIR pyrometer have since been installed at base camp for use with the

VERITAS array. Currently, weather information is obtained from a weather station at the nearby 60” optical telescope and from satellite information available from several weather internet sites.

A further tool for monitoring sky conditions, albeit a crude one, is an optical camera. An Electrim EDC1000L Charged-Coupled Device (CCD), coupled with a 25mm f/0.85 Fujinon lens is mounted on the telescope next to the focus box, with its optic axis close to and parallel to the optic axis of the reflector. This camera has several other uses too. It can also be used as an independent check of telescope pointing and also gives a further warning of any bright stars in the field of view. The camera has a field of view of 8°, and, depending on exposure time, images captured are displayed in the control room and are updated every ten to twenty seconds.

Chapter 4

VHE γ-ray Sources and Ground Based Detectors

4.1 VHE γ-ray Sources

At present no complete sky survey exists at TeV energies, although progress in this area is being made. A map of the known sources including the most recent detections in this energy regime is represented in Figure 4.1. The list of known sources has more than doubled since the newer imaging atmospheric Cherenkov instruments have come on line. It is expected that the list of sources in the northern hemisphere will grow further when VERITAS starts to return scientific results in the coming months along with the expanding HESS catalogue of sources in the southern skies. Of the sources detected, each source is classified as belonging to a particular type or class, due to the nature of the emission from the object. Therefore, a variety of production models have been published that describe the different types of γ-ray emission from these objects. This range of sources include galactic sources such as supernova remnants (SNRs), and the related pulsar wind nebulae (PWN) also known as plerions, microquasars, X-ray binaries, unidentified sources (UIDs or dark accelerators). Of the extragalactic sources, there are active galactic nuclei (AGN), usually blazars, and giant radio galaxies.

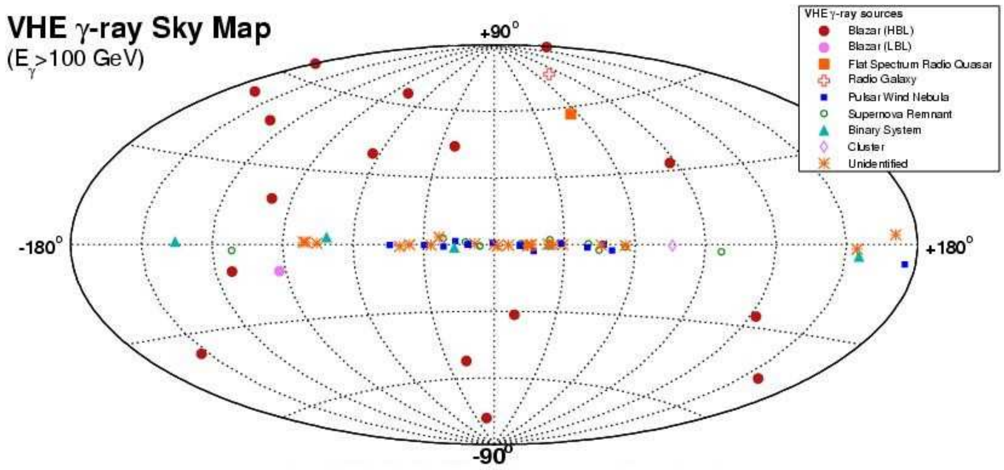

Figure 4.1: Distribution of TeV sources in galactic coordinates. Taken from http://www.mppmu.mpg.de/ rwagner/sources September 20th 2007.

4.1.1 Supernova Remnants

A star's evolution is largely dependent on its mass (Holliday, 1999). When a large star with a mass $\gtrsim 3\ M_\odot$ [1] has used up all its available fuel, its evolution culminates in the catastrophic and destructive transformation into a supernova. Supernovae can occur as a result of corecollapse, such events are classified as *Type Ib* and *Type II* supernovae. The star's instability and collapse occurs as a result of its composition. From fusing lighter atoms together

---

[1] $M_\odot$ = the mass of the Sun : 1.98×10^{30} kg

for millions of years the star has created an ever-increasing amount of heavier atoms. This process, while releasing nuclear energy in a very efficient manner, is ultimately reliant upon the stars quantity of lighter elements. Once this supply is exhausted the stars huge mass can no longer be supported by the dwindling release of nuclear energy. The star succumbs to its own gravity and so contracts. Eventually the core is no longer stable against inverse beta decay. This results in the rapid removal of electrons from the electron gas causing the core to collapse. Tremendous shock waves are generated and the energy released, a large fraction of which is in the form of neutrinos, causes the outside layers of the star to be ejected violently away from the core into space. Approximately 10^{44} J is transferred as kinetic energy to the rapidly moving ejecta.

Supernovae can also occur from binary star systems containing a white dwarf and a red giant. Such *Type Ia* events arise from the white dwarf accreting material from the companion. The dwarf's mass and subsequent internal pressure increase until reaching a critical density ($1.4\ M_{\odot}$) resulting in the uncontrollable fusion of its carbon and oxygen. The thermonuclear explosion of the entire white dwarf releases Iron and other heavier elements into the interstellar medium. A type Ia supernova is recognised by the absence of hydrogen and the presence of elements such as silicon and sulfur in its spectrum. Since all Type Ia events are of similar magnitude they can be used as precise 'standard candles' to measure the distances to their host galaxies.

Supernova explosions have durations of the order of seconds, and are only expected to occur around once every 20 years in our galaxy. The gaseous cloud, composed from the constituents of the former star is termed a Supernova Remnant (SNR). If there remains a core of the original star, it can continue to be quite active. If conditions are right the immediate aftermath of a supernova may result in a rapidly rotating, highly magnetised, sphere of neutrons known as a pulsar, and the supernova remnant or the remaining nebula. (Note, not all supernovae result in the creation of a neutron star. For example, the supernova remnant Cassiopeia A has no known associated neutron star or pulsar.) The supernova remnant is enclosed by an expanding shock wave that consists of ejected stellar material expanding from the explosion, and the interstellar material it sweeps up and accelerates along the way..

There are two main types of SNR: a shell-type SNR (spherical shell) and a plerion that has a filled centre containing a pulsar (Weiler, 1978). It is also possible that the SNR has both a shell and plerionic component. The most famous and most studied SNR is the Crab Nebula. It is a plerion in which the high-energy electrons emit synchrotron radiation from radio energies to X-ray energies, and the production of VHE γ-rays via inverse Compton scattering. Salvati (1973) suggests that the filled interior is constantly replenished by the conversion of the energy outflow from the pulsar into magnetic energy and relativistic particles. As electrons are being continually injected into the nebula, from the pulsar, and then travel through the inner magnetic field, radio to X-ray synchrotron radiation is emitted. Inverse Compton scattering of the synchrotron electrons on the ambient photons generates the TeV emission (Blumenthal & Gould, 1970). Figure 4.2 from Aharonian & Atoyan (1998b)shows the spectral energy distribution of the Crab Nebula and two peaks can be seen that are representative of both types of emission.

VHE γ-ray emission from the Crab Nebula was first reported the 9σ level after 60 hours of observations by the Whipple Observatory between 1987 and 1988 (Weekes et al., 1989). The Crab Nebula has since become the standard candle for VHE astronomy (in the northern hemisphere) due to its continuous

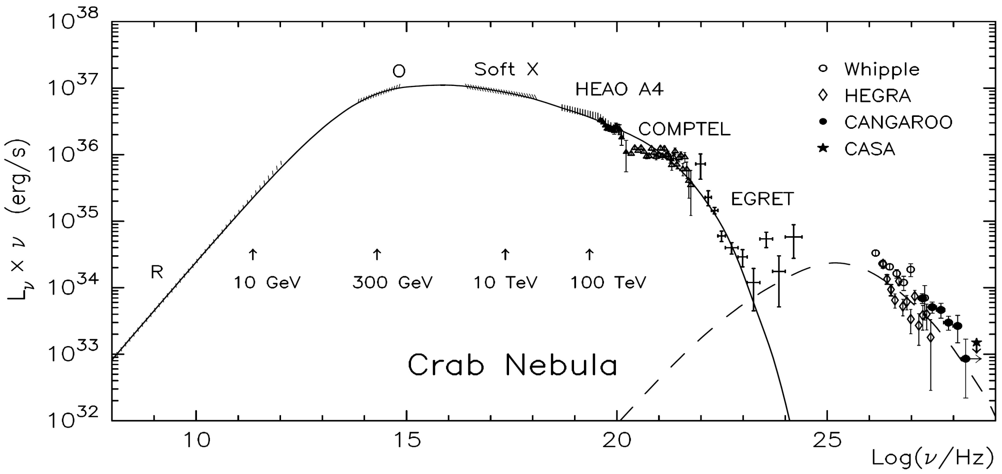

Figure 4.2: The spectral energy distribution of the nonthermal emission from the Crab Nebula. The solid curve represents the synchrotron radiation and the dashed curve corresponds to the inverse Compton component of the radiation. The nonthermal synchrotron radiation extends from radio (R), through optical (O), soft and hard X-ray region and into the lower energy γ-ray region. The second peak that extends to $\sim$ 50 TeV is consistent with inverse Compton scattering of relativistic electrons on lower-energy background photons. Figure taken from Aharonian & Atoyan (1998b).

emission of VHE γ-rays. It is routinely used for instrument calibration and the development and testing of analysis techniques. It is believed VHE emission from the Crab Nebula is generated in two separate accelerating regions within the remnant itself. The first comes from the SNR, with the particle acceleration believed to occur in the shell shock front. The second acceleration mechanism is due to the PWN, with the energy required for particle acceleration coming from the spin down of the pulsar. The most widely accepted production models associated with the Crab Nebula supernova remnant are now described.

SNR - acceleration in the Shell Shock Front

Cosmic rays are most likely accelerated by SNRs in the shock waves (Section 4.1.1) created by the initial supernova explosion (Bell, 1978; Drury et al., 1994). These shock waves can last for thousands of years after the supernova occurs. After the explosion, the shock waves propagate into interstellar space and can be seen as the expanding shells of gas and debris of SNRs. Fermi acceleration, also known as diffusive shock acceleration, is the acceleration that charged particles undergo when reflected by a magnetic mirror. First-order Fermi (Fermi-I) acceleration is thought to be the main mechanism by which charged particles gain energy beyond the thermal energy in astrophysical shock waves (Ellison et al., 1990; Reynolds & Ellison, 1992). Shock waves can have magnetic inhomogeneities both preceding and following them. If a charged particle traveling through the shock wave (upstream) encounters a moving change in the magnetic field, it can be reflected back (downstream) through the shock at an increased velocity. If a similar process occurs in the opposite direction, the particle will again be accelerated and gain energy. Figure 4.3 illustrates this mechanism of shock acceleration.

This type of acceleration is a possible candidate model that could be used to explain shock acceleration of hadrons up to energies 100 TeV (Jones et al., 1998). Fermi acceleration occurs with

$$\frac{dE}{dt} \propto \nu E \tag{4.1}$$

where E is the energy of the particle being accelerated and ν is the velocity of the upstream region of the shock relative to the downstream region. As the shock wave moves out into interstellar space it gathers mass. If typical interstellar density is 1 proton cm^{-3}, then it will take $\sim 10^3$ years for 10

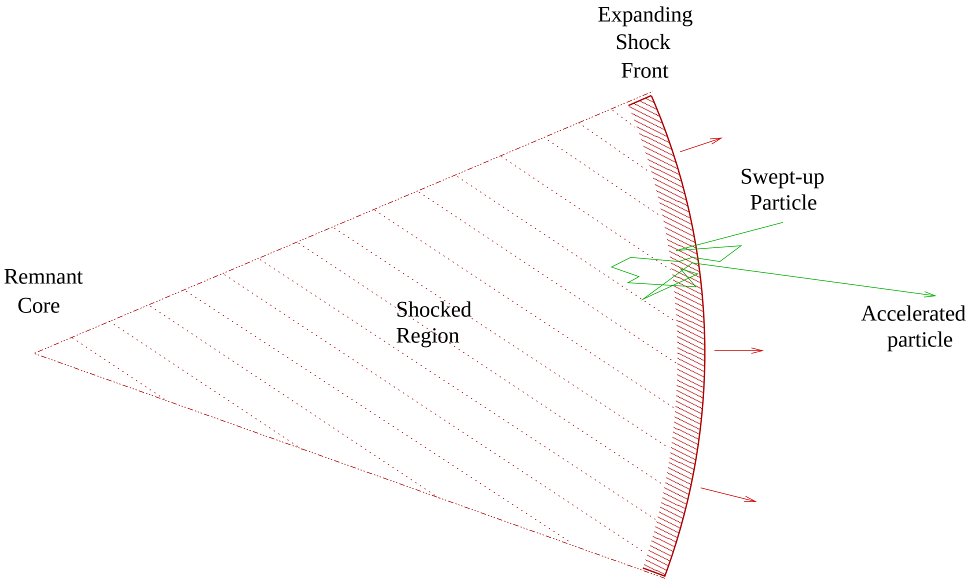

Figure 4.3: First-order Fermi acceleration by the shock wave of a supernova remnant. Figure taken from Dunlea (2001).

$M_\odot$ of material moving at 5000 km s^{-1} to gather its own mass of interstellar material (Gaisser, 1990). This period of time is when the shock is thought to be most efficient at accelerating particles and is known as the Sedov Phase and can last until the shock is up to 10^4 to $\sim 10^5$ years old. High-energy protons accelerated to very high energies in the shock region would interact with nuclei in the Crab Nebula to create secondary particles, including π^0 particles, which then decay creating VHE γ-rays.

Pulsar Emission Models

It is thought that pulsed emission from pulsars comes from the slowing of a spinning neutron star as it loses angular momentum. Developing ideas first proposed by Pacini (1967) and Gold (1968), Goldreich & Julian (1969) have shown that, for a spinning neutron star in a vacuum, huge surface electric fields (as big as 6×10^{10} V m^{-1}) would exist parallel to the magnetic field lines, thus ejecting charged particles from the surface of the star, resulting in the formation of a co-rotating plasma called the magnetosphere. They defined different regions around the rotating neutron star with the main region known as the *light-cylinder*. The light cylinder is a boundary region surrounding the neutron star with a radius of $R_L = c/\omega$ where ω is the angular velocity of the pulsar and c is the speed of light. However, such a co-rotating plasma is not possible since, for certain regions of the plasma, the light-cylinder would be forced to move faster than the speed of light. The field lines become open at the point where ωR becomes equal to c. It is at this point that particles can be ejected from the magnetosphere. Charges cannot always be easily replenished from the surface of the neutron star. Hence, the out-flow of particles from the system can, in certain regions of the magnetosphere, lead to a reduction in the charge density. These regions are just above the surface of the neutron star at the pole (the polar cap) and along the edge of the closed magnetosphere near to the light cylinder (the outer gap). The result here is that in these regions, the electric field is not constrained by the plasma to be perpendicular to the magnetic field and particle acceleration can occur. Since there are two regions where emission can occur, there are two main types of pulsar models. The polar cap model and the outer gap model. Both are consistent with observed emission.

Polar Cap Model of γ-ray Emission

Polar cap models describing γ-ray emission from pulsars were first proposed by Sturrock (1971) and Ruderman & Sutherland (1975) who built upon the work of Goldreich & Julian (1969). In his work, Sturrock predicted the presence of a strong electrical potential perpendicular to the polar cap that is strong enough to liberate charged particles from the surface and accelerate them along magnetic field lines. Ruderman and Sutherland proposed the existence of a vacuum gap and a potential drop of around 10^{12} V above the poles where the particles are accelerated to high energies. There have since been improved models of high-energy emission proposed by Harding (1981) and Daugherty & Harding (1982) that have become the basis of subsequent polar cap models.

In these models, particles from the neutron star surface are accelerated in vacuum gaps above the magnetic polar regions of the rotating neutron star. It is possible for the particles to emit radiation by either of two mechanisms. Daugherty & Harding (1996) suggest that electrons emit curvature radiation as they travel along magnetic field lines. Curvature radiation occurs when an electron is moving in a strong magnetic field ($\sim 10^{12}$ G) and, due to damping by synchrotron radiation, is constrained to follow the magnetic field lines closely in such a way that the curvature of the magnetic field line itself causes the electron to radiate. The energy of the emitted radiation depends on the energy of the electron, the magnetic field strength and the curvature of the magnetic field line. Hence, the energy spectrum is similar to that of synchrotron radiation. Since the photons must cross neighbouring highly magnetised field lines, they are likely to pair produce into electron-positron pairs (Sturrock, 1971). These pair-produced particles then emit curvature or synchrotron radiation of their own there by creating a pair production cascade which may explain radio frequency emission from this type of source.

The second mechanism describes electrons from the same polar regions upscattering thermal photons via magnetic Compton scattering (Sturner & Dermer, 1994). The electron energy requirements of this model are of several hundred GeV whereas the curvature model requires energies of several TeV.

In both models, however, observed emission is limited to several GeV due to pair production of γ-rays . This important fact is consistent with the absence of any observed VHE pulsed emission. The early models had assumed a double pole emission region in an attempt to explain the observed pulsing effect of the emission. These models were later modified (Daugherty & Harding, 1994) to include emission from a hollow cone around a single pole as seen in Figure 4.4.

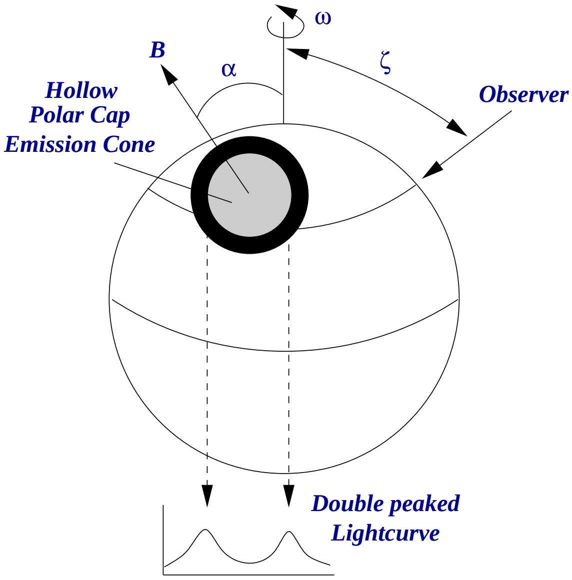

Figure 4.4: Schematic of the revised polar cap model by Daugherty & Harding (1994). They suggest the origin of the double peaked light curve from a single rotator can be explained if the observer is located at an angle ξ to the rotation axis. The observers will observe a light-curve with two emission peaks from a polar cap hollow cone of emission. The two peaks occur when the edges of the cone pass through the observers field of view. Figure courtesy of Kildea (2002)

The Outer Gap Model of γ-ray Emission

Outer gap models provide an alternative model for high energy pulsar emission. The models were developed by Cheng et al. (1986a,b) and later reworked by other researchers (Romani, 1996; Hirotani, 2001). The models suggest that a region of null surfaces exist along which there is no net charge and which separates regions of positive and negative charge within the magnetosphere. The outer gap model predicts γ-ray production in vacuum gaps of the outer magnetosphere. Since the magnetic field is weaker in the outer magnetosphere, high energy photons undergo less magnetic pair-production attenuation, resulting in the possibility of TeV emission. Romani (1996) predicts a TeV flux of around 1% of that of GeV energies which new experiments, like HESS, VERITAS and GLAST may detect. The vacuum gaps can occur between an open magnetic field line and the null charged surface of the charge separated magnetosphere. Acceleration models predict that electron-positron pairs are created in these gaps and then accelerated by the large electric field. γ-rays can be created by curvature radiation or by inverse Compton scattering. Like the polar cap models, early outer gap models were bipolar and were later adapted to include double-peaked emission from a single pole.

Both models have predicted energy spectra consistent with those observed by the EGRET experiment (Romani & Yadigaroglu, 1995). The main difference between the models however is the energy at which emission is cut off. In general, outer gap models predict a steeper γ-ray spectrum with a cut-off in the region of 10-100 GeV whereas polar cap models predict a cut-off of several GeV. However this energy region has been poorly observed to date. A schematic of the geometries of both the polar cap model and the outer gap model is shown in Figure 4.5.

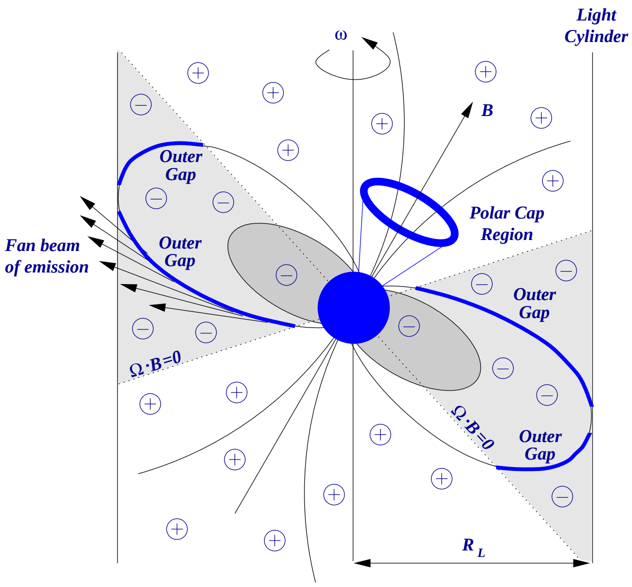

Figure 4.5: Emission regions as predicted by the polar cap and outer gap models. The thick lines on the outer gap area represent the vacuum gaps following the last closed magnetic field lines within the light cylinder. The dotted lines indicate the null surfaces separating oppositely charged regions of the magnetosphere. Figure courtesy of Kildea (2002).

4.1.2 Other SNR Detections

As mentioned, the Crab Nebula is located in the skies of the Northern hemisphere, however Plerions have also been observed at TeV energies in the southern hemisphere. PSR 1706-44 was observed at 12σ above 1 TeV by the CANGAROO experiment (Kifune et al., 1995). It was later confirmed by the Durham Group (Chadwick et al., 1998). However, observations by the HESS experiment did not find any evidence of TeV emission (Aharonian et al., 2005g). Studies of the Vela pulsar have also yielded upper limits (Aharonian et al., 2006d) and reported detections of VHE emission (Yoshikoshi et al., 1997).

Name	Class	Detection	Reference
Crab Nebula	PWN	Whipple	Weekes et al. (1989)
PSR 1706-44	PWN	CANGAROO	Kifune et al. (1995)
Vela	PWN	CANGAROO	Yoshikoshi et al. (1997)
G313.3+0.1	PWN	HESS	Aharonian et al. (2006b)
MSH 15-52	PWN	HESS	Aharonian et al. (2005c)
RX J0852.0-4622	SNR	HESS	Aharonian et al. (2005b)
RX J1713.7-3946	SNR	CANGAROO	Muraishi et al. (2000)
G0.9+0.1	SNR	HESS	Aharonian et al. (2005g)
Cas A	SNR	HEGRA	Aharonian et al. (2001)
HESS J1420-607	PWN	HESS	Aharonian et al. (2006b)
HESS J1632-478	X-ray Pulsar	HESS	Aharonian et al. (2006f)
HESS J1634-472	X-ray Pulsar	HESS	Aharonian et al. (2006f)
HESS J1640-465	PWN	HESS	Aharonian et al. (2005a)
HESS J1702-420	SNR	HESS	Aharonian et al. (2006f)
HESS J1713-381	SNR	HESS	Aharonian et al. (2006f)
HESS J1718-385	PWN	HESS	Aharonian et al. (2007a)
HESS J1745-290	SNR	HESS	Aharonian et al. (2004)
HESS J1804-216	SNR/PWN	HESS	Aharonian et al. (2005a)
HESS J1813-178	PWN	HESS	Aharonian et al. (2005a)
HESS J1825-137	PWN	HESS	Aharonian et al. (2005a)
HESS J1834-087	SNR	HESS	Aharonian et al. (2005a)
HESS J1837-069	SNR/PWN	HESS	Aharonian et al. (2005a)
HESS J1912-101	PWN	HESS	Aharonian et al., in prep
W28	SNR	HESS	Aharonian et al., in prep
LS 5039	Microquasar	HESS	Aharonian et al. (2005e)
LS I +61303	Microquasar	MAGIC	Albert et al. (2006c)
PSR B1259-63	Binary	HESS	Aharonian et al. (2005d)
Kes 75	PWN	HESS	Djannati-Atai et al. (2007)
G21.5-0.9	PWN	HESS	Djannati-Atai et al. (2007)
HESS J1357-645	PWN	HESS	Lemiere et al. (2007)
HESS J1718-385	PWN	HESS	Lemiere et al. (2007)
HESS J1809-193	PWN	HESS	Lemiere et al. (2007)

Table 4.1: A summary of known Supernova Remnant and pulsar wind nebula TeV Sources. Known microquasars are also listed. (Correct up to November 2007.)

There are also reported detections of shell-type SNRs. The first was detected by the CANGAROO Collaboration in 1997 by Tanimori et al. (1998). After observations showing a strong X-ray flux, TeV emission from SN1006 was shown to originate in the northeast rim of the shell. This provided the first direct evidence for acceleration of particles to TeV energies at a shock front. A shock front can be formed as a result of supernova ejecta traveling into the interstellar medium. Particles crossing the shock front may be scattered back and forth repeatedly across the shock boundary and gain energy by first-order Fermi acceleration.

Unfortunately observations by the HESS collaboration have only reported upper limits for SN1006 (Aharonian et al., 2005j) and have not confirmed TeV emission from SN1006. Based on observations made with the Whipple 10 m telescope, upper limits on TeV emission from other shell-type SNRs have been reported by Buckley et al. (1998) and by Lessard et al. (1999). Major new detections of supernova remnants and pulsar wind nebulae came from the High Energy Stereoscopic System (HESS) survey of the Galactic Plane (Aharonian et al., 2005a, 2006f). The survey covered the galactic longitude range from -30° to +30° and the galactic latitude range -3° to +3°and revealed ten new TeV sources as indicated in Figure 4.6. Initially fifteen of these sources were thought to be unidentified, that is to say, do not have a counterpart at other wavelengths. However, follow-up observations of several of these sources at other wavelengths have revealed emission from associated objects. Most of these new sources turned out to be of the supernova remnant or pulsar wind nebula type. A full list of these new TeV sources as well as other confirmed SNR/PWN and microquasars is given in Table 4.1. However, there are detections of several objects, including six new objects reported at the recent 30th International Cosmic Ray Conference, that currently have

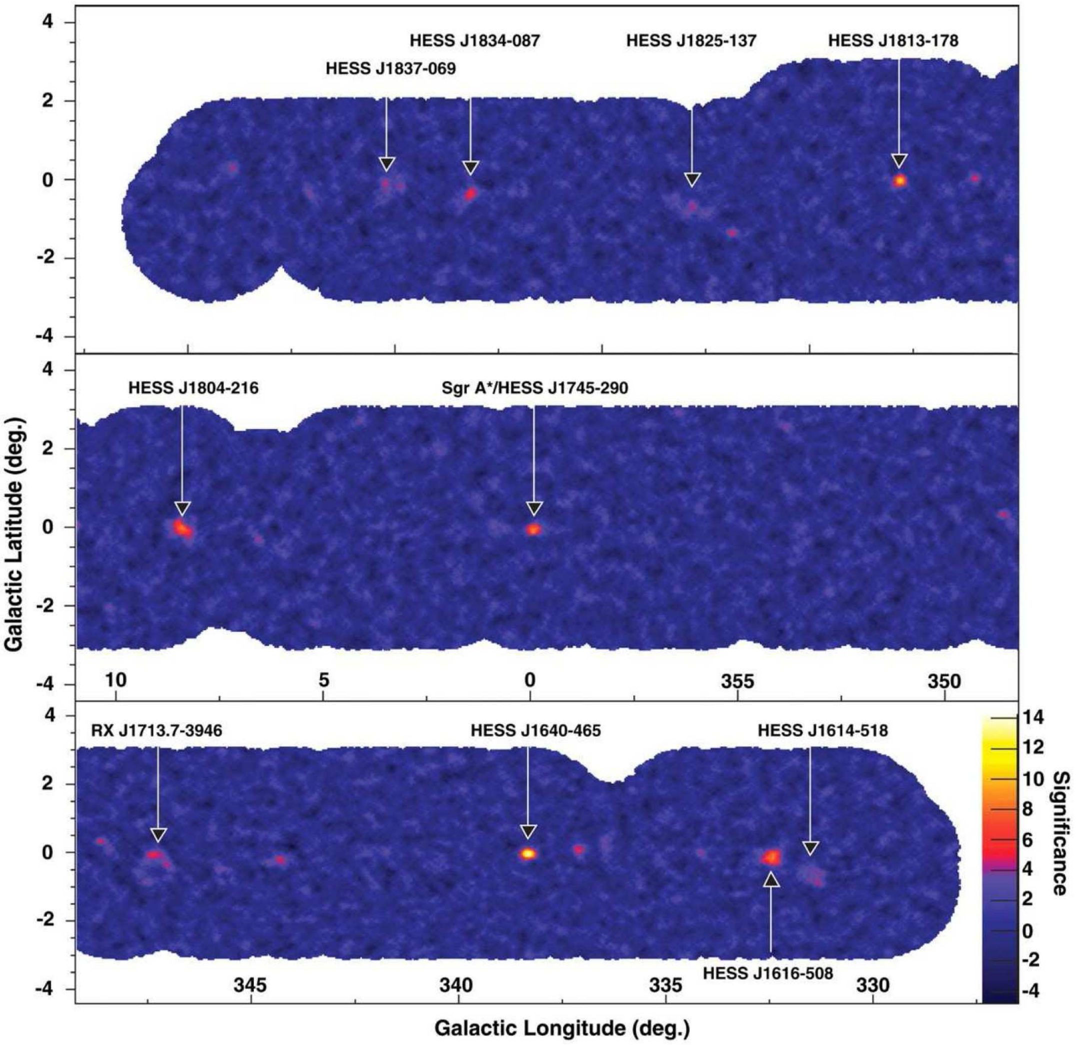

Figure 4.6: A sky map indicating the extent of the 2004 HESS survey of the galactic plane. The colours represent the range in significance values detected in the different regions of the Milky Way galactic plane. The extent of the survey was from galactic longitude -30° to +30° and latitude -3° to +3°. Figure from Aharonian et al. (2005a).

no counterparts at other wavelengths.

4.1.3 Unidentified sources

During its operational lifetime, the EGRET (Energetic Gamma-Ray Experiment Telescope) aboard NASA's Compton Gamma-Ray Observatory (CGRO) detected over 200 unidentified sources of γ-ray emission. This accounts for approximately two thirds of the total number of sources seen by this instrument. As these objects have not been identified with any known astrophysical objects, their origin remains a mystery. The poor angular resolution of the EGRET instrument is more than likely the reason these objects are unidentified. However, it is possible that some of these objects do constitute a new class of astrophysical object that emit only in γ-rays and are also referred to as dark accelerators. A major key to the identification of many of these unidentified sources will be the successor to EGRET, GLAST (Gamma-ray Large Area Space Telescope), and new low-energy threshold ground-based detectors.

With regard to unidentified sources detected at TeV energies, the first discovery was TeV J2032+4130. This object was discovered serendipitously by the Crimean Astrophysical Observatory during observations of Cygnus X-3 (Neshpor et al., 1995). During independent observations of the Cygnus X-3 region, the High Energy Gamma Ray Astronomy (HEGRA) group detected TeV J2032+4130 while observing a separate object (Aharonian et al., 2002). TeV J2032+4130 currently has no known counterpart at other wavelengths. It has been suggested that the VHE γ-ray emission from TeV J2032+4130 may be associated with the strong OB stellar association of the Cygnus region (Aharonian et al., 2002). It is possible that the stellar winds of the hot young stars in the OB association of Cygnus OB2 are the source of the accel-

Name	Possible Counterpart	Class	Detection
HESS J1023-575	WR association	Uid	HESS
HESS J1303-631	Cen OB1	Uid	HESS
HESS J1614-518	-	Uid	HESS
HESS J1616-508	PSR J1617-5055	PWN	HESS
HESS J1702-420	-	Uid	HESS
HESS J1708-410	-	Uid	HESS
HESS J1745-303	3EG J1744-3011	Uid	HESS
TeV 2032+4131	-	Uid	HEGRA
HESS J1427-608	-	Uid	HESS
HESS J1626-490	-	Uid	HESS
HESS J1731-347	-	Uid	HESS
HESS J1841-055	-	Uid	HESS
HESS J1857+026	-	Uid	HESS
HESS J1858+020	-	Uid	HESS

Table 4.2: A summary of current unidentified sources and possible counterparts (where there is a possible association). Included in this table are six new unidentified objects as reported by Kosack et al. (2007) at the 30th International Cosmic Ray Conference.

erating component of the hadrons of the cosmic radiation that results in the production of γ-rays. HESS J1616-508, a recently reported dark accelerator, is similar to TeV J2032+4130 in that it lies in a region of sky containing several other astrophysical objects of interest. However, it is likely that HESS J1616-508 is powered by the pulsar wind nebula PSR J1617-5055. Figure 4.7 shows a sky map containing the source HESS J1616-508.

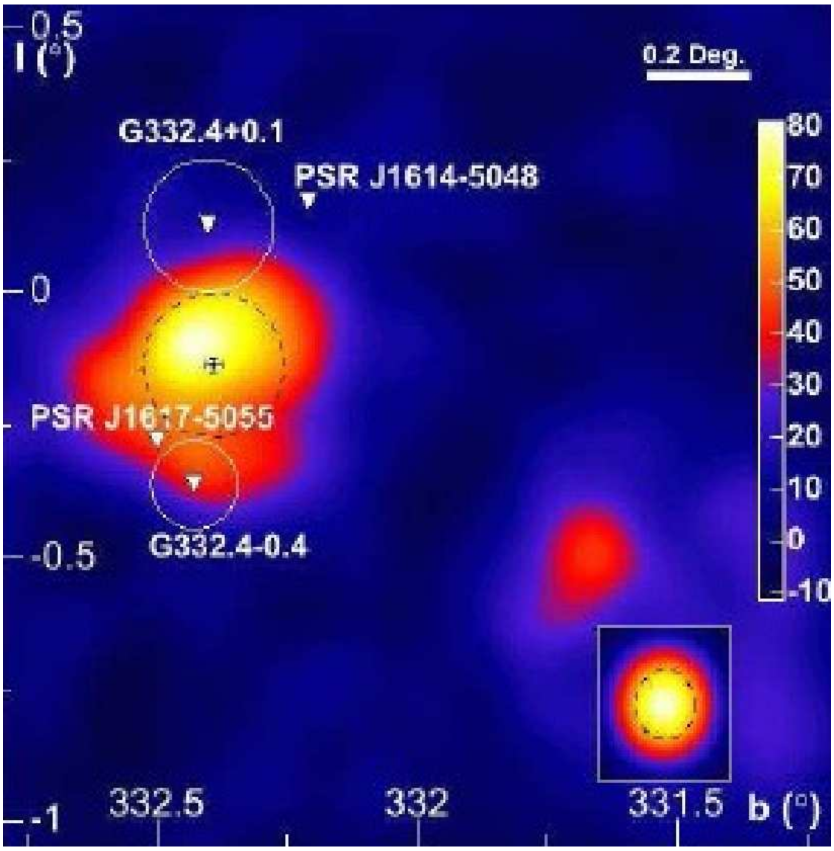

Figure 4.7: A TEV sky map illustrating the crowded region of sky containing the source HESS J1616-508 taken from Aharonian et al. (2006f).

Another source was discovered by HESS in the same manner as TeV J2032+4130. During observations of the binary pulsar PSR B1259-63, the new object, HESS J1303-631, was detected in the same field of view (Aharonian et al., 2005h; Beilicke et al., 2005b,a). HESS J1303-631 was discovered approximately 0.6° north of PSR B1259-63 and, like TeV J2032+4130, is close to an association of OB stars, namely Cen OB 1 (Hartkopf et al., 1999; Aharonian et al., 2005h). More observations, including multi-wavelength observations, of these sources are required to try and clarify their origin, as happened in the case of many of the initial unidentified sources. Multi-wavelength observations will help confirm or reject, the possible counterparts associated with some of the objects. Table 4.2 lists the current catalogue of unidentified VHE sources. Note here that a possible counterpart is given in some cases. If a counterpart is not confirmed, it is possible that the unidentified sources mentioned above represent a new form of previously unknown dark TeV γ-ray emitter or “dark accelerator”. Very recently, during the 30th International Cosmic Ray Conference, the HESS collaboration announced the detection of a further six unidentified VHE γ-ray sources (Kosack et al., 2007).

4.1.4 Dark Accelerators

The term dark accelerator has come to be associated with VHE sources that appear to have no detectable signal at other wavelengths. Dark accelerators are the newest classification designated to some of the most recent and as yet unidentified sources of VHE γ-rays. These sources tend to have low galactic latitudes, with only a few arcmin of angular size, and hence they are believed to be galactic in origin. As mentioned, they appear to have no known counterparts at other wavelengths and may show variability in TeV γ-rays. There have been several proposals suggested for the origin of VHE photons from these objects. The main production models regarding dark accelerators are discussed in Chapter 7 along with a discussion on the results of the analysis performed on TeV J2032+4130 as part of this project.

4.1.5 Other Sources of TeV γ-rays

There are many other important sources of VHE γ-rays in the universe, some of which are briefly mentioned here.

Active Galactic Nuclei

Active Galactic Nuclei (AGN) is the collective term used to refer to quasars, blazars, Seyfert galaxies, and radio galaxies. AGN are the most powerful sources of luminosity in the universe. The activities of these galaxies comes from an energy source located at its centre. A characteristic of AGN is the observed variability of their brightness. In fact emission from AGN can be variable on time scales of months to years and in some cases the variability can have time scales of days and hours. The variability of VHE γ-ray emission provides information regarding the size of the object emitting the radiation and leads to the conclusion that the immense energy emanating from AGN comes from a relatively small volume. The central sources of energy of AGN are thought to be powered by supermassive black holes which draw surrounding matter into a rotating accretion disk. The accreted matter then loses angular momentum through turbulent forces. Thermal emission from the accretion disk peaks at UV/X-ray wavelengths. Beyond the accretion disk lies a region, commonly regarded as torus shaped, which absorbs visible and UV light along some lines of sight. Along the axis of rotation of the accretion disk, jets of energetic particles stream perpendicularly away from the plane of the host galaxy.

These jets of relativistic particles and plasma outflows are thought to be the source of some of the most energetic processes in the Universe and exhibit emission from radio to γ-ray energies. This model of AGN suggests that the observed emission energy from AGN is a function of the observation angle in relation to the relativistic jet, with the highest energy emission beamed along the direction of the jet. Those AGN whose jets are aligned with the the line of sight of an observer on Earth are called blazars or BL Lac objects.

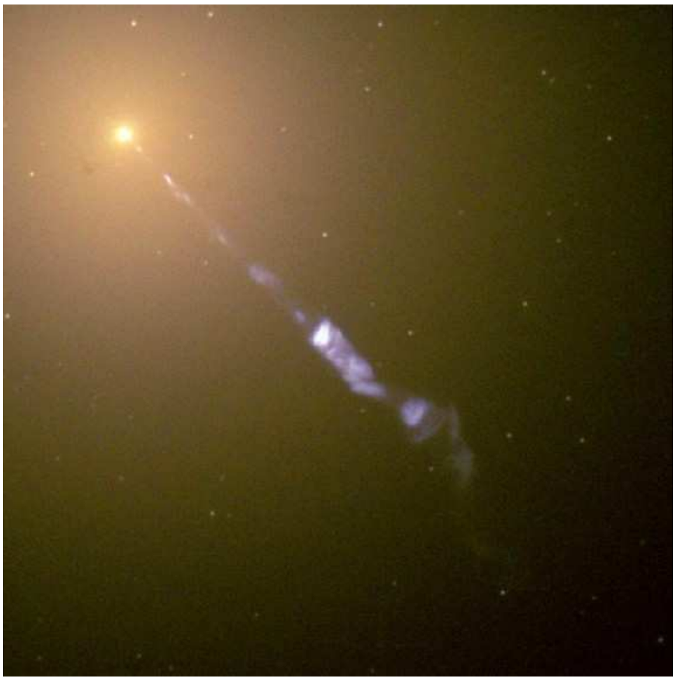

Figure 4.8: A Hubble Space Telescope image of the giant radio galaxy M87 clearly showing the plasma jet emanating from its core. Figure courtesy of the Hubble Heritage Team (heritage.stsci.edu).

During its lifetime, EGRET detected many AGN at X-ray energies, which prompted the Whipple collaboration to implement an observational campaign concentrating on AGN detected by EGRET. The first AGN detected at TeV energies was Markarian 421 (Punch et al., 1992). Subsequent and ongoing observations of Markarian 421 have produced many publications on this object and its generation of very powerful VHE emission flares. For example, in May 1996 the γ-ray flux was observed as increasing steadily finally reaching a level of 14 γ-rays per minute (Gaidos et al., 1996). A second flare in May 1996 from Markarian 421 only took around 15 minutes to double in intensity. Since this initial detection of VHE emission from the blazar Markarian 421, there have been detections from several other blazars including the detection of VHE emission from the giant radio galaxy M87 (Aharonian et al., 2003; Protheroe et al., 2003; Aharonian et al., 2006g), an image of which can be seen in Figure 4.8. Table 4.3 lists all the AGN known to emit γ-rays. A detailed study on AGN can be found in Urry & Padovani (1995).

Name	Class	Detection	Reference
1ES 1101-232	Blazar	HESS	Aharonian et al. (2006a)
Mrk 421	Blazar	Whipple	Punch et al. (1992)
Mrk 180	Blazar	MAGIC	Albert et al. (2006b)
1ES 1218+304	Blazar	MAGIC	Albert et al. (2006a)
H 1426+428	Blazar	Whipple	Horan et al. (2002)
PG 1553+113	Blazar	MAGIC	Aharonian et al. (2006c)
Mrk 501	Blazar	Whipple	Quinn et al. (1996)
1ES 1959+650	Blazar	7 Telescope Array	Nishiyama (1999)
PKS 2005-489	Blazar	HESS	Aharonian et al. (2005f)
PKS 2155-304	Blazar	HESS	Chadwick et al. (1999)
1ES 2344+514	Blazar	Whipple	Catanese et al. (1998)
H 2356-309	Blazar	HESS	Aharonian et al. (2006a)
M87	Radio Galaxy	HEGRA	Protheroe et al. (2003)

Table 4.3: A summary of known Active Galactic Nuclei VHE sources to date.

Galactic Centre

One of the most interesting and active regions of our Milky Way Galaxy is its centre. A suspected supermassive black hole called Sgr A*, with a mass of 2.6×10^6 $M_\odot$, is believed to be located at the galactic centre (Genzel & Townes, 1987; Schödel et al., 2002; Atoyan & Dermer, 2004). The Chandra X-ray Observatory recently revealed the presence of several compact objects surrounding the black hole (Baganoff et al., 2003). The X-ray variability of these objects suggests that they can be identified as neutron stars or black holes. The galactic centre was detected by the Whipple 10 m telescope in 2004 (Kosack et al., 2004) and by two other experiments that year (Aharonian et al., 2004; Tsuchiya, 2004). The HESS collaboration have recently reported the detection of γ-ray emission from the source HESS J1745-290 located 0.1° from the galactic centre (Aharonian et al., 2006e). However, as there is a high density of candidate objects emitting non-thermal radiation from within the source region, the nature of the emission from HESS J1745-290 is at present unclear.

4.2 Major Imaging Atmospheric Cherenkov Experiments

Ground-based γ-ray detectors are unique in astronomy as they do not interact directly with the primary photon. Imaging atmospheric Cherenkov telescopes detect the extensive air shower induced by the primary particle (with energy between 100 GeV and 50 TeV), after it collides with nuclei in the Earth's atmosphere. Since the first theoretical prediction (Morrison, 1958), the practical techniques of ground-based γ-ray detection have had to deal with several natural limits:

- Since the Earth's atmosphere is opaque to VHE photons, even at mountain altitudes, the primary photon will interact electromagnetically with the nuclei in the atmosphere. The thicker the atmosphere the more interaction there will be and hence the energy of the primary will be dissipated more rapidly. Due to this atmospheric absorption it is necessary to locate γ-ray detectors either above the atmosphere onboard satellites or balloons, or to use indirect methods to detect γ-rays from the ground.

- The flux of VHE γ-rays from astrophysical sources is low and decreases rapidly with increasing energy.
- At very high energies the cosmic ray flux is much higher than the γ-ray flux. Hence the need for cosmic ray rejection techniques is essential in VHE γ-ray astronomy.

There have been several innovative experiments developed since the 1960s that have attempted to address these problems. These experiments have evolved into several international collaborations, in both the northern and southern hemispheres, that have led to many major discoveries in this young area of astronomy. Imaging atmospheric Cherenkov telescopes have become the most sensitive instruments used for the detection of VHE γ-rays. The four main experiments that are either in development, or are currently making valuable contributions to VHE astronomy, are described below.

4.2.1 HESS

Located in Namibia, the HESS Collaboration operates the major imaging atmospheric Cherenkov experiment in the southern hemisphere. It has been in operation as Phase-I since 2003, and is the leader in the field of ground-based γ-ray astronomy. The HESS array is comprised of four 12 m telescopes arranged in a square configuration with each side 120 m. Each reflector is based on the Davies-Cotton design (Hermann, 1997) with a focal plane camera consisting of 960 pixels. The array was completed in 2003 and the HESS Collaboration has reported many new discoveries of VHE γ-ray sources since it was comissioned. To date the HESS catalogue contains 35 sources. Several of these objects were discovered in the central part of our galaxy, two of which are reported as dark accelerators (Aharonian et al., 2005a). The HESS collaboration has also reported a detection of the Crab Nebula at 21σ in 4.7 hours (Hinton, 2004). In Phase-II of HESS, it is planned to add a fifth large diameter telescope at the centre of the current array, increasing the angular resolution, energy range, and sensitivity of the instrument further.

4.2.2 The VERITAS Collaboration

The VERITAS (Very Energetic Radiation Imaging Telescope Array System) Collaboration is the successor to what was known as the Whipple Collaboration. It is led by the Smithsonian Astrophysical Observatory and currently consists of scientists from academic institutions in the United States of America, the United Kingdom, Canada and Ireland. The main objective of the group is the search for, and study of, galactic and extra-galactic sources of Very High Energy γ-rays. The collaboration operates and maintains a 10 m imaging atmospheric Cherenkov telescope at the Fred Lawrence Whipple Observatory on Mount Hopkins, in Southern Arizona. The Whipple 10 m imaging atmospheric Cherenkov telescope was the first ground-based instrument that successfully used the Cherenkov Imaging Technique to detect VHE γ-rays at ground level (Weekes et al., 1989).

The current generation of imaging atmospheric Cherenkov experiments consists of arrays of several reflectors and the VERITAS Collaboration is now operating an array of four twelve-metre reflectors (Kieda, 2007; Weekes, 2007). Results from early observations were reported at the 30th International Cosmic-Ray Conference. The combined array of telescopes provides the maximum sensitivity in the energy range 50 GeV to 10 TeV. VERITAS and HESS will effectively complement GLAST as there will finally be an overlapping sensitive energy range between ground-based detectors and space-based detectors.

Each telescope is based on the design of the Whipple Telescope, employing the Davies-Cotton reflector design and a PMT camera of 499 pixels (Weekes, 1997; Holder et al., 2006b). The main difference between the Whipple imaging atmospheric Cherenkov telescope, and the individual VERITAS telescopes, is the increase in aperture size, resulting in an f/1.0 system. In addition, there is a major change in detector electronics with the use of 500 MHz flash analogue to digital converters (FADCs). The use of FADCs allows the system to detect and record the time profile of the light in Cherenkov images, and in turn allows a more sophisticated method of rejecting noise due to fluctuations in the light level of the night sky background. The big step forward from the Whipple 10 m to VERITAS is that VERITAS is an array system. Hence it will be able to combine images of the same shower taken from different locations, a technique known as stereo imaging, thus improving the sensitivity of the detector (Hughes, 2007).

VERITAS can also operate as four single detectors or even as two subarrays. VERITAS was the first of the current Cherenkov telescope systems to be designed. However, due to funding difficulties and problems with site approval, it was the last to come on line. The VERITAS project began construction in 2002 and was originally designed as a seven telescope array, with each telescope situated at the vertices and center of a hexagon of side 80 m as shown in Figure 4.9. However, VERITAS was constructed as a sub array of four identical telescopes. Initially a single prototype was built in 2003 and

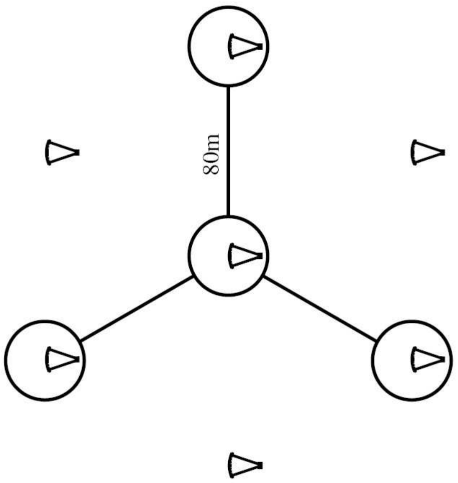

Figure 4.9: A schematic of the original seven telescope VERITAS array. The locations of the telescopes of the VERITAS-4 sub array are also shown.

operated in engineering mode for several months in order to test and develop custom-made hardware and software (Holder et al., 2006a). The second stage of development saw the construction of three more identical telescopes at the base camp of the Fred Lawrence Whipple Observatory. VERITAS is expected to substantially increase the catalogue of very high energy γ-ray sources in the northern hemisphere and greatly improve measurements of established sources. Holder et al. (2006b) provides a current report of the VERITAS project. In addition to the new array system, the VERITAS Collaboration continues to operate the Whipple 10 m telescope for deep observations of AGN and supernova targets.

4.2.3 MAGIC

The MAGIC Collaboration is composed of research institutions from Italy, Germany and Spain, with the telescope located at an altitude of 2200 m in La Palma, Spain (Cortina et al., 2005). MAGIC differs from the other current imaging atmospheric Cherenkov instruments in that it is comprised of only one reflector. The reflector is 17 m in diameter and is supported by a light weight carbon-fibre frame. The camera is constructed from advanced hemispherical PMTs and utilises a 300 MHz flash analog-to-digital-converter system similar to the VERITAS system. MAGIC has detected the Crab Nebula at the 16σ level in just over one hour (Wagner et al., 2005) and detected Mrk 421 at 29σ in 277 minutes (Albert et al., 2007a). MAGIC has a low-energy threshold between 20 GeV and 30 GeV (Fonseca, 1999; Flix et al., 2004) and, due to its light weight frame, has a rapid slew time making it ideal to respond quickly to γ-ray burst alerts. The MAGIC Collaboration are currently building a second telescope, MAGIC-II (Baixeras et al., 2005), on the same site on La Palma, at 85m distance from MAGIC while the collaboration continues to study galactic and extragalactic sources (Albert et al., 2007b).

4.2.4 CANGAROO-III

CANGAROO-III is a second imaging atmospheric Cherenkov telescope collaboration located in the southern hemisphere (Enomoto et al., 2002, 2006). It is operated by the Australian-Japanese CANGAROO group. Originally it was an array-type system with four telescopes arranged in a square. The spacing between the sides of the square array of telescopes is 100 m. However, one of the telescopes has since been retired and the array is now comprised of three telescopes. CANGAROO differs from HESS and VERITAS in that a parabolic mirror is used in the optical design. The focal plane camera is composed of 427 pixels.

4.3 The Milagro Detector

The previous sections detail the main experiments that use the imaging atmospheric Cherenkov technique. However, Milagro is an experiment based on a different detection technique that has a relevance to the detection of unidentified sources of VHE γ-rays. The Milagro γ-ray detector (Smith, 2005) is located in the Jemez Mountains of northern New Mexico (35.9.° N, 106.7. ° W) at an altitude of 2630 m above sea level. It is a water Cherenkov air-shower detector and is comprised of a 5000 m^2 pond surrounded by 175 outrigger tanks totaling an area of 40 000 m^2. The main tank contains 6 million gallons of water and has two layers of PMTs. The first layer is used to detect the Cherenkov light from the relativistic particles produced by the interaction of γ-rays and particles in the atmosphere and is placed under 4 radiation lengths of water. The second layer of PMTs is used to help in background rejection of cosmic rays which tend to have a more penetrating component. This second layer of PMTs is placed under 16 radiation lengths of water. The overall system results in Milagro having an energy threshold of around 250 GeV. However, compared to imaging atmospheric Cherenkov telescopes, Milagro has a higher energy threshold with the median energy of detected events about 20 TeV. It also has a reduced angular resolution of about 1°.

A major advantage of this kind of detector over Cherenkov telescopes is the fact that they can operate continuously with the result that a large portion of the sky can be monitored. Milagro detected the Crab Nebula and the AGN Mrk 421 during a galactic plane survey (Atkins et al., 2004). The Milagro experiment recently reported the detection of two objects, C1 and C2, in the Cygnus region of the sky with no known counterparts at other wavelengths (Abdo et al., 2007). Also reported was the detection of a source consistent with the reported location of TeV J2032+4130. The source MGRO J2031+41 was observed in an area with the largest concentration of molecular and atomic gas in the Cygnus region. The authors also reported that the spatial extent of MGRO J2031+41 is much larger than the extent of TeV J2032+4130 and leads to the conclusion that there is another source, or sources, contributing to the Milagro detection.

4.4 Summary

Apart from the main collaborations described above, there are also other imaging atmospheric Cherenkov telescopes operational today. These include CACTUS, PACT, STACEE, TACTIC and Whipple. A full list of the main operational imaging atmospheric Cherenkov telescope experiments is shown in Table 4.4. CACTUS, PACT and STACEE are wavefront sampling telescopes that detect the Cherenkov radiation at many different locations on the ground using large mirror arrays. With this wide range of instruments, with improved sensitivities and lower thresholds, now devoted to VHE γ-ray astronomy, it is expected that many more sources of VHE γ-ray emission will be detected over the course of their lifetime and will thus expand the catalogue of VHE sources further. As the experiments are located in both the northern and southern hemispheres, a complete map of the very high energy universe can finally be constructed. When the next generation of space-based detectors are operational their energy ranges will overlap those of the new ground-based experiments. This will result in a crucial gap in the electromagnetic spectrum finally being accessible for study. Coverage of the VHE spectrum will also be improved by the next generation of ground-based telescopes (e.g. MAGIC II and HESS II).

Group	Location	Aperture	Threshold	1st Light
Whipple	Arizona, USA	10 m	0.25 TeV	1984
Crimea	Crimea	6 × 2.4 m	1.0 TeV	1989
TACTIC	India	10 m	0.3 TeV	1997
CANGAROO III	Australia	4 × 10 m	0.1 TeV	2003
HESS	Namibia	4 × 12 m	0.01 TeV	2004
MAGIC	La Palma	17 m	0.05 TeV	2004
VERITAS	Arizon, USA	4 × 12 m	0.1 TeV	2007

Table 4.4: Operational imaging atmospheric Cherenkov telescope systems, their location, approximate energy threshold and when each saw first light.

Chapter 5

VERITAS Reflector Alignment and Point Spread Function.

5.1 Introduction

The previous chapter detailed the Imaging Atmospheric Cherenkov Technique and its associated instrumentation. At the outset of this project, VERITAS, the current generation of atmospheric Cherenkov telescopes located in the Northern Hemisphere, was beginning to come on-line. The VERITAS Collaboration has recently completed and are currently operating a four-telescope array system in Southern Arizona as the successor to the Whipple 10 m atmospheric Cherenkov telescope (Figure 5.1).

The four VERITAS telescopes are based on the Whipple 10 m design. Each telescope has an aperture of 12 m and focal length of 12 m, resulting in an f/1 system, thus reducing the optical aberrations of the telescope. Each telescope has a 499 pixel camera with a field of view of 3.5° and consists of $\sim$ 350 mirror facets. It is anticipated that an energy threshold of $\sim$ 100 GeV will be achieved when all four telescopes have been fully optimised and

Figure 5.1: An aerial photo of the VERITAS array as currently located at Basecamp.

calibrated.

The VERITAS mirror facets are hexagonal in shape. Each facet has an area of 0.322 m^2 resulting in a total reflective area of $\sim$ 110 m^2 for each telescope. The facets are made from glass, slumped and polished by D.O.T.I., (Roundrock, Texas), cleaned, aluminised and anodised at the VERITAS optical coating laboratory. Figure 5.2 shows the reflectivity of the coated mirrors at normal incidence as a function of wavelength and is measured to be $> 90\%$ up to 400 nm. As the optical structure of VERITAS is based on the Davies-Cotton design, it was possible to employ the method of alignment used to align the mirror facets on the Whipple 10 m. This chapter describes the alignment procedures that were developed on the Whipple 10 m and are now used on the VERITAS telescopes. Results of measurements of the Point Spread Function (PSF) of the first VERITAS telescope, known as Telescope 1 (T1) are also presented, along with recent bias alignment results.

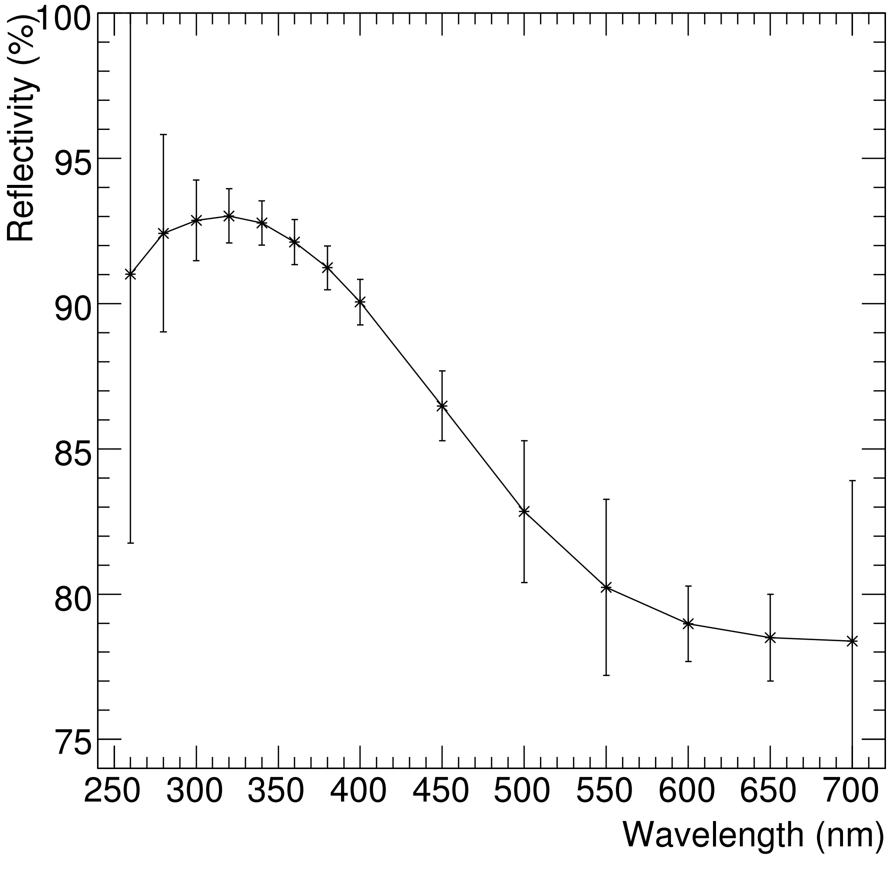

Figure 5.2: Mirror reflectivity as a function of wavelength for light normally incident to the mirror surface.

5.2 Point Spread Function

All optical systems suffer to some extent from aberrations. The image of a point source such as a star acts as a good measure of the degree of degradation caused by aberrations. When an optical system images a point source, the image of this source will not be a point. The optical system will introduce a certain amount of blur in the resulting image and thus distorts our view of the object being observed. This degradation can be represented by means of a Point Spread Function (PSF).

Mirror alignment is performed on the mirror facets of the VERITAS telescopes (and the Whipple 10 m) with the aim of producing as small a PSF as possible. However the PSF will always have some intrinsic width due to optical aberrations that are associated with the Davies-Cotton reflector design. For on-axis images the main aberrations are spherical, coma and most significantly astigmatism. With off-axis images coma becomes the dominant aberration (Lewis, 1990). PSF measurement involves the imaging of a bright star on the focal plane of the camera. A CCD camera mounted in the centre of the reflector is used to record the optical image of the star that is seen on a target screen covering the PMT camera. Star images are captured at several elevations and the Full Width at Half Maximum (FWHM) of the PSF is then calculated using the *skycat* image processing programme and is used as a measure of the degree of alignment of the facets.

The PSF's of the VERITAS reflectors are measured regularly throughout the observing season to look for signs of misalignment of the mirror facets. Depending on the amount of degradation, a realignment of some or all of the mirror facets may be required. Following PSF measurements of the Whipple 10 m taken during 2001/2002 observing season it was noted that the FWHM of the PSF grew significantly with increasing elevation Kildea (2002). The

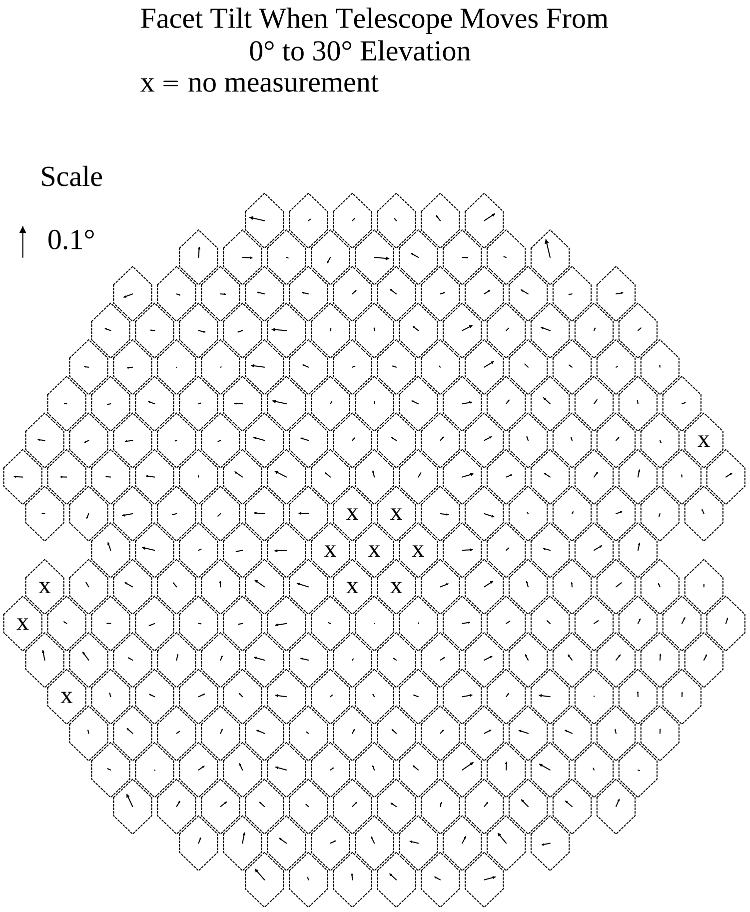

Figure 5.3: Vector plot representation of the size and direction of the movement of the mirror facets of the Whipple 10 m when the telescope pointing is changed in elevation from 0° to 30°. Figure courtesy of Schroedter (2004).

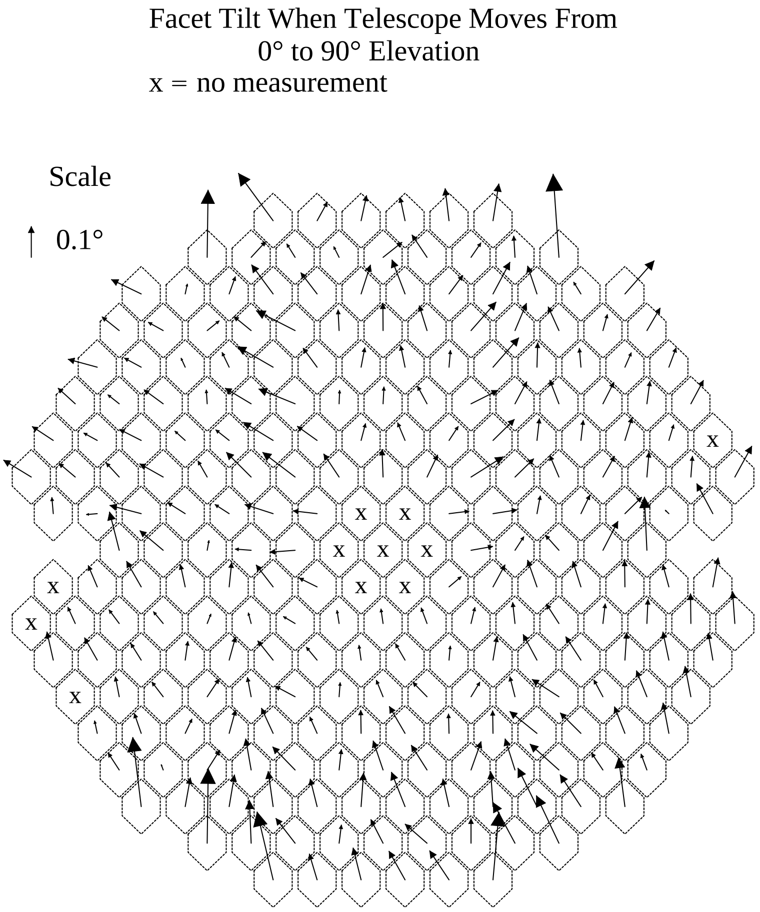

Figure 5.4: Vector plot representation of the size and direction of the movement of the mirror facets of the Whipple 10 m when the telescope pointing is changed in elevation from 0° to 90°. Figure courtesy of Schroedter (2004)).

conclusions drawn from these measurements suggested that when the optical support structure, quadrapod arms, and PMT camera increased in elevation the change in the weight distribution caused the mirrors to change position slightly.

Since the optical support structure is not completely rigid, the steel structure will bend and twist in a complex way due to the relative change of direction of the force of gravity on each section of the optical support structure as the telescope's elevation changes. Since the mirrors are attached to the optical support structure via a triangular mount, which itself is connected to two separate optical support structure beams, it is reasonable to assume that they will move slightly due to sagging of the optical support structure and hence get misaligned at higher elevations. Figures 5.3 and 5.4 show vectors on each facet representing the measured size and direction of the movement (relative to the optical support structure) of the mirrors with increasing elevation. In an effort to reverse this misalignment a bias alignment method was derived to improve the optical qualities of the Whipple reflector.

5.3 Optical Alignment

For the Davies-Cotton reflector design to be used as an effective light collector, each of its individual mirror elements must be correctly aligned. Every facet is required to reflect an incoming beam of light that is parallel to the optic axis to a point in the center of the focal plane. A beam of light whose incoming angle is offset slightly with respect to the optic axis will be displaced in proportion to the plate-scale factor (Section 3.1.1). To facilitate alignment, each facet is attached to the optical support structure using three adjustable bolts, arranged at the corners of a triangular mount (Figure 5.5).

When correctly aligned, the normal vector at the centre of each facet will be aligned to a point on the optic axis twice the focal length[1] of the telescope, away from the centre of the telescope, and the instrument will form an image at the focal plane. Figure 5.6 illustrates why this is the case; the centre of the facet (A), the centre of the image plane (B), and the 2f point on the optic axis (C), form an isosceles triangle since the angles x, y & z are equal. The alignment procedure consists of placing a laser at the 2f point, or alignment point, on the optic axis and adjusting the pointing of each of the 350 facets so that they retro-reflect as shown in Figure 5.6.

Figure 5.5: A picture of an individual mirror facet mount clearly showing the mounting bolts for the mirror facets.

---

[1] Twice the focal length is 24 m for the VERITAS telescopes and 14.6 m for the Whipple 10 m telescope.

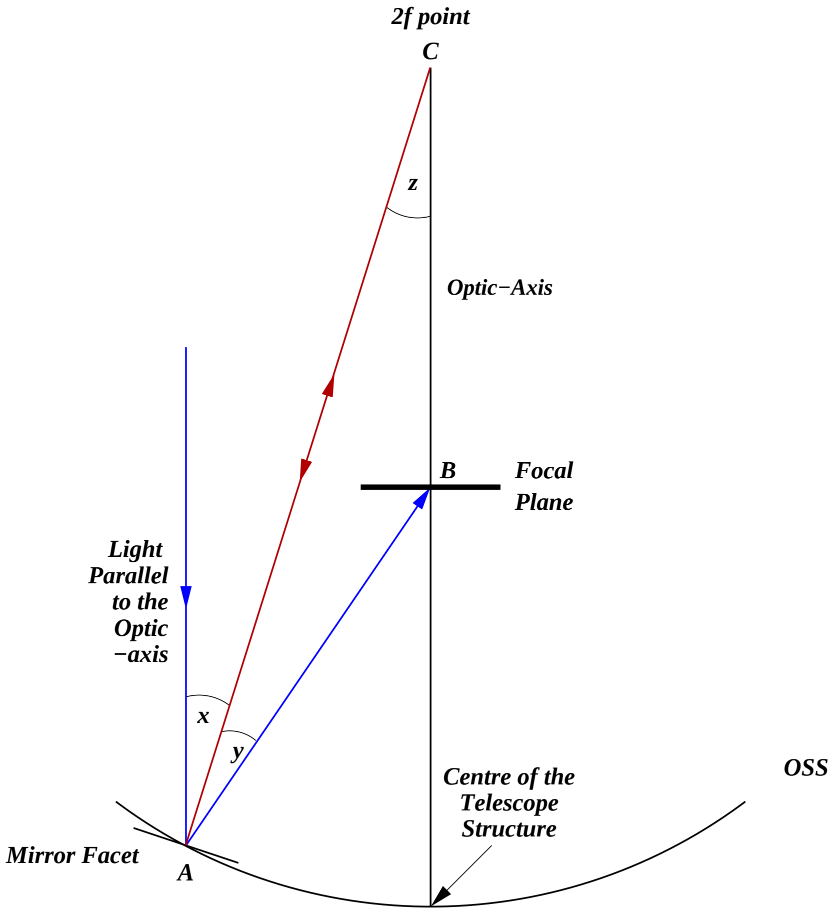

Figure 5.6: Ray tracing diagram of the mirror layout required for correct alignment.

If regular checks for mirror misalignment and point spread function measurements are not carried out, the instrument's ability to differentiate between γ-rays and hadrons could be compromised. It was found with the Whipple 10 m telescope, re-alignment of the mirror facets needed to be carried out on the telescope at least once per observing season as the position of the mirrors would change slightly over time. This degradation in mirror alignment can be caused by a variety of factors including optical support structure flexure, mirror mount stability, and on rare occasions, due to extreme weather conditions at the Mount Hopkins site. However initial checks of mirror alignment on T1 suggest that alignment is holding for longer periods than with the Whipple 10 m telescope. For example it was found that with the Whipple 10 m telescope, realignment was required at least once every season, where as with T1, no realignment was required after its initial alignment.

5.3.1 Manual Alignment Procedure

The manual or standard alignment procedure is undertaken while the telescope is located in the "home" position and was developed as a means to align the mirror facets of the Whipple 10 m telescope. The home position has the optic axis of the telescope lying horizontally and pointing towards the alignment point. The manual alignment system consists of a diverging laser beam, located at the alignment point, which is directed onto the target facet via a beam splitter. The beam is spread out to cover as much of the mirror as possible. This ensures any imperfections in the surface of the mirror are averaged out. The return beam can then be viewed on a screen (see Figure 5.7).

The telescope must be accurately positioned such that the mechanical axis is aligned with its 2f point. The operator then manually aims the instrument at the target facet and views the reflected image on the screen. If the mirror is correctly aligned the image will be in the centre of the screen. Otherwise appropriate instructions are given to a second person located near the target facet, who then adjusts the mounting bolts until the reflected image is centered. This process is then repeated for each mirror facet. The entire procedure can take a crew of ~ 6 people up to eight hours to complete.

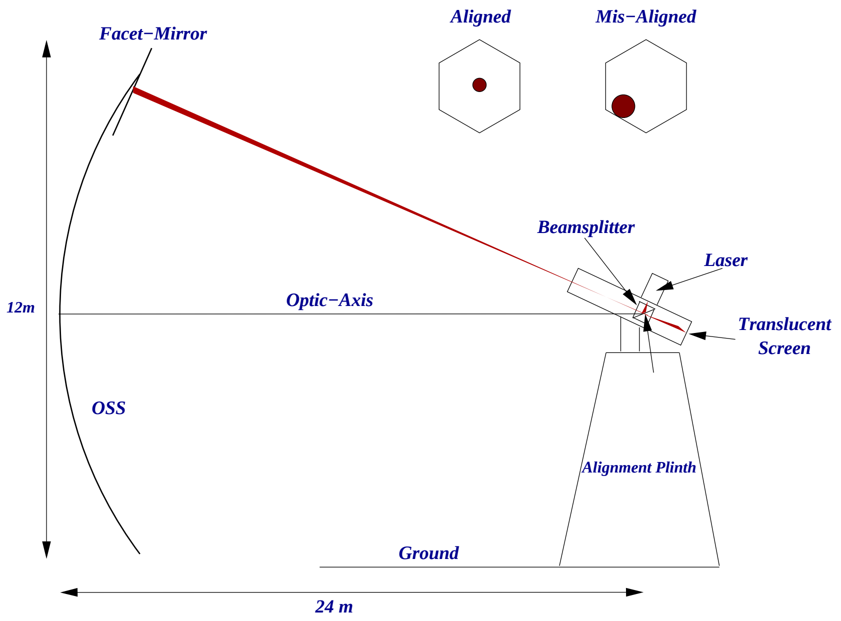

Figure 5.7: A schematic of the manual alignment system. The section at the top right is a representation of how the laser would appear on an aligned and missaligned mirror facet.

According to Lewis et al. (1998), this method can align individual facets to an accuracy of around 0.1 degree, however the method has several drawbacks. Firstly, it is time consuming and tedious, and requires significant manpower. Aiming the alignment instrument at a facet can prove difficult. Secondly, it is difficult judge as to whether or not an image of the laser is centered or focused on the screen as the human eye reacts logarithmically to light. The unfocused reflected laser images are due to the difference in the radius of curvature of the mirror facets (twice that of the dish) and the telescope structure. Also, the 2f point is not the exact center of curvature of the outer facets and the reflected images from diverged beams are not always tightly focused. The quality of alignment can then be assessed by measuring the width of the point spread function of the telescope. Using the manual method discussed here, point spread functions with FWHM values of 0.12 degrees have been achieved.

5.3.2 Semi-Automated Alignment System

With the limitations of the standard alignment procedure in mind, a semi-automated system was designed and constructed at NUI Galway to be used in the alignment of the mirror facets of the new VERITAS array. The VERITAS reflectors are of similar design to the 10 m telescope, but have a longer focal length of 12 m. The motivation behind the semi-automated alignment system was to provide a quick and efficient method of maintaining the alignment of over 1400 individual facets. A prototype of the system was built by NUI Galway and tested on the Whipple 10 m reflector (Kildea, 2002).

The basic principles behind the semi-automated alignment system are the same as the standard alignment method; the telescope is moved to the home position, a light source is located at the alignment point and retro-reflected to a screen. At this point the semi-automated alignment system then determines the quality of mirror alignment and then returns information to the operator. This information details the adjustments required to be made to the facet in order to bring the mirror into optimum alignment. The diode laser then moves by means of a pan-tilt-unit to the next mirror to be adjusted and the process is repeated. Figure 5.8 shows a schematic of the semi-automated alignment system as used on the telescopes of the VERITAS array. A detailed description follows below outlining the operation and use of the semi-automated alignment system.

5.3.3 System description

This system consists of a diode laser and 5 cm cubed double prism beam splitter mounted on a pan-tilt-unit. The pan-tilt-unit (PTU) is basically a small motorised alt-azimuth device. It has the provision for mounting a diode laser to it to enable it to point in a specific direction, *i.e.* either in elevation or azimuthal directions. The pan-tilt-unit is mounted (along with a screen and CCD camera) on a 60 cm x 30 cm optical table as seen in Figure 5.9. The pan-tilt-unit is a Model 46-70NR from Directed Perceptions Inc. and the CCD is a model ST-5C from the Santa-Barbara Imaging Group. Software for both devices was developed at NUI Galway and is written in the C programming language. A dedicated laptop computer operating under the Red Hat 9 Linux operating system accompanies the alignment system. The software controls the pan and tilt angles of the pan-tilt-unit to point the laser beam in any required direction and, when instructed, the CCD camera will record any resulting image on the screen and calculate the image centroid.

The optical table is positioned on a concrete plinth such that the beam splitter is located at the alignment point of the telescope. The mechanical axis of the telescope must be aligned with the instrument. The positioning of the the mechanical axis of the telescope can be confirmed by use of fixed alignment co-ordinates [2] and the use of reference points on the telescope structure. When the telescope is at the alignment co-ordinates, the 2f point of the telescope matches the location of the alignment system. The alignment point is initially found by mounting a laser at the centre of the optical support structure while the centre PMT or PMT number 1 is removed from the camera to allow the laser to shine through the camera housing. This determines the azimuth and elevation coordinates of the 2f point. The 2f

---

[2] Alignment co-ordinates for the VERITAS T1: 359.87°Azimuth and 1.62°in elevation.

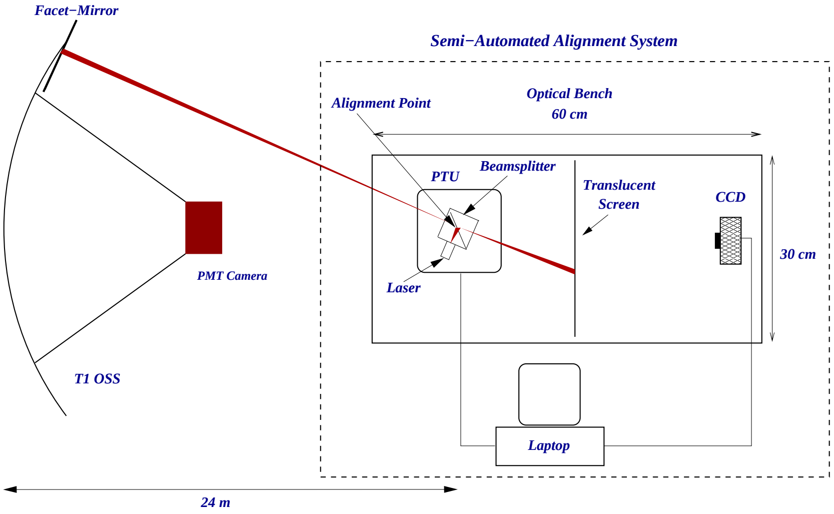

Figure 5.8: A schematic of the semi-automated alignment system as used on the VERITAS telescopes. Note here that the alignment instrument as shown here is drawn to a scale different than the telescope.

distance is determined using a measuring tape.

Unlike the manual alignment method, the laser beam is not intentionally diverged and the laser spot size on a facet is of the order of 3 cm in diameter. Since the optical quality of the VERITAS facets is high, a small spot size is sufficient. The advantage of using an undiverged beam is that the reflected images are small in size.

5.3.4 Calibration

During calibration, an operator directs the laser on the pan-tilt-unit to the centre of each facet in turn and the software then records the pan/tilt coordinates for every facet on the telescope. Then, for each facet the pan-tilt-unit is rotated through 180 degrees so that the laser is directed onto the point on the screen corresponding to the return position of the laser for a perfectly

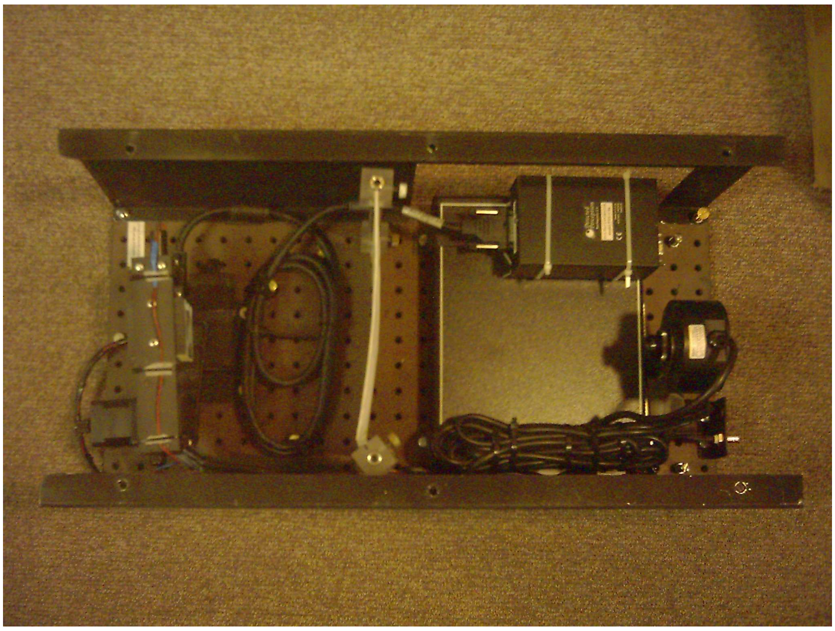

Figure 5.9: A picture of semi-automated alignment system system taken from above.

aligned mirror. The CCD pixel coordinates of this location are then recorded by the software, resulting in a process where the precise positioning of the CCD camera is not important. It also eliminates the complications associated with distortion produced by the short focal length lens of the CCD. If there is any movement of any of the system components (pan-tilt-unit, screen, camera) the calibration must be repeated.

5.3.5 Semi-automated Alignment Procedure

When the system selects a facet for alignment, the pan-tilt-unit points the laser at the centre of the facet and compares the position of the reflected spot with the ideal position as determined during the CCD calibration process. The software then calculates the amount of adjustment required of two of the three bolts holding that facet to bring the reflected spot to the ideal position. Instructions are relayed to an assistant located near the facet who must adjust the bolts manually. Thus the system can be considered a semi-automated system. Using this semi-automated system an alignment of all 350 facets can now be completed in ∼ four hours by two people. This is a significant improvement in terms of manpower and time requirements compared with the manual method.

5.4 Results

5.4.1 PSF of the VERITAS telescopes

Recently the final telescopes of the VERITAS array were aligned using a modified version of the original semi-automated alignment system, built at NUI Galway. After analysis of several CCD images of Polaris, at an elevation of 31° the FWHM of the PSF of T1 was found to be ∼ 0.08°±5% (Holder et al., 2006b). Early measurements of the PSFs of T1 of the VERITAS array, at various elevations, are listed in Table 5.1.

Elevation /°	**FWHM /°**
31.0	0.076
39.5	0.080
51.0	0.092
60.5	0.098
72.0	0.145

Table 5.1: Results of a recent PSF measurement of T1 of the VERITAS array.

As the VERITAS array has only recently seen first light the task of fully aligning all the mirror facets of the four telescopes has only recently been completed. Early PSF measurements at observing elevations suggest an average PSF FWHM of approximately 0.09°, which is well under the size of a single PMT (0.15°) as seen in Figure 5.10. Figure 5.11 shows the PSF FWHM of T1 for a star at the centre of the field of view as a function of elevation degrading with increased elevation. Figure 5.12 shows the actual optical effect of changing elevation on the resulting image of a point source. The circles in the image indicate the size of a VERITAS PMT.

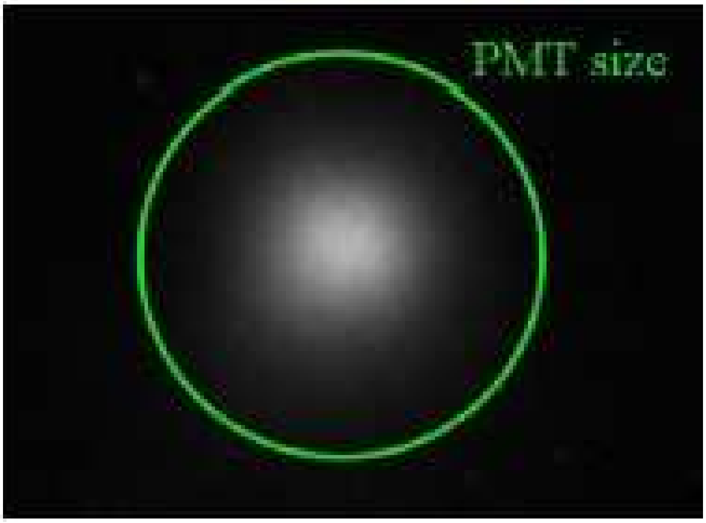

Figure 5.10: Image of a star as seen at the focal point of T1 of the VERITAS array. Superimposed is a ring representing the size of a single PMT.

Offset /°	**FWHM /°**
0.0	0.1015
0.3	0.0979
0.4	0.1027

Table 5.2: The Point Spread Function for off-axis images taken at typical observation elevations of $\sim 65°$.

Off-axis PSF measurements of T1 were recently taken and are summarised in Table 5.2. Something to note here is that these values were measured prior to a bias alignment (Section 5.5).

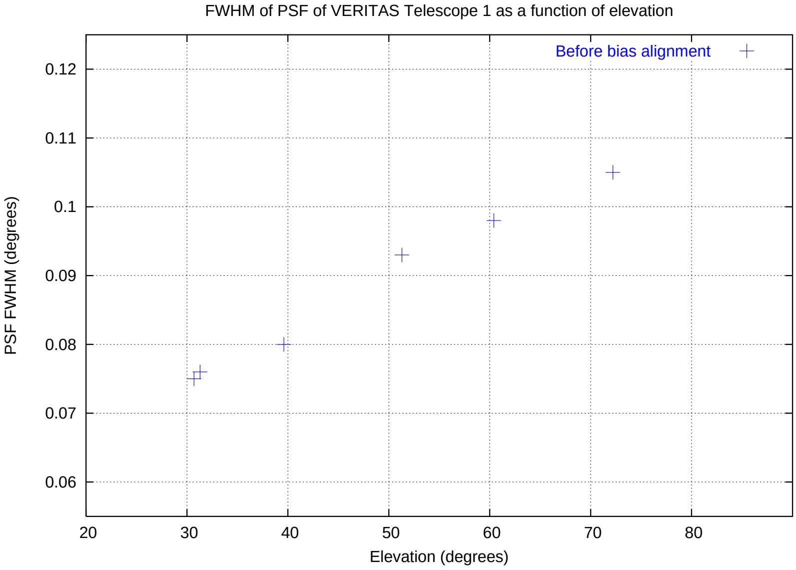

Figure 5.11: Results of a recent PSF measurement of the first 12m telescope of the new VERITAS array. The plot shows the PSF as a function of increasing elevation and illustrates the degradation of the PSF as the elevation of telescope is increased.

5.5 Bias Alignment

In the past a biased alignment has been successfully carried out on the Whipple 10 m reflector. This technique involves carrying out a mirror survey in an attempt to characterise the elevation-dependent misalignment experienced by each facet. To measure the elevation-dependent misalignment, a diode laser is mounted on each mirror facet and pointed at the focal plane of the telescope. An image of the laser spot on the focal plane is recorded using a CCD

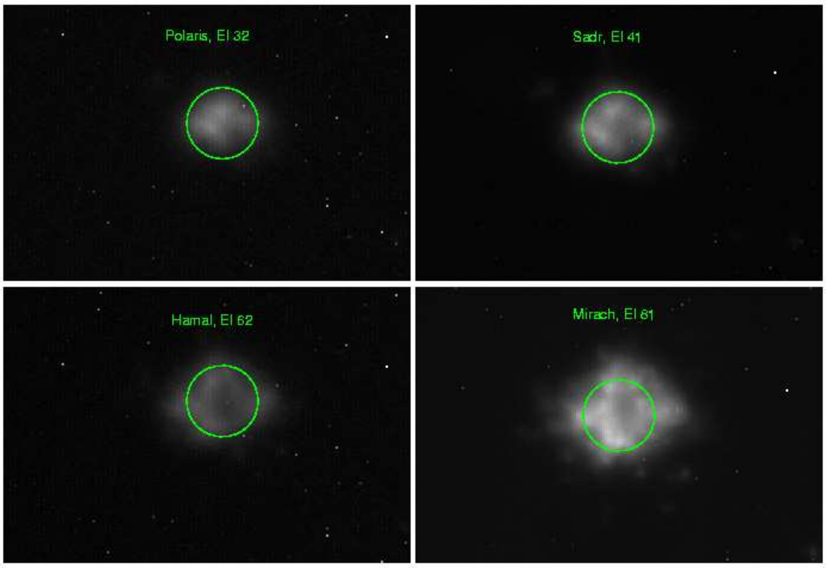

Figure 5.12: Optical PSF images from T1 of the VERITAS array showing the different levels of degradation, as elevation increases, emphasising the importance of the bias alignment procedure. The circle illustrates the 0.15° PMT size.

mounted at the center of the reflector at zero degrees elevation and then at typical observing elevations (65°). This gives a direct measurement of the amount each mirror moved during the transition between the home position (where alignment is carried out) and average observing elevations.

With this information now at hand, modifications can then be made to the semi-automated alignment system control software that will result in the alignment system instructing the persons carrying out the alignment to deliberately misalign the facets while in the home position in such a way that they self-align as the telescope moves into normal observing positions. This method is known as *"bias alignment"* and was successfully carried out on the Whipple 10 m reflector during the 2001/2002 observing season and was recently carried out on T1, T2 and T3 of the VERITAS array. Figure 5.13

shows recent measurements of the FWHM of the PSF of T1 of the VERITAS array as a function of elevation for PSF measurements before and after bias alignments and clearly illustrates the benefit of this technique.

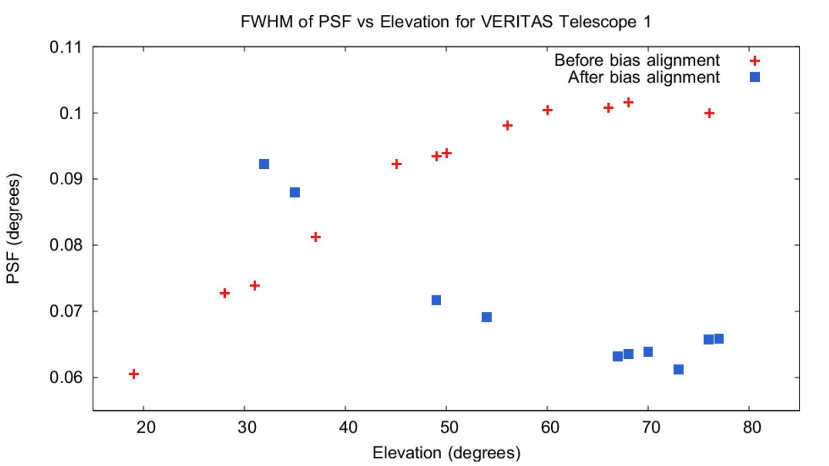

Figure 5.13: PSF measurements for T1 of the VERITAS array, as a function of elevation, before and after bias alignment. The reduction in the measured FWHM at higher elevations is quite clear. Normal observing is carried out over the elevation range 40° - 80°.

After bias alignment the PSF of T1 was found to be 0.06° at an elevation of 65°. At present a full bias alignment is being applied to the VERITAS array using the semi-automated alignment system on all of the facets of each of the four VERITAS telescopes with the aim of achieving a PSF of $< 0.06°$ (less than half the width of a single PMT pixel) FWHM over the 40° - 80° elevation range where normal observing is carried out.

Chapter 6

Iterative Deconvolution of Whipple Cherenkov Data

6.1 Introduction

Deconvolution is a mathematical technique used in image restoration to reverse the effects of convolution on recorded data. The concept of deconvolution is widely used in the techniques of signal processing and image processing, particularly in the area of optical astronomy. When an optical telescope collects an image of a star or galaxy, the light recorded by the instrument has been changed by a finite amount, most significantly by slight imperfections or abberations in the optics of the telescope itself. This is the process of convolution as mentioned above. For optical instruments the amount by which the image has been manipulated or convolved, can be calculated by measuring the impulse response, or point spread function (PSF), of the telescope. The ultimate goal of the deconvolution process is to extract the original un-degraded image, using knowledge of the PSF and the blurred image.

Since deconvolution is a mathematical operation, many methods have been developed for use in image restoration projects. However, each method comes with its own list of advantages and disadvantages. For example, Fourier-transform methods are successful, but are only so when noise levels in the degraded image are moderate or small (Harris, 1966)(McGlamery, 1966). One of the more popular methods, particularly in optical astronomy and medical physics, is known as the Richardson - Lucy algorithm. It was developed in the early 1970's independently by Richardson and Lucy (Richardson, 1972)(Lucy, 1974) and is derived from Bayes' theorem. Today it remains a popular method of deconvolution due to its ability to produce reconstructed images of good quality even in the presence of high noise levels. This project was the first attempt to apply a deconvolution algorithm of any kind to imaging atmospheric Cherenkov images in attempt to enhance the γ-ray signal in Cherenkov data.

6.2 Richardson - Lucy algorithm

The Richardson - Lucy method of deconvolution is an iterative method of restoring degraded images. The Richardson - Lucy method of deconvolution has been popular in optical astronomy for many years, and has been the favored method of image restoration for early degraded Hubble Space Telescope images (Ricort et al., 1993). The method was developed from Bayes' theorem and as such considers images, PSFs, and degraded images, as probability-frequency functions, and then applies Bayes' theorem. Because it relates conditional probabilities, the algorithm takes into account statistical fluctuations in the signal and therefore has the ability to reconstruct noisy images. Considering this, the Richardson - Lucy algorithm was chosen as the preferred method to apply to Cherenkov images as these images can contain Poisson fluctuations in the Cherenkov signal, night-sky background fluctuations and electronic noise fluctuations. Since a major goal of γ-ray astronomy is the attainment of as high a signal to noise ratio as possible, this project was deemed worthy in its attempt to improve the signal to noise ratio of the Whipple telescope. Bayes' Theorem is a mathematical theorem based on the definition of conditional probabilities. Conditional probability is defined as:

$$P(B|A) = \frac{P(A \cap B)}{P(A)}, \tag{6.1}$$

where $P(B|A)$ is the probability of observing the event B given the fact that A has occurred, $P(A \cap B)$ is the probability that both A and B occur, and $P(A)$ is the probability of B in the first place. Rearranging 6.1 we get:

$$P(A \cap B) = P(B|A)P(A) = P(A|B)P(B); \tag{6.2}$$

Rearranging again gives us the formal definition of Bayes' theorem:

$$P(B|A) = \frac{P(A|B)P(B)}{P(A)} \tag{6.3}$$

For our purposes we can assume that a blurred image H can be described by $H = W * S$, where S is the PSF of the instrument, W is the original image and $*$ signifies the mathematical procedure of convolution. Our task here is to extract the original image W using what we know of the blurred image and the PSF. Here we use Bayes' theorem to express the conditional probability of an event at W_i given an event at H_k,

$$P(W_i|H_k) = \frac{P(H_k|W_i)P(W_i)}{\sum_j P(H_k|W_j)P(W_j)}; \tag{6.4}$$

$$i = \{1, I\}, \quad j = \{1, J\}, \quad k = \{1, K\},$$

The subscripts used here indicate the location of, and value in, the associated array, for example, W_i refers to the W array value at the ith location in the array. H_k is an arbitrary cell of *H*.

By taking all the H_k and their dependence on W_i in accordance with *S*, and since $P(W_i|H_k) = P(W_i \cap H_k)/P(H_k)$ (from Equation 6.1), then

$$P(W_i) = \sum_k P(W_i \cap H_k) = \sum_k P(W_i|H_k)P(H_k) \tag{6.5}$$

By substituting Equation 6.4 in Equation 6.5 gives

$$P(W_i) = \sum_k \frac{P(H_k|W_i)P(W_i)P(H_k)}{\sum_j P(H_k|W_j)P(W_j)} \tag{6.6}$$

Note that in the right side of this equation, $P(W_i)$, is the desired solution. Since we don't know this when starting the deconvolution process, a common practice (McGlamery & Gray, 1963) is to use an estimate of the $P(W_i)$ function to obtain, from Equation 6.4, an approximation of $P(W_i|H_k)$. Thus Equation 6.6 becomes

$$P_{r+1}(W_i) = P_r(W_i) \sum_k \frac{P(H_k|W_i)P(H_k)}{\sum_j P(H_k|W_j)P_r(W_j)} \tag{6.7}$$

$$r = \{0, 1, 2, \ldots\}.$$

Equation 6.7 can now be reworked into a more usable form by taking the empirical probability of W_i, i.e. $P(W_i) = W_i/W$, $P(H_k) = H_k/H = H_k/W$, and as the restoration process is conservative, W=H. In addition, $P(H_k|W_i) =$

$P(S_{i,k}) = S_{i,k}/S$. For a single dimension, Equation 6.7 now becomes

$$W_{i,r+1} = W_{i,r} \sum_{k} \frac{S_{i,k} H_k}{\sum\limits_{j} S_{j,k} W_{j,r}} \tag{6.8}$$

At this point equation 6.8 can be used to explain the restorative process. The denominator here is H_k for the current estimate of W. If the H_k estimate is too big then $H_k/H_k estimate < 1$. Therefore all of W_i will be adjusted by this amount as well as being scaled by S.

Equation 6.8 can now be expanded into a two dimensional form, and due to the finite size of the arrays can be written as:

$$W_{i,j,r+1} = W_{i,j,r} \sum_{m=i}^{e} \sum_{n=j}^{f} \frac{H_{m,n} S_{m-i+1,n-j+1}}{\sum\limits_{p=a}^{b} \sum\limits_{q=c}^{d} W_{q,p,r} S_{m-p+1,n-q+1}},^{1} \tag{6.9}$$

This results in a two dimensional deconvolution iterative process that can then be applied to Whipple Cherenkov data. This equation was developed as a algorithmic function/subroutine and written in the C programming language. The subroutine was then integrated into the standard analysis software prior to the application of the picture and boundary thresholds and

---

[1] where

$$a = (1, m - K + 1)_{max}; \qquad b = (m, I)_{min};$$

$$c = (1, n - L + 1)_{max}; \qquad d = (n, J)_{min};$$

$$e = i + K - 1; \qquad f = j + L - 1;$$

$$i = \{1, I\}; \quad j = \{1, J\} \quad r = \{0, 1, 2, \ldots\}.$$

K,L are dimensions of $S_{k,l}$ and I,J are dimensions of $W_{i,j}$

then applied to test images and real data. As discussed in Section 3.4, the picture and boundary thresholds are what define the boundaries of the image. Picture and boundary thresholds were optimised and set at 4.25σ and 2.25σ respectively (Punch et al., 1991).

6.3 Algorithm Development

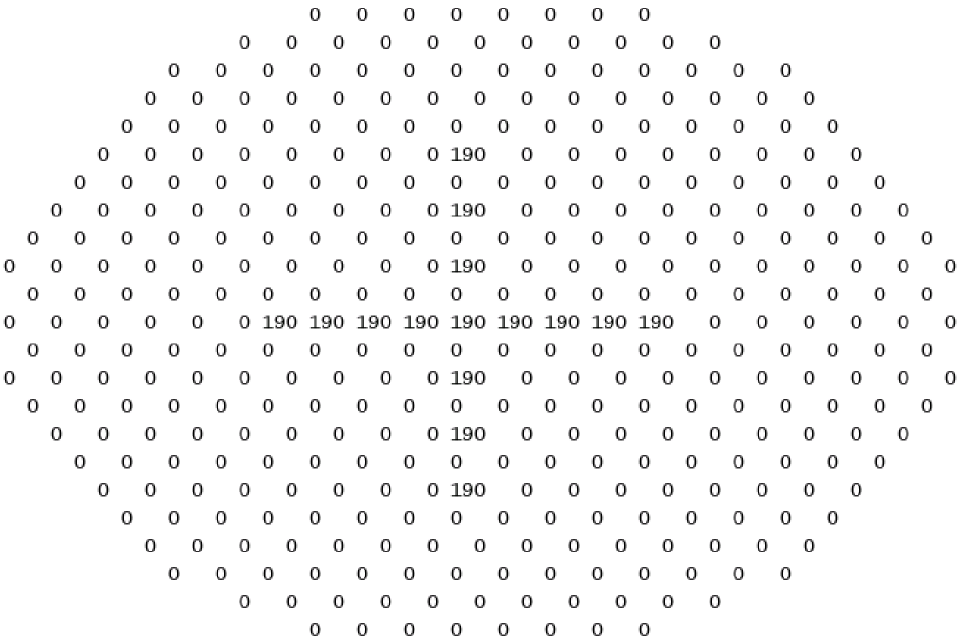

```
                             0   0   0   0   0   0   0   0
                       0   0   0   0   0   0   0   0   0   0   0
                 0   0   0   0   0   0   0   0   0   0   0   0   0   0
               0   0   0   0   0   0   0   0   0   0   0   0   0   0   0
             0   0   0   0   0   0   0   0   0   0   0   0   0   0   0   0
           0   0   0   0   0   0   0   0 190   0   0   0   0   0   0   0   0
         0   0   0   0   0   0   0   0   0   0   0   0   0   0   0   0   0   0
       0   0   0   0   0   0   0   0   0 190   0   0   0   0   0   0   0   0   0
     0   0   0   0   0   0   0   0   0   0   0   0   0   0   0   0   0   0   0   0
   0   0   0   0   0   0   0   0   0   0 190   0   0   0   0   0   0   0   0   0   0
     0   0   0   0   0   0   0   0   0   0   0   0   0   0   0   0   0   0   0   0
   0   0   0   0   0   0 190 190 190 190 190 190 190 190 190   0   0   0   0   0   0
     0   0   0   0   0   0   0   0   0   0   0   0   0   0   0   0   0   0   0   0
   0   0   0   0   0   0   0   0   0   0 190   0   0   0   0   0   0   0   0   0   0
     0   0   0   0   0   0   0   0   0   0   0   0   0   0   0   0   0   0   0   0
       0   0   0   0   0   0   0   0   0 190   0   0   0   0   0   0   0   0   0
         0   0   0   0   0   0   0   0   0   0   0   0   0   0   0   0   0   0
           0   0   0   0   0   0   0   0 190   0   0   0   0   0   0   0   0
             0   0   0   0   0   0   0   0   0   0   0   0   0   0   0   0
               0   0   0   0   0   0   0   0   0   0   0   0   0   0   0
                 0   0   0   0   0   0   0   0   0   0   0   0   0   0
                       0   0   0   0   0   0   0   0   0   0   0
                             0   0   0   0   0   0   0   0
```

Figure 6.1: A simulated test image showing camera pixel values before convolution.

The derivation of the final algorithm as outlined above is for use with standard CCD images that are either square or rectangular in shape. However, as described in Chapter 3, the layout of the pixels of the Whipple 10 m telescope camera is not the same as a standard CCD camera. Figure 6.1 shows an undeconvolved simulated test image of camera pixel values that illustrates the unconventional shape of the Whipple 10 m camera. To rectify the non-rectangular shape of the camera, raw data were mapped into a rectangular grid shape and the edges of the hexagonal PMT camera were padded out with zeros. This padded camera can be seen in Figure 6.2. To test the algorithm, a series of simulated images were created and then convolved with a Gaussian PSF based on the average measured full width half maximum (FWHM) of the telescope PSF, which was found to be 0.125° (Figure 6.3). The PSF here is not symmetrical in order for it to be compatible with the

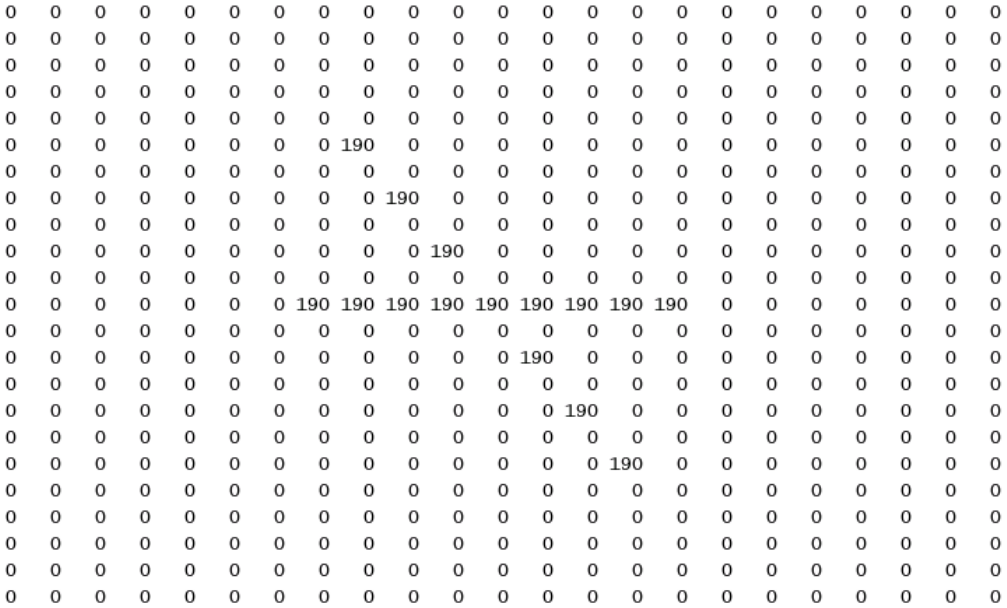

```
0   0   0   0   0   0   0   0   0   0   0   0   0   0   0   0   0   0   0   0   0   0   0
0   0   0   0   0   0   0   0   0   0   0   0   0   0   0   0   0   0   0   0   0   0   0
0   0   0   0   0   0   0   0   0   0   0   0   0   0   0   0   0   0   0   0   0   0   0
0   0   0   0   0   0   0   0   0   0   0   0   0   0   0   0   0   0   0   0   0   0   0
0   0   0   0   0   0   0   0   0   0   0   0   0   0   0   0   0   0   0   0   0   0   0
0   0   0   0   0   0   0   0 190   0   0   0   0   0   0   0   0   0   0   0   0   0   0
0   0   0   0   0   0   0   0   0   0   0   0   0   0   0   0   0   0   0   0   0   0   0
0   0   0   0   0   0   0   0   0 190   0   0   0   0   0   0   0   0   0   0   0   0   0
0   0   0   0   0   0   0   0   0   0   0   0   0   0   0   0   0   0   0   0   0   0   0
0   0   0   0   0   0   0   0   0   0 190   0   0   0   0   0   0   0   0   0   0   0   0
0   0   0   0   0   0   0   0   0   0   0   0   0   0   0   0   0   0   0   0   0   0   0
0   0   0   0   0   0   0 190 190 190 190 190 190 190 190 190   0   0   0   0   0   0   0
0   0   0   0   0   0   0   0   0   0   0   0   0   0   0   0   0   0   0   0   0   0   0
0   0   0   0   0   0   0   0   0   0   0   0 190   0   0   0   0   0   0   0   0   0   0
0   0   0   0   0   0   0   0   0   0   0   0   0   0   0   0   0   0   0   0   0   0   0
0   0   0   0   0   0   0   0   0   0   0   0   0 190   0   0   0   0   0   0   0   0   0
0   0   0   0   0   0   0   0   0   0   0   0   0   0   0   0   0   0   0   0   0   0   0
0   0   0   0   0   0   0   0   0   0   0   0   0   0 190   0   0   0   0   0   0   0   0
0   0   0   0   0   0   0   0   0   0   0   0   0   0   0   0   0   0   0   0   0   0   0
0   0   0   0   0   0   0   0   0   0   0   0   0   0   0   0   0   0   0   0   0   0   0
0   0   0   0   0   0   0   0   0   0   0   0   0   0   0   0   0   0   0   0   0   0   0
0   0   0   0   0   0   0   0   0   0   0   0   0   0   0   0   0   0   0   0   0   0   0
0   0   0   0   0   0   0   0   0   0   0   0   0   0   0   0   0   0   0   0   0   0   0
```

Figure 6.2: The mapped camera pixels padded with zero pixels

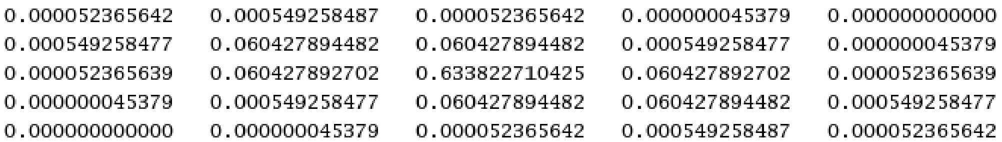

```
0.000052365642   0.000549258487   0.000052365642   0.000000045379   0.000000000000
0.000549258477   0.060427894482   0.060427894482   0.000549258477   0.000000045379
0.000052365639   0.060427892702   0.633822710425   0.060427892702   0.000052365639
0.000000045379   0.000549258477   0.060427894482   0.060427894482   0.000549258477
0.000000000000   0.000000045379   0.000052365642   0.000549258487   0.000052365642
```

Figure 6.3: PSF used to test deconvolution algorithm. FWHM is 0.125°. Note here that the PSF has been shifted in the same manner as the camera pixels in Figure 6.2 to ensure correct convolution.

shape and pixel layout of the 10 m camera. The convolved image is shown in Figure 6.4. The effects of convolution can clearly be seen here. Looking at the blurred or convolved image we can see that the most affected pixels are those closest to the main non-distorted image pixels. The total amount of light in the camera remains constant but has been spread out to an extent as determined by the PSF. The basic shape of the cross of numbers can still be recognised but it is now much wider. The light in the image has been spread out, and the role of the Richardson - Lucy algorithm is now to undo this spreading of light in the image.

```
                             0   0   0   0   0   0   0   0
                       0   0   0   0   0   0   0   0   0   0   0
                 0   0   0   0   0   0   0   0   0   0   0   0   0   0
               0   0   0   0   0   0   0   0   0   0   0   0   0   0   0
             0   0   0   0   0   0   0  11  11   0   0   0   0   0   0   0
           0   0   0   0   0   0   0  11 121  11   0   0   0   0   0   0   0
         0   0   0   0   0   0   0   0  23  23   0   0   0   0   0   0   0   0
       0   0   0   0   0   0   0   0  12 121  12   0   0   0   0   0   0   0   0
     0   0   0   0   0   0   0   0   0  23  23   0   0   0   0   0   0   0   0   0
   0   0   0   0   0   0   0   0   0  12 121  12   0   0   0   0   0   0   0   0   0
     0   0   0   0   0  12  23  23  23  35  35  23  23  23  12   0   0   0   0   0
   0   0   0   0   0  11 132 143 143 143 144 143 143 143 132  11   0   0   0   0   0
     0   0   0   0   0  12  23  23  23  35  35  23  23  23  12   0   0   0   0   0
   0   0   0   0   0   0   0   0   0  12 121  12   0   0   0   0   0   0   0   0   0
     0   0   0   0   0   0   0   0   0  23  23   0   0   0   0   0   0   0   0   0
       0   0   0   0   0   0   0   0  12 121  12   0   0   0   0   0   0   0   0
         0   0   0   0   0   0   0   0  23  23   0   0   0   0   0   0   0   0
           0   0   0   0   0   0   0  11 121  11   0   0   0   0   0   0   0
             0   0   0   0   0   0   0  11  11   0   0   0   0   0   0   0
               0   0   0   0   0   0   0   0   0   0   0   0   0   0   0
                 0   0   0   0   0   0   0   0   0   0   0   0   0   0
                       0   0   0   0   0   0   0   0   0   0   0
                             0   0   0   0   0   0   0   0
```

Figure 6.4: Camera pixel values after convolution

6.3.1 Testing the algorithm

After applying the Richardson - Lucy algorithm to the simulated image and iterating 20 times, the resulting image is shown in Figure 6.5. The reconstructed image is clearly much closer to the original image with a small difference in the worst affected pixel compared to the original values. Any further iterations of the algorithm on the image did not improve upon the image as shown.

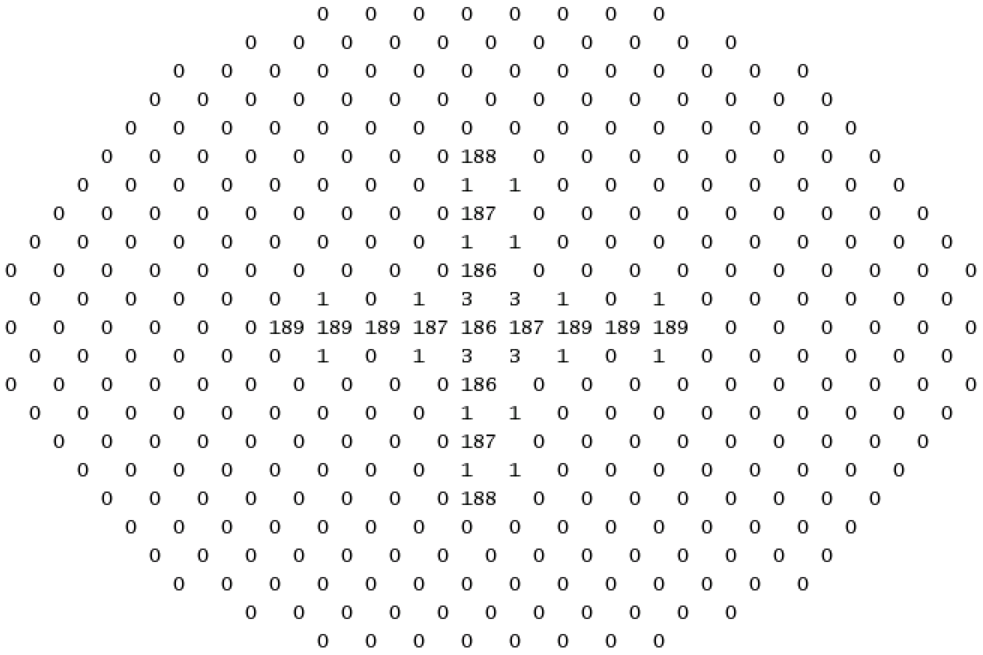

```
                             0   0   0   0   0   0   0   0
                       0   0   0   0   0   0   0   0   0   0   0
                 0   0   0   0   0   0   0   0   0   0   0   0   0   0
               0   0   0   0   0   0   0   0   0   0   0   0   0   0   0
             0   0   0   0   0   0   0   0   0   0   0   0   0   0   0   0
           0   0   0   0   0   0   0   0 188   0   0   0   0   0   0   0   0
         0   0   0   0   0   0   0   0   1   1   0   0   0   0   0   0   0   0
       0   0   0   0   0   0   0   0   0 187   0   0   0   0   0   0   0   0   0
     0   0   0   0   0   0   0   0   0   1   1   0   0   0   0   0   0   0   0   0
   0   0   0   0   0   0   0   0   0   0 186   0   0   0   0   0   0   0   0   0   0
     0   0   0   0   0   0   1   0   1   3   3   1   0   1   0   0   0   0   0   0
   0   0   0   0   0   0 189 189 189 187 186 187 189 189 189   0   0   0   0   0   0
     0   0   0   0   0   0   1   0   1   3   3   1   0   1   0   0   0   0   0   0
   0   0   0   0   0   0   0   0   0   0 186   0   0   0   0   0   0   0   0   0   0
     0   0   0   0   0   0   0   0   0   1   1   0   0   0   0   0   0   0   0   0
       0   0   0   0   0   0   0   0   0 187   0   0   0   0   0   0   0   0   0
         0   0   0   0   0   0   0   0   1   1   0   0   0   0   0   0   0   0
           0   0   0   0   0   0   0   0 188   0   0   0   0   0   0   0   0
             0   0   0   0   0   0   0   0   0   0   0   0   0   0   0   0
               0   0   0   0   0   0   0   0   0   0   0   0   0   0   0
                 0   0   0   0   0   0   0   0   0   0   0   0   0   0
                       0   0   0   0   0   0   0   0   0   0   0
                             0   0   0   0   0   0   0   0
```

Figure 6.5: Camera pixel values after deconvolution - 20 iterations

At this point, as can be seen from the images the algorithm was successfully deconvolving distinctive patterns on the camera. However, these initial images did not have any noise added and in reality Cherenkov images are far from noiseless. To match noise levels in real Cherenkov images, a Gaussian distribution of random numbers with a standard deviation of 2 was generated to simulate noise. This noise was added to the convolved images, see Figure

6.6 (top), and the deconvolution algorithm was again applied to the simulated data. Figure 6.6 (bottom) shows the effect of applying 20 iterations to the noisy image.

Looking at the deconvolved noisy image a hot spot of high pixel values, both positive and negative, has appeared in the top right quadrant of the camera. Several other large pixel values have also appeared in random regions of the camera. It was found that this effect was caused by very small negative values, due to noise fluctuations, that were appearing in the denominator in Equation 6.9 resulting in large negative values. These random fluctuations would change from iteration to iteration and appear in random regions of the camera. For example the large pixel values seen in Figure 6.6 (bottom image) did not appear in the subsequent iterated image, however a different hot spot had appeared in a separate part of the camera. To remedy this, just before the point of applying the algorithm, any negative pixel values were removed from the image, *i.e.* they were zeroed out of the image as can be seen in Figure: 6.7 (top image).

The effect of removing these negative values can be seen in Figure 6.7 (bottom image). Here the random large pixel values are no longer appearing in the deconvolved images, and the algorithm is performing satisfactorily as it did before the addition of the random noise.

Further tests show that the algorithm can successfully restore convolved simulated images close to their original un-degraded form even in the presence of non-negative random noise. However this condition is only true provided the blurring component or PSF used to blur the images is known accurately. For these tests the FWHM value used was 0.125°.

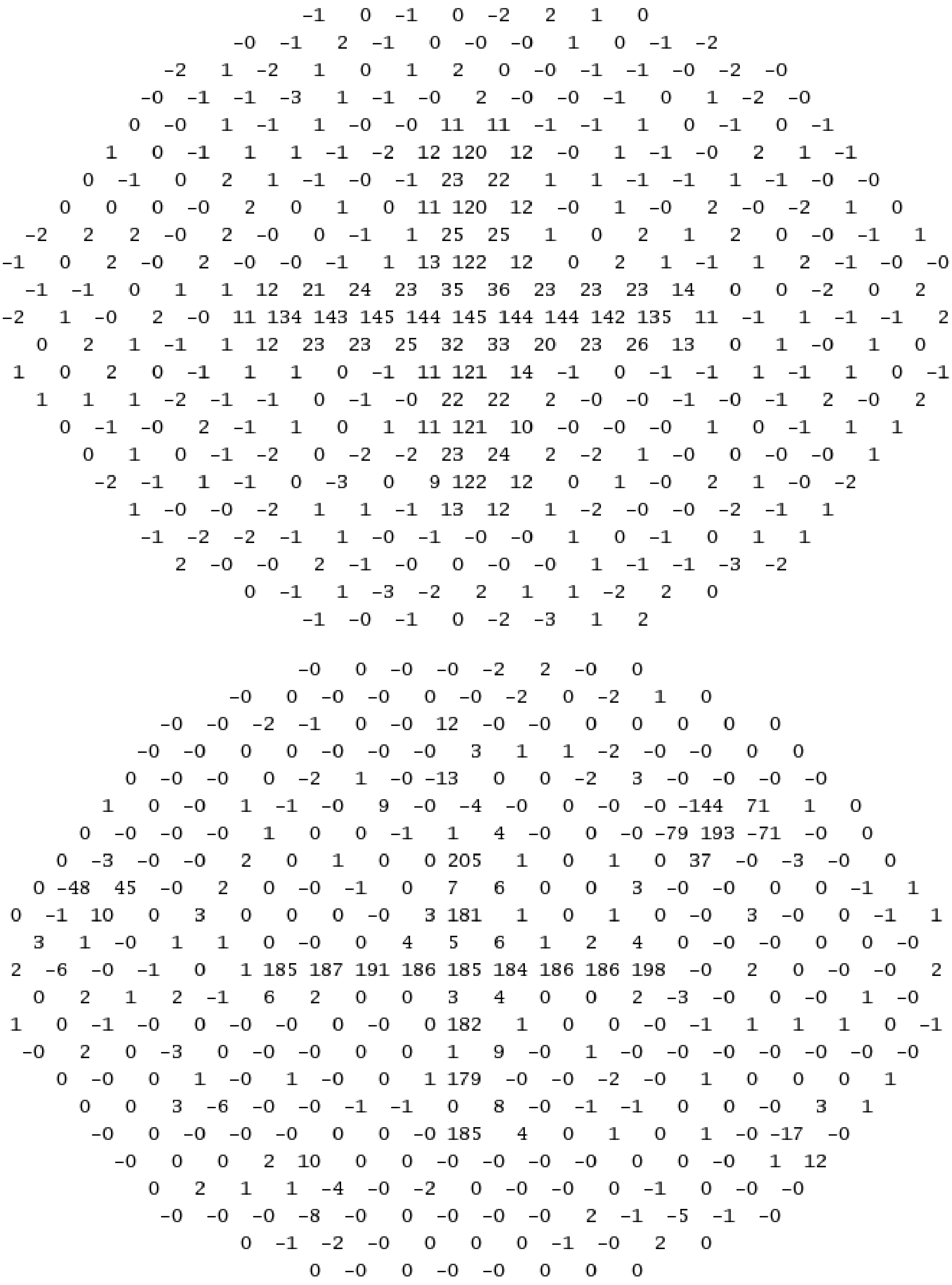

```
                            -1   0  -1   0  -2   2   1   0
                      -0  -1   2  -1   0  -0  -0   1   0  -1  -2
                -2   1  -2   1   0   1   2   0  -0  -1  -1  -0  -2  -0
              -0  -1  -1  -3   1  -1  -0   2  -0  -0  -1   0   1  -2  -0
             0  -0   1  -1   1  -0  -0  11  11  -1  -1   1   0  -1   0  -1
           1   0  -1   1   1  -1  -2  12 120  12  -0   1  -1  -0   2   1  -1
         0  -1   0   2   1  -1  -0  -1  23  22   1   1  -1  -1   1  -1  -0  -0
       0   0   0  -0   2   0   1   0  11 120  12  -0   1  -0   2  -0  -2   1   0
    -2   2   2  -0   2  -0   0  -1   1  25  25   1   0   2   1   2   0  -0  -1   1
  -1   0   2  -0   2  -0  -0  -1   1  13 122  12   0   2   1  -1   1   2  -1  -0  -0
    -1  -1   0   1   1  12  21  24  23  35  36  23  23  23  14   0   0  -2   0   2
  -2   1  -0   2  -0  11 134 143 145 144 145 144 144 142 135  11  -1   1  -1  -1   2
     0   2   1  -1   1  12  23  23  25  32  33  20  23  26  13   0   1  -0   1   0
   1   0   2   0  -1   1   1   0  -1  11 121  14  -1   0  -1  -1   1  -1   1   0  -1
     1   1   1  -2  -1  -1   0  -1  -0  22  22   2  -0  -0  -1  -0  -1   2  -0   2
       0  -1  -0   2  -1   1   0   1  11 121  10  -0  -0  -0   1   0  -1   1   1
         0   1   0  -1  -2   0  -2  -2  23  24   2  -2   1  -0   0  -0  -0   1
          -2  -1   1  -1   0  -3   0   9 122  12   0   1  -0   2   1  -0  -2
             1  -0  -0  -2   1   1  -1  13  12   1  -2  -0  -0  -2  -1   1
              -1  -2  -2  -1   1  -0  -1  -0  -0   1   0  -1   0   1   1
                 2  -0  -0   2  -1  -0   0  -0  -0   1  -1  -1  -3  -2
                       0  -1   1  -3  -2   2   1   1  -2   2   0
                            -1  -0  -1   0  -2  -3   1   2
```

```
                            -0   0  -0  -0  -2   2  -0   0
                      -0   0  -0  -0   0  -0  -2   0  -2   1   0
                -0  -0  -2  -1   0  -0  12  -0  -0   0   0   0   0   0
              -0  -0   0   0  -0  -0  -0   3   1   1  -2  -0  -0   0   0
             0  -0  -0   0  -2   1  -0 -13   0   0  -2   3  -0  -0  -0  -0
           1   0  -0   1  -1  -0   9  -0  -4  -0   0  -0  -0-144  71   1   0
         0  -0  -0  -0   1   0   0  -1   1   4  -0   0  -0 -79 193 -71  -0   0
       0  -3  -0  -0   2   0   1   0   0 205   1   0   1   0  37  -0  -3  -0   0
     0 -48  45  -0   2   0  -0  -1   0   7   6   0   0   3  -0  -0   0   0  -1   1
   0  -1  10   0   3   0   0   0  -0   3 181   1   0   1   0  -0   3  -0   0  -1   1
     3   1  -0   1   1   0  -0   0   4   5   6   1   2   4   0  -0  -0   0   0  -0
   2  -6  -0  -1   0   1 185 187 191 186 185 184 186 186 198  -0   2   0  -0  -0   2
     0   2   1   2  -1   6   2   0   0   3   4   0   0   2  -3  -0   0  -0   1  -0
   1   0  -1  -0   0  -0  -0   0  -0   0 182   1   0   0  -0  -1   1   1   1   0  -1
    -0   2   0  -3   0  -0  -0   0   0   1   9  -0   1  -0  -0  -0  -0  -0  -0  -0
       0  -0   0   1  -0   1  -0   0   1 179  -0  -0  -2  -0   1   0   0   0   1
         0   0   3  -6  -0  -0  -1  -1   0   8  -0  -1  -1   0   0  -0   3   1
          -0   0  -0  -0  -0   0   0  -0 185   4   0   1   0   1  -0 -17  -0
            -0   0   0   2  10   0   0  -0  -0  -0  -0   0   0  -0   1  12
               0   2   1   1  -4  -0  -2   0  -0  -0   0  -1   0  -0  -0
              -0  -0  -0  -8  -0   0  -0  -0  -0   2  -1  -5  -1  -0
                       0  -1  -2  -0   0   0   0  -1  -0   2   0
                             0  -0   0  -0  -0   0   0   0
```

Figure 6.6: Camera with noise added before (top) and after (bottom) deconvolution

```
                             0   0   0   0   0   2   1   0
                       0   0   2   0   0   0   0   1   0   0   0
                 0   1   0   1   0   1   2   0   0   0   0   0   0   0
               0   0   0   0   1   0   0   2   0   0   0   0   1   0   0
             0   0   1   0   1   0   0  11  11   0   0   1   0   0   0   0
           1   0   0   1   1   0   0  12 120  12   0   1   0   0   2   1   0
         0   0   0   2   1   0   0   0  23  22   1   1   0   0   1   0   0   0
       0   0   0   0   2   0   1   0  11 120  12   0   1   0   2   0   0   1   0
     0   2   2   0   2   0   0   0   1  25  25   1   0   2   1   2   0   0   0   1
   0   0   2   0   2   0   0   0   1  13 122  12   0   2   1   0   1   2   0   0   0
     0   0   0   1   1  12  21  24  23  35  36  23  23  23  14   0   0   0   0   2
   0   1   0   2   0  11 134 143 145 144 145 144 144 142 135  11   0   1   0   0   2
     0   2   1   0   1  12  23  23  25  32  33  20  23  26  13   0   1   0   1   0
   1   0   2   0   0   1   1   0   0  11 121  14   0   0   0   0   1   0   1   0   0
     1   1   1   0   0   0   0   0   0  22  22   2   0   0   0   0   0   2   0   2
       0   0   0   2   0   1   0   1  11 121  10   0   0   0   1   0   0   1   1
         0   1   0   0   0   0   0   0  23  24   2   0   1   0   0   0   0   1
           0   0   1   0   0   0   0   9 122  12   0   1   0   2   1   0   0
             1   0   0   0   1   1   0  13  12   1   0   0   0   0   0   1
               0   0   0   0   1   0   0   0   0   1   0   0   0   1   1
                 2   0   0   2   0   0   0   0   0   1   0   0   0   0
                       0   0   1   0   0   2   1   1   0   2   0
                             0   0   0   0   0   0   1   2

                             0   0   0   0   0   2   1   0
                       0   0   2   0   0   0   0   2   0   0   0
                 0   1   0   1   0   1   2   0   0   0   0   0   0   0
               0   0   0   0   1   0   0   2   0   0   0   0   1   0   0
             0   0   1   0   1   0   0   0   0   0   0   1   0   0   0   0
           1   0   0   0   1   0   0   0 187   0   0   0   0   0   2   1   0
         0   0   0   2   1   0   0   0   2   2   0   1   0   0   1   0   0   0
       0   0   0   0   2   0   1   0   1 182   1   0   0   0   2   0   0   1   0
     0   2   2   0   2   0   0   0   1   6   6   0   0   3   0   3   0   0   0   1
   0   0   2   0   3   0   0   0   0   2 183   1   0   1   0   0   1   2   0   0   0
     0   0   0   1   0   1   0   1   3   5   6   1   2   4   1   0   0   0   0   2
   0   1   0   2   0   0 187 186 190 186 186 184 186 184 193   0   0   1   0   0   2
     0   2   0   0   1   2   2   1   2   3   4   0   1   3   0   0   2   0   2   0
   1   0   2   0   0   1   0   0   0   0 182   2   0   0   0   0   1   0   1   0   0
     1   2   0   0   0   0   0   0   0   1   4   2   0   0   0   0   0   2   0   2
       0   0   0   3   0   1   0   1   0 182   0   0   0   0   1   0   0   1   0
         0   1   0   0   0   0   0   0   1   5   1   0   1   0   0   0   0   0
           0   0   1   0   0   0   0   0 187   2   0   1   0   2   0   0   0
             1   0   0   0   1   1   0   0   1   0   0   0   0   0   0   1
               0   0   0   0   1   0   0   0   0   2   0   0   0   1   1
                 2   0   0   2   0   0   0   0   0   2   0   0   0   0
                       0   0   1   0   0   3   0   1   0   3   0
                             0   0   0   0   0   0   1   2
```

Figure 6.7: Camera with image and noise (no negative values) before (top) and after (bottom) deconvolution

6.4 Observations and Analysis

To test the deconvolution process on real Cherenkov data, a group of 10 *ON/OFF* Crab nebula pairs were chosen from the 2003/2004 observing season. These data files are listed in Table 6.1. The selection was chosen as a PSF measurement had been taken close to the time the data were collected. The measured FWHM of the PSF varied between 0.12° and 0.14° depending on the corresponding telescope elevation of between 60° and 80°.

Date	***ON* run id no.**	***OFF* run id no.**
031022	25505	25506
031023	25526	25527
031120	25738	25739
031120	25740	25741
031121	25759	25760
031121	25761	25762
031121	25763	25764
031122	25781	25782
031122	25783	25784
031124	25828	25829

Table 6.1: Selected data file identification numbers of the Crab pairs used to test deconvolution algorithm

For comparison purposes the data were analysed using the standard *Supercuts* analysis software. The deconvolution algorithm was then incorporated into the analysis software at the stage before the application of picture and boundary thresholds as mentioned earlier. Prior to the deconvolution of the images, the normal analysis procedures were carried out on the data (including software padding) up to the point of zeroing any negative pixels. Negative pixels were zeroed in order to avoid errors arising from a small negative denominator in Equation 6.9. Once all negative pixels have been eliminated from the image, the deconvolution algorithm was applied to each image and iterated a number of times. It was found the images converged after about 14 iterations (*i.e.* the maximum number of iterations applied to the images after which the algorithm had no further effect on the image).

The initial impact of the algorithm was the extended length of time the deconvolution analysis procedure took. This could be as long as 50 to 60 minutes (on a 2 GHz Pentium machine) per *ON/OFF* run as compared with the 1 to 2 minutes per *ON/OFF* run for normal analysis. Once the 14 iterations were completed normal picture and boundary thresholds were applied to the resulting image, *i.e.* non-image pixels were zeroed. From this point on the data were analysed as normal, and the standard *Supercuts* (Punch et al., 1991) method of selecting γ-rays were applied.

Not-deconvolved	**Deconvolved**
12.36 σ	9.88 σ

Table 6.2: Standard analysis results from the selected Crab data set using standard Supercuts on non-deconvolved data and deconvolved data. The FWHM of the PSF used to deconvolve was 0.13°

The initial results from this analysis using the standard *Supercuts* values showed a reduction in the significance as compared to standard analysis procedures. Table 6.2 shows the significance found using the standard *Supercuts* and picture and boundary threshold values of 4.25 and 2.25 on non-deconvolved and deconvolved data. It was expected that a reoptimisation of the cut values would be required to gain the most out of the image restoration process. However, upon examination of the camera events before and after deconvolution, it became apparent that deconvolving the images produces small islands of signal that were passing the standard picture and boundary thresholds, see Figure 6.8

6.4.1 Picture and Boundary thresholds

By studying and comparing deconvolved and non-deconvolved images it is clear that the deconvolution algorithm has by its nature increased the amount of light in the central region of the image. In other words it has sharpened the image by gathering part of the image that was previously excluded from further analysis, by the picture and boundary thresholds, and is now including it. The result of this effect is to increase the value of the *size* parameter of the image significantly. A further effect of the deconvolution was to increase the signal, in the same manner, in singular or small groupings or islands of pixels in the camera (Figure 6.8).

When the signal in these island pixels is sufficient to pass the picture and boundary thresholds, they are included as image pixels and as such they cause a candidate γ-ray to be rejected later in the analysis when the parameter cuts are applied. There is the possibility that the island signals may be an indication of local muonic components and could provide a means to improve hadronic/γ discrimination. The presence of the island signals prompted a full re-optimisation of the picture and boundary threshold levels along with a re-optimisation of the parameter cuts using the test data mentioned above. Due to the length of time it takes to deconvolve one data run, it was deemed impractical to perform a standard picture and boundary optimisation. The standard method requires that for each picture and boundary value the events are parameterised once. For this work each picture and boundary value parameterised dataset would require deconvolving.

This involved modifying the standard analysis code to save the decon-

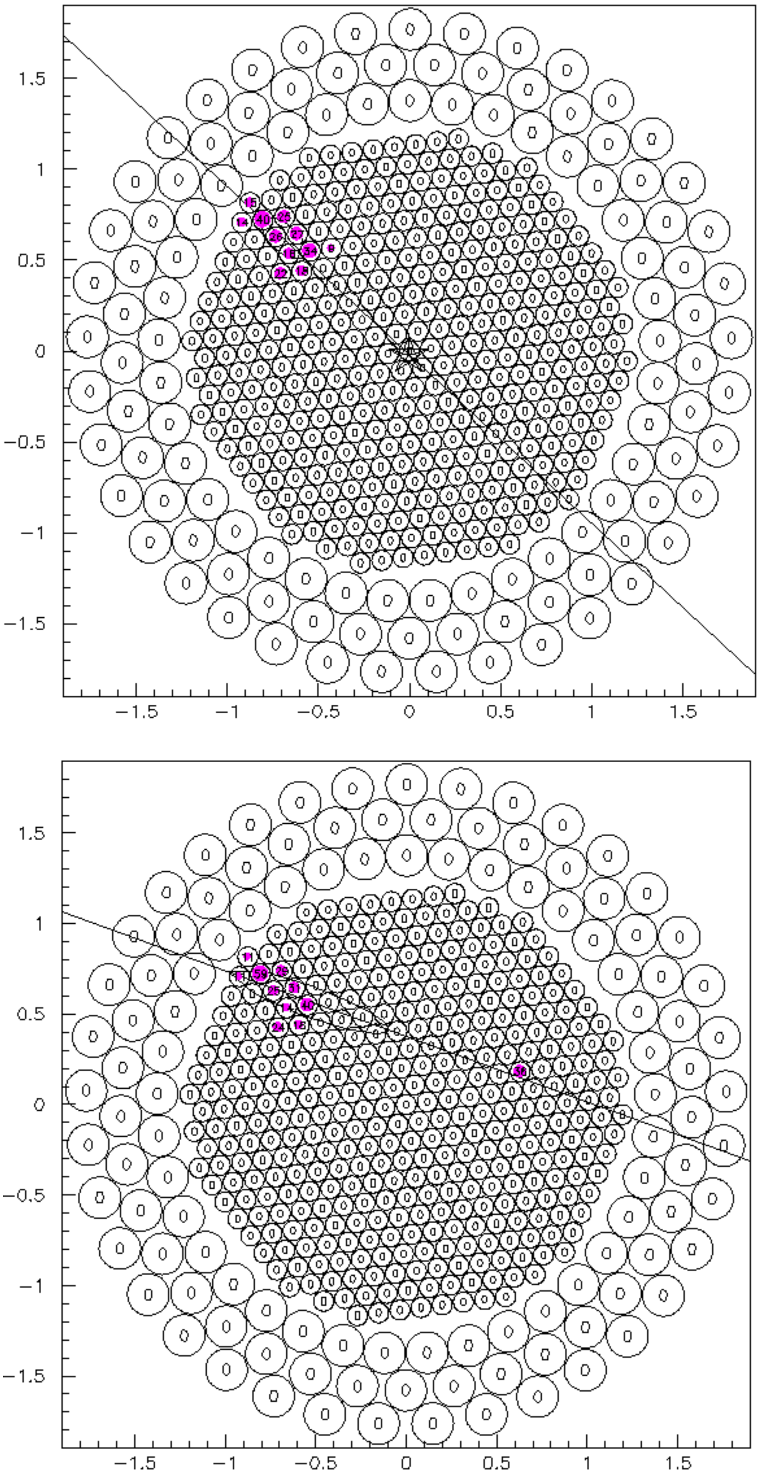

Figure 6.8: Candidate γ-ray images before (top) & after deconvolution (bottom)

volved Cherenkov images for subsequent input to the optimisation stage. Then a full range of picture and boundary values was applied to the deconvolved data and a parameterised data file for each picture and boundary value then returned. Cut values were then optimised on each of these parameterised data files.

6.4.2 Cut Optimisation

The standard method of cut optimisation involves varying a single cut value over a suitable range while all other cuts are held at a predetermined set of values. Normally the variation in significance, as the upper and lower bounds of each parameter cut are changed, is plotted. The plots are then used to find the optimum cut values, *i.e.* those values for which the statistical significance of the excess is highest. To test cut values obtained from an optimisation, the process is repeated on an independent set of data.

In this experiment a different approach to cut optimisation was carried out. The method involved optimising values for the cuts on *length, width, alpha, length/size* and on *max 1* and *max 2*. The cuts were optimised by producing a five dimensional (one dimension per parameter) distribution of all the events to be optimised for the *ON* and *OFF* data *i.e.* all events in the *ON* and *OFF* data were binned in five dimensional parameter spaces. The bin sizes were 0.01° for *length* and *width*, 1 ° for *alpha*, 0.00001° for *length/size* and 10 for *max 1 and 2*. Each distribution was then integrated along each axis creating a distribution that had a value for the number of events that passed each particular bin. The significance could then be determined for each bin using the *ON* and *OFF* distributions using the Li & Ma (1983) method.

The bin containing the peak significance was chosen as the optimised cut value. The values of the lower cut values for *length* and *width* were found by repeating the above process with the exception of changing the lower cut values in a manner similar to the standard optimisation procedure. The procedure returned lower bound cut values that were equal to the standard lower bounds of the *Supercuts* values.

6.5 Results

Using this quicker method of analysis the data were then deconvolved several times using a full range of PSF values in order to ensure the full range of possible and extreme telescope PSF values were examined. The PSF values used, and the results obtained, can be seen in Table 6.3. For comparison purposes the data in its non-deconvolved state were used to fully optimise the picture and boundary thresholds and the cuts. The method used was identical to that used on the deconvolved data. The maximum significance obtained (for non-deconvolved data) was 16.77σ.

PSF/ °	**Significance/ σ**
0.11	16.28
0.12	16.68
0.13	16.77
0.14	16.99
0.15	16.24
0.16	16.87
0.17	16.19
0.18	16.42
0.19	16.27

Table 6.3: Results after deconvolving the selected Crab data with various FWHM values for the PSF

After an extensive analysis of the test data using a wide range of PSF values, the deconvolution process proves to be of no benefit with regard to increasing the significance of the analysis results. For each PSF value, a full re-optimisation of the picture and boundary levels and parameter cuts was carried out in order to find the maximum significance. The results of the optimisation procedures is shown in the form of a contour plot in Figure 6.9. The figure shows contour levels of significance values for various picture and boundary values for un-deconvolved data (top) and deconvolved data (bottom). The resulting effect of the deconvolution is to shift the peak in significance to higher picture and boundary levels. However the peak significance of the deconvolved data is not significantly increased compared to un-deconvolved data. The FWHM value of the PSF used in the plot shown was 0.14°.

Finally, the original cuts and optimised cuts were applied to an independent data set for comparison purposes. Using *Supercuts* a maximum significance of 10.23σ was found. After applying the optimised cuts to the un-deconvolved independent data set the significance dropped to 8.71σ, a reduction of 15% from the *Supercuts* value. The independent data set was then deconvolved using the same procedures outlined above. Subsequent to deconvolution of the independent data set, a significance was 9.41σ returned, a reduction of 8%.

6.6 Conclusions

The peak signal seen from the independent data set before deconvolution was 10.23σ with picture and boundary thresholds set at 5.00 and 3.00 respectively. After deconvolution a peak signal of 9.41σ (an 8% decrease) with picture and boundary thresholds set at 7.00 and 3.50 was found. As mentioned previously

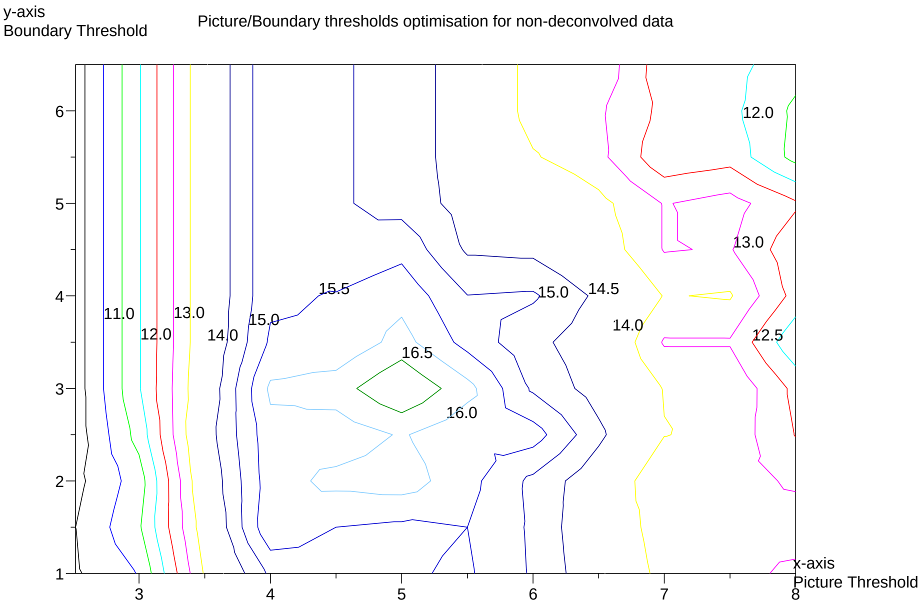

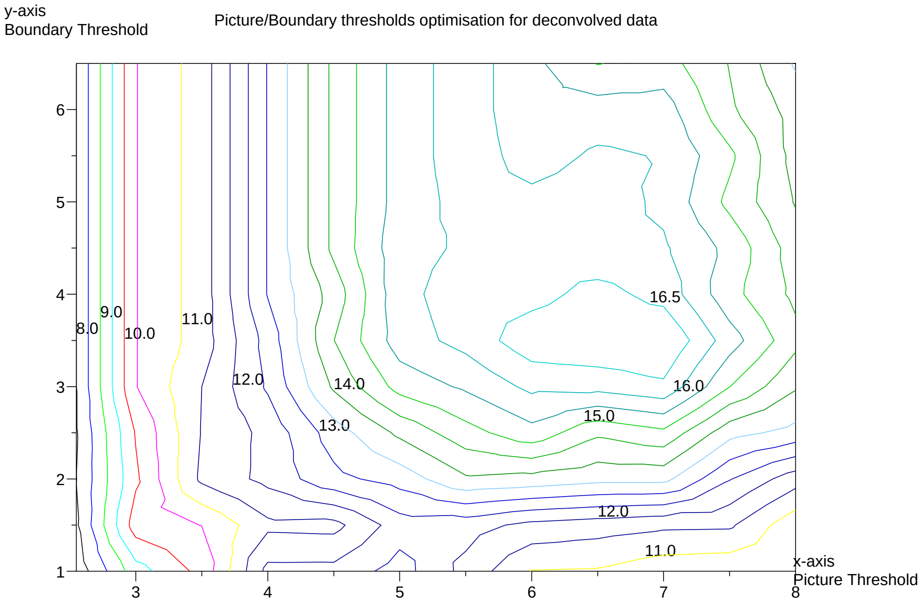

Figure 6.9: Contour plots of significance levels before (top) and after deconvolution (bottom) showing how the picture and boundary threshold values were obtained.

the deconvolution process is increasing the amount of light in groupings of pixels resulting in the necessary re-optimisation of the picture and boundary thresholds. The effect of this can be seen in the contour plots. In effect the *size* of each Cherenkov image has been increased by an amount so as to require raising the picture and boundary threshold levels by 65% and 55% respectively. The cut values used to achieve the obtained significance values are shown in Tables 6.4 and 6.5. Using the optimum cut values found from optimising the non-deconvolved data with the standard analysis software gave a significance of 8.71σ.

Cut	**Value**
Length	$< 0.20°$
Width	$< 0.08°$
Alpha	$< 9°$
Length/size	$< 0.00032°$
Max 1 & 2	> 100
Picture	7.00
Boundary	3.50

Table 6.4: Optimum cut values for deconvolved data.

Cut	**Value**
Length	$< 0.22°$
Width	$< 0.09°$
Alpha	$< 11°$
Length/size	$< 0.00031°$
Max 1 & 2	> 60
Picture	5.00
Boundary	3.00

Table 6.5: Optimum cut values for non-deconvolved data.

It must be made clear that this increase in the *size* of the image is caused by the sharpening of the image and the extra light required for this increase was previously being zeroed out as it was spread across several pixels. In other words, part of the image signal that was perviously omitted as it was not high enough to pass the picture and boundary thresholds is now being included to the final stages of the analysis. Further investigation to determine the significance of the increase in the average value of the *size* image parameter, with respect to the energy of the primary particle, has not been carried out here.

Something of note here is that optimising the picture and boundary levels with non-deconvolved data resulted in a peak in significance with the picture and boundary levels at 5.00 and 3.00. This is an increase of 18% and 33% on the current picture and boundary level settings used in a standard *Supercuts* analysis, and could prompt a need to look at new picture and boundary levels in the analysis of archived data. The original threshold values were derived in 1991 (Punch et al., 1991) and have been used with the standard analysis since then.

The work described here has demonstrated that the iterative deconvolution of the point spread function from Cherenkov images does not enhance the sensitivity of the atmospheric Cherenkov imaging technique. It was hoped that by deconvolving the Cherenkov images in the data set, candidate images would be sharpened up to the degree that true γ-ray events that were being rejected by *Supercuts* would, subsequent to deconvolution, pass the selection criteria. It was also hoped that non-γ-ray event images would also be sharpened thus revealing detail that would allow enhanced discrimination between γ-ray events, hadronic events and other noise events.

Chapter 7

Reanalysis of archival data of the unidentified TeV source TeV J2032+4130

7.1 Introduction

The unidentified TeV source TeV J2032+4130, located in the Cygnus region, has been confirmed as a source of very high energy γ-rays (Aharonian et al., 2005a; Lang et al., 2004). Since its serendipitous discovery by the HEGRA group in 2002 (Aharonian et al., 2002), TeV J2032+4130 has been the subject of on-going study. Observations of Cygnus X-3 were taken with the Whipple 10 m imaging atmospheric Cherenkov telescope during the 1989/1990 observing season searching for a γ-ray signal from this crowded region of sky. However, no γ-ray emission of any kind was detected from Cygnus X-3 (O'Flaherty et al., 1992) and the data were consigned to the archives. At the time of the original analysis, only a point source analysis at the centre of the field of view was carried out as this was the standard analysis technique at that time.

Following the unexpected detection of TeV J2032+4130 by the HEGRA group, Lang et al. (2004) carried out an analysis of the Cygnus dataset over the entire field of view of the telescope. This technique, known as a two-dimensional analysis (Lessard et al., 2001), yielded a 3.3σ excess at the position of the source detected by HEGRA and was reported by the authors, thus TeV J2032+4130 was confirmed as a TeV γ-ray emitter. The levels of interest in this object motivated a further reanalysis of the archival dataset here with the aim of improving the significance of the detected signal and refining the estimated flux levels of this TeV source for the epoch 1989/1990. This chapter details the methods used in this attempt at increasing the signal to noise ratio, details the determination of the differential and integral flux values and presents the results obtained.

7.2 Observations

During the 1988-1990 epoch, observations of Cygnus X-3 were carried out in the *ON/OFF* mode. However there were slight differences in the length of the observation runs as well differences in the PMT camera configuration to that of the camera configuration used for the analysis described in Chapter 5. For observations of this source a right ascension position that is more distant than normal, is required for a suitable dark region of sky for the *OFF* run and thus avoid a bright region of sky. Subsequently, due to the extended right ascension position, the length of the observations is altered. In this case the *ON/OFF* mode tracked the object for 38 minutes (the *ON* run), then over the next 2 minutes the telescope was slewed to a position 40 minutes later in right ascension and this “dark” region of the sky was tracked for 38 minutes (the *OFF* run).

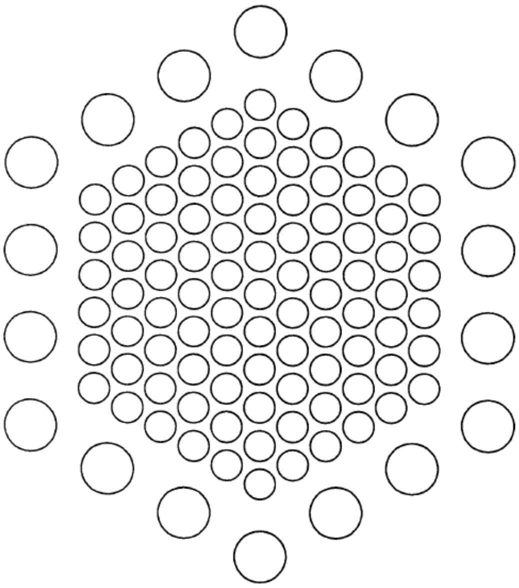

Figure 7.1: A schematic of the arrangement of the older 109 pixel Whipple 10 m camera with a total field of view of 3.5°.

Year	1989	1990
Mode	ON/OFF	ON/OFF
No. of Pairs	43	40
Duration	26.8 hours	23.5 hours
Total Duration ON-source		50.4 hours

Table 7.1: Breakdown of the dataset of TeV 2032+4130 used in this work.

In relation to the PMT camera, the 1989/1990 Whipple 10 m camera configuration was significantly different to the set up as described in Chapter 3. The system used at the time consisted of an array of 109 photomultiplier tubes in the focal plane. This older array consisted of ninety one 2.9 cm PMTs in a hexagonal matrix surrounded by an outer ring of eighteen 5 cm

PMTs resulting in a field of view of 3.5°. Figure 7.1 shows a schematic of this camera arrangement. The camera triggered when two of the inner 91 tubes exceeded a threshold of 40 digital counts in a 10 ns interval and the recorded analogue signal in each pixel was then amplified and then converted to a digital signal (Cawley et al., 1990). The conversion factor for each digital count to photoelectrons was one digital count to 1.15 photoelectrons. During this period the data were originally recorded to 1/2 inch reel to reel tape and then archived on digital audio tapes. A small amount of the original dataset was corrupted and could not be recovered. Fortunately the remainder of the dataset was available for reanalysis (see Table 7.1). Figure 7.2 shows the

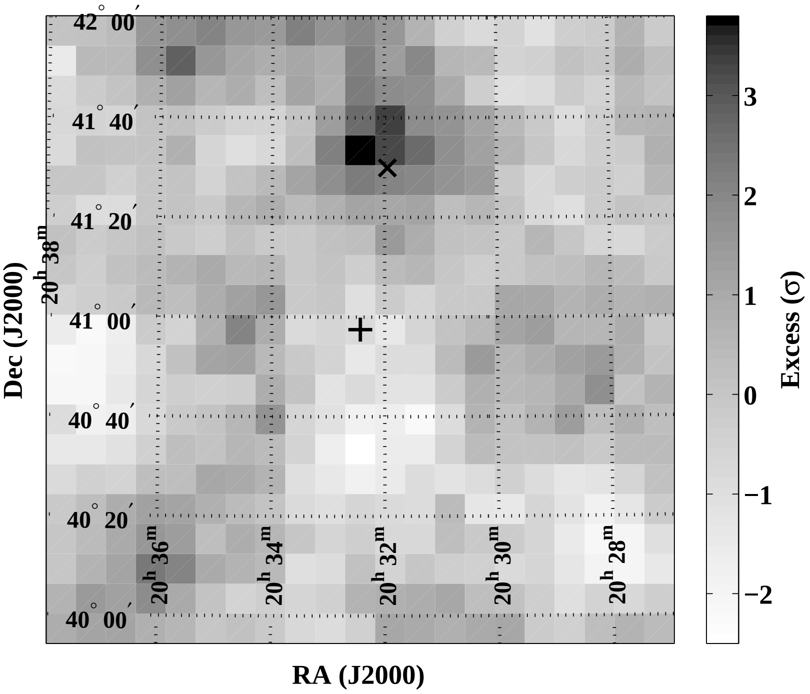

Figure 7.2: Sky map of the Cygnus X-3 region of sky showing the peak in significance at the HEGRA position (marked with an ×) of TeV J2032+4130. Cygnus is at the centre of the sky map and is marked with a +. Taken from Lang et al. (2004)

results of the two-dimensional analysis of the entire field of view of the 109 PMT camera data conducted by Lang et al. in 2004. As shown there is an excess of events, confirming the presence of a weak TeV emitter, at the reported location of the HEGRA unidentified source. Note here that there is no indication of an excess of events from the centre of the field of view, *i.e.*, the position of Cygnus X-3.

The remainder of the work for this Ph.D project attempted three separate methods to optimise the significance of the detected signal and extract the maximum number of γ-rays from the archived dataset. A further goal was the determination of refined differential and integral flux values from this archival Cygnus dataset. The three analysis methods are listed here.

- Optimisation of *Supercuts*.
- Optimisation of energy-dependent cuts.
- *Kernel* Analysis.

7.3 *Supercuts* Optimisation

7.3.1 Background

Normally, for each version of the Whipple PMT-camera, *Supercuts* are optimised to give the maximum γ-ray significance on a dataset from the Crab Nebula and then tested on a subset of similar Crab data and other confirmed TeV sources. The cut optimisation process carried out in this study was a standard optimisation of an offset[1] dataset from the Crab Nebula that was divided in two in order to provide two datasets. One set was used for

---

[1] An offset source is one which the dominant γ-ray signal is not at the centre of the field of view of the telescope

***Supercuts* selection criteria**
$0.0730° <$ *Width* $< 0.15°$
$0.16° <$ *Length* $< 0.30°$
$0.51° <$ *Distance* $< 1.1°$
$0° <$ *Alpha* $< 15°$
Trigger: 2 PMTs > 40 digital counts

Table 7.2: Original *Supercuts* selection criteria used to analyse the Cygnus dataset.

optimisation and the second, or independent, set was used to test the *new* cuts. In 1988-89, a Crab Nebula dataset containing on-axis data was used to optimise the original γ-ray selection cuts (Punch et al. 1991), which led to the definition of the selection process known as *Supercuts*. The use of *Supercuts* led to significant improvements in the sensitivity of the instrument and was subsequently accepted as the standard analysis technique used by the Whipple collaboration (Reynolds et al. 1993).

Over the years, *Supercuts* has undergone many modifications to get to the values listed in Table 3.3, as used with the 379 PMT camera. However, during the period over which the Cygnus data were collected, the *Supercuts* selection criteria were as listed in Table 7.2.

As the original dataset was centered on Cygnus X-3, the source of interest was now off-centre in the field of view. This required the field of view of the camera to be de-rotated by the parallactic angle in order for the orientation of the entire field of view to remain constant. The parallactic angle[2] can be determined using the following equation:

$$\phi = Tan^{-1}\left(\frac{-Cos\ \theta\ Sin\ h}{Sin\ \delta\ Cos\ \theta\ Cos\ h - Cos\ \delta\ Sin\ \theta}\right) \tag{7.1}$$

---

[2] The parallactic angle is defined as the angle of rotation between the sky-coordinate system and the camera coordinate system.

where ϕ is the parallactic angle, θ is the latitude of the Whipple 10 m telescope, δ is the declination coordinates of the source being observed and h is the hour angle of the source. After a two-dimensional analysis of the Cygnus dataset, Lang et al. (2004) reported an excess with a significance of 3.3σ at the reported HEGRA position. At that time no attempt was made to optimise the selection criteria. Fortunately, during the same epoch, a series of off-axis observations were made on the Crab Nebula. During these observations the position of the Crab Nebula was deliberately offset from the centre of the field of view by 1° in order to determine the off-axis efficiency of the telescope. This Crab dataset, like the Cygnus dataset, was archived

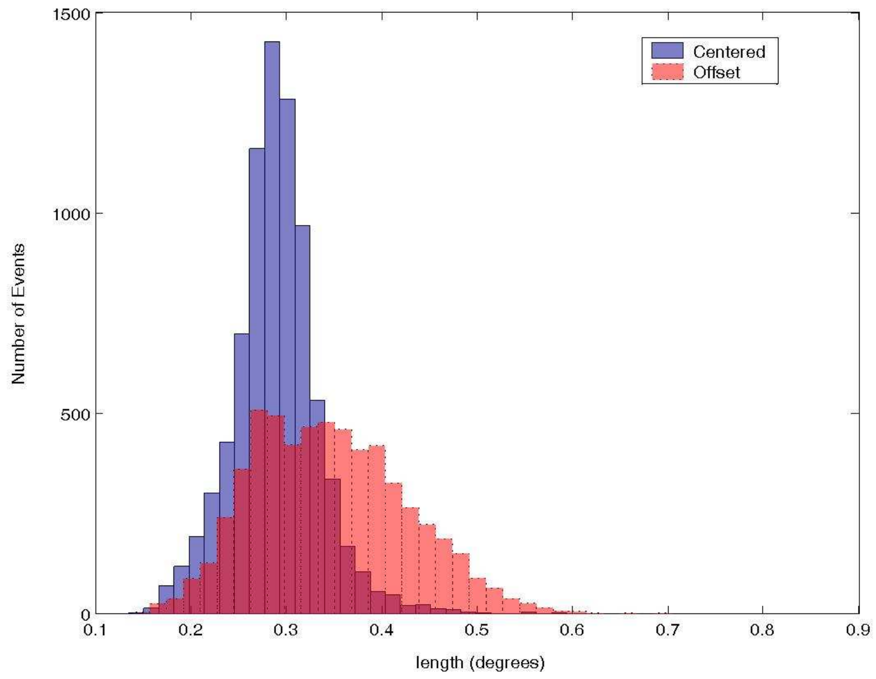

Figure 7.3: Length distribution of 1 TeV simulated γ-rays from a centered source and from a source with a 1° offset position in the field of view.

as binary files on magnetic tapes. The entire 109-pixel camera database was transferred to digital audio tape during the 1990's. It was from these tapes that the archived data were retrieved in 2004. Unfortunately there was only a limited amount of Crab offset data retrievable from the digital audio tapes. In total, 13 pairs (∼ 5 hrs) of 1° offset data were obtained from the archives. Although not an ideal amount of data to attempt a cut optimisation, it was deemed to be a worth-while task as, if successful, it would result in an improvement of the significance of the detection.

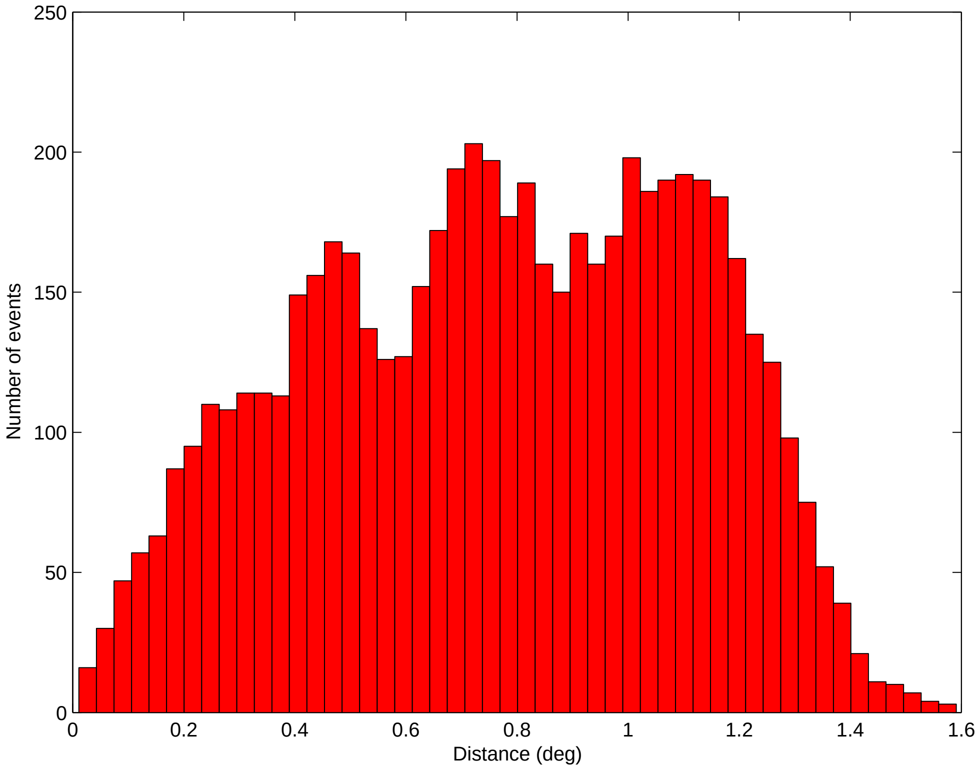

Figure 7.4: *Distance* distributions for a database of 1 TeV simulated γ-rays with a 1° offset position in the field of view.

A further motivation for re-optimisation of *Supercuts* for an offset source was the effect the actual distance of the source, from the centre of the field of view, had on some of the image parameters. In particular *length* values can be ∼ 25% longer for offset sources. Figure 7.3 shows the *length* distributions of simulated 1 TeV showers for an on-axis source and a source offset by 1° from the centre of the field of view. The difference in the *length* distribution for on-axis and offset source can be clearly seen. A similar effect is seen when the *width* parameter distributions are examined. However the effect is not as pronounced as for *length*. The *distance* parameter is also altered with an off-axis source but will be discussed at a later stage.

7.3.2 Optimisation Method and Results

The optimisation method used in this piece of work was the *single parameter variation* method, where a particular parameter is set to an initial starting value and then adjusted over a reasonable range in order to search for the optimum value for that parameter. This initial optimum value is the first best estimate value and then replaces the initial starting value. The procedure is then repeated for each individual parameter. The whole procedure is then repeated to find the next best estimate, which then replaces the previous best estimate. This operation is then continued until each new best estimate value converges on its optimised values.

Upon concluding the optimisation procedure, it was found that the optimum values converged to values close to the original *Supercuts*. However, when these new optimised cuts were applied to the independent dataset a reduction in significance was observed. This suggests that the original cuts were correctly optimised to begin with. The optimisation procedure was carried out initially on data with the signal from the Crab Nebula centred in the field of view. It was then applied to Crab data offset by 1° in the field of view and a final attempt was also made to optimise the cuts using the

Optimised *Supercuts* used in this work
$0.075° <$ *Width* $< 0.16°$
$0.16° <$ *Length* $< 0.31°$
$0.50° <$ *Distance* $< 1.6°$
$0° <$ *Alpha* $< 15°$
Trigger: 2 PMTs $>$ 40 digital counts

Table 7.3: Optimised cuts after optimisation on a small dataset of off-axis Crab Nebula data.

off-axis TeV J2032+4130 dataset.

After an extensive optimisation attempt of the *Supercuts* analysis technique, the results have shown that the parameter cut values converged very close to those used in the original analysis (Table 7.2). This is the case despite the fact that an offset source generally will have elongated *length* values. Since the location of the source in field of view is given by *distance*, and is calculated relative to the putative source location, then for an off-axis source the radial distribution will be asymmetric. The cut values that were found to be optimum on the test dataset of off-axis Crab Nebula data are shown in Table 7.3. Like the centred data, when these optimised cuts were applied to an independent off-axis dataset a reduction in significance was recorded. The significance recorded at the HEGRA position using the *Supercuts* was 2.37σ and using the optimised *Supercuts* was 2.26σ. Tables 7.4 and 7.5 summarise the results of the attempted optimisation of *Supercuts*.

7.4 Energy-Dependent Cuts

As mentioned, looking at Figure 7.3 it appears that the standard *length* cut value is not appropriate for use in off-axis analysis. This is also true for the

Standard *Supercuts* Significance Results

Source	Crab On-axis	Crab Off-axis	TeV J2032
Test data	11.84σ	4.19σ	—
Independent data	10.79σ	3.08σ	—
All data	—	—	3.98σ

Optimised *Supercuts* Significance Results

Source	Crab On-axis	Crab Off-axis	TeV J2032
Test data	12.74σ	4.38σ	—
Independent data	8.37σ	3.07σ	—
All data	—	—	3.89σ

Table 7.4: Summary of significance results obtained using *Supercuts* and the optimisation of *Supercuts* as described in the text.

Standard *Supercuts* Rate Results

Source	Crab On-axis	Crab Off-axis	TeV J2032
Test data	0.85±0.07	0.28±0.06	—
Independent data	0.73±0.07	0.23±0.07	—
All data	—	—	0.08±0.02

Optimised *Supercuts* Rate Results

Source	Crab On-axis	Crab Off-axis	TeV J2032
Test data	0.31±0.07	0.31±0.07	—
Independent data	0.50±0.06	0.22±0.07	—
All data	—	—	0.04±0.02

Table 7.5: Summary of the rate (γ min^{-1}) values obtained using standard *Supercuts* and optimised *Supercuts*.

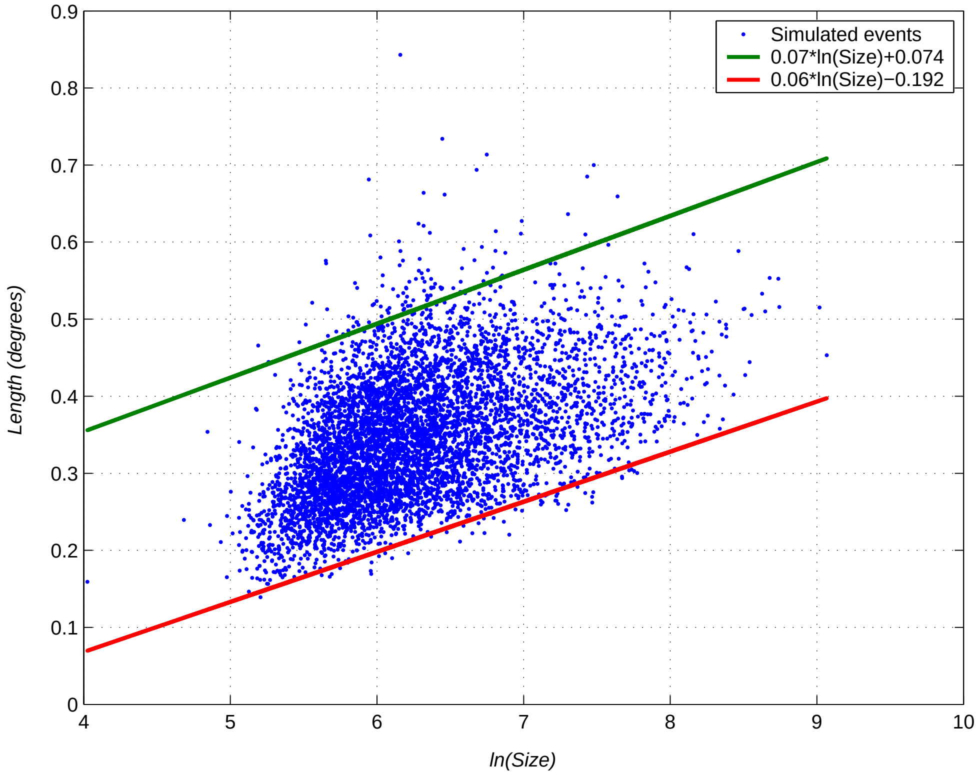

Figure 7.5: *Length* versus ln(*size*) distribution of simulated γ-rays with a 1° offset position in the field of view. The lines are representative of the upper and lower bounds of the energy-dependent cuts applied to the dataset The upper line is given by the equation 0.07ln(*size*)+0.074 and the lower line is 0.06ln(*size*)-0.192.

width parameter, but to a lesser extent. Figure 7.5, which displays the *length* vs ln(*size*) distributions for simulated γ-rays, shows that the *length* of an image appears to be dependent on its *size*. This then led us to investigate what effect applying a set of energy-dependent cuts had on the analysis outcome. With energy-dependent cuts, the actual values of the cuts vary from event to event, depending on the value of their *size* parameter, which in turn is an indication of the actual energy of the primary event.

In order to determine a starting point for values of the energy-dependent

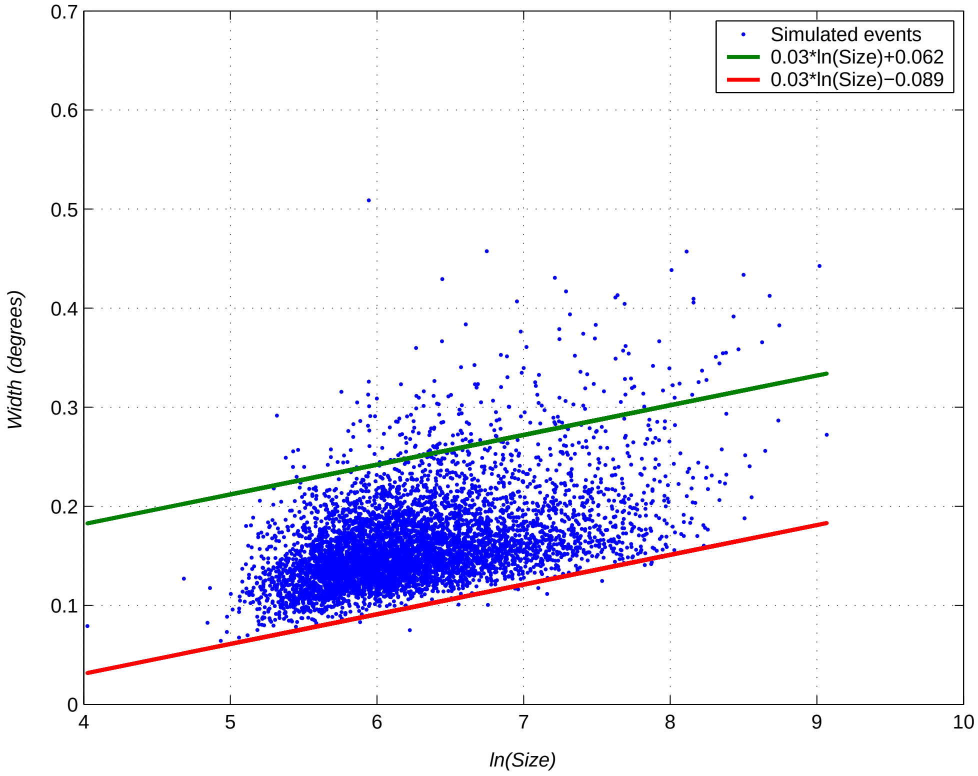

Figure 7.6: *Width* versus ln(*size*) distribution of simulated γ-rays with a 1° offset position in the field of view. The lines are representative of the upper and lower bounds of the energy-dependent cuts applied to the dataset The upper line is given by the equation 0.03ln(*size*)+0.062 and the lower line is 0.03ln(*size*)-0.089.

cuts the *length* vs ln(*size*) distributions were studied to look for any correlations between *length* and *size*. Figure 7.5 shows the *length* vs ln(*size*) distributions for simulated γ-rays and illustrates two straight lines that can be fitted to the data that are representative of the upper and lower cut boundaries. Initially these lines are fitted loosely to the data as starting values for the cut optimisation process. Similar lines are fitted to determine the starting cut values for the *width* parameter which are shown in Figure 7.6.

A major difference between imaging an on-axis source and an off-axis

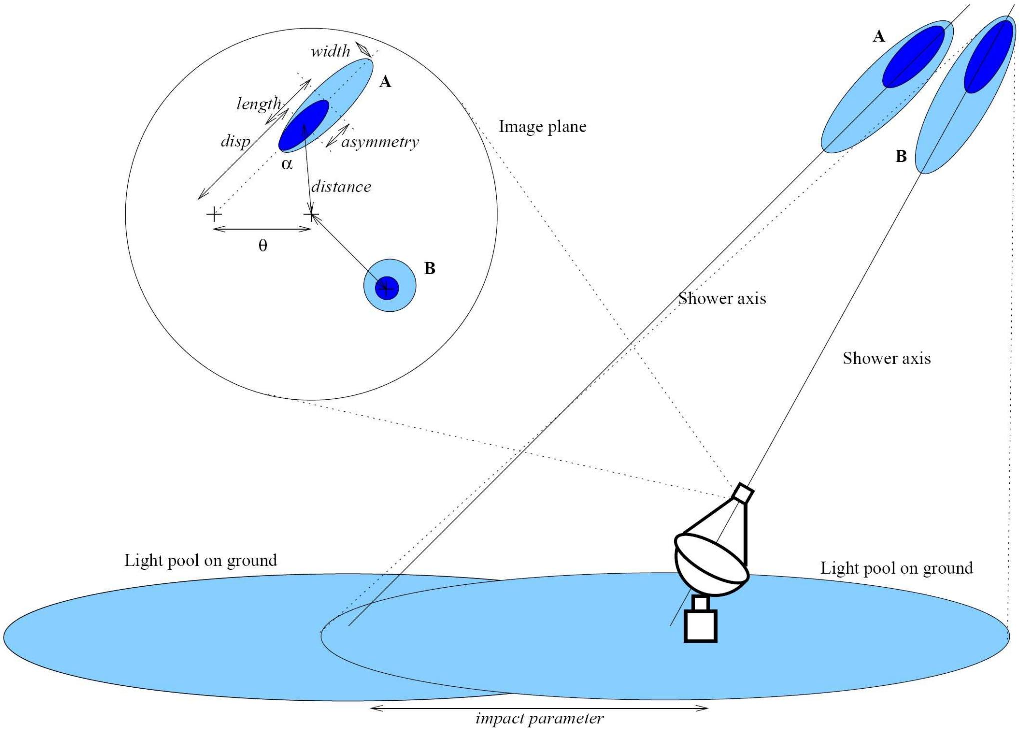

Figure 7.7: A schematic representation of the Cherenkov light produced in an air shower. Also shown are the Hillas parameters including a definition of the *disp* parameter. Taken from Lessard et al. (2001)

source is the effect an off-axis signal has on the *distance* parameter. With an on-axis source, the upper *distance* cut normally eliminates those events that are incident at the edge of the camera as they can be truncated and the lower *distance* cut is used to remove events that are too circular (as imaged by the camera). Thus, if the *distance* cut is not applied, edge events can lead to the analysis software miss-identifying events.

In the case of an off-axis source, naturally the desirable events are much closer to the edge of the camera than those from an on-axis source, hence an alternative parameter to *distance* is preferred. Instead of using the *distance*, the *disp* parameter method was chosen. In their paper describing the *disp* method, Lessard et al. (2001) noted that the elongation of an image can be expressed as the ratio of its angular *width* and *length*. *Disp* is calculated as *disp* = ξ(1 - *Width/Length*) and is shown schematically in Figure 7.7. The ξ parameter is a value determined using simulations or data from a known source of steady TeV emission like the Crab Nebula and can be calculated by:

$$\xi = \frac{Distance}{1 - Width/Length} \tag{7.2}$$

However for an off-axis source the ξ parameter value can span a range of values and in this case it was required to place limiting cut values on the ξ parameter similar to those of the *width* and *length* parameters. Following the methodology used by Walker (2004), the off-axis ξ versus ln(*max1* + *max2*) distributions were determined from simulations for a source with a Crab-like spectrum and are shown in Figure 7.8. The upper and lower cut bounds are shown as lines that are functions of ln(*max1* + *max2*).

Plots similar to Figure 7.8 gave an indication of the starting points of the energy-dependent cut optimisation process. As with the *Supercuts* optimisation, the upper and lower bound of each parameter was individually optimised by changing the y-axis intercept values of the fitted lines. Figures 7.5, 7.6 and 7.8 show the fitted lines that represent the final cuts of each of the three parameters shown. As this optimisation process was for use with off-axis data, only the small Crab Nebula off-axis dataset was used in the attempted optimisation. As with the *Supercuts* optimisation attempt, the dataset was again split in two in order to provide an independent dataset to test the optimised cuts with.

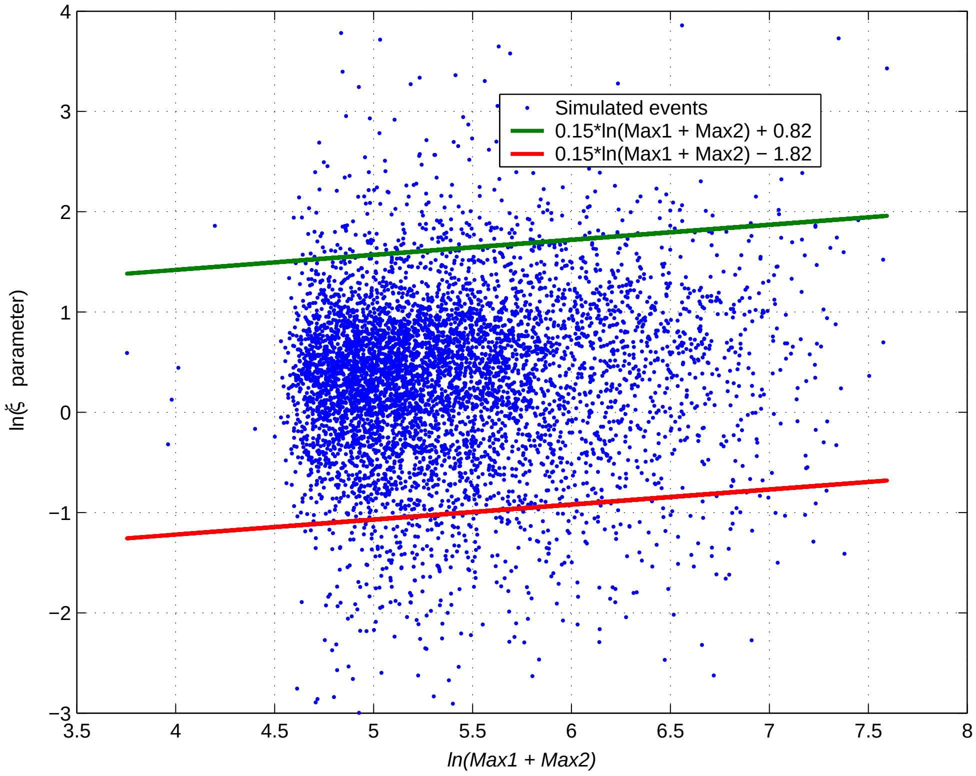

Figure 7.8: ln(ξ parameter) versus ln($max1$ + $max2$) distribution of simulated γ-rays with a 1° offset position in the field of view. The upper line is given by the equation 0.15ln($max1$ + $max2$)+0.82 and the lower line is 0.15ln($max1$ + $max2$)-1.82.

7.4.1 Energy-Dependent Cuts Results

Using the distribution of parameter values of simulated γ-rays as a guide to the starting points of the energy-dependent cut values, a series of new optimised cut values was derived that initially showed an increase in significance in the test dataset. However, after the application of these optimised cuts on the independent dataset, no significant improvement in the very high energy signal was detected. The optimised energy dependent cuts derived are listed below.

- *width* lower: $0.03 \times \ln(size)$ - 0.089
- *width* upper: $0.03 \times \ln(size) + 0.062$
- *length* lower: $0.06 \times \ln(size)$ - 0.192
- *length* upper: $0.07 \times \ln(size) + 0.074$
- *disp* lower: $0.15 \times \ln(max1 + max2)$ - 0.82
- *disp* upper: $0.15 \times \ln(max1 + max2) + 1.82$
- *alpha* $< 15°$

The maximum significance obtained from the test dataset was 4.77σ using the cut values listed above. Using the standard *Supercuts* on the same reduced dataset, a significance of 4.19σ is found. This is represents an increase of 14% over the values obtained from *Supercuts*. When these cut values were applied applied to the independent dataset a reduction of 21% was returned. Also, when the optimised cuts were applied to the Cygnus dataset, a reduction in significance of 22% was observed. The results obtained from the energy-dependent analysis are summarised in Table 7.6 and Table 7.7.

A possible explanation for the lack of success in the optimisation process of both *Supercuts* and the energy-dependent cuts, could be due to the small size of the Crab Nebula offset dataset. Due to this, the results quoted above may be normal statistical fluctuations. To carry out an accurate optimisation requires a reasonable amount of data with a reasonable signal and a dataset of similar quality for use as an independent dataset. In other words the cuts tend to lose generality when tested with small datasets. The off-axis Crab Nebula dataset available for this work contained only 13 pairs of data with a total of 290 minutes of data available to attempt an optimisation. This

Energy-Dependent cuts Significance Results

Source	Crab On-axis	Crab Off-axis	TeV J2032
Test data	9.28σ	4.77σ	—–
Independent data	9.96σ	2.41σ	—–
All data	—–	—–	3.09σ

Table 7.6: Summary of significance results obtained using the energy-dependent cuts technique described in this work.

Energy-Dependent cuts Rate Results

Source	Crab On-axis	Crab Off-axis	TeV J2032
Test data	0.63±0.07	0.46±0.09	—–
Independent data	0.61±0.06	0.31±0.11	—–
All data	—–	—–	0.05±0.02

Table 7.7: Summary of the rate (γ min^{-1}) values obtained using standard *Supercuts*.

resulted in a test dataset of only 7 pairs and an independent dataset of only 6 pairs.

7.4.2 Gamma-Ray Simulations

The remainder of this project involved the reanalysis of TeV J2032+4130 using the *Kernel* analysis technique. A requirement of the *Kernel* technique is a database of accurate γ-ray simulations. Simulations were previously used to illustrate the distribution of Hillas parameters with respect to energy, and provided starting cut values while attempting the optimisation of the energy-dependent cuts. However, since γ-ray simulations are an integral part of the *Kernel* analysis procedure, the generation of the simulated γ-ray database that was representative of the 1989/1990 Whipple camera was of crucial importance and is described here.

The Monte Carlo simulations used in this work were generated by the GrISU (Grinnell - Iowa State University) simulations package (Duke & LeBohec, 2006). The GrISU package was developed to produce simulations for use with the VERITAS experiment and can be separated into three sections; extensive air shower simulation, Cherenkov emission simulation and the simulation of the detector in question. The extensive air shower simulation generation is carried out by a modified version of the *Kascade* extensive air shower simulation software developed by Kertzman & Sembroski (1994).

Kascade uses a model of the atmosphere, follows each particle of the extensive air shower until it reaches ground level, and builds a three dimensional map of every particle's trajectory. The next stage of the simulations process sees the *Cherenkf* software use the three dimensional map, generated by *Kascade*, to simulate Cherenkov emission from each particle as it passes through the model atmosphere until it interacts, decays, or reaches ground level. The final part of the simulations package models the detection of the Cherenkov radiation by the Whipple 10 m telescope (or the VERITAS array depending on the configuration file[3] used). The software used in this instance is the *GrISUDet* program. At this point each Cherenkov photon is traced as it is reflected off the mirror facets and on to the PMT camera. *GrISUDet* then models the charge pulses produced by the PMTs and associated electronics. As the package was developed for the VERITAS experiment, the detector simulation section of the package is geared towards simulating the response of the VERITAS detectors and the later configurations of the Whipple camera, *i.e.* the 379 PMT configuration used from 2003 to the present.

Since the TeV J2032+4130 dataset was obtained during 1989-1990, when

---

[3] Configuration files contain information relevant to the instrument whose response is being simulated *e.g.* no. of PMTs, PMT gains, PMT locations *etc.*

Technical information required to accurately simulate the response of the 109 PMT Whipple camera to simulated EAS
PMT threshold in mV
PMT current gain
Minimum number of channels to trigger the camera
Equivalent system impedance
Quantum efficiency curve (QE as a function of wavelength)
Mirror reflectivity curve (Reflectivity as a function of wavelength)
X, Y coordinates of each pixel in the focal plane of camera
Each PMT radius
No. of PMTs surrounding each individual PMT (Nearest neighbours)
A list of Each PMTs nearest neighbours ID number
Mirror reflectivity degradation factor

Table 7.8: Summary of the technical information required for the modification of the 379 PMT camera to the 109 PMT camera.

the 109 PMT Whipple camera had very different characteristics, there was no configuration file available for the 109 PMT camera. Because of this, some effort was made to modify the configuration file of the 379 PMT camera to produce a configuration file for the 109 PMT camera by piecing together specific technical information from various areas.

7.4.3 Simulations for off-axis sensitivity of the 109 PMT Whipple Camera

The GrISU simulations package has several user-changeable *pilot* files that can be used with or without modification if so desired. Each *pilot* file contains the input parameters for each different section of the simulation process. For example, the *pilot* file for *Kascade* contains details on how many showers to create, the energy range to be used, the type of particle, *etc.* The *pilot* file for *GrISUDet* tells the software which detector configuration file to use while simulating the detector response. It also contains information regarding where the simulated source is in the field of view, the number of pedestal events to record and the noise characteristics of the field of view. Most of these variables are quite straight-forward to adjust and generally the detector configuration file is chosen from a database of files and depends on which generation of telescope is under study.

109 PMT Configuration File

As this work required the first application of GrISU simulations package relative to the 109 camera, a suitable PMT configuration file was required in order to generate an accurate database of simulations for use with the *Kernel* analysis software. Camera configuration files contain details, amongst an abundance of other information, regarding PMT thresholds, PMT gain, mirror reflectivities, pixel size, spacing and position. Table 7.8 lists the technical specifics required to generate a suitable camera configuration file to simulate the response of the 109 PMT camera. Most of the information regarding pixel positions, nearest neighbours, quantum efficiency and size, *etc.*, were obtained from files associated with the older ISU simulations software (Duke, 2005)(Kildea, 2005)(Sembroski, 2005).

Along with these details there were several other important elements to be gathered. Of crucial importance were details regarding the performance of the electronics components associated with the 109 PMT camera, *i.e.* the PMT triggering thresholds, the system impedance and the PMT current gain. Of these, the triggering threshold was determined by looking at archived observer log sheets and old bias curves and was estimated at 83 mV. The equivalent system impedance[4] was taken to be 152 Ω. This value was taken from a modified configuration file for the 1995 camera set as supplied by (Schroedter, 2005) and was based on camera measurements taken in 1994.

Since the queued analogue to digital converters (QADCs) were the same in the 109 camera, the QADC input impedance and the QADC conversion factor were taken to be the same as that for the 1995 camera, *i.e.* 50 Ω and 0.25 respectively. The gain in e^- per photoelectron (pe) for the 109 PMT camera was found to be 0.59×10^6 and was derived from the dc/pe (digital counts per photoelectron) ratio of 1.15 as reported in Hillas et al. (1998) using Equation 7.3.

$$dc/pe = \frac{Charge\ in\ pC \times System\ Impedance}{QADC\ impedance \times QADC\ conversion\ factor} \tag{7.3}$$

There were also further modifications to be made to ensure the database of γ-ray simulations were an accurate representation of real γ-rays . The simulated night sky noise was set so it matched the observed night sky pedestal variations (Section 3.3.4) as seen in the data. A good match was found with simulated noise levels set at 380 photoelectrons $\mathrm{ns^{-1}m^{-2}str^{-1}}$ in the simulation pilot files resulting in a matching of the average pedvar values of ~ 3.14 digital counts.

In addition, the mirror degradation factor was adjusted so it matched the event size threshold as seen in Figure 7.9. Degradation in mirror reflectivity can help explain a high energy threshold as well as a decline in statistical significance (Reynolds et al., 1993). The optimum value for the reflectivity degradation factor, that gave a good match to the real data with the *size* distribution, was 0.54. This low degradation factor can be supported by ob-

---

[4] Conversion factor in ohm between amps on the output of the PMT voltages on the analogue signal processors.

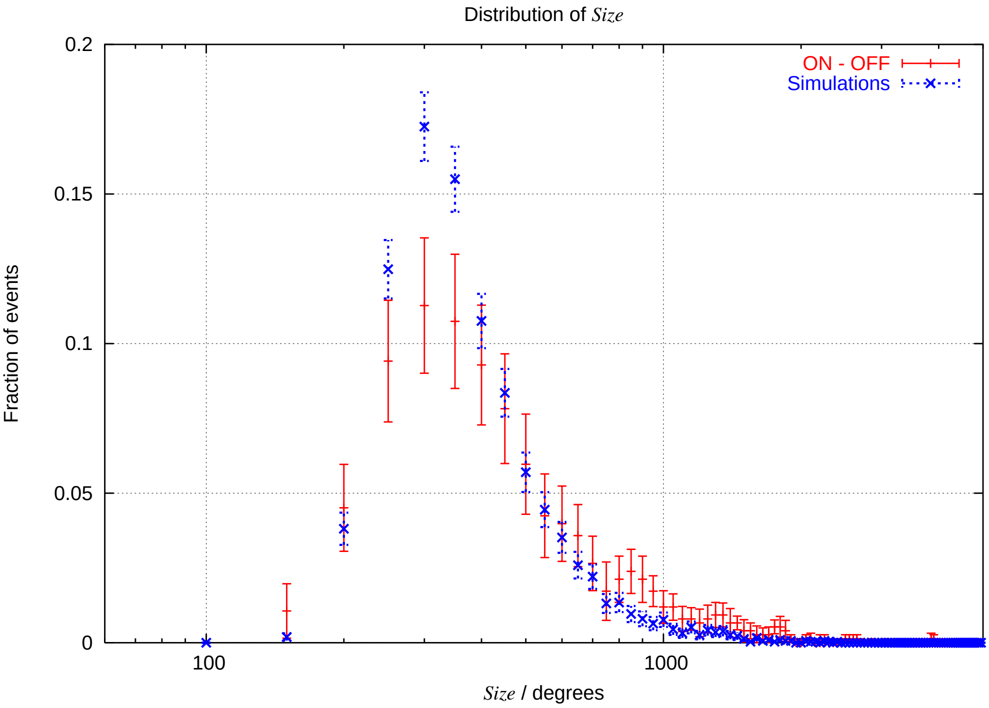

Figure 7.9: *Size* distributions of real and simulated events showing the matching peak number of events in the corresponding *size* bin after the reflectivity degradation factor in the simulations package has been changed to 0.54.

served reflectivity degradation at that epoch. Prior to these observations, the mirror facets were last re-coated in 1988. Hence, it is reasonable to assume that, after extended exposure to harsh weather conditions, the mirrors' ability to reflect faint flashes of Cherenkov light would be diminished. Further evidence that supports the reduced reflectivity factor comes in the form of a drop in the Crab Nebula γ-ray rate over that time period (Lang et al., 1991). In their work, the authors reported γ-ray rates of 272.9 γ min^{-1} for the epoch 1988 to 1989, 227.5 γ min^{-1} for the epoch 1989 to 1990 and 174.0 γ min^{-1} for the epoch 1990 to 1991.

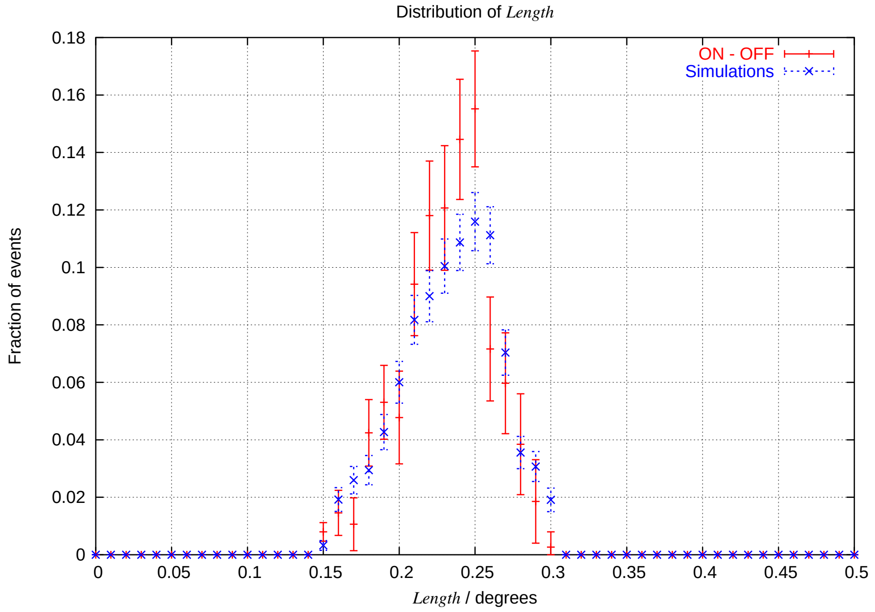

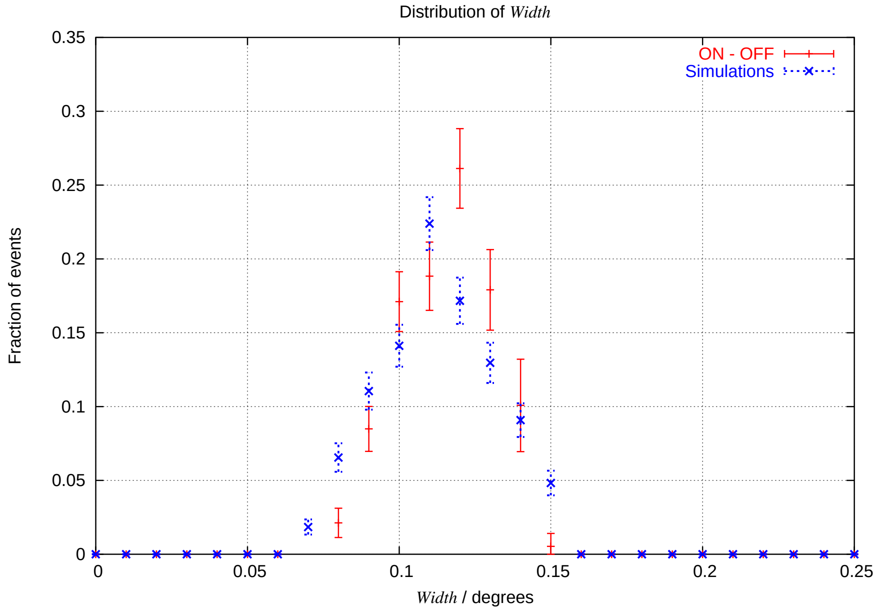

7.10: *Length* distributions (top) and *width* distributions (bottom) of real and simulated events showing the matching peak number of events in the corresponding *length* and *width* bins after the reflectivity degradation factor in the simulations package has been changed to 0.54.

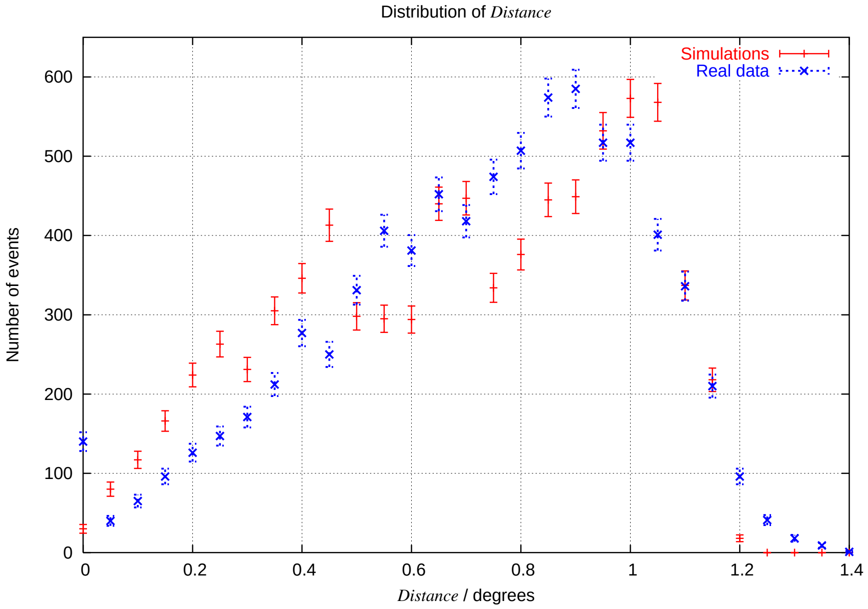

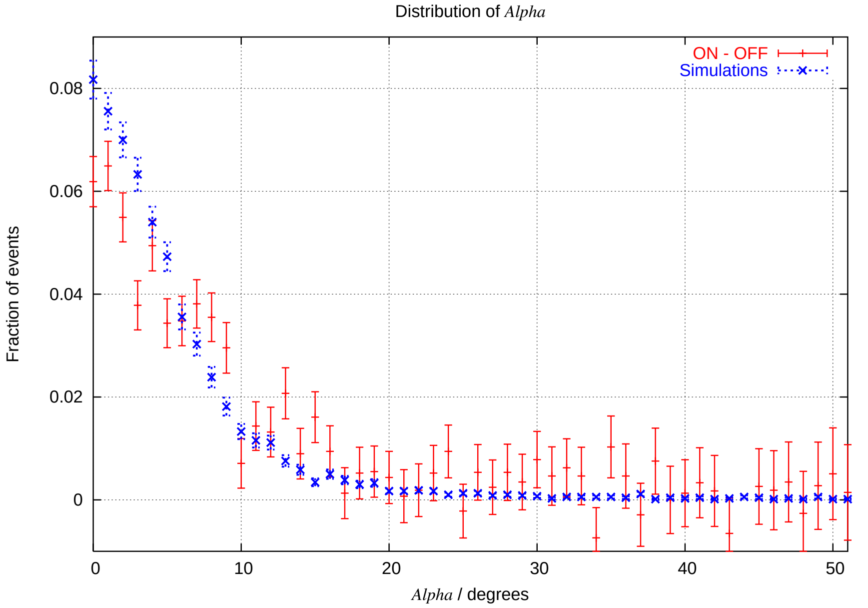

7.11: *Distance* distributions (top) and *alpha* distributions (bottom) distributions of real and simulated events showing a good match between real and simulated events after the reflectivity degradation factor in the simulations package has been changed to 0.54.

The parameter distributions are shown in Figure 7.10 and 7.11. Note that *Supercuts* were applied to both real events and the simulated γ-rays. Additional evidence that suggests a high confidence in the quality of the simulations can be seen by looking at Figure 7.12, which shows the distribution of the energy of the events. If the threshold value is estimated as the energy at which the number of triggered events reaches one half its maximum value then this suggests an energy threshold of $\sim$ 450 GeV. This compares well to the known energy threshold of the 1989/1990 Whipple camera configuration of 400 to 500 GeV (Reynolds et al., 1993)(Hillas et al., 1998).

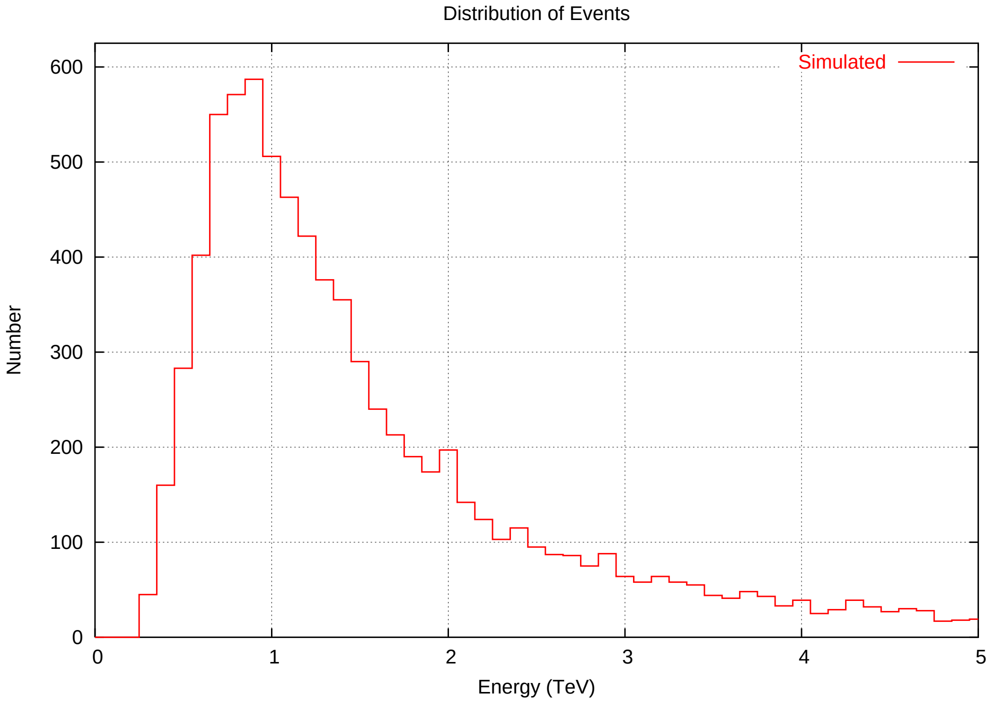

Figure 7.12: Energy distributions of the simulated events showing the number of triggered events peaking at an energy of $\sim$ 900 GeV.

7.5 The ***Kernel*** Analysis Method

Since the optimisation of the parameter cut values did not lead to an enhanced signal, the alternative analysis method known as *Kernel* analysis was employed. The *Kernel* analysis procedure has been discussed in detail in Chapter 3. This section will continue the discussion with respect to the results of the application of this alternative approach to the analysis of the archival TeV J2032+4130 data. Figure 7.13 summarises the main steps involved in the *Kernel* analysis procedure.

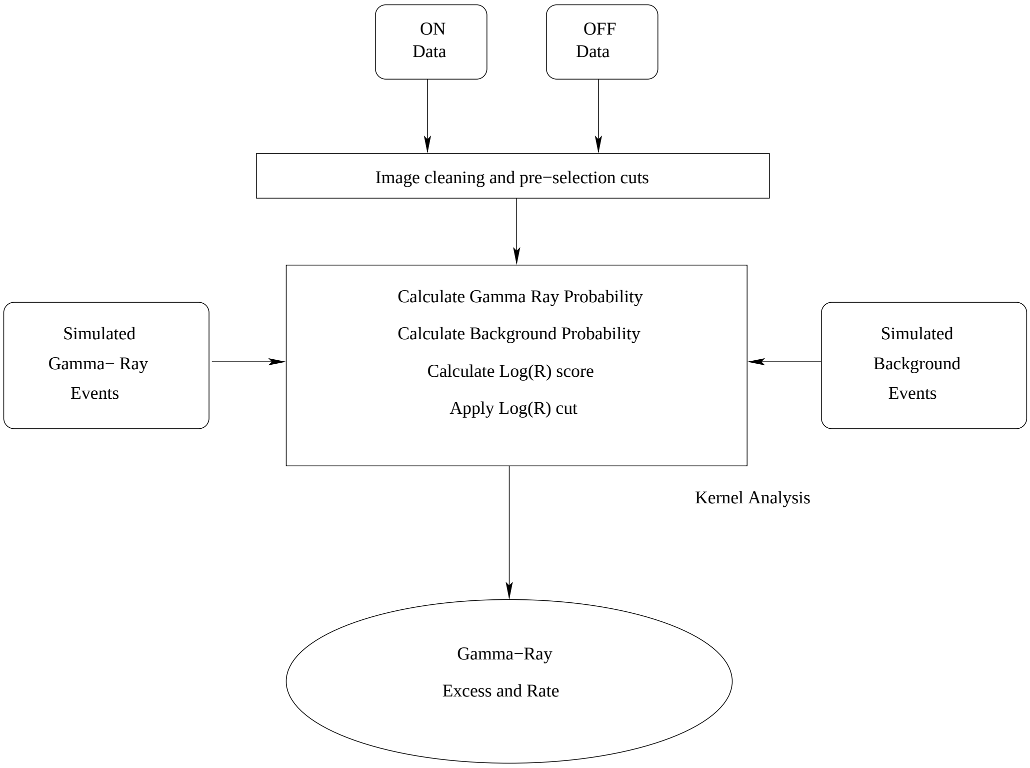

Figure 7.13: The *Kernel* analysis procedure for *ON/OFF* data.

7.6 Kernel Results

The *Kernel* analysis technique was originally developed using Whipple data that had been analysed with other techniques including *Supercuts* and neural networks in order to compare the different techniques. Since its development, the *Kernel* technique has been used in several studies (Dunlea et al., 2001; Kildea, 2002) as an established analysis technique to extract the maximum number of γ-rays from a given dataset resulting in an optimum signal to noise ratio. The *Kernel* analysis carried undertaken in this Ph.D followed the established techniques of the *Kernel* analysis procedures.

7.6.1 Pre-Selection

As every event is compared with every γ-ray simulation and with every background event, the *Kernel* process can be a computationally intensive procedure. In an attempt to reduce the *Kernel* analysis time, a method of pre-selecting events was carried out as part of this work. The pre-selection method has been investigated previously by Dunlea (2001). By using the pre-selection technique, many background events can be rejected by applying a set of loose parameter cuts on the data prior to the actual *Kernel* analysis. By doing this, the process can be performed with a noticeable reduction in analysis time.

7.6.2 Kernel Cut Optimisation

Unlike the *Supercuts* analysis, where each of the main image parameters is optimised in turn, the *Kernel* technique effectively merges the five main Hillas parameters (*length, width, distance, size* and *alpha*) into a single $\log(R)$ score where $R = f_\gamma/f_b$ with f_γ being the likelihood that the event is γ-ray initiated and f_b is the likelihood that is a background event (See Section 3.4.3). This essentially means only one parameter is required to be optimised. In this work the $\log(R)$ parameter was initially optimised using the archival database of on-axis and off-axis 1989/1990 Crab Nebula data. As with *Supercuts* optimisation, the *Kernel* $\log(R)$ cut was optimised by looking for the maximum obtainable significance from the dataset. Figure 7.14 is a plot of the off-axis Crab Nebula excess γ-ray significance against $\log(R)$.

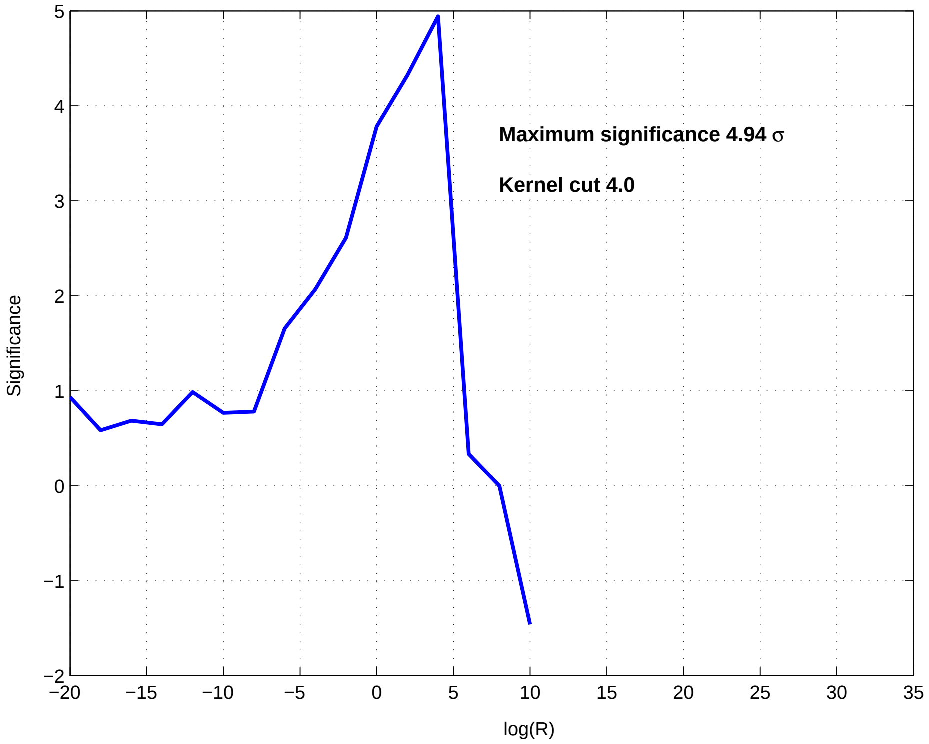

Figure 7.14: Optimisation of the *Kernel* cut on off-axis Crab Nebula data yielded a maximum significance of 4.94σ with a *Kernel* cut of 4.0

The peak in this plot of significance versus $\log(R)$ is the value taken as the $\log(R)$ score which gives the optimum signal to noise ratio. From this figure, a value of 4.0 for $\log(R)$ (the *Kernel* cut) returns a significance of 4.94 σ for

Kernel analysis Significance Results

Source	Crab On-axis	Crab Off-axis	TeV J2032
Test data	10.75σ	3.74σ	—
Independent data	11.14σ	3.21σ	—
All data	—	—	2.43σ

Table 7.9: Summary of significance results obtained using the *Kernel* analysis technique.

the off-axis dataset of Crab Nebula data. When the technique is applied to the on-axis data, the peak value of $\log(R)$ is also found to be 4.0 and returns a maximum significance of 14.31 σ. When the technique is applied to the TeV J2032+4130 dataset a reduction in significance of 27% (compared to the value returned by standard *Supercuts*) is reported. Unfortunately these significance values do not represent an improvement in the detected signal over the original *Supercuts* analysis results or the *energy-dependent* cuts as attempted in this work. This is possibly due to the fact that the *Kernel* technique does not always perform well when applied to a dataset containing a weak γ-ray signal, as it has a tendency to reject small events (Moriarty et al., 1997). In addition to containing a weak signal, the source is also offset from the centre of the field of view, which may also affect the effectiveness of the *Kernel* analysis technique. Tables 7.9 and 7.10 provide a summary of the significance and rate results after application of the *Kernel* analysis technique. The results from the HEGRA position, using the various analysis methods described here, returned, on average, a reduction in significance of 39% when compared to the value returned by *Supercuts*.

Kernel Analysis Rate Results

Source	Crab On-axis	Crab Off-axis	TeV J2032
Test data	0.63±0.06	0.31±0.10	—
Independent data	0.67±0.06	0.21±0.10	—
All data	—	—	0.04±0.02

Table 7.10: Summary of the rate (γ min^{-1}) values obtained using the *Kernel* analysis technique.

7.7 Energy Threshold and Flux Calculation

As already stated in Section 7.4.3, Figure 7.12 suggested an energy threshold of $\sim$ 450 GeV. This value can be regarded as an estimate. For a more formal calculation of the energy threshold of the imaging atmospheric Cherenkov telescope, the collection area of the detector must be calculated first. The collection area gives a clearer indication of the performance and efficiency of the imaging atmospheric Cherenkov telescope at a given energy.

Collection area is calculated using the simulated γ-rays that fell randomly over the area A_o [5]. A_o is chosen to be large enough to contain all triggering events. (It is assumed that events outside A_o never trigger the camera). The number of events that trigger the camera (located at the centre of A_o) and pass analysis are recorded, as are the total number of simulated γ-rays generated. The collection area is defined as:

$$A(E) = A_o \left(\frac{No.\ of\ simulated\ gammas\ triggering\ at\ energy\ E}{No.\ of\ simulated\ gammas\ at\ energy\ E} \right) \tag{7.4}$$

The collection area is representative of the area over which Cherenkov events trigger the telescope and is much larger than the physical dimensions of

---

[5] $A_o = \pi(250\text{m})^2$ and 250m is the impact radius or the distance between the shower axis and the instrument. Also known as the impact parameter.

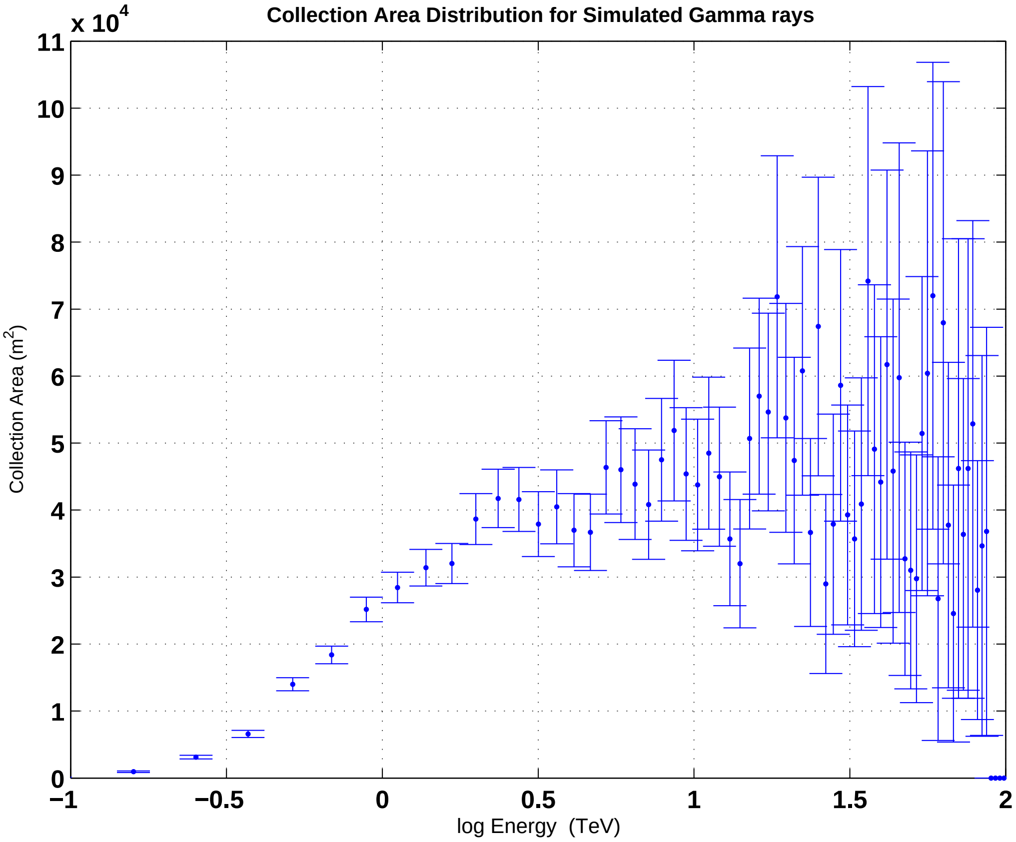

Figure 7.15: Collection area for γ-ray simulations generated for the 1989/1990 camera configuration.

the telescope. Figure 7.15 illustrates collection area curve as a function of energy. From this plot a collection area of $\sim 55 \times 10^3$ m^2 is found. This value compares favorably with the curve previously derived in Krennrich et al. (2001) and Kildea (2002). For the collection area to be useful for more than just investigating the sensitivity of the telescope to γ-rays of different energies, *i.e.* to provide information regarding the response of the detector to a given source, the collection area is convolved with the particular energy spectrum of the source being observed (Kertzman & Sembroski, 1994). This

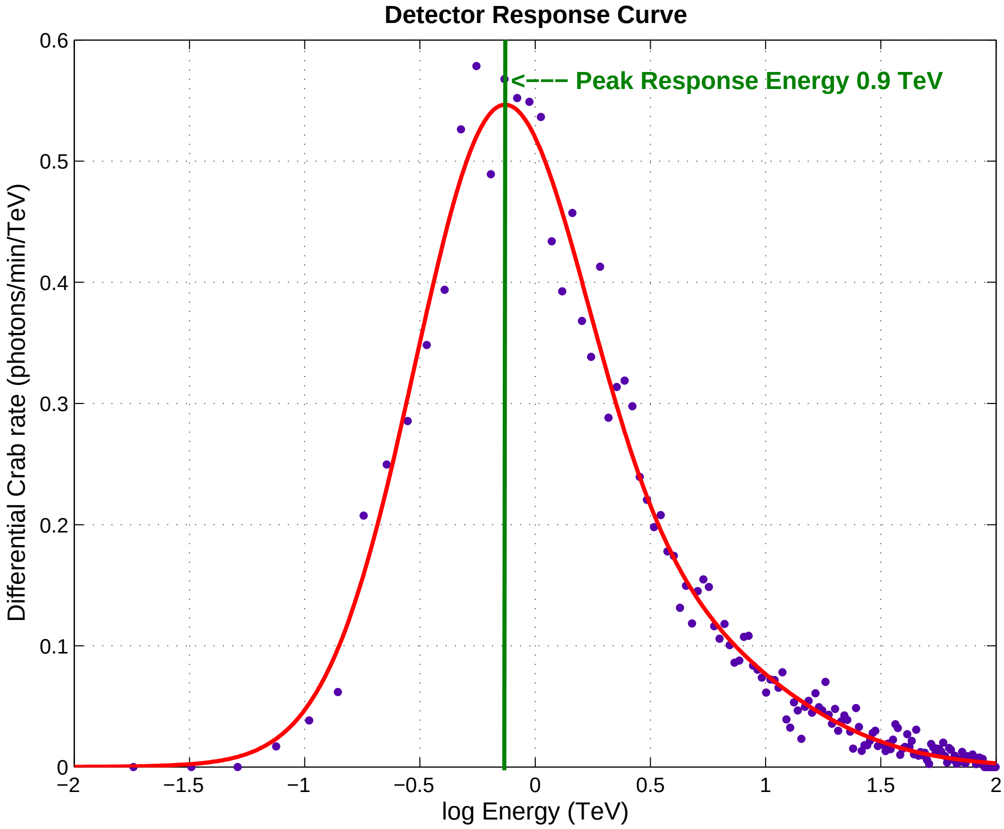

Figure 7.16: Differential response curve derived using simulations describing the response of the Whipple 10 m telescope to a source with a Crab Nebula like spectrum. The peak response energy is found to occur at approximately 900 GeV.

results in the production of a differential response curve and is defined as:

$$\frac{dr}{dE} = A(E).N_o.E^{-\alpha} \tag{7.5}$$

where r is the γ-ray rate, N_o is the flux constant and α is the differential spectral index. The differential response curve provides a measure of the true sensitivity of the telescope to γ-rays from the source under investigation. Figure 7.16 shows the differential response curve for the *Kernel* analysis, fitted with a two-term Gaussian distribution curve, and was obtained using the differential spectrum of the Crab Nebula: ($3.20 \times 10^{-7} \times (\mathrm{E}/1\ \mathrm{TeV})^{-2.49}$ $\mathrm{m}^{-2}\mathrm{s}^{-1}\mathrm{TeV}^{-1}$) taken from Hillas et al. (1998).

The peak position on the differential response curve is representative of the instrument's peak response energy. The peak response energy for an on-axis Crab Nebula signal, as shown in Figure 7.16, occurs at 900 GeV and compares well to the previous estimate (Section 7.4.3) and to measurements taken when the 109 PMT camera was in operation. The peak response energy for an off-axis Crab Nebula signal was found to be $\sim$ 1 TeV. The differential response curve can also be used to provide an accurate measurement of the energy threshold of the instrument, however the method used to determine this value must be defined. Kertzman & Sembroski (1994) quote three different definitions for energy threshold and emphasise the importance of reporting which method was used to determine the energy threshold. The three methods are

- The maximum in the differential response curve.
- The energy at which the differential response curve reaches one half its maximum value.
- The energy such that the integral of the differential response curve is 95% of the total rate.

For the work carried out in this project, the energy threshold of the detector is defined as the energy at which the differential response curve reaches one half its maximum value. This corresponds to a threshold energy of $\sim$ 480 GeV for on-axis Crab Nebula data and to $\sim$ 620 GeV for off-axis Crab Nebula data. Again these values compare well to previous values quoted of energy threshold of the Whipple 10 m telescope configured with the 109 PMT camera (Reynolds et al., 1993; Hillas et al., 1998).

The differential response curve defined in Equation 7.5 can also be expressed as:

$$\frac{dr}{dE} = A_o.R(E).N(E) \tag{7.6}$$

where *N(E)* is the source spectrum and *R(E)* is the fraction of events triggering the camera at energy E. The source spectrum, *N(E)* is defined as:

$$N(E) = N_o.E^{-\alpha} \tag{7.7}$$

When the area under the differential response curve is integrated, it returns the number of γ-ray events per unit time: $\mathrm{N}_\gamma/\mathrm{T}$ *i.e.* the rate of γ-ray detection from the source under investigation. Equation 7.8 defines this relationship:

$$\int_0^\infty A_o.R(E).N(E)\ dE = \frac{N_\gamma}{T} \tag{7.8}$$

Equation 7.8 can be expanded and rewritten as:

$$A_o.N_o \int_0^\infty R(E).E^{-\alpha}\ dE = \frac{N_\gamma}{T} \tag{7.9}$$

Since the measured significance of the γ-ray signal from the off-axis database of TeV J2032+4130 is not high enough to determine the spectral index, *a priori* knowledge regarding the source's γ-ray spectrum was assumed. Equation 7.9 can be rearranged to provide a means of calculating the differential flux and hence the integral flux of the source being studied

$$N_o = \frac{N_\gamma}{T.A_o \int_0^\infty R(E).E^{-\alpha}\ dE} \tag{7.10}$$

The implication of Equation 7.10 is that the only required input to return a value for the differential flux is the spectral index α. By using this technique the differential flux of the Crab Nebula was calculated to be (3.4 ±0.2 ±0.2) × 10^{-7} × (E/1 TeV)$^{-2.49}$ m^{-2}s^{-1}TeV^{-1} which yields an integral flux of (2.3 ±0.2 ±0.3) × 10^{-7} m^{-2}s^{-1} above 1 TeV. The first uncertainty represents the statistical uncertainties in the calculation and was obtained using knowledge of the reported significance of the source and the reported flux values. The second uncertainty represents the systematic uncertainties in the flux and was obtained by combining the percent uncertainties on the spectral index of the source and the percent uncertainties on *R(E)*. It was found that the systematic uncertainties were dominated by the uncertainties in the spectral index. When the same approach is applied to simulations from an offset source with a Crab-like spectrum, a differential flux of (3.0 ±0.6 ±0.3) × 10^{-7} × (E/1 TeV)$^{-2.49}$ m^{-2}s^{-1}TeV^{-1} is found. This leads to an offset integral flux of (2.0 ±0.4 ±0.2) × 10^{-7} m^{-2}s^{-1}. These flux values for an offset source are encouraging as they are within the tolerance limits of the accepted values of the differential (3.20 ±0.17 ±0.6) × 10^{-7} × (E/1 TeV)$^{-2.49}$ m^{-2}s^{-1}TeV^{-1} and integral flux (2.1 ±0.2 ±0.3) × 10^{-7} m^{-2}s^{-1} of the Crab Nebula as reported by Hillas et al. (1998) and thus provide confidence in the methodology used to determine these flux values.

When the calculation is performed using simulations of an offset source with a spectral index matching that of the HEGRA value (Aharonian et al., 2005i) found after a spectral analysis of TeV J2032+4130, the differential flux was found to be (1.2 ±0.4 ±0.4) × 10^{-8} × (E/1 TeV)$^{-1.9}$ m^{-2}s^{-1}TeV^{-1}. The integral flux was determined to be (1.3 ±0.4 ±0.5) × 10^{-8} m^{-2}s^{-1} above 1 TeV. This represents a value of 6.2% of the Crab Nebula flux and is consistent with the value calculated by the HEGRA collaboration which lends strength to the argument that TeV J2032+4130 is a steady source of TeV γ-rays. This is an important result in the quest to the determine the nature of the TeV emitter TeV J2032+4130 and will be discussed further in the next chapter.

Chapter 8

Discussion

8.1 Summary of Work

The work carried out in this thesis can be viewed as two separate entities. In the early stages of the project, a twofold approach to try and improve the optical performance of the 10 m class of imaging atmospheric Cherenkov telescope was undertaken. The two approaches were designed and undertaken to complement one another in the manner in which the optical improvement would be carried out. One was an attempt to physically improve the optical characteristics of the telescope by reducing the Point Spread Function (PSF) to as small a value as possible, and the other would use this improved PSF to computationally *"sharpen"* the recorded Cherenkov images to allow better discrimination between γ-ray initiated EAS and hadronic showers.

As was noted in Chapter 5, the sharpening of the images was not successful in improving the signal to noise ratio of the telescope. However the semi-automated alignment system constructed in NUI, Galway was successful and is in use aligning the telescopes of the new VERITAS array system in Southern Arizona.

Subsequent to this subproject the main objective of the project was undertaken. This involved a detailed reanalysis an archived Cygnus dataset that contained a *"hot-spot"* offset in the camera's field of view in the region of the HEGRA unidentified object TeV J2032+4130. The main objective of this reanalysis was the determination of the integral flux of VHE γ-ray photons from the source TeV J2032+4130. This was of particular interest as recent results from Aharonian et al. (2005i) and Konopelko et al. (2007) suggest that TeV J2032+4130 is a steady source of VHE γ-rays with integral fluxes determined to be 5% and 8% of the Crab Nebula flux respectively. These results are reported for data from 1999 to 2002 for HEGRA and from 2003 to 2005 for the VERITAS Whipple 10 m telescope data. However, Lang et al. (2004) estimated, from the 1989/1990 dataset, the integral flux to be 12% of the Crab Nebula flux, thus suggesting possible source variability over the timescale of initial observations to the most recent observations. Since the detected off-axis signal contained in the Cygnus dataset was very weak, it was not within the scope of this project to determine the TeV spectrum of TeV J2032+4130.

In addition to determining the γ-ray flux from TeV J2032+4130, the archival data was reanalysed using methods, that at the time of the original observations, were not in use, such as two dimensional analysis and the *Kernel* technique, with the aim of improving the statistical excess of the signal. During this part of the project, and to facilitate the *Kernel* analysis procedure, a database of γ-ray simulations was generated after the creation of the configuration file, as described in Chapter 6, to represent the 109 PMT camera configuration.

These alternative analysis methods used here were a final attempt at improving the detected γ-ray significance from TeV J2032+4130. As the

Kernel technique was not fully developed at the time of the original analysis of the Cygnus data, this effort was the first time such an analysis was carried out on the offset VHE signal contained in the archived Cygnus dataset.

After applying a full analysis on the on-axis and off-axis Crab Nebula data sets and on the Cygnus dataset using the alternative analysis methods described in Chapter 6, no improvement in significance from any of the three data sets was found.

8.2 Flux Determination of TeV J2032+4130

After deriving the effective collection area and the peak response energy from the simulations database it was possible, with confidence in the γ-ray simulations, to calculate the differential and integral flux values that appear to confirm TeV J2032+4130 as a steady source of TeV γ-rays as indicated by Aharonian et al. (2005i) and Konopelko et al. (2007). The method used to carry out these calculations has been described in Section 7.7. As a test of the validity of this method, the calculations to determine differential and integral flux were first performed on the dataset of on-axis Crab Nebula data. The resultant value was found to be within the tolerances of the accepted integral flux value (Hillas et al., 1998).

The calculation was repeated on the off-axis Crab Nebula dataset and again a value was returned that was within the tolerances of the accepted integral flux value, confirming that the procedure could be carried out on off-axis data. The procedure was then carried out on the dataset containing the weak signal from TeV J2032+4130 and the integral flux value was calculated to be $(1.3 \pm 0.4 \pm 0.5) \times 10^{-8}$ $\mathrm{m^{-2}s^{-1}}$ above 1 TeV.

Assuming a spectral index of -1.9, the integrated flux value was found to be $\sim$ 6.2% of that of the Crab Nebula above 1 TeV. This value returned from archived data is consistent with the findings of the HEGRA group, (who found the integral flux of TeV J2032+4130 to be $\sim$ 5% of the Crab Nebula above 1 TeV (Aharonian et al., 2005i)) and the VERITAS collaboration (who found the flux to be $\sim$ 8% of the Crab Nebula (Konopelko et al., 2007)). These results indicate that the source appears to be a steady emitter of TeV γ-rays on the timescales measured here. HEGRA reported that the source was extended at $\sim$ 6 arcmins. In contrast to this, the archival Whipple data is consistent with a point source. However, this point source appearance is probably due to the weak signal in the dataset and the low resolution of the older PMT camera. But Konopelko et al. (2007) did report the possibility of structure in their analysis but at a marginal statistical significance.

8.3 Science Discussion

The unidentified source TeV J2032+4130 has been of considerable astrophysical interest since its serendipitous discovery by the Crimean Astrophysical Observatory and also the HEGRA CT-System at La Palma from observations originally taken on Cygnus X-3 (Neshpor et al., 1995; Aharonian et al., 2002). The source was initially seen by the Crimean Astrophysical Observatory at a position $\sim 0.7^\circ$ north of Cygnus X-3. A γ-ray integral flux of 3×10^{-11} cm^{-2}s^{-1} was reported (Neshpor et al., 1995) with an assumed spectral index of -1.5. This corresponds to 1.7 times the flux of the Crab Nebula. This large flux value is hard to explain especially since all other reported flux values are between 5% and 8% of the Crab Nebula flux. However, the possibility of a steady source and an other variable type source, in the same region (possibly an AGN coincident within the source location), should not be ruled out yet.

Support for this hypothesis comes from the detection of the Milagro source MGRO J2031+41 as the spatial extent of MGRO J2031+41 (3.0 ±0.9°) is reported as being much larger than the extent of TeV J2032+4130 (Abdo et al., 2007). The position of the source detected by the Crimean group is consistent with that reported by the HEGRA group. However, follow up observations by the Crimean group did not reveal any signal.

Follow-up observations to the HEGRA detection of 2002 by Aharonian et al. (2005i) provided an accurate measurement of the source position, which was reported at right ascension: 20^h31^m57 and declination: 41°29' with the angular extent of the source reported as 6.2' ±1.2' ±0.9'. Recent observations by the VERITAS collaboration of the HEGRA position reported a significance level of 6.1σ from 65.5 hours of data (Konopelko et al., 2007). In this case the estimated integral flux was reported as $\sim$ 8% of the Crab Nebula. Of note here is the location of Whipple hot-spot is offset by around 9' northeast of the HEGRA position. However, since the statistical and systematic uncertainties in the source position in the Whipple field of view are 4' and 6', the position of the excess signal is consistent with the HEGRA position. Prior to this work Lang et al. (2004) found that the position of an off-axis signal in the field of view was also consistent the HEGRA position (*i.e.* within the errors of the source position). In that work an estimation of the integral flux was reported as 12% of that of the Crab Nebula which suggested that emission from TeV J2032+4130 was variable on the time scale of decades. The flux value quoted by Lang et al. (2004) is larger than that quoted in this work. Possible reasons for this difference may be due to the fact that the earlier estimation assumed a linear fall off in sensitivity with distance from the centre of the field of view. In addition, this new work has the benefit of more detailed information regarding the response of the detector as obtained from the large database of simulations, which were not available in the initial analysis presented by Lang et al. (2004).

Observations of variability of the γ-ray flux from astrophysical sources are important since they can tell us a great deal about the production mechanisms involved in the creation of VHE γ-rays. Models suggest that non-variable sources could be galactic objects similar to pulsars or supernova remnants interacting with surrounding molecular clouds (McLaughlin et al., 1996; Torres et al., 2001). Models suggesting a high-flux variability include isolated magnetised black holes and microquasars, and extragalactic sources like blazars (McLaughlin et al., 1996; Tavani et al., 1997). By studying the flux evolution through different observational periods of a particular source, evidence should emerge supporting one astrophysical model over another. The results of the work carried out here suggest that variable emission from TeV J2032+4130 is unlikely and that the VHE γ-ray emission appears non-variable, at least in the timescales measured in recent studies. Considering the work carried out here, along with recent observations, there is the possibility that VHE emission from TeV J2032+4130 was moderately steady for a timescale of over a decade. However, mystery still remains regarding the identification, in terms of astrophysical processes, of the γ-ray source TeV J2032+4130.

Further evidence that can help explain VHE γ-ray emission from astrophysical objects can come from information gained from observations at other wavelengths. There have been observations at radio (Butt et al., 2006a; Paredes et al., 2007; Martí et al., 2007) and X-ray (Butt et al., 2003, 2006b) wavelengths of this region of the sky, however as yet there are no confirmed counterparts to this source, and hence it remains as an unidentified object. The Milagro source MGRO J2031+41 was also recently detected in the locality of Cygnus (Abdo et al., 2007). However, at present all reports suggest TeV J2032+4130 has no radio, optical or X-ray counterpart. Hence, this source is currently considered unidentified and is regularly referred to as a "dark accelerator". Dark accelerators are a new class of VHE γ-ray source whose characteristics include having no known counterpart at other wavelengths. This indicates an absence of prominent leptonic synchrotron radiation leading to the possibility that these type of particle accelerators only accelerate protons. At present these dark accelerators are not well understood and further observations, at all wavelengths, are a priority that will hopefully shed some light on these mysterious objects. The leading production models related to dark accelerators are described here.

Association with Stellar Winds

The detection of γ-ray emission from dark accelerators using the model of associated winds from massive hot stars in OB associations[1] and Wolf-Rayet (WR) type associations appears to be the most plausible explanation. At least two of the current unidentified sources listed in Table 4.2, namely TeV J2032+4130 (Aharonian et al., 2002) and HESS J1303-631 (Hartkopf et al., 1999; Aharonian et al., 2005h), lie close to OB stellar associations. It has been shown theoretically that particles can be accelerated up to energies of hundreds of TeV due to the combination of effects of strong stellar winds and supernova explosions (Bykov & Fleishman, 1992). In this scenario, the stellar winds and supernova explosions at the core of the associations produce large scale shocks in which there are particles traveling at relativistic velocities. If these particles were to collide with a dense medium, then, via second-order Fermi acceleration (Fermi-II), significant γ-ray emission may be

---

[1] An OB association is a gravitationally unbound group of stars formed from the same interstellar cloud, containing a number of early spectral type (O and B) stars.

produced. Fermi-II acceleration is similar to Fermi acceleration (Fermi-I), except that while Fermi-I occurs due to isolated acceleration shock regions, Fermi-II relates to energy gained during the motion of a charged particle due to randomly changing magnetic field directions. Bykov (2001) and Cesarsky & Montmerle (1983) describe Fermi-II acceleration as due to a system of multiple interacting acceleration regions. Fermi-I is the acceleration of charged particles when reflected by a magnetic mirror. Fermi-II occurs when the magnetic mirror is either moving towards or away from the particle randomly. The energy gained is proportional to the square of the velocity of the moving magnetic mirror.

By definition, OB stars are hot, massive stars that are short lived, and during their lifetime lose a significant fraction of their masses via their stellar winds. The much rarer WR stars represent an evolutionary phase in the lives of massive hot stars during which they also undergo heavy mass loss. The result of these mass losses and the associated stellar winds, is the returning of mass to the interstellar medium (ISM). If this mass is considered to be moving at high velocity, and then collides with the stationary ISM, there is the possibility for Fermi acceleration. Domingo-Santamaría & Torres (2006) have shown that for a typical grouping of tens of OB stars, collective stellar winds of the order of 1000 km s^{-1} may exist containing masses as high as a few solar masses. In their work, the authors developed a model that describes the collective stellar winds from a grouping of N stars uniformly distributed, in close proximity to each other, within a radius R_c. The combined effects of the magnetic fields of these stars were considered to be typical of that of the ISM. In their hypothesis, the authors considered that if one of the stars in the grouping is close to R_c, then its contribution on the overall magnetic field at its position will be large. However, its magnetic field contribution to the opposite side of the grouping (2 R_c) will be negligible. The authors considered the hadronic processes up to distances of 10 - 20 R_c. At a distance of 1 pc, the authors show that the attenuation of the VHE γ-rays (due to pair production) was low enough to allow them escape the core region and thus be visible from Earth. However, Reimer (2003) has shown that the absorption optical depth for γ-rays in these intense stellar environments can be underestimated if the radiation fields of all the stars in the group are not taken into account.

Since the main goal regarding dark accelerators now lies in the identification of an accurate production model for TeV γ-rays, it has been mentioned already that observations at wavelengths other than TeV energies are required to help clarify the nature of these mysterious objects. In 2003 and 2006, a search of the Cygnus region using the Chandra X-ray Observatory (Butt et al., 2003, 2006b) found no plausible diffuse X-ray counterpart of TeV J2032+4130. However, Butt et al. (2006b) detected 240 point-like X-ray sources within the region. The authors speculate that the VHE emission from this region may be a composite source that has the observed point-like X-ray sources as its counterpart. Further evidence of this scenario was contained in a recent report detailing the detection of numerous point-like X-ray sources in the field of TeV J2032+4130 (Mukherjee et al., 2006). It was shown that the brightest of these X-ray sources were a mixture of early and late-type stars. Mukherjee et al. (2006) have suggested a region of diffuse X-ray emission from within the error circle of TeV J2032+4130. However, they concluded that no convincing point source counterpart to the source was found in the X-ray band. In a recent paper, Horns et al. (2007) reported the detection of an X-ray counterpart to TeV J2032+4130. However this was disputed by Butt (2007a) who preferred the scenario where the observed

X-ray emission was due to a population of faint X-ray sources that happen by chance to be distributed at an angular size similar to TeV J2032+4130 and were previously reported (Butt et al., 2006b).

Butt et al. (2006b) state that at least 36 of the 240 detected X-ray sources are massive stars and 2 are possible radio emitters. In their work, the authors suggest that there is a critical distance from the core of the association where VHE γ-ray emission, due to hadronic interactions in the shock front $\sim$ 1 pc from the hot OB stars, outweighs absorption due to pair production. They argue that this is the case for Cygnus OB2. Butt et al. (2003) have shown that there is a sufficient grouping of catalogued OB stars that coincide with TeV J2032+4130 $\sim$ 10 pc from the core of the association and they favour the emission scenario described above. However further observations and analysis are required to confirm this hypothesis.

Gamma-Ray Burst Remnants

The unidentified TeV source HESS J1303-631 was recently the subject of a study that suggests the identification of the source as the remnant of a Gamma-Ray Burst (GRB) that occurred in our Galaxy several tens of thousands of years ago (Atoyan et al., 2006). GRBs are bursts of γ-rays coming from seemingly random places in the sky, and at random times, that last from milliseconds to many minutes. They are often followed by “afterglow” emission at longer wavelengths (X-ray, UV, optical, IR, and radio) and at the moment of occurrence they are the most luminous events known in the universe. GRBs are currently detected about 2 to 3 times a week by orbiting satellites. GRB models suggest that the intense, but brief, emission of energy may be caused by the core-collapse of a rapidly rotating high-mass star into a singularity resulting in collimated emission. There is also a subclass of GRBs (“short” bursts) that appear to be due to other processes, possibly the collision of two neutron stars orbiting in a binary system.

During a GRB, it is thought that there is a highly relativistic and energetic outflow of matter forming a pair of opposite jets. The energy output during the duration of the burst (≥ 2s) can be $\sim 6 \times 10^{62}$ eV (Atoyan et al., 2006). The relativistic shocks then accelerate particles in the plasma to relativistic energies. It is believed that the energy of these particles can be up to $\sim$ 100 times higher than the accelerated particles produced in typical supernova remnants (Berezinskii et al., 1990). If, from the estimated Galactic GRB rate, there is between one and several GRBs of age $\sim 10^4$ years in the ISM at distances up to 10-20 kpc from Earth, then the associated shock of accelerated multi-TeV particles would diffuse over distances of around 100 pc. In this case, the detected VHE photons from GRB remnants should appear as large centre-filled nebulae in the ISM. In their work Atoyan et al. (2006) argue that one of the unidentified TeV sources, HESS J1303-631, can be identified with the remnant of a GRB that happened in the Milky Way some ten thousand years ago. Atoyan et al. (2006) predict that a main feature of a GRB remnant is that a significant amount of the burst energy is eventually transferred to high-energy protons. Relativistic electrons would only receive a much smaller amount of energy during the point of non-relativistic evolution of the GRB shell. According to Livio & Waxman (2000), the shock from a GRB will become non-relativistic in less than one year and, by this stage in their evolution, the associated magnetic fields would be around 0.1 G (Berger et al., 2004) and electrons will have cooled down via synchrotron emission to a few GeV, thus providing an explanation for the lack of observed synchrotron emission at high energies.

Old SNR Associations

Another proposal put forward to explain VHE emission from dark accelerators is the VHE γ-ray emission from old ($> 10^5$ years) supernova remnants (Yamazaki et al., 2006). In their work, the authors find that the ratio of the VHE flux to the X-ray or radio flux can be greater than 100, making it very difficult to detect these sources at longer wavelengths. The authors detail the possible encounter, and interaction, between an old SNR and a giant molecular cloud. They suggest that if an old SNR interacts with a giant molecular cloud, VHE emission will occur via the Fermi-I process as the SNR shock interacts with the dense giant molecular cloud. X-ray emission will be negligible due to energy losses of the electrons over the lifetime of the SNR. Two scenarios for particle acceleration are described. One where the shock collides with the giant molecular cloud and one where the VHE emission comes from the giant molecular cloud being illuminated by accelerated protons at the SNR shock. They noted that the maximum energy of accelerated electrons is much smaller, resulting in the generation of VHE γ-rays being dominated by the acceleration of hadrons and their interaction within the molecular cloud. The particles emit VHE γ-rays through π^0 decay and X-ray synchrotron emission from secondary electrons generated by charged pions. However, the study showed that the shock created when a SNR older than $\sim 5 \times 10^4$ years collides with a giant molecular cloud, particle acceleration in the shock is not efficient enough to produce VHE emission. Yet, the high density of the giant molecular cloud can act as a target for the high energy protons resulting in the production of pions. The possibility here is that this type of hadronic acceleration could be the origin of VHE emission from dark accelerators.

Supernova-OB Associations

In a model put forward by Montmerle (1979), γ-ray emission from dark accelerators may be due to a combination of the stellar winds from OB associated stars and a related SNR. Considering the size of the OB association in Cygnus, it is possible that some of the oldest and more massive (10-20 $M_{\odot}$) member stars have already evolved into supernovae and that some of the lower mass stars are still relatively close.

Microquasar emission

The models described above, or a combination of them, suggest steady emission of VHE γ-rays. Hence these models appear to be the most plausible explanations for the emission of VHE γ-rays from dark accelerators, in particular TeV J2032+4130 given the results of this work and other recent studies. There is, however, another suggestion that explains the VHE emission and lack of detections at other energies. Aharonian et al. (2002) have suggested an alternate accelerator, in the form of a microquasar, as a possible source of variable γ-ray emission dark accelerators (Paredes et al., 2000). A microquasar consists of a binary system in which a normal star orbits around, and loses matter to, a nearby compact object. This object may be either a black hole or a neutron star. The lost matter enters a fast-spinning accretion disk, is heated to millions of degrees, and then either falls onto the compact object or is ejected as a bipolar flow.

A possible scenario for VHE emission in this case involves a jet-driven termination shock at the boundary, where a relativistic jet interacts with the interstellar medium and where accelerated electrons produce synchrotron emission and inverse-Compton emission (Aharonian & Atoyan, 1998a). In fact the microquasar Cyg X-3 can be considered to be in the vicinity of TeV

J2032-4130, at a distance of 70 pc, if it is at the same distance from Earth ($\sim$ 8.5 kpc). A recent report (Butt et al., 2006a), detailing a radio survey of the TeV J2032+4130 region, has revealed a weak diffuse radio source within the Whipple hotspot and, to a lesser degree the HEGRA position. The radio source appears as a dual-lobed non-thermal source, however, a definite determination on the nature of the source has not yet been made. It is also not clear whether the source is Galactic or extragalactic. If it is Galactic, there is a possibility that it is a microquasar. Thus it is still unclear if this object is related to the VHE γ-ray emission observed from TeV J2032+4130.

Counterparts at Lower Energies

With regard to observations of TeV J2032+4130 in lower energy regimes, there have been several tentative detections at radio and infrared frequencies (Butt et al., 2006a; Paredes et al., 2007; Martí et al., 2007) of weak diffuse sources in the region of sky consistent with the location of TeV J2032+4130. Martí et al. (2007) have created a catalogue of 153 objects at the 49 cm wavelength. Figure 8.1 shows a sky map of the radio signal from the Cygnus region and a close-up of the dual-lobed radio source located within the Whipple hot-spot as mentioned above. The detection of a weak non-thermal shell-like supernova remnant type object was also reported (Butt et al., 2006a). Results of these radio frequency observations appear to suggest the existence of one or more supernova remnants or large-scale cluster shocks caused by the association of the large amount of massive stars in Cyg OB2 (Butt et al., 2007). Despite these detections at radio frequencies near TeV J2032+4130, any physical association between them and TeV J2032+4130 has not yet been determined with certainty.

If these sources of diffuse X-ray emission and radio frequency emission

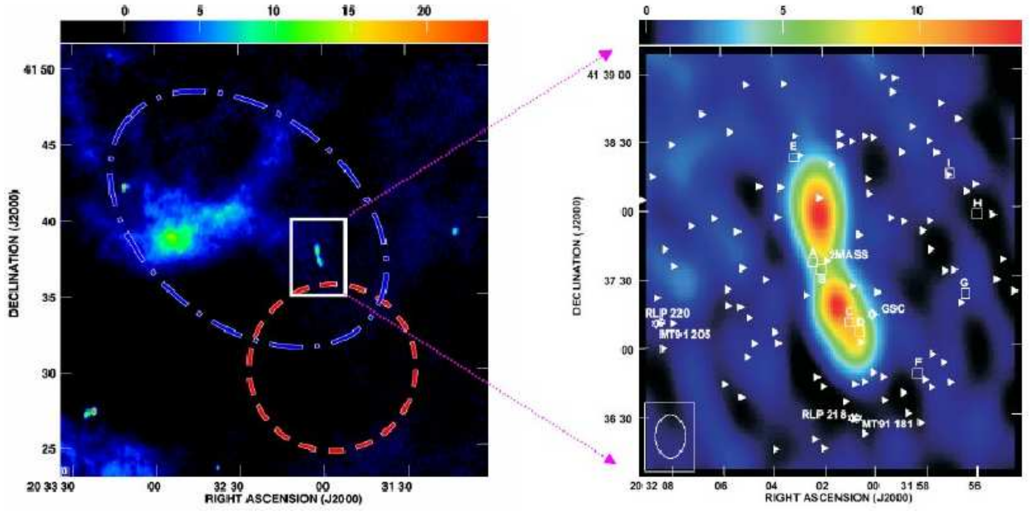

Figure 8.1: On the left a radio sky map of the Cygnus region. The blue oval is representative of the Whipple VHE γ-ray hot-spot and the red circle represents the extended region containing the HEGRA emission. On the right is a close up of the dual-lobed non-thermal radio source located within the Whipple hotspot. □ represent the locations of the CHANDRA point-like X-ray sources and ▶ represent 2MASS infrared point sources. Figure courtesy of Butt et al. (2006a).

are confirmed as being associated with TeV J2032+4130 by further observations, it should help to constrain the origin of TeV γ-ray emission from this region of sky and assist in determining whether the emission is electronic or hadronic in origin. Since there are a variety of nearby astrophysical sources associated with Cygnus region, there is some credence in the theory that the VHE γ-ray emission is due to a termination shock caused by supersonic stellar winds breaking out into the inter stellar medium. In fact very recent results from the HESS collaboration (Aharonian et al., 2007b) have detailed the detection of VHE γ-ray emission from the powerful stellar association Westerlund 2, in the southern sky, containing the Wolf-Rayet binary WR

20a. The discovery of this source, HESS J1023-575, represents a new breed of astronomical γ-ray source. Due to the similarities in their local regions, *i.e.* strong stellar winds from the hot massive stars in the cluster, it has been speculated that TeV J2032+4130 may be a member of the same class of astrophysical object as HESS J1023-575 (Butt, 2007b). If this is the case, the most likely scenario explaining the VHE emission from these objects is the supersonic winds of charged particles emanating from the many massive stars and or supernova remnants in these regions. These stellar winds accelerate the particles resulting in VHE γ-ray emission via second-order Fermi acceleration.

8.4 Conclusions

Currently, a major goal in VHE astrophysics is the explanation of VHE γ-ray emission from dark accelerators. Information that could help in the identification of a relevant production model may come from the VHE γ-ray emitter being associated with other astrophysical objects that lie within the vicinity of the object under study. To illustrate the crowded region of sky that TeV J2032+4130 lies in, Figure 8.2 (taken from the recent analysis by Konopelko et al. (2007)) shows a contour map indicating the significance values of the γ-ray emission from the Cygnus region. The Whipple hot-spot is shown as is the HEGRA location of TeV J2032+4130, and the EGRET GeV γ-ray source 3EG J2033+4118. The positions of Cygnus X-3 and the extent of the Cygnus OB2 association are also shown. As mentioned in the previous section, the location of TeV J2032+4130 lies close to the large Cyg OB2 stellar association, and the VHE emission may be linked to the many hot massive energetic stars that are grouped in this association. One scenario, suggesting VHE emission due to the OB association, is hadronic in nature (Aharonian et al., 2002). A second possibility explains the VHE

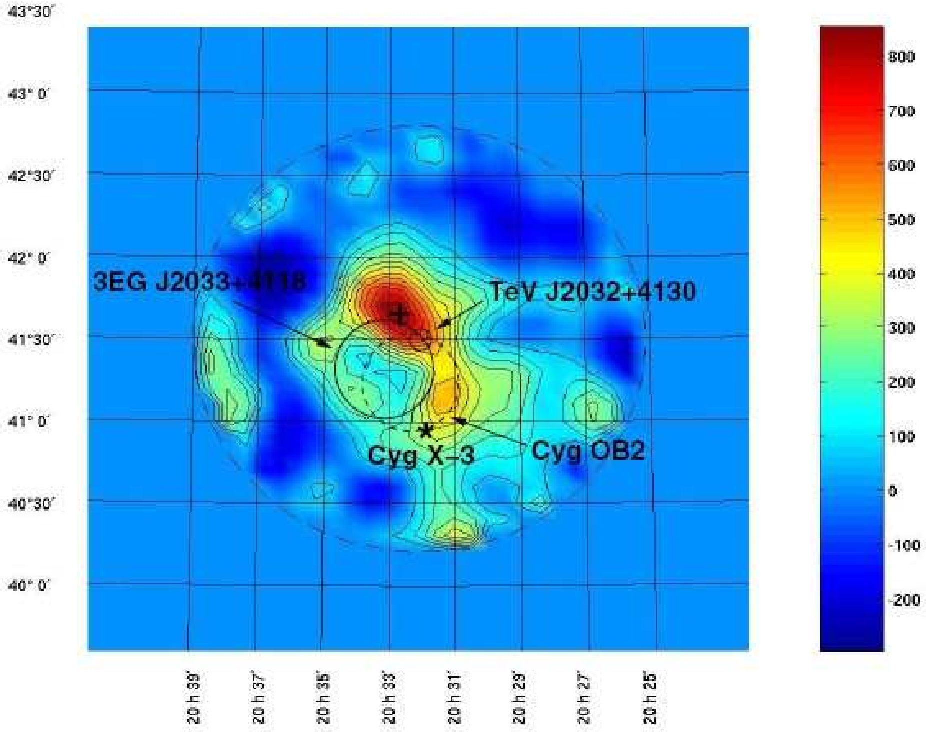

Figure 8.2: A VHE sky map of excess counts of the Cygnus region from observations taken with the Whipple 10 m imaging atmospheric Cherenkov telescope. Overlayed are the positions of various other astrophysical objects of note in this region. The centre circle is the source location of TeV J2032+4130 as reported by the HEGRA group. Also shown is the GeV γ-ray EGRET source 3EG J2033+4118 as well as the extent of the Cygnus OB association. Taken from Konopelko et al. (2007).

γ-ray emission as synchrotron and inverse Compton scattering in a jet-driven termination shock from Cygnus X-3. There is also the possibility the jet could originate from an as yet undetected microquasar or a class of high energy γ-ray source. However, since the work carried out here suggests steady emission of VHE γ-rays from TeV J2032+4130, the conclusion is that the source is not variable in nature. Had variability been confirmed, then VHE emission from a compact type object (such as a microquasar) would have been the favoured model to conclude with. However, steady emission is more consistent with what one might expect from an extended type source, such as association with stellar winds and the ISM. There is added credibility to this conclusion as HEGRA report TeV J2032+4130 as an extended source ($\sim$ 6').

It is important to note that Cyg OB2 is the largest OB association known in the Milky Way Galaxy and contains $\sim$ 2600 OB stars (Lozinskaya et al., 2002). With this many OB, stars the implications are for a substantial mechanical power density generated in the combined stellar winds of these OB stars. An associated possibility here comes from the likelihood that the combined stellar winds cause further acceleration by providing the required injection of low energy particles from the OB association into a nearby supernova remnant shell where shock acceleration occurs. This possibility is known as supernova-OB associations and have been described in Section 8.3 (Montmerle, 1979). The OB association appears to be the most plausible explanation to the origin of VHE γ-rays from this region of the Galaxy, however there are several other explanations that cannot be ruled out, for example the γ-ray burst remnant scenario or the association of an old supernova remnant, as described in the previous section.

It is clear that we are edging ever closer to solving the mystery of VHE γ-ray emission from TeV J2032+4130. However, for a clearer understanding of the VHE γ-ray production mechanisms of TeV J2032+4130, it is of crucial importance that further observations at VHE energies and other wavelengths be undertaken. As more sensitive and advanced ground-based detectors like VERITAS and space-based detectors like GLAST are starting to come online, it is only a matter of time before the issues surrounding unidentified and dark accelerator candidates, like TeV J2032+4130, will be resolved. Future observations with VERITAS and MAGIC will be critical in determining the nature of TeV J2032+4130 as they will be able to accurately map the spatial extent of the source.

8.5 Future Possibilities in Ground Based γ-ray Astronomy

In the last few years the field of ground-based γ-ray astronomy has taken a great leap forward with improved technologies and better funding. With the HESS array fully functional in the southern hemisphere, and the VERITAS array now online in the northern hemisphere, the entire sky can now be observed with unprecedented sensitivity using similar instruments. The ever expanding HESS catalogue is an example of the potential for discovery these new Cherenkov arrays possess and provides great motivation for the continued development in the field. When GLAST comes online in early 2008, a gap in the high energy spectrum will be closed as its upper energy threshold will overlap with the lower energy thresholds of HESS and VERITAS. With all this in mind, one must ask a question regarding the future of this field, what next?

Generally, progress in astronomy can be seen in two distinct areas of activity. One involves the use of existing technologies on a much larger scale than before. For example the scaling up from a single 10 m Cherenkov telescope (Whipple 10 m) to an array of four 12 m Cherenkov telescopes (VERITAS array) and the second phase of the HESS program, *i.e.* the addition of a fifth large diameter Cherenkov telescope at the centre of the array. Another example is the MAGIC collaboration's addition of a second telescope 85 m distance from the original, known as MAGIC II. The second area results from technological breakthroughs and resulting improvements in sensitivity. For example, optical astronomy took a huge leap forward due to the development of CCD detectors, that subsequently replaced photographic plates resulting in improved sensitivity and a convenient method of image analysis and data storage. A significant breakthrough for ground-based γ-ray astronomy would be the development of detectors with significant improvements in quantum efficiency. However, progress in new technologies relating to VHE astronomy have been slow to come about.

Currently progress in ground-based γ-ray astronomy is based on the method of building more, and bigger versions of the early successful experiments. For example the next generation extensive air shower detector, HAWC (High Altitude Water Cherenkov) (Smith et al., 2007), is based on the existing MILAGRO detector. To make advances in ground based γ-ray astronomy, several areas must be looked at and then decide whether it is practical or possible to move the development in a particular direction. For example, desirable improvements include reducing the energy threshold of a detector, increasing the field of view, increasing the collection area *etc.* In relation to the work carried out in Chapter 6 of this project, it is clear that an improved field of view would be of benefit when it comes to making serendipitous discoveries of hitherto undetected sources like TeV J2032+4130. Larger fields of view may be obtained by using larger optical systems and cameras with larger PMT cameras. An increase in collection area may be obtained by using more imaging atmospheric Cherenkov telescopes, *i.e.* larger arrays. A larger array of telescopes would improve sensitivity especially if the array were larger than the Cherenkov light pool as it is seen from the ground.

The Cherenkov Telescope Array (CTA) project is an initiative with the objective of building a large array of many Cherenkov telescopes to detect emission from VHE γ-ray sources (Hermann et al., 2007). It is proposed that CTA will serve as an open observatory to a wide astrophysics community to study the non-thermal high-energy universe between 10 GeV and 100 TeV. The project will be based at two sites, one in the northern hemisphere and the other in the southern hemisphere and both will be run as a global collaboration. The estimated cost of the project is in the region of 150 M euro. At present, CTA is being considered as a potential next generation ground-based γ-ray detector in the 2006 road map report of the European Strategy Forum on Research Infrastructures (ESFRI).

A second proposal for a large area array is the Advanced Gamma-ray Imaging System (AGIS) (Buckley, 2007). The basic concept of AGIS is a large array of detectors of aperture 7 m to 12 m. The system design is similar to that of CTA. Like CTA there are a couple of array layouts being discussed. One possibility is a large one square kilometer array of Cherenkov telescopes comprised of one hundred identical telescopes. The other is a layout comprising of three large detectors located at a central position, surrounded by second closely grouped array of smaller telescopes, which in turn is surrounded (more sparsely) by a third group of telescopes.

Another possible project is HE-ASTRO (High Energy - All Sky Transient Radiation Observatory) (Vassiliev & Fegan, 2005). HE-ASTRO is designed as an array of two hundred and seventeen 7 m imaging atmospheric Cherenkov telescopes. It is proposed that all telescopes could be pointed at a single source for maximum sensitivity, or each one could pointed at different parts of the sky covering a much larger portion of the sky with reduced sensitivity. It is predicted that the sensitivity of individual HE-ASTRO telescopes, to observations of the Crab Nebula, would match that of VERITAS ($23\sigma/(\text{hour})^{1/2}$) and when operated as a full array, its sensitivity would be $166\sigma/(\text{hour})^{1/2}$, *i.e.* it would detect the Crab Nebula at 5σ in ~ 3 seconds (Swordy, 2007). The obvious and major drawback with this proposal is the projected cost which is similar to that of CTA. To accomplish a project of this nature, with such high costs, would require a wider international collaboration combined with the development and utilisation of new technologies. The realisation of this would represent one of the biggest advances in this field since its foundation.

Whatever the method used to advance the field of ground based γ-ray astronomy, it is probable that larger arrays at higher altitudes (> 3000 m) with lower energy thresholds will be developed. It is also probable that this field of science will grow significantly in the coming years as collaborations grow in size due to the large personnel requirements of such large experiments. In conclusion, these proposed developments offer great potential for making many new discoveries in the coming years and will surely lead to exciting times ahead.

Appendix A

Hillas parameters

An image seen on the camera can be parameterised using information about the *size* of the signal seen in each phototube. Suppose the ith PMT is given coordinates x_i, y_i (in degrees) and contains a signal S_i. The origin of the coordinate system is in the centre of the array of PMTs. An ellipse is fitted to the image and the Hillas parameters are calculated relative to the centre. By taking the moments of the image, the following parameters can be determined.

$$\begin{array}{rr}
\langle x\rangle = \frac{\sum s_i x_i}{\sum s_i} & \langle y\rangle = \frac{\sum s_i y_i}{\sum s_i} \\
\langle x^2\rangle = \frac{\sum s_i x_i^2}{\sum s_i} & \langle y^2\rangle = \frac{\sum s_i y_i^2}{\sum s_i} \\
\langle xy\rangle = \frac{\sum s_i x_i y_i}{\sum s_i} & \langle x^3\rangle = \frac{\sum s_i x_i^3}{\sum s_i} \\
\langle y^3\rangle = \frac{\sum s_i y_i^3}{\sum s_i} & \langle x^2 y\rangle = \frac{\sum s_i x_i^2 y_i}{\sum s_i}
\end{array}$$

$$\langle xy^2\rangle = \frac{\sum s_i x_i y_i^2}{\sum s_i}$$

$$\sigma_{x^2} = \langle x^2 \rangle - \langle x^2 \rangle$$

$$\sigma_{y^2} = \langle y^2 \rangle - \langle y^2 \rangle$$

$$\sigma_{xy} = \langle xy \rangle - \langle x \rangle \langle y \rangle$$

$$\sigma_{x^3} = \langle x^3 \rangle - 3 \langle x \rangle \langle x^2 \rangle + 2 \langle x \rangle^3$$

$$\sigma_{y^3} = \langle y^3 \rangle - 3 \langle y \rangle \langle y^2 \rangle + 2 \langle y \rangle^3$$

$$\sigma_{x^2y} = \langle x^2y \rangle - 2 \langle xy \rangle \langle x \rangle + 2 \langle x \rangle^2 \langle y \rangle - \langle x^2 \rangle \langle y \rangle$$

$$\sigma_{xy^2} = \langle xy^2 \rangle - 2 \langle xy \rangle \langle y \rangle + 2 \langle x \rangle \langle y \rangle^2 - \langle x \rangle \langle y^2 \rangle$$

By defining the following:

$$\begin{array}{ll}
k = \sigma_{y^2} - \sigma_{x^2} & l = \sqrt{k^2 + 4\sigma_{xy}^2} \\
m = \langle y^2 \rangle - \langle x^2 \rangle & n = \sqrt{m^2 + 4 \langle xy \rangle^2} \\
u = 1 + \frac{k}{l} & v = 2 - u
\end{array}$$

the Hillas parameters are calculated as follows:

$$\begin{aligned}
&\langle Size\rangle = \sum s_i \\
&\langle Length\rangle^2 = \tfrac{\sigma_{x^2}+\sigma_{y^2}+1}{2} \\
&\langle Width\rangle^2 = \tfrac{\sigma_{x^2}+\sigma_{y^2}-1}{2} \\
&\langle Miss\rangle^2 = \tfrac{u\langle x\rangle^2+v\langle y\rangle^2}{2} - \tfrac{2\langle xy\rangle\sigma_{xy}}{l} \\
&\langle Azwidth\rangle^2 = \tfrac{\langle x\rangle^2+\langle y\rangle^2-n}{2} \\
&\langle Dis\tan ce\rangle^2 = \langle x\rangle^2 + \langle y\rangle^2 \\
&\langle Alpha\rangle = \sin^{-1}\left(\tfrac{\langle Miss\rangle}{\langle Dis\tan ce\rangle}\right)
\end{aligned}$$

The calculation of the parameter asymmetry requires the angle, ψ, between the x-axis and the major axis of the ellipse:

$$\psi = \tan^{-1}\left(\tfrac{(k+l)\langle y\rangle+2\sigma_{xy}\langle x\rangle}{2\sigma_{xy}\langle y\rangle-(k-l)\langle x\rangle}\right),$$

$$p = \sigma_{x^3}\cos^3\psi + 3\sigma_{x^2y}\sin\psi\cos^2\psi + 3\sigma_{xy^2}\cos\psi\sin^2\psi + \sigma_{y^3}\sin^3\psi,$$

$$\langle Asymmetry\rangle^3 = \tfrac{p}{\langle Length\rangle}$$

Appendix B

Publications List

Refereed Journal Publications:

A. Konopelko, & the VERITAS Collaboration including G.E. Kenny, 2007 **Observations of the Unidentified TeV Gamma-Ray Source TeV J2032+4130 with the Whipple Observatory 10 m Telescope.** *The Astrophysical Journal*, Volume 658, p. 1062.

J. Holder, & the VERITAS Collaboration including G.E. Kenny, 2006 **VERITAS: Status and Performance.** Submitted to Proceedings of "*Science with New Generation of High Energy Gamma-ray Experiments*", Elba.

J. Holder, & the VERITAS Collaboration including G.E. Kenny, 2006. **The First VERITAS Telescope.** *Astroparticle Physics*, Volume 25, Issue 6, p. 391-401

J. S. Perkins, & the VERITAS Collaboration including G.E. Kenny, 2006.

TeV Gamma-Ray Observations of the Perseus and Abell 2029 Galaxy Clusters. *The Astrophysical Journal*, Volume 644, Issue 1, pp. 148-154.

P. F. Rebillot, & the VERITAS Collaboration including G.E. Kenny, 2006. **Multiwavelength Observations of the Blazar Markarian 421 in 2002 December and 2003 January.** *The Astrophysical Journal*, Volume 641, Issue 2, pp. 740-751.

E. Linton, & the VERITAS Collaboration including G.E. Kenny, 2006. **A Search For Primordial Black Hole Evaporations using the Whipple Gamma-ray Telescope.** *Journal of Cosmology and Astroparticle Physics,* Issue 01, pp. 013.

M. Schroedter, & the VERITAS Collaboration including G.E. Kenny, 2005. **A Very High Energy Gamma-Ray Spectrum of 1ES 2344+514.** *The Astrophysical Journal*, Volume 634, Issue 2, pp. 947-954.

M. Blazejowski, & the VERITAS Collaboration including G.E. Kenny, 2005. **A Multi-wavelength View of the TeV Blazar Markarian 421: Correlated Variability, Flaring, and Spectral Evolution.** *Astrophysical Journal,* 630 (1), 130-141.

M.K. Daniel, & the VERITAS Collaboration including G.E. Kenny, 2005. **Spectrum of Very High Energy Gamma-Rays from the blazar 1ES 1959+650 during Flaring Activity in 2002.** *Astrophysical Journal* 621 181.

S.J. Fegan, & the VERITAS Collaboration including G.E. Kenny, 2005. **A Survey of Unidentified EGRET Sources at Very High Energies.** *Astrophysical Journal* 624 638.

A. Falcone, & the VERITAS Collaboration including G.E. Kenny, 2004. **A Search for TeV Gamma-Ray Emission form High-Peaked Flat Spectrum Radio Quasars Using the Whipple Air-Cherenkov Telescope.** *Astrophysical Journal* 613 710.

D. Horan, & the VERITAS Collaboration including G.E. Kenny, 2004. **Constraints on the very high energy emission from BL Lacertae objects.** *Astrophysical Journal* 603 (1): 51-61 Part 1.

K. Kosack, & the VERITAS Collaboration including G.E. Kenny, 2004. **TeV Gamma-Ray Observations of the Galactic Center.** *Astrophysical Journal,* 608 97.

S. Le Bohec, & the VERITAS Collaboration including G.E. Kenny, 2004. **Observation of M87 at 400GeV with the Whipple 10m telescope.** *Astrophysical Journal,* 610 (1), 156-160.

F. Krennrich, & the VERITAS Collaboration including G.E. Kenny, 2003. **VERITAS: the Very Energetic Imaging Telescope Array System.** *New Astronomy Reviews.* Vol 48, Issues 5-6, pp. 345-349.

Noncollaboration conference papers:

J. Toner, V. Acciari, A. Cesarini, G.G. Gillanders, D. Hanna, G. E. Kenny, J. Kildea, A. McCann, M. McCutcheon, M.J. Lang, P. Reynolds, M. Schroedter, A. Smith, J. E. Ward, T. Weekes, B. Zitzer. **ICRC2007 Bias Alignment of the VERITAS Telescopes.** To be published in the proceedings of the 30th International Cosmic Ray Conference, Merida, Mexico.

G.E. Kenny, Gillanders, G.H., Lang, M.J., 2005. **Point Spread Function Deconvolution of an Atmospheric Cherenkov Telescope** *Proceedings of the 28th International Cosmic Ray Conference, Pune, India*

G.E. Kenny, November 2004. **The Study of Very High Energy Gamma-ray Emission from Astrophysical Objects.** Poster presentation at the Second IRCSET Annual Research Symposium in Dublin.

G.E. Kenny, November 2003. **The Study of Very High Energy Gamma-ray Emission from Astrophysical Objects using the Imaging Atmospheric Cherenkov Technique.** Poster presentation at the First IRCSET Annual Research Symposium in Dublin.

G.E. Kenny, March 2003. **An Overview of Gamma Ray Astronomy and the Imaging Atmospheric Cherenkov Technique.** Galway Physics Society colloquium presentation.

VERITAS conference papers:

O. Celik, & the VERITAS Collaboration including G.E. Kenny, 2007. **Observations of the Crab Nebula and Pulsar with VERITAS.** To be published in the proceedings of the 30th International Cosmic Ray Conference, Merida, Mexico.

P. Colin, & the VERITAS Collaboration including G.E. Kenny, 2007. **Observation of the galaxy M87 with VERITAS.** To be published in the proceedings of the 30th International Cosmic Ray Conference, Merida, Mexico.

P. Fortin, & the VERITAS Collaboration including G.E. Kenny, 2007. **Observations of the high-frequency-peaked BL Lac object 1ES 1218+304 with VERITAS.** To be published in the proceedings of the 30th International Cosmic Ray Conference, Merida, Mexico.

J. Grube, & the VERITAS Collaboration including G.E. Kenny, 2007. **Observations of the Crab Nebula with the Whipple 10 m Telescope.** To be published in the proceedings of the 30th International Cosmic Ray Conference, Merida, Mexico.

D. Horan, & the VERITAS Collaboration including G.E. Kenny, 2007. **Observations of Gamma-ray Bursts with VERITAS and Whipple.** To be published in the proceedings of the 30th International Cosmic Ray Conference, Merida, Mexico.

T. B. Humensky, & the VERITAS Collaboration including G.E. Kenny, 2007.

Observation of the Supernova Remnant IC 443 with VERITAS. To be published in the proceedings of the 30th International Cosmic Ray Conference, Merida, Mexico.

D. B. Kieda, & the VERITAS Collaboration including G.E. Kenny, 2007. **A VERITAS Search for VHE -Ray Point Sources Near Selected MILAGRO Target Regions.** To be published in the proceedings of the 30th International Cosmic Ray Conference, Merida, Mexico.

A. Konopelko, & the VERITAS Collaboration including G.E. Kenny, 2007. **Observations of Pulsar Wind Nebulae with the VERITAS Array of Imaging Atmospheric Cherenkov Telescopes.** To be published in the proceedings of the 30th International Cosmic Ray Conference, Merida, Mexico.

H. Krawczynski, & the VERITAS Collaboration including G.E. Kenny, 2007. **Blazar Observations with VERITAS.** To be published in the proceedings of the 30th International Cosmic Ray Conference, Merida, Mexico.

G. Maier, & the VERITAS Collaboration including G.E. Kenny, 2007. **Observation of the binary system LS I +61 303 in Very-High Energy Gamma-Rays with VERITAS.** To be published in the proceedings of the 30th International Cosmic Ray Conference, Merida, Mexico.

G. Maier, & the VERITAS Collaboration including G.E. Kenny, 2007. **VERITAS: Status and Latest Results.** To be published in the proceedings of the 30th International Cosmic Ray Conference, Merida, Mexico.

A. Smith, & the VERITAS Collaboration including G.E. Kenny, 2007. **TeV and X-ray Monitoring of LS I +61 303With VERITAS, Swift, and RXTE.** To be published in the proceedings of the 30th International Cosmic Ray Conference, Merida, Mexico.

D. Steele, & the VERITAS Collaboration including G.E. Kenny, 2007. **Results from the Blazar Monitoring Campaign at the Whipple 10m Gamma-ray Telescope.** To be published in the proceedings of the 30th International Cosmic Ray Conference, Merida, Mexico.

P. Cogan, & the VERITAS Collaboration including G.E. Kenny, 2007. **Observations of 1ES 0647+250 and 1ES 0806+524 with VERITAS.** To be published in the proceedings of the 30th International Cosmic Ray Conference, Merida, Mexico.

P. Cogan, & the VERITAS Collaboration including G.E. Kenny, 2007. **Analysis of Flash ADC Data With VERITAS.** To be published in the proceedings of the 30th International Cosmic Ray Conference, Merida, Mexico.

P. Cogan, & the VERITAS Collaboration including G.E. Kenny, 2007. **VEGAS, the VERITAS Gamma-ray Analysis Suite.** To be published in the proceedings of the 30th International Cosmic Ray Conference, Merida, Mexico.

M. K. Daniel, & the VERITAS Collaboration including G.E. Kenny, 2007. **The VERITAS standard data analysis.** To be published in the proceedings of the 30th International Cosmic Ray Conference, Merida, Mexico.

M. K. Daniel, & the VERITAS Collaboration including G.E. Kenny, 2007. **Application of radiosonde data to VERITAS simulations.** To be published in the proceedings of the 30th International Cosmic Ray Conference, Merida, Mexico.

S. J. Fegan, & the VERITAS Collaboration including G.E. Kenny, 2007. **Observations of Mrk 421 and Mrk 501 in Spring 2006 with VERITAS.** To be published in the proceedings of the 30th International Cosmic Ray Conference, Merida, Mexico.

D. Hanna, & the VERITAS Collaboration including G.E. Kenny, 2007. **Calibration Techniques for VERITAS.** To be published in the proceedings of the 30th International Cosmic Ray Conference, Merida, Mexico.

E. Hays, & the VERITAS Collaboration including G.E. Kenny, 2007. **VERITAS Data Acquisition.** To be published in the proceedings of the 30th International Cosmic Ray Conference, Merida, Mexico.

C.M.Hui, & the VERITAS Collaboration including G.E. Kenny, 2007. **Laser Atmospheric Studies with VERITAS.** To be published in the proceedings of the 30th International Cosmic Ray Conference, Merida, Mexico.

M.P. Kertzman, & the VERITAS Collaboration including G.E. Kenny, 2007. **The Whipple Strip Sky Survey.** To be published in the proceedings of the 30th International Cosmic Ray Conference, Merida, Mexico.

G. Maier, & the VERITAS Collaboration including G.E. Kenny, 2007. **Monte Carlo studies of the VERITAS array of Cherenkov telescopes.** To be published in the proceedings of the 30th International Cosmic Ray Conference, Merida, Mexico.

T. Nagai, & the VERITAS Collaboration including G.E. Kenny, 2007. **Focal Plane Instrumentation of VERITAS.** To be published in the proceedings of the 30th International Cosmic Ray Conference, Merida, Mexico.

A. J. Syson, & the VERITAS Collaboration including G.E. Kenny, 2007. **A Probability Density Method for VHE Gamma-Ray Source Analysis.** To be published in the proceedings of the 30th International Cosmic Ray Conference, Merida, Mexico.

A. Weinstein, & the VERITAS Collaboration including G.E. Kenny, 2007. **The VERITAS Trigger System.** To be published in the proceedings of the 30th International Cosmic Ray Conference, Merida, Mexico.

S. A. Wissel, & the VERITAS Collaboration including G.E. Kenny, 2007. **Studies of Direct Cherenkov Emission with VERITAS.** To be published in the proceedings of the 30th International Cosmic Ray Conference, Merida, Mexico.

J. Holder, & the VERITAS Collaboration including Kenny, G.E. 2005. **Introduction to VERITAS.** *Proceedings of the 28th International Cosmic Ray Conference, Pune, India*, 2005.

P. Cogan, & the VERITAS Collaboration including Kenny, G.E. 2005. **Telescope 1 observations of AGN.** *Proceedings of the 28th International Cosmic Ray Conference, Pune, India*, 2005.

G. Maier, & the VERITAS Collaboration including Kenny, G.E. 2005. **Monte Carlo results for Telescope 1.** *Proceedings of the 28th International Cosmic Ray Conference, Pune, India*, 2005.

B. Humensky, & the VERITAS Collaboration including Kenny, G.E. 2005. **Muon calibration of Telescope 1.** *Proceedings of the 28th International Cosmic Ray Conference, Pune, India*, 2005.

J. Hall, & the VERITAS Collaboration including Kenny, G.E. 2005. **Observations of local galaxies.** *Proceedings of the 28th International Cosmic Ray Conference, Pune, India*, 2005.

J. Holder, & the VERITAS Collaboration including Kenny, G.E. 2005. **Exploiting VERITAS' timing information.** *Proceedings of the 28th International Cosmic Ray Conference, Pune, India*, 2005.

J. Perkins, & the VERITAS Collaboration including Kenny, G.E. 2005. **10m Observations of Perseus Cluster.** *Proceedings of the 28th International Cosmic Ray Conference, Pune, India*, 2005.

R. Atkins, & the VERITAS Collaboration including Kenny, G.E. 2005. **10m Observations of the Cygnus Arm.** *Proceedings of the 28th International*

Cosmic Ray Conference, Pune, India, 2005.

J. Grube, & the VERITAS Collaboration including Kenny, G.E. 2005. **Spectral Monitoring of Mrk-421.** *Proceedings of the 28th International Cosmic Ray Conference, Pune, India*, 2005.

J. Holder, & the VERITAS Collaboration including Kenny, G.E. 2005. **Status and performance of the First VERITAS Telescope.** *Proceedings of the 28th International Cosmic Ray Conference, Pune, India*, 2005.

R. Rebillot, & the VERITAS Collaboration including Kenny, G.E. 2005. **Intensive Multiwavelength Observations of the Blazar Mrk421 in December 2002 and January 2003.** *Proceedings of the 28th International Cosmic Ray Conference, Pune, India*, 2005.

J. Kildea, & the VERITAS Collaboration 2003. **A Search for Pulsed TeV Gamma-Ray Emission from the Crab Pulsar using the Whipple High Resolution GRANITE III Camera.** *Proceedings of the 28th International Cosmic Ray Conference, Tsukuba,* pp. 2377-2380.

T.A. Hall, & the VERITAS Collaboration including Kenny, G.E. 2003. **Very High Energy Observations of PSR B1823-13.** *Proceedings of the 28th International Cosmic Ray Conference, Tsukuba,* pp. 2497-2500.

K. Kosack, & the VERITAS Collaboration including Kenny, G.E. 2003. **TeV Observations of the Galactic Center.** *Proceedings of the 28th International Cosmic Ray Conference, Tsukuba,* pp. 2513-2516.

S. Le Bohec, & the VERITAS Collaboration including Kenny, G.E. 2003. **Search for a WIMP annihilation signature in the core of the globular cluster M15.** *Proceedings of the 28th International Cosmic Ray Conference, Tsukuba,* pp. 2521-2524.

G. Walker, & the VERITAS Collaboration including Kenny, G.E. 2003. **Whipple Telescope Observations of Potential TeV Gamma-Ray Sources Found by the Tibet Air Shower Array.** *Proceedings of the 28th International Cosmic Ray Conference, Tsukuba,* pp. 2563-2566.

D. Horan, & the VERITAS Collaboration including Kenny, G.E. 2003. **VHE Observations of BL Lacertae Objects: 1995-2000.** *Proceedings of the 28th International Cosmic Ray Conference, Tsukuba,* pp. 2567-2570.

I. de la Calle-Perez, & the VERITAS Collaboration including Kenny, G.E. 2003. **Search for Very High Energy Gamma Rays from an X-ray Selected Blazar sample.** *Proceedings of the 28th International Cosmic Ray Conference, Tsukuba,* pp. 2571-2574.

A. Falcone, & the VERITAS Collaboration including Kenny, G.E. 2003. **Search for TeV Emission at the Location of Milagro Sky Survey Hot Spot Using the Whipple Gamma-Ray Telescope.** *Proceedings of the 28th International Cosmic Ray Conference, Tsukuba,* pp. 2579-2582.

P.F. Rebillot, & the VERITAS Collaboration including Kenny, G.E. 2003. **Intensive TeV Gamma-Ray and X-Ray Observations of the Blazar**

Mrk 421 in December 2002 and January 2003. *Proceedings of the 28th International Cosmic Ray Conference, Tsukuba,* pp. 2599-2602.

F. Krennrich, & the VERITAS Collaboration including Kenny, G.E. 2003. **Hourly Spectral Variability of Mrk 421.** *Proceedings of the 28th International Cosmic Ray Conference, Tsukuba,* pp. 2603-2606.

J. Holder, & the VERITAS Collaboration including Kenny, G.E. 2003. **Whipple observations of 1ES1959+650: an Update.** *Proceedings of the 28th International Cosmic Ray Conference, Tsukuba,* pp. 2619-2622.

S. LeBohec, & the VERITAS Collaboration including Kenny, G.E. 2003. **Observation of M87 with the Whipple 10m telescope.** *Proceedings of the 28th International Cosmic Ray Conference, Tsukuba,* pp. 2627-2630.

T. Nagai, & the VERITAS Collaboration including Kenny, G.E. 2003. **Observations of Starburst Galaxies.** *Proceedings of the 28th International Cosmic Ray Conference, Tsukuba,* pp. 2635-2638.

D. Horan, & the VERITAS Collaboration including Kenny, G.E. 2003. **Observations of H1426+428 from 1999 to 2002 with The Whipple Observatory 10 m Telescope.** *Proceedings of the 28th International Cosmic Ray Conference, Tsukuba,* pp. 2647-2650.

V.V. Vassiliev, & the VERITAS Collaboration including Kenny, G.E. 2003. **Search for TeV annihilation radiation from supersymmetric dark matter in nearby galaxies.** *Proceedings of the 28th International Cosmic*

Ray Conference, Tsukuba, pp. 2679-2682

S.P. Wakely, & the VERITAS Collaboration including Kenny, G.E. 2003. **The VERITAS Prototype.** *Proceedings of the 28th International Cosmic Ray Conference, Tsukuba,* pp. 2803-2806.

Appendix C

Data files used

***ON* run id**	***OFF* run id**	**Date**
25505	25506	031022
25526	25527	031023
25738	25739	031120
25740	25741	031120
25759	25760	031121
25761	25762	031121
25763	25764	031121
25781	25782	031122
25783	25784	031122
25828	25829	031124

Table C.1: *ON/OFF* data used in the in the iterative deconvolution analysis of the Crab Nebula Cherenkov images.

***ON* run id**	***OFF* run id**	**Date**
cr5117	cr5116	901015
cr5118	cr5119	901015
cr5148	cr5149	901016
cr5150	cr5151	901016
cr5152	cr5153	901016
cr5229	cr5230	901021
cr5231	cr5232	901021
cr5255	cr5256	901022
cr5257	cr5258	901022
cr5259	cr5260	901022
cr5261	cr5262	901022
cr5281	cr5282	901023
cr5283	cr5284	901023
cr5285	cr5286	901023
cr5287	cr5288	901023
cr5311	cr5312	901024
cr5314	cr5315	901024
cr5336	cr5335	901025
cr5339	cr5338	901025
cr5351	cr5352	901026
cr5353	cr5354	901026
cr5355	cr5356	901026
cr5389	cr5388	901028
cr5397	cr5396	901029
cr5399	cr5398	901029
cr5820	cr5821	901219
cr5827	cr5828	901219
cr5850	cr5851	901220
cr5852	cr5853	901220
cr5854	cr5855	901220
cr5939	cr5940	910113
cr5941	cr5942	910113
cr6006	cr6007	910118
cr6008	cr6009	910118
cr6028	cr6029	910119
cr6030	cr6031	910119
cr6032	cr6033	910119
cr6034	cr6035	910119

Table C.2: *ON/OFF* on-axis Crab Nebula data files.

ON **run id**	***OFF*** **run id**	**Date**
co5461	co5462	901113
co5463	co5464	901113
co5465	co5466	901113
co5480	co5481	901114
co5500	co5501	901115
co5502	co5503	901115
co5504	co5505	901115
co5506	co5507	901115
co5508	co5509	901115
co5589	co5590	901116
co5591	co5592	901116
co5615	co5616	901116
co5617	co5618	901116

Table C.3: *ON/OFF* off-axis Crab Nebula data files.

***ON* run id**	***OFF* run id**	**Date**
cy1920	cy1921	890510
cy1939	cy1938	890512
cy1946	cy1947	890513
cy2065	cy2064	890607
cy2082	cy2081	890609
cy2086	cy2085	890609
cy2093	cy2094	890610
cy2095	cy2096	890610
cy2103	cy2104	890611
cy2105	cy2106	890611
cy2111	cy2112	890612
cy2129	cy2128	890614
cy2363	cy2362	890925
cy2394	cy2395	890927
cy2412	cy2413	890928
cy2429	cy2430	890929
cy2431	cy2432	890929
cy2449	cy2448	890930
cy2451	cy2450	890930
cy2453	cy2452	890930
cy2473	cy2472	891001
cy2474	cy2475	891001
cy2476	cy2477	891001
cy2495	cy2496	891002
cy2497	cy2498	891002
cy2570	cy2569	891023
cy2571	cy2572	891023
cy2573	cy2574	891023
cy2587	cy2588	891024
cy2589	cy2590	891024
cy2607	cy2608	891025
cy2609	cy2610	891025
cy2626	cy2627	891027
cy2628	cy2629	891027
cy2648	cy2649	891028

Table C.4: *ON/OFF* TeV J2032+4130 data files (continued on next page).

ON **run id**	***OFF*** **run id**	**Date**
cy2650	cy2651	891028
cy2673	cy2674	891029
cy2675	cy2676	891029
cy2695	cy2696	891030
cy2697	cy2698	891030
cy2734	cy2735	891102
cy2755	cy2756	891103
cy2888	cy2889	891122
cy4724	cy4725	900725
cy4726	cy4727	900725
cy4730	cy4731	900725
cy4732	cy4733	900725
cy4755	cy4756	900727
cy4767	cy4768	900728
cy4804	cy4805	900819
cy4806	cy4807	900819
cy4808	cy4809	900819
cy4810	cy4811	900819
cy4812	cy4813	900819
cy4846	cy4847	900822
cy4857	cy4856	900823
cy4859	cy4858	900823
cy4861	cy4860	900823
cy4870	cy4869	900824
cy4872	cy4871	900824
cy4874	cy4873	900824
cy4876	cy4875	900824
cy4878	cy4877	900824
cy4887	cy4888	900825
cy4889	cy4890	900825
cy4891	cy4892	900825
cy4893	cy4894	900825
cy4895	cy4896	900825
cy4905	cy4906	900826
cy4907	cy4908	900826

Table C.5: *ON/OFF* TeV J2032+4130 data files (continued on next page).

ON **run id**	***OFF*** **run id**	**Date**
cy4909	cy4910	900826
cy4911	cy4912	900826
cy4924	cy4923	900911
cy4926	cy4925	900911
cy5026	cy5027	901010
cy5029	cy5028	901010
cy5054	cy5055	901013
cy5076	cy5077	901014
cy5101	cy5102	901015
cy5128	cy5127	901016
cy5131	cy5132	901016
cy5212	cy5211	901021
cy5213	cy5214	901021

Table C.6: *ON/OFF* TeV J2032+4130 data files.

Bibliography

1 Abdo, A. A., et al. 2007, *Astrophys. J. Lett.*, 664, L91

2 Abraham, J., et al. 2007, *Science*, 318, 938

3 Aharonian, F., et al. 2001, *Astronomy and Astrophysics*, 370, 112

4 Aharonian, F., et al. 2002, *Astronomy and Astrophysics*, 393, L37

5 Aharonian, F., et al. 2003, *Astronomy and Astrophysics*, 403, L1

6 Aharonian, F., et al. 2004, *Astronomy and Astrophysics*, 425, L13

7 Aharonian, F., et al. 2005a, *Science*, 307, 1938

8 Aharonian, F., et al. 2005b, *Astronomy and Astrophysics*, 437, L7

9 Aharonian, F., et al. 2005c, *Astronomy and Astrophysics*, 435, L17

10 Aharonian, F., et al. 2005d, *Astronomy and Astrophysics*, 442, 1

11 Aharonian, F., et al. 2005e, *Science*, 309, 746

12 Aharonian, F., et al. 2005f, *Astronomy and Astrophysics*, 436, L17

13 Aharonian, F., et al. 2005g, *Astronomy and Astrophysics*, 432, L9

14 Aharonian, F., et al. 2005h, *Astronomy and Astrophysics*, 439, 1013

15 Aharonian, F., et al. 2005i, *Astronomy and Astrophysics*, 431, 197

16 Aharonian, F., et al. 2005j, *Astronomy and Astrophysics*, 437, 135

17 Aharonian, F., et al. 2006a, *Nature*, 440, 1018

18 Aharonian, F., et al. 2006b, *Astronomy and Astrophysics*, 456, 245

19 Aharonian, F., et al. 2006c, *Astronomy and Astrophysics*, 448, L19

20 Aharonian, F., et al. 2006d, *Astronomy and Astrophysics*, 448, L43

21 Aharonian, F., et al. 2006e, *Phys. Rev. Lett.*, 97, 221102

22 Aharonian, F., et al. 2006f, *Astrophys. J.*, 636, 777

23 Aharonian, F., et al. 2007a, *Astronomy and Astrophysics*, 472, 489

24 Aharonian, F., et al. 2007b, *Astronomy and Astrophysics*, 467, 1075

25 Aharonian, F., Akhperjanian, A. G., Bazer-Bachi, A. R., & et al. 2006g, *Science*, 314, 1424

26 Aharonian, F. A. 2004, Very high energy cosmic gamma radiation : a crucial window on the extreme Universe (River Edge, NJ: World Scientific Publishing,2004)

27 Aharonian, F. A., & Atoyan, A. M. 1998a, *New Astronomy Review*, 42, 579

28 Aharonian, F. A., & Atoyan, A. M. 1998b, in Neutron Stars and Pulsars: Thirty Years after the Discovery, ed. N. Shibazaki, 439

29 Albert, J., et al. 2006a, *Astrophys. J. Lett.*, 642, L119

30 Albert, J., et al. 2006b, *Astrophys. J. Lett.*, 648, L105

31 Albert, J., et al. 2006c, *Science*, 312, 1771

32 Albert, J., et al. 2007a, *Astrophys. J.*, 663, 125

33 Albert, J., et al. 2007b, *Astrophys. J. Lett.*, 665, L51

34 Allen, G. E., et al. 1997, *Astrophys. J. Lett.*, 487, L97

35 Atkins, R., et al. 2004, *Astrophys. J.*, 608, 680

36 Atoyan, A., Buckley, J., & Krawczynski, H. 2006, *Astrophys. J. Lett.*, 642, L153

37 Atoyan, A., & Dermer, C. D. 2004, *Astrophys. J. Lett.*, 617, L123

38 Atoyan, A. M., & Aharonian, F. A. 1999, *Monthly Notices of the Royal Astr. Soc.*, 302, 253

39 Baganoff, F. K., Maeda, Y., & Morris, M. 2003, *Astrophys. J.*, 591, 891

40 Baixeras, C., et al. 2005, in Proc. 29^{th} Int. Cosmic Ray Conf., Pune, Vol. 5, 227

41 Barthelmy, S. D., et al. 2001, in American Institute of Physics Conference Series, Vol. 587, Gamma 2001: Gamma-Ray Astrophysics, ed. S. Ritz, N. Gehrels, & C. R. Shrader, 781

42 Beilicke, M., et al. 2005a, in Proc. 29^{th} Int. Cosmic Ray Conf., Pune, Vol. 4, 147

43 Beilicke, M., Khelifi, B., Masterson, C., de Naurois, M., Raue, M., Rolland, L., Schlenker, S., & Hess Collaboration. 2005b, in American Institute of Physics Conference Series, Vol. 745, High Energy Gamma-Ray Astronomy, ed. F. A. Aharonian, H. J. Völk, & D. Horns, 347

44 Bell, A. R. 1978, *Monthly Notices of the Royal Astr. Soc.*, 182, 147

45 Bennett, K. 1990, Nuclear Physics B Proceedings Supplements, 14, 23

46 Berezinskii, V. S., Bulanov, S. V., Dogiel, V. A., & Ptuskin, V. S. 1990, Astrophysics of cosmic rays (Amsterdam: North-Holland, 1990, edited by Ginzburg, V.L.)

47 Berger, E., Kulkarni, S. R., & Frail, D. A. 2004, *Astrophys. J.*, 612, 966

48 Bird, D. J., et al. 1995, *Astrophys. J.*, 441, 144

49 Blackett, P. 1948, Physical Society Gassiot Committee Report 34

50 Blumenthal, G. R., & Gould, R. J. 1970, *Reviews of Modern Physics*, 42, 237

51 Bosch-Ramon, V., Romero, G. E., & Paredes, J. M. 2006, *Astronomy and Astrophysics*, 447, 263

52 Bradbury, S. M., & Rose, H. J. 2002, *Nuclear Instruments and Methods is Physics Research A*, 481, 521

53 Buckley, J. 2007, Agis: (advanced gamma-ray imaging system) toward the future of very high energy gamma-ray astronomy, Presentation

54 Buckley, J. H., et al. 1998, *Astronomy and Astrophysics*, 329, 639

55 Butt, Y. 2007a, ArXiv e-prints: 0705.0189, 705

56 Butt, Y., et al. 2003, in Bulletin of the American Astronomical Society, Vol. 35, Bulletin of the American Astronomical Society, 863

57 Butt, Y. M. 2007b, *Nature*, 446, 986

58 Butt, Y. M., et al. 2006a, ArXiv Astrophysics e-prints: astro-ph/0611731

59 Butt, Y. M., et al. 2007, ArXiv Astrophysics e-prints: astro-ph/0703017

60 Butt, Y. M., Drake, J., Benaglia, P., Combi, J. A., Dame, T., Miniati, F., & Romero, G. E. 2006b, *Astrophys. J.*, 643, 238

61 Bykov, A. M. 2001, *Space Science Reviews*, 99, 317

62 Bykov, A. M., & Fleishman, G. D. 1992, *Monthly Notices of the Royal Astr. Soc.*, 255, 269

63 Catanese, M., et al. 1998, *Astrophys. J.*, 501, 616

64 Cawley, M. F., et al. 1990, *Experimental Astronomy*, 1, 173

65 Cawley, M. F., & Weekes, T. C. 1995, *Experimental Astronomy*, 6, 7

66 Cesarsky, C. J., & Montmerle, T. 1983, *Space Science Reviews*, 36, 173

67 Chadwick, P. M., et al. 1998, *Astroparticle Physics*, 9, 131

68 Chadwick, P. M., et al. 1999, *Astrophys. J.*, 513, 161

69 Cheng, K. S., Ho, C., & Ruderman, M. 1986a, *Astrophys. J.*, 300, 500

70 Cheng, K. S., Ho, C., & Ruderman, M. 1986b, *Astrophys. J.*, 300, 522

71 Cherenkov, P. A., Frank, I. M., & Tamm, I. 1958, *Nature*, 182, 1275

72 Clark, G. W., Garmire, G. P., & Kraushaar, W. L. 1968, *Astrophys. J. Lett.*, 153, L203

73 Cortina, J., et al. 2005, in Proc. 29th Int. Cosmic Ray Conf., Pune, Vol. 5, 359

74 Cowsik, R., & Sarkar, S. 1980, in Non-Solar Gamma-Rays, ed. R. Cowsik & R. D. Wills, 57

75 Daugherty, J. K., & Harding, A. K. 1982, *Astrophys. J.*, 252, 337

76 Daugherty, J. K., & Harding, A. K. 1994, *Astrophys. J.*, 429, 325

77 Daugherty, J. K., & Harding, A. K. 1996, *Astrophys. J.*, 458, 278

78 Davies, J. M., & Cotton, E. S. 1957, *Solar Energy Sci. Eng.*, 1, 16

79 de Jager, O. C., Harding, A. K., Michelson, P. F., Nel, H. I., Nolan, P. L., Sreekumar, P., & Thompson, D. J. 1996, *Astrophys. J.*, 457, 253

80 Djannati-Atai, A., et al. 2007, in To appear in Proc. 30^{th} Int. Cosmic Ray Conf., Merida

81 Domingo-Santamaría, E., & Torres, D. F. 2006, *Astronomy and Astrophysics*, 448, 613

82 Dowdall, C. 2003, M.Sc thesis, Galway-Mayo Institute of Technology (unpublished)

83 Drury, L. O., Aharonian, F. A., & Voelk, H. J. 1994, *Astronomy and Astrophysics*, 287, 959

84 Duke, C. 2005, Private communication

85 Duke, C., & LeBohec, S. 2006, http://www.physics.utah.edu/gammaray/GrISU

86 Dunlea, S. 2001, Ph.D. thesis, National Universtity of Ireland (unpublished)

87 Dunlea, S., Moriarty, P., & Fegan, D. J. 2001, in Proc. 27^{th} Int. Cosmic Ray Conf., Hamburg, 2939

88 Ellison, D. C., Reynolds, S. P., & Jones, F. C. 1990, *Astrophys. J.*, 360, 702

89 Enomoto, R., et al. 2002, *Astropart. Phys.*, 16, 235

90 Enomoto, R., et al. 2006, *Astrophys. J.*, 638, 397

91 Feenberg, E., & Primakoff, H. 1948, *Physical Review*, 73, 449

92 Fegan, D. J. 1996, *Space Science Reviews*, 75, 137

93 Fegan, D. J. 1997, *Journal of Physics G Nuclear Physics*, 23, 1013

94 Fegan, D. J., McLaughlin, D., Clear, J., Cawley, M. F., & Porter, N. A. 1983, *Nuclear Instruments and Methods*, 211, 179

95 Fegan, S. J. 2003, Ph.D. thesis, The University of Arizona (unpublished)

96 Fichtel, C. E. 1973, in *Bulletin of the American Astronomical Society*, Vol. 5, 342

97 Fichtel, C. E., Hartman, R. C., Kniffen, D. A., Thompson, D. J., Ogelman, H., Ozel, M. E., Tumer, T., & Bignami, G. F. 1975, *Astrophys. J.*, 198, 163

98 Finley, J. P., et al. 2001, in Proc. 27^{th} Int. Cosmic Ray Conf., Hamburg, Vol. 7, 2827

99 Flix, J., et al. 2004, in Astronomical Society of the Pacific Conference Series, Vol. 327, Satellites and Tidal Streams, ed. F. Prada, D. Martinez Delgado, & T. J. Mahoney, 52

100 Fonseca, V. 1999, *Acta Physica Polonica B*, 30, 2331

101 Gaidos, J. A., et al. 1996, *Nature*, 383, 319

102 Gaisser, T. K. 1990, Cosmic Rays and Particle Physics (Cambridge, Cambridge University Press)

103 Genzel, R., & Townes, C. H. 1987, *Ann. Rev. Astron. Astrophys.*, 25, 377

104 Gold, T. 1968, *Nature*, 218, 731

105 Goldreich, P., & Julian, W. H. 1969, *Astrophys. J.*, 157, 869

106 Hanbury-Brown, R. 1966, *Philips Tech Rev*, 27, 141

107 Hand, D. J. 1982, Kernel Discriminant Analysis (Somerset, N.J.: John Wiley and Sons, Inc.)

108 Harding, A. K. 1981, *Astrophys. J.*, 245, 267

109 Harris, J. L. 1966, *J. Opt. Soc. Am.*, 56, 569

110 Hartkopf, W. I., Mason, B. D., Gies, D. R., Ten Brummelaar, T., McAlister, H. A., Moffat, A. F. J., Shara, M. M., & Wallace, D. J. 1999, *Astron. J.*, 118, 509

111 Hartman, R. C., et al. 1999, *Astrophys. J. Suppl.*, 123, 79

112 Hartman, R. C., Kniffen, D. A., Thompson, D. J., Fichtel, C. E., Ogelman, H. B., Tumer, T., & Ozel, M. E. 1979, *Astrophys. J.*, 230, 597

113 Hayakawa, S. 1952, *Prog. Theo. Phys.*, 8, 571

114 Hermann, G. 1997, in Very High Energy Phenomena in the Universe; Moriond Workshop, ed. Y. Giraud-Heraud & J. Tran Thanh van, 141

115 Hermann, G., Hofmann, W., Schweizer, T., Teshima, M., & CTA consortium, f. t. 2007, ArXiv e-prints, 709

116 Hess, V. F. 1912, *Phys.Zeitschr.*, 13, 1084

117 Hillas, A. M. 1985, in Proc. 19th Int. Cosmic Ray Conf., La Jolla, Vol. 3, 445

118 Hillas, A. M. 1996, *Space Science Reviews*, 75, 17

119 Hillas, A. M. 1997, Collobration communication

120 Hillas, A. M., et al. 1998, *Astrophys. J.*, 503, 744

121 Hillier, R. 1984, Gamma ray astronomy (Oxford, Clarendon Press, 1984, 210 p.)

122 Hinton, J. A. 2004, *New Astronomy Review*, 48, 331

123 Hirotani, K. 2001, *Astrophys. J.*, 549, 495

124 Hofmann, W., et al. 2000, in American Institute of Physics Conference Series, Vol. 515, American Institute of Physics Conference Series, ed. B. L. Dingus, M. H. Salamon, & D. B. Kieda, 500

125 Holder, J., et al. 2006a, *Astroparticle Physics*, 25, 391

126 Holder, J., et al. 2006b, ArXiv Astrophysics e-prints: astro-ph/0611598

127 Holder, J., et al. 2003, *Astrophys. J. Lett.*, 583, L9

128 Holliday, K. 1999, Introductory Astronomy (Introductory Astronomy, by Keith Holliday, pp. 326. ISBN 0-471-98331-4. Wiley-VCH , January 1999.)

129 Horan, D., et al. 2002, *Astrophys. J.*, 571, 753

130 Horns, D., Hoffmann, A. I. D., Santangelo, A., Aharonian, F. A., & Rowell, G. P. 2007, *Astronomy and Astrophysics*, 469, L17

131 Hughes, S. B. 2007, *International Journal of Modern Physics A*, 22, 2461

132 Jelley, J. V., & Porter, N. A. 1963, *Quarterly Journal of the Royal Astronomical Society.*, 4, 275

133 Jones, T. W., et al. 1998, *Publ. Astr. Soc. Pacific*, 110, 125

134 Kanbach, G., et al. 1988, *Space Science Reviews*, 49, 69

135 Kertzman, M. P., & Sembroski, G. H. 1994, *Nucl. Instrum. Methods A*, A343, 629

136 Kieda, D. B. 2007, in American Institute of Physics Conference Series, Vol. 921, American Institute of Physics Conference Series, 80

137 Kifune, T., et al. 1995, *Astrophys. J. Lett.*, 438, L91

138 Kildea, J. 2002, Ph.D. thesis, National Universtity of Ireland, Dublin (unpublished)

139 Kildea, J. 2005, Private communication

140 Konopelko, A., et al. 2007, *Astrophys. J.*, 658, 1062

141 Kosack, K., et al. 2007, in To appear in Proc. 30^{th} Int. Cosmic Ray Conf., Merida

142 Kosack, K., et al. 2004, *Astrophys. J. Lett.*, 608, L97

143 Kraushaar, W., Clark, G. W., Garmire, G., Helmken, H., Higbie, P., & Agogino, M. 1965, *Astrophys. J.*, 141, 845

144 Kraushaar, W. L., Clark, G. W., Garmire, G. P., Borken, R., Higbie, P., Leong, V., & Thorsos, T. 1972, *Astrophys. J.*, 177, 341

145 Krawczynski, H., Coppi, P. S., & Aharonian, F. 2002, *Monthly Notices of the Royal Astr. Soc.*, 336, 721

146 Krennrich, F., et al. 2001, Collobration communication

147 Lang, M. J., et al. 1991, in Proc. 22^{nd} Int. Cosmic Ray Conf., Dublin, Vol. 1, 204

148 Lang, M. J., et al. 2004, *Astronomy and Astrophysics*, 423, 415

149 Lemiere, A., et al. 2007, in To appear in Proc. 30^{th} Int. Cosmic Ray Conf., Merida

150 Lessard, R. W., et al. 1999, in Astronomical Society of the Pacific Conference Series, Vol. 171, LiBeB Cosmic Rays, and Related X- and Gamma-Rays, ed. R. Ramaty, E. Vangioni-Flam, M. Cassé, & K. Olive, 170

151 Lessard, R. W., Buckley, J. H., Connaughton, V., & Le Bohec, S. 2001, *Astroparticle Physics*, 15, 1

152 Lewis, D. A. 1990, *Experimental Astronomy*, 1, 213

153 Lewis, D. A., Biller, S., Cawley, M. F., Fishman, J., Kaaret, P., & Mattox, J. 1998, Internal VERITAS Coll. Memo (unpublished)

154 Li, T.-P., & Ma, Y.-Q. 1983, *Astrophys. J.*, 272, 317

155 Livio, M., & Waxman, E. 2000, *Astrophys. J.*, 538, 187

156 Lozinskaya, T. A., Pravdikova, V. V., & Finoguenov, A. V. 2002, *Astronomy Letters*, 28, 223

157 Lucy, L. B. 1974, *Astron. J.*, 79, 745

158 Mannheim, K. 1993, *Astronomy and Astrophysics*, 269, 67

159 Maraschi, L., Ghisellini, G., & Celotti, A. 1992, *Astrophys. J. Lett.*, 397, L5

160 Martí, J., Paredes, J. M., Ishwara Chandra, C. H., & Bosch-Ramon, V. 2007, *Astronomy and Astrophysics*, 472, 557

161 Mattox, J., et al. 1996, *Memorie della Societa Astronomica Italiana*, 67, 607

162 McGlamery, B. L. 1966, *J. Opt. Soc. Am.*, 57, 293

163 McGlamery, B. L., & Gray, P. 1963, *Operations Research*, 12, 175

164 McLaughlin, M. A., Mattox, J. R., Cordes, J. M., & Thompson, D. J. 1996, *Astrophys. J.*, 473, 763

165 Mereghetti, S., et al. 2000, in American Institute of Physics Conference Series, Vol. 515, American Institute of Physics Conference Series, ed. B. L. Dingus, M. H. Salamon, & D. B. Kieda, 467

166 Mohanty, G. 1995, Ph.D. thesis, Iowa State University (unpublished)

167 Montmerle, T. 1979, *Astrophys. J.*, 231, 95

168 Moriarty, P., Masterson, C., Fegan, D. J., Buckley, J. H., Catanese, M., Quinn, J., Reynolds, P. T., & Krennrich, F. 1997, *Astropart. Phys.*, 7, 315

169 Moriarty, P., & Samuelson, F. W. 2000, in Proc. GeV-TeV Gamma-ray Astrophysics Workshop, Snowbird, Utah, 1999. AIP Conf. Proc., Vol. 515, 338

170 Morrison, P. 1958, *Il Nuovo Cimento*, 7, 858

171 Morselli, A. 2003, *Chinese Journal of Astronomy and Astrophysics Supplement*, 3, 523

172 Mukherjee, R., et al. 1997, *Astrophys. J.*, 490, 116

173 Mukherjee, R., Gotthelf, E. V., & Halpern, J. P. 2006, *Astrophysics. Space Sci.*, 158

174 Muraishi, H., et al. 2000, *Astronomy and Astrophysics*, 354, L57

175 Neshpor, I. Y., et al. 1995, in Proc. 24^{th} Int. Cosmic Ray Conf., Rome, Vol. 2, 385

176 Nishiyama, T. 1999, in Proc. 26^{th} Int. Cosmic-ray Conf., Salt Lake City, 370

177 O'Flaherty, K. S., et al. 1992, *Astrophys. J.*, 396, 674

178 Pacini, F. 1967, *Nature*, 216, 567

179 Paredes, J. M., Martí, J., Ishwara Chandra, C. H., & Bosch-Ramon, V. 2007, *Astrophys. J. Lett.*, 654, L135

180 Paredes, J. M., Martí, J., Ribó, M., & Massi, M. 2000, *Science*, 288, 2340

181 Protheroe, R. J., Donea, A.-C., & Reimer, A. 2003, *Astroparticle Physics*, 19, 559

182 Punch, M., et al. 1992, *Nature*, 358, 477

183 Punch, M., et al. 1991, in Proc. 22^{nd} Int. Cosmic Ray Conf., Dublin, 464

184 Quinn, J., et al. 1996, *Astrophys. J. Lett.*, 456, L83

185 Reimer, A. 2003, in Proc. 28^{th} Int. Cosmic Ray Conf., Tsukuba, Vol. 4, 2505

186 Reynolds, P. T., et al. 1993, *Astrophys. J.*, 404, 206

187 Reynolds, S. P., & Ellison, D. C. 1992, *Astrophys. J. Lett.*, 399, L75

188 Richardson, W. 1972, *Journal of the Optical Society of America*, 62, 55

189 Ricort, G., Lanteri, H., Aristidi, E., & Aime, C. 1993, *Pure Applied Optics*, 2, 125

190 Rodgers, A. J. 1997, Ph.D. thesis, University of Leeds (unpublished)

191 Romani, R. W. 1996, *Astrophys. J.*, 470, 469

192 Romani, R. W., & Yadigaroglu, I.-A. 1995, *Astrophys. J.*, 438, 314

193 Romero, G. E., Torres, D. F., Kaufman Bernadó, M. M., & Mirabel, I. F. 2003, *Astronomy and Astrophysics*, 410, L1

194 Rose, H., et al. 1995, in Proc. 24^{th} Int. Cosmic Ray Conf., Rome, Vol. 3, 766

195 Ruderman, M. A., & Sutherland, P. G. 1975, *Astrophys. J.*, 196, 51

196 Salvati, M. 1973, *Astronomy and Astrophysics*, 27, 413

197 Samuelson, F. W. 1999, Ph.D. thesis, Iowa State University (unpublished)

198 Schödel, R., et al. 2002, *Nature*, 419, 694

199 Schroedter, M. 2004, Ph.D. thesis, the University of Arizona (unpublished)

200 Schroedter, M. 2005, Private communication

201 Scott, D. 1992, Multivatiate Density Estimation (New York: John Wiley and Sons, Inc)

202 Sembroski, G. H. 2005, Private communication

203 Smith, A. J. 2005, in Proc. 29^{th} Int. Cosmic Ray Conf., Pune, Vol. 10, 227

204 Smith, A. J., et al. 2007, *Journal of Physics Conference Series*, 60, 131

205 Sturner, S. J., & Dermer, C. D. 1994, *Astrophys. J. Lett.*, 420, L79

206 Sturrock, P. A. 1971, *Astrophys. J.*, 164, 529

207 Swanenburg, B. N., et al. 1981, *Astrophys. J. Lett.*, 243, L69

208 Swordy, S. 2007, *Journal of Physics Conference Series*, 60, 139

209 Tanimori, T., et al. 1998, *Astrophys. J. Lett.*, 497, L25

210 Tavani, M., et al. 1997, *Astrophys. J. Lett.*, 479, L109

211 Torres, D. R., Pessah, M. E., & Romero, G. E. 2001, *Astronomische Nachrichten*, 322, 223

212 Tsuchiya, K. 2004, *Astrophys. J. Lett.*, 606, 115

213 Urry, C. M., & Padovani, P. 1995, *Publ. Astr. Soc. Pacific*, 107, 803

214 Vassiliev, V., & Fegan, S. 2005, ArXiv Astrophysics e-prints: astro-ph/0511342

215 Wagner, R. M., et al. 2005, in Proc. 29th Int. Cosmic Ray Conf., Pune, Vol. 4, 163

216 Walker, G. 2004, Ph.D. thesis, University of Utah (unpublished)

217 Weekes, T. 2007, APS Meeting Abstracts, 3002

218 Weekes, T. C. 1988, *Physics Reports*, 160, 1

219 Weekes, T. C. 1997, in Very High Energy Phenomena in the Universe; Moriond Workshop, ed. Y. Giraud-Heraud & J. Tran Thanh van, 161

220 Weekes, T. C. 1999, ArXiv Astrophysics e-prints: astro-ph/9903263

221 Weekes, T. C. 2003, Very High Energy Gamma-Ray Astronomy (Bristol: Institute of Physics Publishing)

222 Weekes, T. C., et al. 1989, *Astrophys. J.*, 342, 379

223 Weekes, T. C., et al. 2002, *Astropart. Phys.*, 17, 221

224 Weekes, T. C., Fazio, G. G., Helmken, H. F., O'Mongain, E., & Ricke, G. H. 1972, *Astrophys. J.*, 174, 165

225 Weekes, T. C., & Turver, K. E. 1977, in ESA Special Publication, Vol. 124, Recent Advances in Gamma-Ray Astronomy, ed. R. D. Wills & B. Battrick, 279

226 Weiler, K. W. 1978, *Memorie della Societa Astronomica Italiana*, 49, 545

227 Wilson, A. 2001, in HST Proposal, 5471

228 Winkler, C., et al. 2003, *Astronomy and Astrophysics*, 411, L1

229 Yamazaki, R., Kohri, K., Bamba, A., Yoshida, T., Tsuribe, T., & Takahara, F. 2006, *Monthly Notices of the Royal Astr. Soc.*, 371, 1975

230 Yoshikoshi, T., et al. 1997, *Astrophys. J. Lett.*, 487, L65